Stellingen

behorende bij het proefschrift: *Ontwerp van "the Fancier", een instrument voor fabrikage en analyse van nanostructuren door gecombineerde ionen en elektronen sturing.*

---

1. Beperken van de chromatische bijdrage aan de probe afmeting van een gefocusseerde ionenbundel met een energiefilter leidt tot de hoogste produktiviteit bij nanometer resolutie en optimale bundelenergie.

2. Bij het maken van een afbeelding met een resolutie beter dan 10 nanometer zal meer dan één atomaire laag worden weggesputterd als gebruik wordt gemaakt van ionen.

3. De combinatie van een scannende transmissie elektronen microscoop (STEM) met een secundaire elektronen detector en een gefocusseerde ionenbundel (FIB) maakt het mogelijk een preparaat eerst in SEM mode te bekijken, daarna lokaal dun te maken met de FIB om het in TEM mode te kunnen bekijken, terwijl het preparaat onder ultra hoog vacuüm condities blijft.

4. Bundel geïnduceerd etsen en deponeren met ionen, met een energie kleiner dan 100 keV, resulteert in een grotere produktie-opbrengst per geladen deeltje en een kleinere spreiding van de interactie met het preparaat dan met elektronen met dezelfde energie.

5. De energie om de endotherme reactie tussen preparaat en precursor op gang te brengen, is bepalend voor de produktie-opbrengst en de resolutie van bundel geïnduceerd etsen en deponeren.

6. Met Röntgen foto-elektron spectroscopie (XPS) kan het reactieprincipe van een endotherme reactie tussen preparaat en precursor worden bepaald.

7. In een optisch systeem van een gefocusseerde ionenbundel met een energiefilter op basis van een 90°-afbuiger is geen massafilter nodig om de isotopen van een AuSi of PdBAs bron te kunnen scheiden.

8. Aan de eisen met betrekking tot dynamisch bereik en stabiliteit van de preparaathouder in "the Fancier", met uitzondering van de drift-stabiliteit, is te voldoen zonder actieve stabilisatie.

9. De dienstregeling van openbaar stadsvervoer bevindt zich in een labiel evenwicht.

10. Het Amerikaanse verkeersbord voor slipgevaar, toont slipsporen van een auto die bestuurbaar blijft. De Nederlandse versie van dit bord toont een onbestuurbaar geworden voertuig.

Patrick de Jager
16 juni 1997

Propositions

added to the thesis: *Design of "the Fancier", an Instrument for Fabrication and Analysis of Nanostructures Combining Ion and Electron Regulation.*

---

1. Limiting the chromatic contribution to the probe size of a focused ion beam system with an energy filter leads to the largest productivity at nanometer resolution and optimum beam current.

2. When imaging with a resolution better than 10 nanometers more than one monolayer will be sputtered if ions are used.

3. The combination of a scanning transmission electron microscope (STEM) with a secondary electron detector and a focused ion beam (FIB) makes it possible to image a specimen in SEM mode first, then locally thin it with the FIB in order to image it in TEM mode, while the specimen stays under ultra high vacuum conditions.

4. Beam induced etching and deposition with ions, at an energy less than 100 keV, results in a larger production yield per charged particle and a smaller spreading of the interactions with the specimen than in case of electrons at equal energy.

5. The energy to induce a chemical reaction between specimen and precursor is determining the production yield and the resolution of beam induced etching and deposition.

6. With X-ray photo-electron spectroscopy (XPS) it is possible to determine the reaction principle of an endothermic reaction between specimen and precursor.

7. In case of an optical system of a focused ion beam with an energy filter based on a 90°-deflector a mass filter is not needed to separate the isotopes of a AuSi or PdBAs source.

8. The demands on dynamic range and stability of the specimen holder in "the Fancier", except for drift-stability, can be fulfilled without active stabilization.

9. The timetable of public city transport is unstable.

10. The American road sign for danger of skidding, shows skid marks of a car that is still controllable. The Dutch version of this sign shows a vehicle which is out of control.

Patrick de Jager
June 16, 1997

Design of "the Fancier"

An instrument for Fabrication and Analysis of Nanostructures Combining Ion and Electron Regulation

Design of "the Fancier"

An instrument for Fabrication and Analysis of Nanostructures Combining Ion and Electron Regulation

Ontwerp van "the Fancier"

Een instrument voor fabrikage en analyse van nanostructuren door gecombineerde ionen en elektronen sturing

PROEFSCHRIFT

ter verkrijging van de graad van doctor
aan de Technische Universiteit Delft
op gezag van de Rector Magnificus Prof.dr.ir. J. Blaauwendraad,
in het openbaar te verdedigen ten overstaan van een commissie,
door het College van Dekanen aangewezen,
op maandag 16 juni 1997 te 10.30 uur

door

Pieter Willem Herman DE JAGER

natuurkundig ingenieur
geboren te Rotterdam

Dit proefschrift is goedgekeurd door de promotor:
Prof.dr.ir. P. Kruit

Samenstelling Promotiecommissie:

Rector Magnificus	voorzitter
Prof.dr.ir. P. Kruit	Technische Universiteit Delft, promotor
Prof.dr.ir. E.H.A. Granneman	Technische Universiteit Delft
Prof.dr. A.W. Kleyn	Universiteit van Amsterdam
Prof.dr.ir. A.F. Mehlkopf	Technische Universiteit Delft
Prof.dr. A. van Veen	Technische Universiteit Delft
Dr. L.J. Geerligs	Technische Universiteit Delft
Dr. H.W.P. Koops	Deutsche Telekom Technologie Zentrum

CIP-DATA KONINKLIJKE BIBLIOTHEEK, DEN HAAG

de Jager, P.W.H.

Design of "the Fancier" : An instrument for Fabrication and Analysis of Nanostructures Combining Ion and Electron Regulation / P.W.H. de Jager. - Delft : Delft University Press. - Illustrations.
Thesis Delft University of Technology. - With ref. - With summary in Dutch.
ISBN 90-407-1478-9.
NUGI 812.
Subject headings: physics/particle optics/ion beam pattern generation

Printed in the Netherlands

1. Introduction to nanotechnology

Introduction

How will the world look like if things can be made with details as large as atoms, the building blocks of nature? "If electrical components can be made so small, the 24 parts of the Encyclopaedia Brittanica should fit on the top of a needle", predicted the physicist Richard Feynman in 1959. Sometimes physicists dream of a world where mesoscopic structures can be made as easy as houses. "The technologies that we currently use are still largely based on removing material from a larger block, much as a sculptor carves a statue. However, we may now look forward to significant advances in molecular engineering technologies that will enable us to construct our devices atom by atom, much as a builder constructs a house brick by brick or as nature evolves living cells" (Brodie, 1992). Also Dutch physisists have ideas about nanotechnology. An example (Mooij, 1996): "Het hoogtepunt zal bereikt worden als meerdere met uiterste precisie vervaardigde quantum dots op goed gecontroleerde wijze aan elkaar gekoppeld worden. Met deze technologie zal een echte quantumcomputer kunnen worden gebouwd. De hele schakeling is één quantumsysteem , waarin parallel gerekend wordt op een wijze die in het geheel niet vergelijkbaar is met algorithmen die nu worden gebruikt. Sommige bewerkingen verlopen exponentieel sneller dan in een conventionele computer. Als Quantum DOS 1.0 te koop is, zijn de microscopische en de macroscopische wereld in elkaar gegroeid. De mesoscopische fysica is daarmee verleden tijd." However before that *occurs fabrication techniques for nanostructures have to be developed.*

Not only the products are new, so are the fabrication facilities: all fabrication techniques for nanotechnology have to be invented since the present-day techniques will fail at the nanometer scale. Moving the samples from one machine to the other through air is impossible. The molecules in the air would react with the sample surface and destroy the nanostructures. So all machines have to be connected with vacuum tubes. Everything has to be realized with enormous accuracy: a nanometer structure on a sample of 1 cm^2 means the same as a map of Delft with details smaller than a match.

In this chapter the impact of nanotechnology on physics will be demonstrated with a few examples. But mainly the methods to fabricate these structures will be described since this thesis deals with one of these techniques: focused ion and electron beams; towards new realms in mesoscopic physics.

1.1. Possibilities of nanotechnology

Mesoscopic physics is the study of effects connected with reduced dimensionality in the solid state (Altshuler, 1991). Mesoscopic is everything in between microscopic and macroscopic. More than a few atoms, less material than can be seen with the human eye. Mesoscopic physics origins from a question from the electronic industry: how will the properties of the transistor, the building block of modern electronics, change with continuing miniaturization? It was found that a material of several thousands of atoms - so not microscopic small- has total different fundamental properties than the macroscopic material of 10^{23} atoms.

Therefore two different ways can be foreseen in which new nanofabrication techniques will affect the mesoscopic physics. One is coupled with the continuation and extension of research lines that already exist. Smaller dimensions lead to higher characteristic energies, stronger effects, observability at higher temperatures and in particular to a higher device potential. The underlying concept of nanotechnology stems from the prediction that the accuracy required in materials processing will ultimately reach the extremely high level of the order of one nanometer. Figure 1.1 shows the historical development of the performance of computers, expressed in 10^6 instructions per second. It also shows the improved accuracy of materials processing for these computers (Tanigushi, 1996), expressed in the line width of memory. It can be expected that the

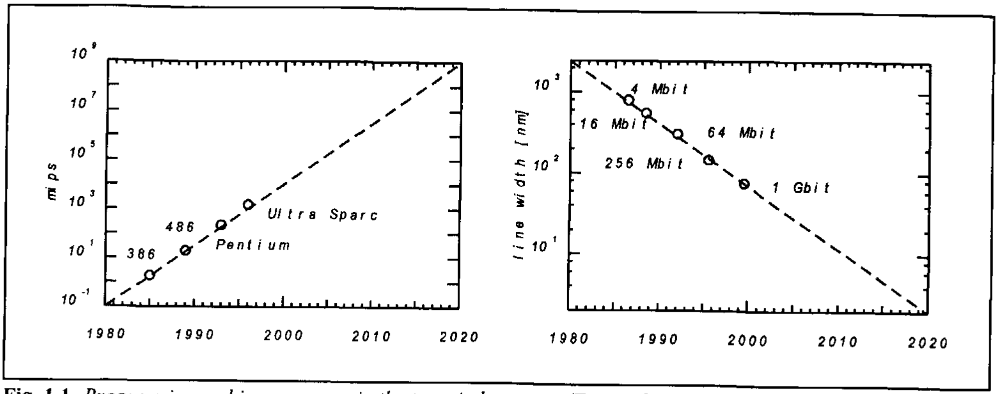

Fig. 1.1. *Progress in machine accuracy in the twentieth century (Tanigushi, 1996).*

attainable processing accuracy reaches the order of nanometers early in the twenty-first century.

The second and most fascinating aspect of the new techniques is the potential for the realization of samples in which essentially and qualitatively new effects will occur. Two examples of these effects will be described shortly. The first example (Harmans, 1994) focusses on the effect a single electron can have on the electrical conductance through a small metallic object. A small metallic grain is embedded inside an insulating environment, e.g. an oxide. Metallic contacts are connected to the structure. Classically, the insulating film will prevent electrons to travel from the contacts to the grain or from the grain to the contacts. Quantum mechanically however a particle can tunnel through the insulating barrier, provided the barrier is not too thick. The electrostatic energy due to the charge Q on the grain with total capacitance C to the contacts is given by

$$U = \frac{Q^2}{2.C} \tag{1.1}$$

If the resistance of the insulating barriers is very large but finite, the number of electrons on the grain is an integer and so the energy required to put the minimum amount of charge, one electron, onto the grain equals

$$U_c = \frac{e^2}{2.C} \tag{1.2}$$

This quantity is called the charging effect. If the capacitance is made very small, by reducing the size of the grain and/or decreasing the temperature, an interesting mesoscopic phenomenon is visible. The current to voltage characteristic does not show a straight line according to the well-known Ohm law but is shows steps. For very small voltages one clearly can see that no current will flow since the energy from the field is too low to transfer a single electron to or from the grain. At larger voltages the current starts to flow rather abruptly in steps. These steps are a consequence of the blockades with 1,2,3... electrons on the grain.

The next example concerns the transport of electrons in a small structure (Harmans, 1994). In the majority of macroscopic cases the fact that electrons do have a wavelength and so an associated phase does not become immediately evident. A structure where this effect becomes apparent has a ring shape, allowing the current to take both arms in traversing it. If an electron is treated as a wave it will split when it enters the ring at one side. The resulting (partial) waves will travel through the two arms of the ring and reunite at the other end. The wave character implies that not only the partial amplitudes will determine the amplitude of the sumwave but just as much the relative phase of the two components. It is effectively electron interference. By a magnetic field through the ring the relative phase can be manipulated according to

$$\Delta\phi = \frac{e}{h}.B.S \qquad (1.3)$$

$\Delta\phi$= phase difference
e= electron charge
h= Plancks constant
B= magnetic field strength
S= area of the ring

The phase difference is commonly called the Aharamov-Bohm phase. If the phase difference is 0 (modulo 2π) there is a maximum probability for the electron wave to travel through the ring or equivalently a minimum resistance of the ring. However if the phase difference is π (modulo 2π) the interference is a destructive one. Summarizing the whole sequence shows that the resistance oscillates between the maximum and minimum value due to the interference of the electron waves when the magnetic field is increased.

These effects are only visible for nanometer sized structures since for larger structures the number of electrons involved is so large that the effect of individual electrons is statistically spread out.

1.2. Fabrication methods for nanostructures

The standard way to produce ultra small devices is by means of a two step approach, see the two rows in figure 1.2. In the first step the pattern is defined in a small chemically inert surface layer, the resist, on top of the Si sample. The transfer of the pattern to the resist is achieved by using the imaging properties of a lens system, more or less like a slide projector, that illuminates a shadow mask having the desired pattern by (ultraviolet) light. Then the wafer is rinsed in a developer, which removes the exposed film. After the remaining resist has been baked, the wafer is etched; where the resist has been removed, the etchant leaves openings in the oxide layer.

In the second step the pattern is transferred into or on the underlying substrate. For example a metal is deposited on the whole surface or the whole wafer is bombarded by ions needed for dopant in a transistor. Finally the unexposed resist, that is left after the first rinsing process, is removed. In this step also the metal on the resist or implanted ions in the resist are removed. The result is deposition on or implantation in the wafer only where there was free excess to the silicon wafer.

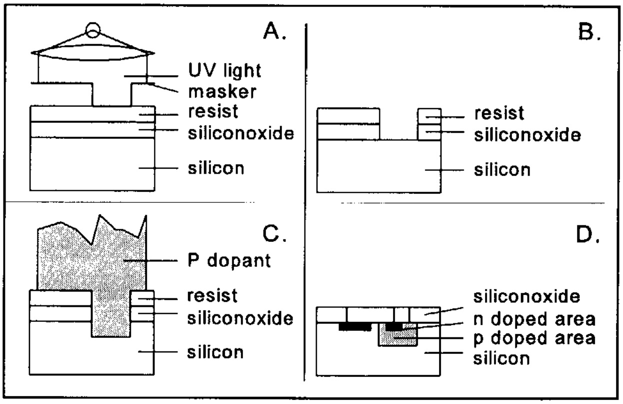

Fig. 1.2. *Conventional fabrication method of an npn-transistor. (a.) light exposure, (b.) etched wafer, (c.) ion implantation, (d.) npn-junction.*

Both steps are essential and must have comparable characteristics with respect to lateral definition and chemical contamination. Lithography has been the preferred tool for pattern definition for more than two decades. However, the limits of this technique come in sight below 100 nm, there are some physical limits which make it very difficult to fabricate devices with lateral dimensions in the range of nanometers. One of the limits is due to the wavelength of the illuminating beam. For structures in the order of the wavelength of the beam diffraction of the beam will occur which makes pattern generation in the conventional way impossible. Therefore there is a constant move to illuminating beams with shorter wavelengths, from visible light, to ultra-violet light, to X-rays and to beams of electrons and ions. Another limit is caused by the finite size of the polymer molecules used in the classical organic resists. Also in the second step, the transfer, there are resolution limits. For instance the etching process introduces impurities near the surface which will cause unacceptable deviations in composition for small structures.

The ideal fabrication method in nanotechnology would build the experimental device atom by atom. There exists only a few options to reach such a new step in perfection of nanostructures. There is growing consensus that the Scanning Tunneling Microscope (STM) and finely focused particle beams for direct fabrication have a good chance for being the best choice in the foreseeable future.

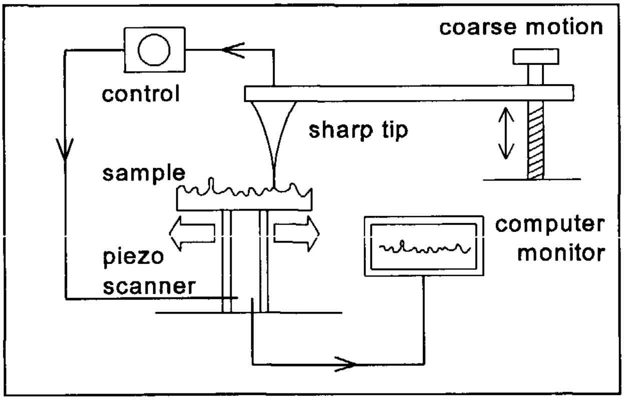

Fig. 1.3. *Scanning Tunneling Microscope (STM).*

In an STM, see figure 1.3, transport of electrons is realized between two conductors that are very weakly coupled: a very sharp metal needle and a conductive sample. The separation could be realized by a narrow gap of vacuum or an insulator. It is already mentioned before that it is quantum mechanically possible that electrons tunnel through this barrier. However there is an exponential decrease of the tunneling current with the thickness of the layer. Therefore a stable measurement of the current at a given voltage dictates the exponent to be stable to this value, and so the width of the barrier should be stable. This makes it possible to scan over the surface and measure its height with atomic resolution. On the other hand the very localized current of electrons can also be used in fabrication of mesoscopic structures, as will be discussed in the next paragraph.

The mechanical movement of the tip is very limited and the energy with which the electrons impact on the sample is only a few electron volts. Larger scan areas and impact with higher energy can be realized when the particles are emitted elsewhere. This improves the flexibility and the production yield. Between the electron source and the sample lenses can be positioned to focus the electrons in a small probe on the sample. Besides electrons also ions can be used which opens possibilities for other structure fabrication techniques. In general it is more difficult to focus the ion or electron beam in a small spot than to concentrate the effect of an STM.

1.3. The NEXT-project

For the Delft University of Technology (TUD) to maintain a leading role in the field of mesoscopic physics, a project is running which aims at the development of a system for nanometer scale fabrication in an all Ultra High Vacuum environment (Radelaar, 1994). This project, called NEXT (Nanoscale Experiments and Technology), combines fabrication, analysis and in-situ measurements. Maskless techniques will be used, where the borders between lithography and actual fabrication disappear. The leading methods of fabrication will include deposition and etching. These methods fulfil the goals of very high spatial resolution combined with flexibility in choice of materials. Electrons tunneling from the STM tip to the substrate on an atomically well-defined lateral scale, or a finely focused particle beam will induce the necessary chemical reactions, because they transfer the energy necessary to induce the reaction. Deposition or etching is the common way to fabricate (micrometerscale) devices, here the reaction is induced by heating the whole wafer to a temperature where the reaction takes place. In this project the resolution will be directly defined by the STM or the focused beam, instead of though the usual resist patterns.

For example an STM is used to modify a Si (111)7x7 surface structure with adsorbed chlorine atoms (Baba, 1994). One Si adatom at the center site is extracted from the surface by field evaporation and the other atom is moved by field-induced diffusion. This modification is caused by the coordinated breaking of bonds and the moving of adatoms to their adjacent areas as a result of Cl chemical reactivity. This chemical reaction is endothermic, so it will only occur where enough energy is available. This energy is transferred by the tunneling current from the STM needle. Therefore patterns are written where the STM needle comes along.

In a third fabrication method clusters, polymers and even single atoms will be manipulated to create devices or introduce modifications in otherwise fabricated structures. This yields the largest potential for creating completely new structures. In this case interfacing to the external world will necessarily be different from methods used previously. This can be realized by other nanoscale fabrication techniques.

An example starts from a blank Cu(111) surface, held in atomically clean conditions. The STM tip is used to position individual Fe atoms onto the Cu surface (Harmans, 1994). This is done by locating the tip above a "Fe atom storage place" somewhere at the surface, and applying a (positive) voltage to the tip: if done properly this makes one of the Fe atoms to become adhered to the tip. Next the tip is brought (with the atom on it) to the place where the atom has to be positioned, followed by applying a negative voltage to the tip to launch the atom into place. The next step in the experiment is to add more Fe atoms in order. Eigler (Eigler, 1993) was able to arrange a total of 48 Fe atoms in a ring forming a so called quantum well.

Fig. 1.4. *The configuration of the NEXT instrumentation.*

The configuration of the NEXT instrumentation is shown in figure 1.4. Units with STM and gas handling facilities for STM controlled chemical vapor deposition and etching will be incorporated as well as a unit dedicated to manipulation of atoms. A particle beam instrument will be used for direct writing in suitable substrates. Also a cryostat and an ESCA (Electron Spectroscopy for Chemical Analysis) system for the analysis of the deposition process will be part of the NEXT system.

1.4. The Fancier

One of the instruments in the NEXT system is "the Fancier": Fabrication and Analysis of Nanostructures Combining Ion and Electron Regulation. It is a particle beam instrument for direct writing that combines a beam of ions and electrons on the same optical axis. The ion beam offers a series of unique fabrication techniques (Kalbitzer, 1996) that cannot be realized with a Scanning Tunneling Microscope or an electron beam:

1. direct implantation. Here the ion ends up in the specimen. By choosing the right ion species it is possible to create doped areas which are necessary in the fabrication of transistors. A special case is direct deposition, here the ion ends up on the specimen surface since its energy is much lower than in case of direct implantation. If the ion is metallic it is possible to create a conductive line.
2. sputtering. Here the energy of the ions is used to release atoms from the specimen.
3. beam induced etching and deposition. Here the energy of the ion beam is used too, but now to induce a chemical reaction between an adsorbed precursor molecule and the specimen. Since the reaction is endothermic the chemical reaction will only occur locally where the ion beam comes along. The effect of the chemical reaction can be deposition of a metal atom which is part of the precursor molecule, or the removing of a specimen atom.

The last fabrication technique can also be achieved using an electron beam. But this will have effect on the production yield and the resolution of the fabricated structures. Figure 1.5 shows the energy and probe current of the ion beam for the different fabrication techniques (Muray, 1984). The probe currents in this figure has to be seen relative to each other and not as absolute values since it is just the production yield that is scaled with this current.

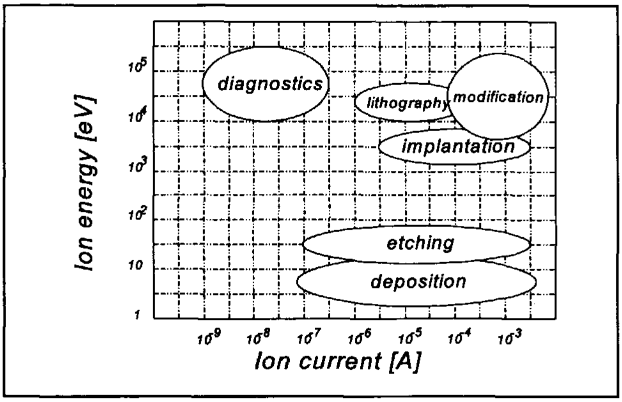

Fig. 1.5. *Fabrication with an ion beam as a function of the ion energy and probe current (Muray, 1984).*

It can be concluded that for (direct) deposition energies of some eV are necessary while for implantation some keV are preferable. This broad band of energies should be covered in "the Fancier".

The ion and electron beam have some advantageous over an STM like the higher production yield, because of larger probe currents, more flexibility, because the beams can be scanned over a larger area than an STM and dynamic range, because the probe size can be adjusted which is not possible with an STM. However there is also at least one important drawback: the resolution. Focused Ion Beam instruments equipped with a Liquid Metal Ion Source, operating at 30 keV can produce ion beams of 20-50 nm resolution in present-day commercial instruments. The best resolution published for a research instrument is 8 nm (Kubena, 1991). An important part in the design of "the Fancier" will deal with the aim to get below this level, see chapter 4.

Also in case of fabrication techniques that do not use resist, pattern generation is performed in two steps: in the first step the beam is focused on the specimen, while in the second step the effect of the beam is transferred into the specimen. Therefore, the resolution of structures fabricated by an ion beam is a combination of the ion beam probe size and the interaction area of an ion with the specimen. For present-day instruments the latter factor is mostly disregarded but it can be of main importance for nanometer resolution. Therefore its influence on the different fabrication techniques will be discussed in chapter 2 an 3. The beam size of ion systems is often limited by the energy spread of the ions in the beam with respect to each other. This problem can be approached from at least four directions for chromatically limited optics (Harriott, 1991):

1. An improved source can be developed with inherently low energy spread. The ion source is discussed in chapter 5.
2. Filtering of the energy of the ions. The energy filtering system is discussed in chapter 6.
3. The chromatic aberrations of the lenses can be reduced or eliminated . The main lens, the objective lens, is discussed in chapter 7.
4. Existing or conventional optics designs can be operated in a more optimum way

Once the structures have been fabricated they need to be observed in a microscope. Since the resolution of an optical microscope is too low, an STM or a beam with shorter wave length, like ions or electrons, has to be used. Here the number of secondary electrons is counted as this number gives information about the material and structure of the specimen. The secondary electron detector is discussed in chapter 8.

It will be argued that ions cannot be used for this purpose because they erode the structures. The main reason is sputtering, indicated by the sputtering yield: the number of removed specimen atoms per incoming particle. For a low noise image about 10^4 incident ions per pixel in the image are necessary (Driesel, 1994). Using a frame-store system and assuming the sputtering yield in the order of unity, about one monolayer is sputtered during image exposure with a resolution of 100 nm. The number of sputtered monolayers will increase with increasing resolution. Therefore mesoscopic structures will be eroded completely during observation with an ion beam.

This is the main reason why "the Fancier" has to combine both an ion and an electron beam for fabrication and analysis of the nanostructures respectively. A Scanning Transmission Electron Microscope (STEM) equipped with a Field Emission Gun (FEG) operating at 100 keV can produce electron beams of 0.2-0.3 nm.

For the fabrication of mesoscopic structures with particle beams there are more elements necessary than just for the focusing of these beams in a small probe. For instance the beams have to be directed along the pattern by a deflection system. It will be described in chapter 9 as one of the fabrication facilities. Also on the specimen extra demands have to be made. It has to be in position with an accuracy better than one nanometer, which is better than parking a car with an accuracy of a human hair. A method to realize this is discussed in chapter 10. Finally chapter 11 will deal with the electronics and the mechanical design of "the Fancier", a unique instrument for the fabrication and analysis of nanometer structures. Figure 1.6 shows the complete instrument.

1.5. Summary

At the Delft University of Technology, significant contributions have been made to the field of mesoscopic physics, the study of effects connected with reduced dimensionality in the solid state. These effects are not only a scaling of the effects of conventional macroscopic structures, it is to be expected that new quantum mechanical physical properties will be observed. To fabricate devices on a molecular level, to investigate

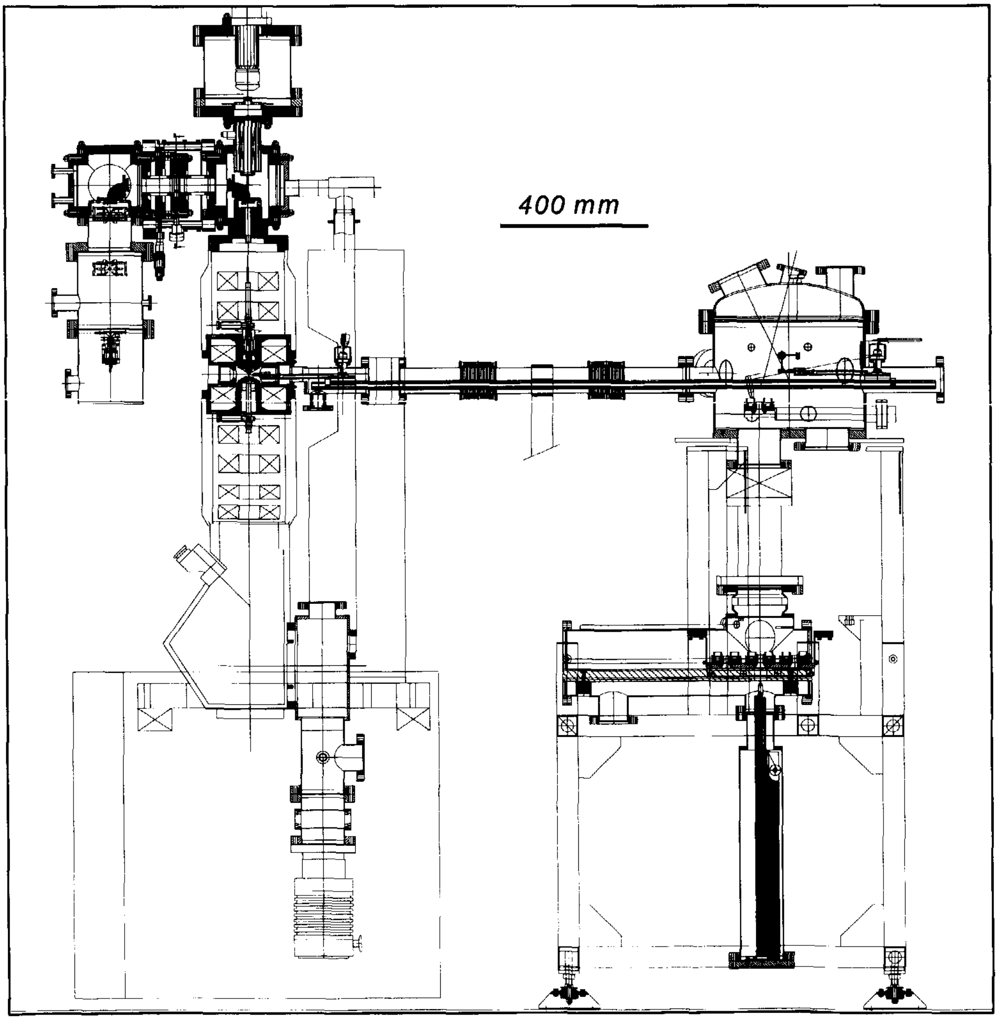

Fig. 1.6. *The Fancier.*

quantum transport and interactions in systems with very few electrons, and to extend mesoscopic phenomena to room temperature, completely new techniques are necessary in the longer run.

The NEXT project, Nanoscale Experiments and Technology, aims to observe the new quantum mechanical phenomena, but first to develop several of the new structure fabrication techniques. Most of the instruments in the NEXT project are based on Scanning Tunneling Microscopes (STM). If the needle of such a microscope is brought to within a nanometer from the specimen an electrical current will start with a quantum mechanical origin: tunneling. With the energy, transferred to the specimen by this tunneling current, a chemical reaction on the specimen surface can be induced. This reaction can result in a nanometer sized metal structure or etched groove. Also manipulation of polymers and atoms is possible using the STM as a hoisting crane. Besides the Scanning Tunneling Microscopes also an instrument with a focused ion and electron beam on the same optical axis, is part of the NEXT system. This is "the Fancier" (Fabrication and Analysis of Nanostructures Combining Ion and Electron Regulation) combining an ion and an electron beam on the same optical axis. The latter is needed for observation since the ion beam would destroy the fabricated structures.

A beam of ions offers several unique fabrication techniques like direct deposition of ions on the specimen surface, direct implantation of ions in the specimen and sputtering of atoms from the specimen. With a particle beam a chemical reaction can be induced resulting in etching or deposition, like with an STM. The production rate and flexibility with a particle beam are much better than with an STM. However it is very hard to obtain fabriction with nanometer resolution with a particle beam. Therefore the main point of research in the Fancier project is to obtain this high resolution.

References

Altshuler, B.L., P.A. Lee and R.A. Webb, *Mesoscopic phenomena in solids*, Noth-Holland, Amsterdam, 1991

Baba, M. and S. Matsui, *Atomic modification of an Si(111)7x7 surface with adsorbed chlorine atoms using a scanning tunneling microscope*, Applied Physics Letters 65 (15), 1994, pp. 1927-1929

Brodie, I. and J.J. Muray, *The Physics of Micro/Nano-Fabrication*, Plenum Press, 1992

Driesel, W., *Micromachining Using Focused Ion Beams*, Phys. stat. sol. (a) 146, 1994, pp. 523-535

Harmans, C., *Mesoscopic physics -an introduction-*, Delft, 1994

Harriott, L.R., *The technology of finely focused ion beams*, Nuclear Instruments and Methods B55, 1991, pp. 802-810

Kalbitzer, S., Ch. Wilbertz, Th. Miller and A. Knoblauch, *Ion beam modifications for submicron technology*, Nuclear Instruments and Methods B113, 1996, pp. 154-160

Kubena, R.L., J.W. Ward, F.P. Stratton, R.J. Joyce and G.M. Atkinson, *A low magnification focused ion beam system with 8 nm spot size*, Journal of Vacuum Science and Technology B9(6), 1991, pp. 3079-3083

Mooij, J.E., *Mesoscopische fysica: van quantum dot naar quantum DOS?*, Nederlands Tijdschrift voor Natuurkunde 1996 (6), pp. 150-153

Muray, J.J., *Physics of Ion Beam Wafer Processing*, Semiconductor International, 1984, pp. 130-135

Radelaar, S., *Nanofabrication by maskless techniques: Towards new realms in mesoscopic physics*, Proposal Intentional Apparatuur Schema, 1994

Tanigushi, N., *Nanotechnology -Integrated Processing Systems for Ultra-precision and Ultra-fine Products-*, Oxford University Press, Tokyo, 1996

2. The impact of charged particles on matter

Introduction

Focused ion beams can be used for the generation of structures. In general, the resolution of these structures is determined in the two steps of the pattern generation: the focusing of the particles in a probe on the specimen and the transfer of the structure to the substrate.

The first step is characterized by the parameters of the lens system like the focal length and the aberration coefficients. Chapter 4 deals with this step in great detail. The second step is characterized by the impact of the incoming particle on the substrate. Especially in case of fabrication of mesoscopic structures this step gets important in defining the resolution, similarly to the proximity effect in resist electron beam lithography.

In the next two chapters a model will be derived which gives the resolution of the transfer step of the pattern generation for the different fabrication techniques. First the impact of the particles on the specimen will be performed, followed by a calculation of the transport and slowing down of the particles. In this model the full collision cascades, phonon transport and secondary electron generation and transport are incorporated. In chapter 3 the actual resolution of the transfer step is determined based on this model.

2.1. Simulation of transfer of the structure to the substrate

The most important parameter to calculate is the lateral spread of the effect of a single incoming particle. This defines the resolution of the transfer step in the fabrication of the structures. To optimize the performance of the instrument it is needed to know this parameter for a wide range of parameters; the ion energy will be in the range from 5 to 100 keV, while the ion mass will be between 4 (He) and 70 (Ga) atomic-mass-units. It is assumed that outside these ranges the practical problems or the resolution of the probe forming step in pattern generation dominates the structure resolution.

Unfortunately the resolution parameters are unknown for the fabrication techniques as discussed in chapter 1, also analytical equations are not known. Therefore it is needed to perform these simulations. They can best be realized by Monte Carlo simulation. The impact, transport and energy effects of ions and electrons on matter can be calculated using these programs. In Monte-Carlo calculations, a large number of particle trajectories is simulated on a computer by varying the most important parameters of the scattering process by random numbers.

Depending on the final quantity to be calculated, e.g. the implantation position of the ions, 10.000-100.000 trajectories will be necessary to get a significantly statistical accuracy. Though no particle will really follow a calculated trajectory, the statistical mean value obtained from a large number of trajectories will agree with experiments. This calculation will be performed for different mass and energy of the particles as these parameters can actually be chosen within certain limits in a charged particle instrument.

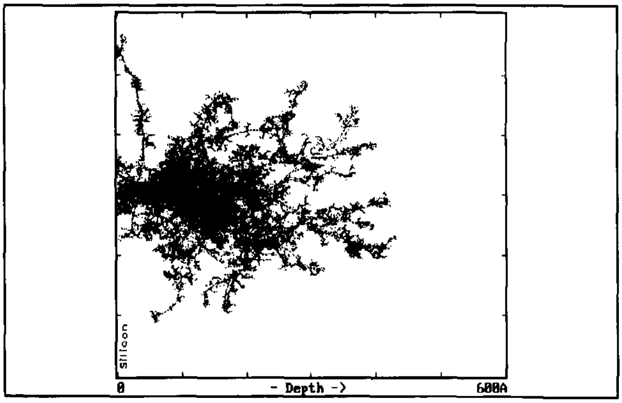

Fig. 2.1. *Monte Carlo calculation of 15 keV argon (Ar) ions in silicon with collision cascade, using TRIM (Ziegler, 1985).*

As an example figure 2.1 shows calculations of Ar ion trajectories in a Si substrate obtained with the TRIM (TRansport of Ions in Matter) computer program. This program to determine the ion trajectories, is developed by Biersack (Biersack, 1980) and Ziegler (Ziegler, 1985). For electrons such a Monte Carlo program is described by Reimer (Reimer, 1986).

Based on the results of this calculation not only the resolution of the transfer step can be calculated, but also parameters like the implantation depth distribution, the sputtering yield and energy and angular distributions of emitted particles. These parameters are well known from experiments and analytical equations. Therefore it is possible to validate the Monte-Carlo simulation by comparing its results with these experiments and analytical equations. In the assumption that this validates the Monte-Carlo model it also gives a quality indication for the results of the resolution.

However not all fabrication techniques can be simulated completely by the available programs. For beam induced etching and deposition the energy at the surface that is available for the chemical reaction has to be calculated. Therefore the programs will be extended to simulate the effect of energy transport through the specimen as a result of the temperature rise by phonons and of secondary electrons. To explain these extensions the basic Monte-Carlo setup is described first.

2.2. The transport of charged particles

The flow diagram of these programs is depicted in figure 2.2, see also (Chapman, 1983). Every incoming particle, the primary particle, starts at a lateral position x=0 and y=0 and at a depth in the specimen z=0 with an energy U. The incoming particle has an angle θ with respect to the z-axis which directs into the specimen, perpendicular to the surface of the specimen and an angle ϕ with respect to the x-axis. First the particle makes a step, the free-flight-path s, into the specimen without interaction with the specimen atoms. If the particle is still in the specimen, this interaction is performed at the end of the path. Here energy is transferred to the specimen atom which is hit by the incoming particle. The nuclear energy transfer ΔU_n is assumed to be the result of an elastic collision between the primary particle and a specimen atom. On its turn this atom can excite other atoms resulting in a collision cascade.

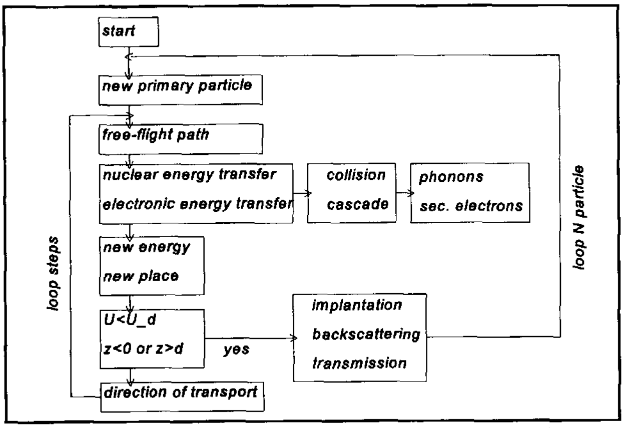

Fig. 2.2. *Simplified flow diagram of a Monte Carlo program for scattering of particles in a specimen.*

However, electronic energy transfer ΔU_e is also possible. This deals with the interaction between the primary particle and electrons of the specimen atoms. For calculation efficiency, the inelastic energy transfer is often treated in a continuous slowing down approximation. This means that the electronic energy transfer is linearly proportional to the traveled path. Based on the above calculations the new parameters of the primary particle can be calculated.

$$\begin{aligned} U_{new} &= U_{old} - (\Delta U_n + \Delta U_e) \\ x_{new} &= x_{old} + s.\sin(\theta).\cos(\phi) \\ y_{new} &= y_{old} + s.\sin(\theta).\sin(\phi) \\ z_{new} &= z_{old} + s.\cos(\theta) \end{aligned} \tag{2.1}$$

In general two special cases can now occur. If the new energy is smaller than a threshold energy U_d, the displacement energy of a specimen atom, implantation of the ion occurs at the calculated position. If the parameter for the depth position is less than zero or larger than the thickness of the specimen, the particle is assumed to be back scattered or transmitted respectively.

In case these situations don't occur, new steps in the specimen are performed after the direction of transport of the ion is determined. This stepwise transport of the particles through the specimen is repeated until the primary particle is implanted, back scattered or transmitted through the specimen.

From the above model it is clear that the energy of the primary particle is transferred to the specimen. This energy is partially used in the collision cascade to displace atoms. If at a position in the cascade there is less energy available than the threshold energy U_d, it is assumed that this energy is released as phonons. On its turn this phonon energy is spread out through the specimen in a diffusion process which results in heating of the specimen. Another part of the total energy is released as ionization energy. This energy is used to generate secondary electrons. These electrons can scatter through the specimen and they have a certain probability to escape from the specimen.

The phonon transport is neglected in most of the electron transport models (Reimer, 1986). Both the phonon transport and secondary electron generation and transport are neglected in most of the ion transport models (Ziegler, 1985). The scatter phenomena that are underlined in the above text are described in greater detail in the next paragraphs of this chapter.

2.3. The free-flight path

Between two scattering events, the incoming particle moves over a distance equal to the free path. If the free-flight path is much larger than interatomic distances, the probability that the incoming particle is scattered within the path length interval s, s+ds becomes

$$dW(s) = N.(\sigma_e + \sigma_n).e^{-s.N.(\sigma_e+\sigma_n)}ds \tag{2.2}$$

W(s)= probability function for path length s
s= free-flight path
N= atomic density of the specimen
σ_e= inelastic or electronic cross-section
σ_n= elastic or nuclear cross-section

The integration necessary to solve the probability function can be done analytically and the inverse function becomes in the exponential decay approximation (Reimer, 1986)

$$s = \frac{-\ln(1-R)}{N.(\sigma_e+\sigma_n)} \tag{2.3}$$

R= pseudo-uniform random number between 0 and 1

The inelastic cross-section determines the energy distribution and number of fast secondary electrons, i.e. knock-on electrons, produced by ionization of atoms. A quantum mechanical treatment of this interaction by Mott and Moller results in the cross-section for production of secondary electrons from valence shell electrons. For electrons as primary particles this is given by

$$\sigma_{e,v} = \int \frac{1}{(4.\pi.\epsilon_0)^2} . \frac{4.\pi.e^4}{U} . \left(\frac{1}{(\Delta U_e)^2} + \frac{1}{(U-\Delta U_e)^2} - \frac{1}{\Delta U_e.(U-\Delta U_e)} \right) .d(\Delta U_e) \tag{2.4}$$

ϵ_0= dielectric constant
e= charge of particle

In the classical approximation the last two terms within brackets vanish, the cross-section becomes according to Joy (Joy, 1987)

$$\sigma_{e,v} = \int \frac{1}{(4.\pi.\epsilon_0)^2} . \frac{4.\pi.e^4}{U.(\Delta U_e)^2} .d(\Delta U_e) \tag{2.5}$$

Gryzinski (Gryzinski, 1965) investigated Coulomb collisions of two moving particles based on the classical binary encounter theory. He derived (semi-empirically) a cross-section for inner shell, or core, ionization of atoms

$$\sigma_{e,c} = \int \frac{1}{(4.\pi.\epsilon_0)^2} . \frac{\pi.e^4}{U.(\Delta U_e)^2} . \left(\frac{U}{U+U_j} \right)^{1.5} . \left(1 - \frac{\Delta U_e}{U} \right)^{\frac{U_j}{U_j+\Delta U_e}} . \left[1 - \frac{U_j}{U} + \frac{4}{3} . \frac{U_j}{\Delta U_e} .\ln \left(2.7 + \sqrt{\frac{U-\Delta U_e}{U_j}} \right) \right] .d(\Delta U_e) \tag{2.6}$$

E_j= binding energy of core electrons

The nuclear scattering of electrons as primary particles is calculated with the Rutherford cross-section (Murata, 1981) (Reimer, 1986)

$$\sigma_n = \int \frac{Z_2^2.e^4}{4.(4.\pi.\epsilon_0)^2.U^2} . \left(\frac{U+U_r}{U+2.U_r} \right)^2 . \frac{1}{(1-\cos\theta+2.\beta_n)^2} .d\Omega \tag{2.7}$$

U_r= electron rest energy, 511 keV
Z_1= atomic number of ion
Z_2= atomic number of specimen atom

The screening parameter of Nigam is given by (Nigam, 1959) (Cailler, 1990)

$$\beta_n = c_1 \cdot \frac{Z_2^{\frac{2}{3}}}{U} \tag{2.8}$$

c_1= constant 4.34 eV or 5.43 eV (Hawryluk, 1974)

This type of cross-section has been utilized in Monte-Carlo simulations of electron scattering by many authors (Murata, 1981) (Ro, 1994) and justified by comparison between calculated and experimental results.

Equation (2.3) can also be written as

$$s = -\ln(R).\lambda \tag{2.9}$$

λ= mean free-flight path

Both for electrons and ions this mean free-flight path has been derived. Measurements for electrons traveling in elemental materials clearly show a universal curve (Seah, 1979). Least squares analysis show that the measurements for energies below 15 eV are described by a power law not significantly different from U^{-2} and those above 75 eV by $U^{0.5}$. This results in the general relation (Luo, 1990)

$$\lambda(U) = d_m \cdot \left[\frac{A_1}{U^2} + A2 . \sqrt{d_m . U} \right] \tag{2.10}$$

d_m= thickness of a monolayer of the substrate
A_1= constant, 538 for the elements of the periodic table (Sea, 1979)
A_2= constant, 0.21 for the elements of the periodic table (Sea, 1979)

This equation is valid for electrons with energies up to 10 keV.

For ions, the mean free-flight path is chosen such that the mean angular deflection per path length λ remains about constant, i.e.

$$\frac{M_2}{M_1} \cdot \frac{\Delta U_n}{U} = \frac{M_2}{M_1} \cdot \frac{\lambda . S_n(U)}{U} = constant \tag{2.11}$$

M_1= mass of the ion
M_2= mass of the specimen atom

according to the Bohr-Williams rule . Introducing an approximate analytic expression for the nuclear stopping power (Biersack, 1980) and choosing the constant to yield an average deflection of about 5° per path interval λ, one obtains (Ziegler, 1985)

$$\lambda = \frac{0.02\left(\frac{M_1+M_2}{M_2}\right)^2}{4.\pi.a^2.N}.\frac{\epsilon^2+0.1\ \epsilon^{1.38}}{\ln(1+\epsilon)} \tag{2.12}$$

$$\epsilon = \frac{a}{Z_1.Z_2}.\frac{M_2}{M_1+M_2}.U \tag{2.13}$$

$$a = \frac{0.8853\ a_0}{\sqrt{Z_1^{\frac{2}{3}}+Z_2^{\frac{2}{3}}}} \tag{2.14}$$

a= Thomas-Fermi screening length (Lehmann, 1977)
a_0= Bohr radius, 0.0529 nm
ϵ= reduced energy

2.4. Electronic energy transfer

The inelastic or electronic energy loss of the primary particle is treated independent of the nuclear energy loss. The reasons for neglecting the correlation between the elastic and inelastic energy losses are twofold. The pragmatic reason is the increased computer efficiency, mainly through the applicability of the λ concept of extended free-flight paths. The other reason is the lack of satisfactory theoretical descriptions or experimental data of the impact parameter dependence of the electronic energy loss. Neglecting impact parameter dependence and straggling at high energies, the electronic energy loss related to the distance s traveled between collisions (Biersack, 1980)

$$\Delta U_e = s.S_e(U) \tag{2.15}$$

$S_e(U)$= electronic stopping power

For the nearly-free-electron metals the stopping power for electrons $S_e(U)$ turns out to be

(Schou, 1988)

$$S_{e,S} = c_F.\frac{U^{2.4}}{N.n_e^{0.85}} \tag{2.16}$$

U= energy [eV]
c_F= proportionality constant, 8.9 10^{-2}
n_e= density of nearly-free electrons [nm^{-3}]

This approximation is fair from the work function up to at least 20 eV above the Fermi energy, it is also in agreement with models that include the electron exchange. For energies from the valence band up to 10 keV the stopping power for electrons has been derived for valence electrons (Müllejans, 1992). U_p is 16.55 eV for a Si sample.

$$S_{e,M} = \frac{U_p^2}{4.a_o.U}.\ln\left(\frac{2.U^2}{5.U_p^2}\right) \quad , \quad U_p^2 = \frac{h^2.n_e.e^2}{4.\pi^2.\epsilon_o.M_e} \tag{2.17}$$

Low velocity ions can be treated using the Lindhard-Scharff formula (Biersack, 1980)

$$S_{e,L} = \frac{1.212\ N.Z_1^{\frac{7}{6}}.Z_2}{\left(Z_1^{\frac{2}{3}}+Z_2^{\frac{2}{3}}\right)^{\frac{3}{2}}}.\sqrt{\frac{U}{M_1}} \tag{2.18}$$

which approximates very well the general trends in the Z_1 and Z_2 dependencies. For electrons at U>>20 eV and ions at

$$U> \left(0.5\ .M_1.Z_1^{\frac{4}{3}}.\left[\frac{c}{137}\right]^2 \wedge 0.5\ .M_1.Z_2^{\frac{4}{3}}.\left[\frac{c}{137}\right]^2\right) \tag{2.19}$$

c= velocity of light

the Bethe-Bloch electronic stopping power becomes valid. At this energy the primary ion is deprived of all its electrons. The bare nucleus of charge Z_1.e interacts with the target electrons via a Coulomb potential and the scattering is described by the Rutherford scattering formula. Then the electronic energy transfer for non-relativistic energies can be expressed as

$$S_{e,B} = \frac{N}{(4.\pi.\epsilon_0)^2}.\frac{2.\pi.Z_1^2.Z_2.e^4}{\frac{M_e}{M_1}.U}.\ln\left(\sqrt{\frac{2.7183}{2}.\frac{M_e}{M_1}.\frac{U}{U_{nl}}}\right) \quad (2.20)$$

The mean ionization energy, U_{nl}, is given by the Bloch constant (Biersack, 1980) and the empirical equation of Sternheimer (Berger, 1964)

$$\begin{aligned} U_{nl} &= 12\ Z_2 + 7 \qquad Z_2 < 13 \\ &= 9.76\ Z_2 + 58.5\ Z_2^{-0.19} \qquad Z_2 \geq 13 \end{aligned} \quad (2.21)$$

Equation (2.20) describes the electronic energy transfer in case the primary particle is an ion. However, this equation is also valid for electrons, if M_1 is set equal to M_e and Z_1 is chosen one. The equation is in agreement with other Bethe-Bloch models (Lehmann, 1977), (Leighton, 1959), (Mulder, 1991), (Murata, 1981) and (Reimer, 1983).

2.5. Nuclear energy transfer

At high and medium energies (ϵ>>1 in equation (2.13)) practically all energy loss of the incoming ion is due to interaction with the electrons of the target material as described in the preceding section. At low energy, where the screening of the particle's atomic nucleus by captured electrons becomes important, nuclear (elastic) collisions between the incoming particle and the target atoms as a whole enter the scene. This nuclear stopping power competes, as the energy decreases, to an increasing extent with the electronic stopping power and eventually dominates. This is shown in figure 2.3 (Sigmund, 1981).

The energy lost by the incoming particle in an elastic collision is related to the nuclear stopping power

$$\Delta U_n = s.S_n(U) \quad (2.22)$$

$S_n(U)$= nuclear stopping power

The nuclear stopping power is the average energy transferred when summed over all impact parameters up to the maximum transferrable energy for a head-on collision

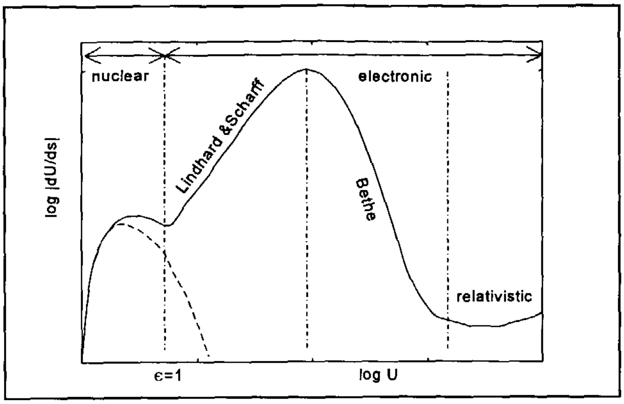

Fig. 2.3. *Schematic description of the stopping power of an ion as a function of energy (Sigmund, 1981).*

$$U_T = \frac{4.M_1.M_2}{(M_1+M_2)^2}.U \tag{2.23}$$

With the expression for the mean free-flight path given by equation (2.12) the nuclear stopping power can be evaluated

$$S_n(U) = 4.\pi.a.Z_1.Z_2.e^2.\frac{M_1}{M_1+M_2}.s_n(\epsilon) \tag{2.24}$$

Depending on the actual scattering angles and simplifications different solutions for the reduced nuclear stopping power are calculated in literature. Respectively given by (Lam, 1990), (Ziegler, 1985), (Matsunami, 1980) and (Lehmann, 1977)

$$s_n(\epsilon) = \frac{0.5\ \ln(1+\epsilon)}{\epsilon+0.10718\ \epsilon^{0.37544}} \tag{2.25}$$

$$s_n(\epsilon) = \frac{\ln(1+1.1383\ \epsilon)}{2\ \epsilon+\ 0.02642\ \epsilon^{0.21226}+0.39186\ \epsilon^{0.5}} \tag{2.26}$$

$$s_n(\epsilon) = \frac{3.441\ \epsilon^{0.5}.\log(2.718+\epsilon)}{6.882\ \epsilon^{1.5}-1.708\ \epsilon+6.355\ \epsilon^{0.5}+1} \tag{2.27}$$

$$s_n(\epsilon) = \frac{\ln(\epsilon)}{2.(\epsilon - \epsilon^{2.49})} \tag{2.28}$$

This analytical expression yielded good agreement between range calculation and experiment (Lam, 1990).

2.6. Collision cascade

This description of the collision cascade is based on the TRIM manual (Ziegler, 1995). Assume an incident ion or an atom in the collision cascade has atomic number Z_1 and energy U. It has a collision within the target with an atom of atomic number Z_2. This collision can be elastic or inelastic. In case the collision is inelastic the transferred energy is released as ionization energy. If it is elastic the collision cascade is continued. After the collision, the incident ion has an energy U_1 and the stuck atom has an energy U_2. Previously specified for the target is the displacement energy, U_d, and therefore the final energy of a moving atom below which it is assumed to be stopped and the binding energy, U_b, of a lattice atom to its site. Data for these energies can be found in literature (Eckstein, 1991).

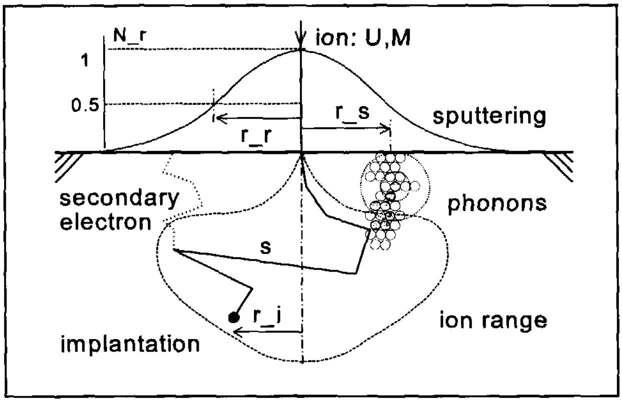

Fig. 2.4. *The trajectory of an ion through a specimen.*

The displacement energy is not a very well defined quantity. It is the energy that a target atom has to receive in order to leave its lattice site and form a stable interstitial. The bulk binding energy is used because it is assumed that a target atom is bound to its lattice site with a certain energy. The energy needed to remove a target atom from its lattice site by an elastic collision is the bulk binding energy.

A displacement occurs if $U_2>U_d$, meaning that a target atom is set in motion in the cascade. A vacancy is the hole left behind when a recoil atom moves from its original site. It occurs if both $U_1>U_d$ and $U_2>U_d$. Both atoms then become moving atoms of the cascade. The energy U_2 is reduced by U_b before it has another collision. If $U_2<U_d$, then the stuck atom does not have enough energy and it will vibrate back to its original site, releasing U_2 as phonons.

If $U_1<U_d$ and $U_2>U_d$ and $Z_1=Z_2$, then the incoming atom will remain at the site and the collision is called a replacement collision with U_1 released as phonons. The atom in the lattice site remains the same atom by exchange. If the two particles involved are of different atomic species, then Z_1 becomes the stopped interstitial atom.

Finally, it can be mentioned that the total number of displacements in a recoil cascade is equal to the sum of vacancies and replacement collisions, while the number of vacancies equals the number of interstitials and sputtered atoms. Sputtering is dealt with in greater detail in chapter 3, but it is already mentioned here: sputtering is the removal of a near-surface atom from the target. When a cascade gives a target atom an energy greater than the surface binding energy, U_s, of the target the atom may be sputtered.

Table 2.1. *The events in a collision cascade with the energy that is released as phonon energy.*
U_d= displacement energy, U_b= binding energy

energy after collision	energy after collision	effect	phonon energy
$U_1>U_d$	$U_2>U_d$	displacement, vacancy/sputtering	
$U_1>U_d$	$U_2<U_d$	displacement	U_2
$U_1<U_d$	$U_2>U_d$	replacement U_2-U_b new cascade	U_1
$U_1<U_d$	$U_2<U_d$		U_1+U_2

2.7. Direction of transport

The elastic and inelastic energy transfer results in a change in the direction of transport of the incoming particle. The inelastic scattering angle is given by Murata (Murata, 1981), using the laboratory coordinate system.

$$\theta_e = \arcsin\sqrt{\frac{\Delta U_e}{U}} \tag{2.29}$$

The elastic scattering angle is known from the classical scattering integral (Biersack, 1980), using the laboratory coordinate system based on the scattering angle in the center of mass system (Heiland, 1990)

$$\theta_n = \arctan\left(\frac{\sin\vartheta_n}{\cos\vartheta_n + \frac{M_1}{M_2}}\right) \tag{2.30}$$

$$\vartheta_n = \pi - 2.\int_{r_0}^{\infty} \frac{b}{r^2.\sqrt{1 - \left(\frac{b}{r}\right)^2 - \frac{(M_1+M_2).V(r)}{M_2.U}}}.dr \tag{2.31}$$

b= impact parameter
V(r)= Coulomb potential

A solution of this integral is obtained by Ziegler (Ziegler, 1985)

$$\theta_n = 2.\arccos\left(\frac{b + r_0 + \delta_1 + \delta_2}{\rho_1 + r_0 + \rho_2}\right) \tag{2.32}$$

The meaning of the parameters in this equation can be found in figure 2.5.

- The smallest impact parameter over the path length s is found in the following way (Biersack, 1980): the probability for finding a target atom at a radial distance between b and b+db is

$$w_1(b).db = N.\lambda.2.\pi.b.db \tag{2.33}$$

The probability for not finding an atom closer than b, i.e. between 0 and b, is

$$w_2(b) = e^{-N.\lambda.\pi.b^2} \tag{2.34}$$

Hence, the probability for finding the closest target atom between b and db, provided no one is closer, becomes the product of the two equations (2.33) and (2.34). This leads to the impact parameter determination.

$$b = \sqrt{\frac{-\ln(R)}{\pi.N.\lambda}} \tag{2.35}$$

Another description of the impact parameter is given by Lee (Lee, 1995). In the amorphous substrate, the position of the atoms is characterized by the Poisson distribution. The ion interacts with an atom at a time by the impact parameter given by

$$b = \sqrt{\frac{R}{\pi.N^{\frac{2}{3}}}} \tag{2.36}$$

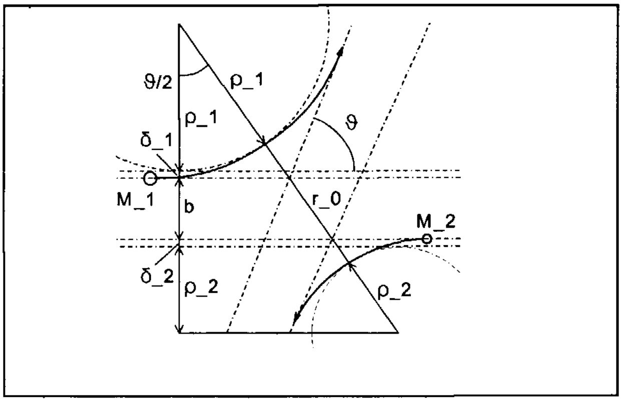

Fig. 2.5. *The particle trajectories in the center of mass system with superimposed scattering triangle, comprised of impact parameter b, distance of closed approach r_0, radii of curvature ρ_1 and ρ_2 and the correction terms δ_1 and δ_2. See also equation (2.32).*

- The Thomas-Fermi model is used to estimate the screened Coulomb potential between atom nuclei (Ziegler, 1985)

$$V(r) = \frac{Z_1.Z_2.e^2}{r}.e^{-\frac{r}{a}} \tag{2.37}$$

Once the screening parameter is specified, then the classical scattering can be calculated. Thomas and Fermi argued that a reasonable approximation might be

$$a = \frac{0.8853\ a_0}{\sqrt{Z_1^{\frac{2}{3}} + Z_2^{\frac{2}{3}}}} \tag{2.38}$$

However the universal potential combines not only interaction between atom nuclei but also e.g. the electrostatic energy between the two electron distributions. This results in the universal potential (Ziegler, 1985)

$$\begin{aligned} V(r) = \frac{Z_1.Z_2.e^2}{r}.[0.1818\ &\exp\left(-\frac{3.2\ r}{a}\right) + \\ 0.5099\ &\exp\left(-\frac{0.9423\ r}{a}\right) + \\ 0.2802\ &\exp\left(-\frac{0.4029\ r}{a}\right) + \\ 0.02817\ &\exp\left(-\frac{0.2016\ r}{a}\right)] \end{aligned} \tag{2.39}$$

$$a = \frac{0.8853\ a_0}{Z_1^{0.23} + Z_2^{0.23}} \tag{2.40}$$

The azimuthal scattering angle is randomly selected using the relation

$$\phi = 2.\pi.R \tag{2.41}$$

2.8. Specimen heating

During the scattering of the incoming particle and during the collision cascade energy is transferred to the substrate in elastic collisions. If this energy is less than the displacement energy of a substrate atom, U_d, it is released as vibration energy: phonon energy. The transport of these phonons through the substrate is not calculated by the available Monte-

Carlo simulation programs. Only data about the phonon energy that is released at a specific substrate position is available in a three dimensional grid matrix. The matrix element defines the position while the contents of the element is the available phonon energy, U_{ph}. The deposition of energy by the beam results in a local temperature rise in the substrate.

From the moment of deposition, the heat diffuses according to the thermal diffusion equation (Özişik, 1993)

$$\rho.C_p.\frac{\partial T(x,y,z,t)}{\partial t} = \nabla.\left[\lambda_h.\nabla T(x,y,z,t)\right] \qquad \textbf{(2.42)}$$

ρ= mass density of the substrate
C_p= specific heat of the substrate
λ_h= thermal conductivity of the substrate
T(x,y,z,t)= the temperature distribution as a function of position and time

The material is usually assumed to be homogeneous, which reduced the first term on the right hand side to $\lambda_h.\nabla^2T(x,y,z,t)$.

The temperature rise at any position in the substrate can be divided in three contributions, according to Mulder (Mulder, 1991). The first contribution is direct heating. This is induced by the incoming particle, at the point of exposure, during the exposure. The second contribution is the temperature rise at a point, due to diffusion of the heat from previously exposed points in its neighborhood. In this contribution the diffusion time and the distance between the points is very important. The third contribution is the homogeneous, global heating of the substrate. The second contribution reduces to the third after sufficient time has passed and the thermal contribution has smoothed to a uniform increase in wafer temperature.

2.8.1. direct heating

Direct heating is the temperature rise at a point of exposure during the exposure. Because the exposure time is very short (order of 10^{-12} seconds), it can be assumed that the adiabatic approximation can be used to calculate the temperature rise. This temperature rise can be calculated based on the Monte-Carlo simulation results for the exposed area of the substrate. The direct temperature rise in the adiabatic approximation can be written as

$$\Delta T_{dr} = \frac{U_{ph}}{V_0 . \rho . C_p} \tag{2.43}$$

U_{ph}= phonon energy

V_0= specific volume in which the phonon energy has been deposited

In literature the direct temperature rise is often calculated without Monte-Carlo simulation. Here for electrons the depth dose function from Everhart and Hoff (Everhart and Hoff, 1971) will be used to calculate the temperature rise. This means that the energy deposited is

$$U_v = \frac{0.6\ \gamma_d . U . D}{R_g} \tag{2.44}$$

γ_d= deposited energy fraction

U= energy of incoming particle

D= dose of exposure

R_g= Grün length (Grün, 1957)

Grün did electron penetration experiments in air. From his results he concluded that when the z-coordinate is scaled with a length that is a function of the acceleration voltage , the depth distribution has the same characteristic form over a wide range of voltages. The characteristic length is called the Grün length and is given by

$$R_g = K_g . \frac{U^{1.75}}{\rho} \tag{2.45}$$

K_g= proportionality constant, $0.22.10^{-9}$ kg/(m^2.$eV^{1.75}$) Si

Using the expression for R_g and the first term of the Everhart-Hoff profile, the direct temperature rise for electrons in the adiabatic approximation can be written as

$$\Delta T_{dr} = \frac{U_v}{\rho . C_p} = \frac{0.6\ \gamma_d . D}{U^{0.75} . C_p . K_g} \tag{2.46}$$

Another description (Svintsov, 1995) leads to the equation

$$\Delta T_{dr} = \frac{U . D}{R_{pr} . \rho . C_p} \tag{2.47}$$

R_{pr}= penetration depth in substrate

It shows clearly that the direct temperature rise is mostly determined by the specific heat of the substrate material.

For the deposition of a copper layer of one nanometer ($8.4\ 10^{22}$ atoms/m^2) on Si by 35 keV Ga ion beam assisted deposition, a minimum dose of 450 C/m^2 is needed because the production yield is 30 atoms/ion at maximum (Della, 1993). The direct temperature rise of Si (γ_d= 0.84, C_p= 0.78 kJ/(kg.K), ρ= 2.2 10^3 kg/m^3) becomes 516 10^3 K!

This is much higher than can be allowed in an actual situation and the coincidence of all maximum contributions of each ion to the temperature rise should be avoided. In practice this is realized, because of a spread in time of the ion dose allowing the heat to conduct to neighboring parts of the specimen.

2.8.2. neighborhood heating

Neighborhood heating is the contribution to the temperature rise due to the diffusion of heat from previously exposed spots at a point where the exposure should take place.

The temperature distribution in a homogeneous, isotopic substrate as a result of a point source U_{ph} at a position r=0 at t=0 can be calculated starting from equation (2.42) in spherical coordinates.

$$\frac{\partial T(r,t)}{\partial t} = \frac{\lambda_h}{\rho.C_p}.\left(\frac{\partial^2 T(r,t)}{\partial r^2} + \frac{2}{r}.\frac{\partial T(r,t)}{\partial r}\right) \tag{2.48}$$

The starting condition is $T=T_0$ at t=0 at $r \neq 0$, while during the whole diffusion process the energy has to be conserved

$$U_{ph} = \int_0^\infty \rho.C_p.T(r,t).4.\pi.r^2.dr \tag{2.49}$$

The source solution for a point source can now be found from the diffusion equation

$$T(x,y,z,t)_b = \frac{U_{ph}}{\rho.C_p.\left(4.\pi.\frac{\lambda_h}{\rho.C_p}.t\right)^{1.5}}.\exp\left(-\frac{x^2+y^2+z^2}{4.\frac{\lambda_h}{\rho.C_p}.t}\right) \tag{2.50}$$

This is the source solution according to Özişik (Özişik, 1993). It can be used to calculate the temperature distribution as a function of position and time. Boundary conditions for limited substrates can be satisfied by using mirror sources (Holtslag,1989). For instance, assume a semi-infinite block of material in which there is no heat conduction perpendicular to the surface. The boundary condition is now dT/dz=0. For a point source below the surface, this condition can be satisfied at z=0 when the substrate is assumed to be infinite with two sources of the same energy placed symmetrically to both sides of the non-conducting plane.

This results in a surface temperature given by

$$T(x,y,0,t)_b = \frac{2.U_{ph}}{\rho.C_p.\left(4.\pi.\frac{\lambda_h}{\rho.C_p}.t\right)^{1.5}}.\exp\left(-\frac{(x-x_{ph})^2+(y-y_{ph})^2+z_{ph}^2}{4.\frac{\lambda_h}{\rho.C_p}.t}\right) \qquad (2.51)$$

x_{ph}, y_{ph}, z_{ph}= position of the point source of phonon energy in the specimen. When there is more than one point source present in the substrate, the individual point sources can be added because they behave as independent sources.

2.8.3. global heating

The temperature rise due to global heating can be calculated from the ratio of the total amount of energy deposited and the product of the volume and the heat capacity, ρC_p. The total amount of energy deposited in the target is proportional to the beam energy, U, and the dose, D, the fraction of the total energy that is deposited (input energy minus the energy of the back scattered and sputtered particles), γ_g. Therefore, the global temperature rise, ΔT_g, of the substrate with a thickness d is given by

$$\Delta T_g = \frac{\gamma_g.D.U}{\rho.C_p.d} \qquad (2.52)$$

In this equation, it is assumed that diffusion to the system and black-body radiation are negligible.

2.8.4. Chemical reaction

Beam induced deposition and etching are based on a chemical reaction that is activated by the energetic particles in the beam. In principle this can be due to local temperature rise as most reaction rates vary exponentially with temperature. This was observed by Arrhenius in an experimental way (Arnold, 1995)

$$\frac{dPY}{dt} = A.e^{-\frac{U_r}{k_B.T}} \qquad (2.53)$$

A= frequency factor
PY= production yield per incoming particle
U_r= reaction activation energy
k_B= Boltzmann constant
T= temperature

2.9. Secondary electrons

During the scattering of the incoming particle and during the collision cascade energy is transferred to the substrate in inelastic collisions. This energy can be used to create secondary electrons. The transport of these secondary electrons through the substrate is not calculated by the available Monte-Carlo simulation programs. Only data about the ionization energy that is released at a specific substrate position is available in a three dimensional grid matrix. The matrix element defines the position while the contents of the element is the available ionization energy U_{io}.

At each grid position secondary electrons are generated which are followed during their scattering in the specimen. This means that at an energy distribution for secondary electrons has to be applied at a grid position. There is not much known about this distribution. It is mentioned (Hofer, 1990) that the internal energy spectrum of free electrons in a substrate is generally assumed to be monotonously decreasing shape such as, for instance, a $1/U_{se}^2$ distribution. It is also found in Monte-Carlo simulations (Murata, 1990). This distribution can be explained based on the length of the free-flight path of low energy secondary electrons in a metal, see the first term of equation (2.10).

Therefore, and for simplicity, it is assumed here that the energy distribution of generated secondary electrons is linearly dependent on the energy of these electrons.

$$dW_1(U_{se}) = \frac{1}{U_{\max}^2}.(U_{\max} - U_{se}).dU_{se} \qquad 0<U_{se}<U_{\max} \tag{2.54}$$

$U_{\max}$ is the maximum energy a secondary electron can get. From the paragraphs 2.3 and 2.4 it is clear that this is

$$U_{\max} = \lambda(U).S_e(U) - U_{nl} \tag{2.55}$$

The mean free-flight path and the electronic stopping power are evaluated at an energy which is equal to the impact energy of the incoming particle as the electronic stopping power of the ions is described by Lindhard-Scharff, equation (2.17).Hence, this leads to the generation of secondary electrons according to

$$U_{se} = (1 - \sqrt{1-R}).U_{\max} \tag{2.56}$$

Further, the probability for generating secondary electrons at a specific grid position is proportional to the available energy there

$$W_2(U_{se}) = C_1.U_{io} \tag{2.57}$$

From their generation point the secondary electrons travel through the specimen. In a very simple model (Samoto, 1983) this process can be treated as isotropic diffusion. In a better model the secondary electron can now move over a distance equal to the mean free path (Sea, 1979) before they scatter. This means in the exponential decay approximation (Reimer, 1986):

$$s = -\ln(1-R).\lambda(U_{se}) \tag{2.58}$$

$$\lambda(U_{se}) = d_m.\left[\frac{A_1}{U_{se}^2} + A2.\sqrt{d_m.U_{se}}\right] \tag{2.59}$$

This means that a secondary electron generated at x_{se}, y_{se} and z_{se} in the substrate with energy U_{se} can be found after one step in the specimen at a position on a sphere. Its position is now given by:

$$\begin{aligned} x &= x_{se} + s.\sin(\theta).\cos(\phi) \\ y &= y_{se} + s.\sin(\theta).\sin(\phi) \\ z &= z_{se} + s.\cos(\theta) \end{aligned} \qquad \textbf{(2.60)}$$

At the end of the free-flight path a collision will occur. In an inelastic collision, a new secondary electron produced by the original secondary electron can be excited from all possible electron shells and can have all possible energies as long as the energy loss of the original secondary electron is less than its energy U_{se} before collision. After Koshikawa and Shimizu (Koshikawa, 1974), it is assumed that for each electron entering the cascade process two secondary electrons appear: the original secondary which has lost some energy and a new secondary which has gained some energy. The total energy of the two particles is conserved taking into account the ionization energy U_{nl}.

The total probability of creating a new secondary electron in such an inelastic collision should be unity, so:

$$X.\left[cn(1).\int_0^{U_{se}-U_{nl}} \frac{d\sigma_{e,v}}{dU}.dU + \sum_{k=2}^{all\ shells} cn(k).\int_0^{U_{se}-U_{nl}} \frac{d\sigma_{e,c}}{dU}.dU \right] = 1 \qquad \textbf{(2.61)}$$

X= normalization factor
cn(1)= number of valence electrons
cn(k)= number of k-shall core electrons
σ_v= inelastic cross-section to excite a secondary electron from the valence shell, see equation (2. 5)
σ_c= inelastic cross-section to excite a secondary electron from the core shell, see equation (2.6)

After an inelastic collision, the probability distribution of producing a tertiair electron with energy U_{te} is:

$$\frac{dN_{te}}{dU_{te}} = X.\left[cn(1).\left(\frac{d\sigma_v}{dU}\right)_{U_{te}} + \sum_{k=2}^{all\ shells} cn(k).\left(\frac{d\sigma_c}{dU}\right)_{U_{te}} \right] \qquad \textbf{(2.62)}$$

In case only valence shell electrons are taken into account, this equation simplifies to

$$dW(U_{te}) = \frac{U_{se}.U_{nl}}{(U_{se}-U_{nl}).(U_{te}+U_{nl})^2}.dU_{te} \tag{2.63}$$

This probability distribution leads to the tertiary electron energy

$$U_{te} = \frac{R.(U_{se}-U_{nl}).U_{nl}}{U_{se}-R.(U_{se}-U_{nl})} \tag{2.64}$$

The diffusion of secondary electrons through the substrate in steps which are related to the free path of the electron, followed by a collision can be repeated. In general the position of a secondary electron in a substrate is given by

$$\begin{aligned} x_i &= x_{se}+\sum_i s_i.\sin(\theta_i).\cos(\phi_i) \\ y_i &= y_{se}+\sum_i s_i.\sin(\theta_i).\sin(\phi_i) \\ z_i &= z_{se}+\sum_i s_i.\cos(\theta_i) \end{aligned} \tag{2.65}$$

This summation or the continuation of secondary electron scattering has to be repeated until $U<U_{nl}$ or $z<0$. In the first case the secondary electron is lost, in the second case emission of the secondary electron or a chemical reaction will appear. The actual point of reaching the surface is given by:

$$r = \sqrt{x_i^2+y_i^2}+z_i.\cos(\theta_i) \tag{2.66}$$

2.9.1. Chemical reaction

Beam induced deposition and etching are based on a chemical reaction that is activated by the energetic particles in the beam. In principle this can be due to a secondary electron that transfers energy to the surface layer.

If a secondary electron reaches the surface with energy $U_{se}>U_r$, the reaction energy, it can induce a chemical reaction. This is a rough approximation. As a more detailed calculation takes into account the energy which can be transferred from the secondary electron to the combination of adsorbed gas molecule and substrate atom. This rate of energy loss for a secondary electron is given by the nuclear and electronic stopping powers:

$$\frac{dU}{ds} = S_n + S_e \tag{2.67}$$

In the above rough model it is assumed that the reaction chance is zero for an available amount of energy less than the reaction energy and above this level the reaction chance is one. This is in agreement with well-known approximations in chemistry (van der Put, 1995). Therefore the reaction rate per incoming secondary electron is given by:

$$PY = TRUNC\left[\frac{A.\int_0^l \frac{dU}{ds}.ds}{U_r}\right] \tag{2.68}$$

A= proportionality constant
l= characteristic length of the energy transfer to be effective for the chemical reaction
U_r= reaction energy

The integral in the above equation must be smaller than the total available energy U_{se}. The energy transferis approximated by the electronic stopping power equation (2.17). For the characteristic length, the distance from a specimen atom at the surface to the center of an adsorbed precursor molecule is used. The truncating function is added to the equation to account for the fact that a secondary electron can induce only an integer number of reactions. The rest energy is disregarded here. This means that the effect of secondary electrons does not add up which is reasonable because the chance is very small that two secondary electrons can excite the same surface atom within the reaction time of typically 10^{-12} seconds.

2.9.2. Free secondary electrons

In order for a secondary electron with energy U_{se} at the surface to escape its energy has to be larger than the work function of the substrate material, ϕ_w. The maximum allowable value of the escape angle α_{max} is determined by taking the normal component of momentum, p_n=p.cos(α). This momentum must exceed the critical normal momentum for escaping:

$$p_{n,c} = \sqrt{2.M_e.\Phi_w} \tag{2.69}$$

M_e= mass of an electron
ϕ_w= work function of the substrate material

Therefore the maximum value for the escape angle is

$$\cos(\alpha_{\max}) = \sqrt{\frac{\phi_w}{U_{se}}} \qquad (2.70)$$

The free secondary electron has now an energy and angle given by

$$U_{se,f} = U_{se} - \phi_w$$
$$\tan(\alpha_f) = \frac{p.\sin(\alpha)}{p.\cos(\alpha) - \sqrt{2.M_e.\phi_w}} = \frac{\sin(\alpha)}{\cos(\alpha) - \sqrt{\frac{\phi_w}{U_{se}}}} \qquad (2.71)$$

α= angle reaching the surface with respect to surface normal

This is in agreement with Luo (Luo, 1990). With these data for energy of the free secondary electron, its angle and place of escape Monte-Carlo simulation results in the yield, energy and angular distribution and the resolution of secondary electrons.

2.10. Summary

The resolution of a structure fabricated by a particle beam is influenced by two process steps. The first process step is focusing of the particles in a small probe, while in the second process step the energy of the ions or electrons is transferred into the specimen: the specimen interaction. This takes into account the lateral spread of the effect of a single impacting particle. Specimen interactions are often disregarded in case of ions since they are only visible when the ions are focused to within a nanoscale probe.

The properties of the specimen interaction have been simulated for energetic particles as a function of their mass and energy by a Monte-Carlo program. The trajectory of individual particles is simulated by repeatedly calculating the nuclear and electronic interaction with the specimen atoms during the scattering of the particle in the specimen. Although Monte-Carlo simulations are very time consuming, they are used since no analytical description of the resolution of specimen interactions is known. For ions these models have been implemented in the computer program TRIM (Transport of Ions in Matter) (Ziegler, 1995). Electron trajectories can be calculated using MOCASIM developed by Reimer (Reimer, 1995). With these programs specific effects of nanofabrication and observation using ion and electron beams can be simulated, e.g. the maximum resolution. In these programs the transport of phonon energy and secondary electrons have been included. Since they are of main importance for pattern generation by beam induced etching and deposition and for observation, models have been described to simulate these effects.

Finally, some drawbacks of this method of simulation will be discussed (Hoondert, 1993). First of all, a target with atoms at random positions is not a realistic approximation for a crystal, where the incoming particle can move great distances through channels formed by crystallographic directions. On the other hand, at low energy the binary collision approximation breaks down, because primary collisions of the incoming particle with a substrate atom and secondary collisions (in the collision cascade) of substrate atoms with each other are spatially very near. Therefore they are no longer independent. At high ion energies the stopping is mainly due to electronic excitations and the nuclear collisions are very far apart.

A second drawback is that the displacement energy, U_d, for the atoms is not well known. However, the results which will be obtained with this simulation will be compared with experimental results to verify the influence of the above approximations. If these experimental results for implantation distribution, sputtering yield and energy and angular distribution agree with the simulation, it is assumed that the results of the simulation are valid with equal accuracy.

References

Arnold, N., *On the spatial confinement in energy beam microprocessing*, Journal of Applied Physics 78(7), 1995, pp. 4805-4807

Berger,M.J. and S.M. Seltzer, National Academy of Science - National Research Council Publications 1133, 1964, pp.205

Biersack, J.P. and L.G. Haggmark, *A Monte Carlo computer program for the transport of energetic ions in amorphous targets*, Nuclear Instruments and Methods 174, 1980, pp. 257-269

Cailler, M. and J. Ganachaud, *Secondary electron emission from solids. II. Theoretical description*, Scanning Microscopy Supplement 4, 1990, pp. 81-100

Chapman, J.N. and A.J. Craven, *Quantitative electron microscopy*, Scottish Universities Summer School in Physics, Glasgow, 1983

Della Ratta, A.D., J. Melngailis and C.V. Thompson, *Focused- ion beam induced deposition of copper*, Journal of Vacuum Science and Technology B 11 (6), 1993, pp. 2195-2199

Eckstein, W., *Computer simulation of ion-solid interactions*, Springer-Verlag, Berlin, 1991

Everhart, T.E. and P.H. Hoff, *Determination of kilovolt electron energy distribution versus penetration distance in solid materials*, Journal of Applied Physics 42(13), 1971, pp. 5837-5846

Grün, A.E, *Lumineszenz-photometische Messungen der Energieabsorption im Strahlungsfeld von Elektronenquallen eindimensionaler Fall im Luft*, Zeitschrift für Naturforschung 12a, 1957, pp. 89

Gryzinski M., *Classical theory of atomic collisions I: theory of inelastic collisions*, Physics Review A 138, 1965, pp. 336-345

Hawryluk, R.J. and A.M. Hawryluk and H.I. Smith, *Energy dissipation in a thin polymer film by electron beam scattering*

Heiland, E., H. Derks and T. Bremer, *Slowing down and scattering of ions in solids*, Scanning Microscopy Supplement 4, 1990, pp. 257-263

Hofer, W.O., *Ion-induced electron emission from solids*, Scanning Microscopy Supplement 4, 1990, pp. 265-310

Holtslag, A.H.M., *Calculations on temperature profiles in optical recording*, Journal of Applied Physics 66(4), 1989, pp. 1530-1543

Hoondert, W.H.B., *Trapping and diffusion of noble gas atoms in some off-stoichiometric ceramics studied by thermal desorption spectroscopy*, Breda, 1993

Joy, D.C., *A model for calculating secondary and backscatter electron yields*, Journal of Microscopy 147, 1987, pp.51-64

Koshikawa T. and R. Shimizu, *A Monte Carlo calculation of low energy secondary electron emission from metals*, Journal of Physics D: Applied Physics 7, 1974, pp. 1303-1315

Lam, N.Q., *Physical sputtering of metallic systems by charged particle impact*, Scanning Microscopy Supplement 4, 1990, pp. 311-352

Lee, H. and H. Chung, *Monte Carlo simulation of focused ion beam lithography in inorganic resists*, Synthetic Metals 71, 1995, pp. 2047-2048

Lehmann Chr., *Interaction of radiation with solids and elementary defect production*, Noth-Holland Publishing company, Amsterdam, 1977

Leighton R.B., *Principles of modern physics*, Mc. Graw-Hill Book Company, New York, 1959

Luo S. and D.C. Joy, *Monte Carlo calculations of secondary electron emission*, Scanning Microscopy Supplement 4, 1990, pp. 127-146

Matsunami, N., e.a., *A semi-empirical formula for the energy dependence of the sputtering yield*, Radiation Effect Letters 57, 1980, pp. 15-21

Mulder, E.H., *On the throughput optimization of electron beam lithography systems*, thesis, Delft, 1991

Müllejans, H., *Secondary electron emission in coincidence with primary energy losses*, thesis, Cambridge, 1992, pp. 311-329

Murata, K., D.F. Kyser and C.H. Ting, *Monte Carlo simulation of fast secondary electron production in electron beam resists*, Journal of Applied Physics 52(7), 1981, pp. 4396-4405

Murata, K., *Monte Carlo simulation of electron scattering in resist film/substrate targets*, Electron Beam Intercations with Solids, AMF O'Hare, Chicago, 1990, pp. 311-329

Nigam, B.P., M.K. Sundaresan and T. Wu, *Theory of multiple scattering: second Born approximation corrections to Moliere's work*, Physics Review 115, 1959, pp. 491-502

Özişik M.N., *Heat conduction*, John Wiley & Sons, New York, 1993

Put, van der, *private communication*, Delft, 1995

Reimer, L. and D. Stelter, *FORTRAN 77 Monte-Carlo Program for Minicomputers Using Mott Cross-Sections*, Scanning 8, 1986, pp. 265-277

Reimer, L., *Manual of program MOCASIM*, 1995

Ro, J.S., C.V. Thompson and J. Meingailis, *Mechanism of ion beam induced deposition of gold*, Journal of Vacuum Science and Technology B 12(1), 1994, pp. 73-77

Samoto, N. and R. Shimizu, *Theoretical study of the ultimate resolution in electron beam lithography by Monte Carlo simulation, including secondary electron generation: energy dissipation profile in polymethylmethacrylate*, Journal of Applied Physics 54, 1983, pp. 3855-3859

Schou, J., *Secondary electron emission from solids by electron and photon bombardment*, Scanning Microscopy 2(2), 1988, pp. 607-632

Sea M.P. and W.A. Dench, *Quantitative electron spectroscopy of surfaces*, Surface and Interface analysis 1(1), 1979, pp. 2-11

Sigmund, P. and A. Claussen, *Sputtering from elastic collision spikes in heavy ion bombarded metals*, Journal of Applied Physics 52, 1981, pp. 990-993

Sigmund, P. and A Gras-Marti, *Theoretical aspects of atomic mixing by ion beams*, Nuclear Instruments and Methods 182/183, 1981, pp. 25-41

Svintsov, A.A. and S.I. Saitsev, *Simulation of heating in powerfull electron lithography*, Microelectronic Engineering 27, 1995, pp. 187-190

Ziegler, J.F., J.P. Biersack and U. Littmark, *The stopping and range of ions in solids*, Pergamon Press, 1985

Ziegler, J.F., *Manual of program TRIM*, Yorktown, 1995

3. The applicability of charged particles for nanotechnology

Introduction

High resolution focused ion and electron beams can be applied in a number of technologically important ways for nanofabrication. Examples of these techniques are direct implantation into semiconducting materials, direct deposition of beam material, sputtering and beam induced etching and deposition of (metallic) structures (Matsui, 1996).

In general, the resolution of the structures is determined in the two steps of the pattern generation: the focusing of the particles in a probe on the specimen and the transfer of the structure to the substrate. In the assumption that the incoming particles can be focused in an infinitesimal small probe the minimum structure size can be calculated based on the scattering of the incoming particle. This minimum structure size is determined in this chapter for the above mentioned fabrication techniques. Also some other parameters, e.g. production yield, will be calculated as a function of the mass and energy of the incoming particle on the substrate. In all calculations the substrate material is chosen to be Si.

Furthermore, for the visualization of the nanostructures secondary electrons coming from the specimen can be counted to make an image of the specimen. The generation of *secondary electrons as a function of the parameters of the incoming primary particle will be discussed.*

All simulations are performed with the computer programs based on the model described in the former chapter.

3.1. Direct implantation

The first important applications of ion beam implantation to materials have been in the field of semiconductor doping although fabrication of structures on the specimen surface is also possible as will be demonstrated at the end of this paragraph. As silicon is an element of the fourth division of the periodic table, the elements of the fifth division can be used as n-type dopant. They have one valence electron more than silicon. So after completing the tetrahedral bound of the silicon there is one electron left: this will be free electron in n-type silicon. For the same reasons the elements of the third division are electropositive and can be used as p-type dopant: free holes can be found in p-type silicon (Kalbitzer, 1992).

Focused ion application offers the possibility of modulation doping (Shukuri, 1984) and lateral band gap modulation on a mesoscopic scale. In situ processing of mesoscopic structures by implantation is also used to fabricate e.g. resonant tunneling devices (Petroff, 1992) or nano cantilevers (Steckl, 1992).

In the model of chapter two implantation occurs at the position where the incoming ion has less than the displacement energy, U_d. Figure 3.1 shows the energy loss in both depth and lateral direction for 100 keV antimoon (Sb) ions in silicon. It is a combination of electronic loss and nuclear energy loss. The resulting implantation distribution is also given in this figure. The characteristic values for the implantation depth and the lateral implantation resolution are the median values of these distributions. Biersack (Biersack, 1981) derived an analytical equation for the depth projected range.

$$\frac{dz}{dU} = \frac{1}{S_e(U)+S_n(U)} - \frac{\frac{M_2}{M_1}.S_n(U)}{2.\left(S_e(U)+S_n(U)\right).U}.z \qquad (3.1)$$

U= energy of the ions

M_1= mass of the ions

M_2= mass of a sample atom

$S_e(U)$= electronic stopping power

$S_n(U)$= nuclear stopping power

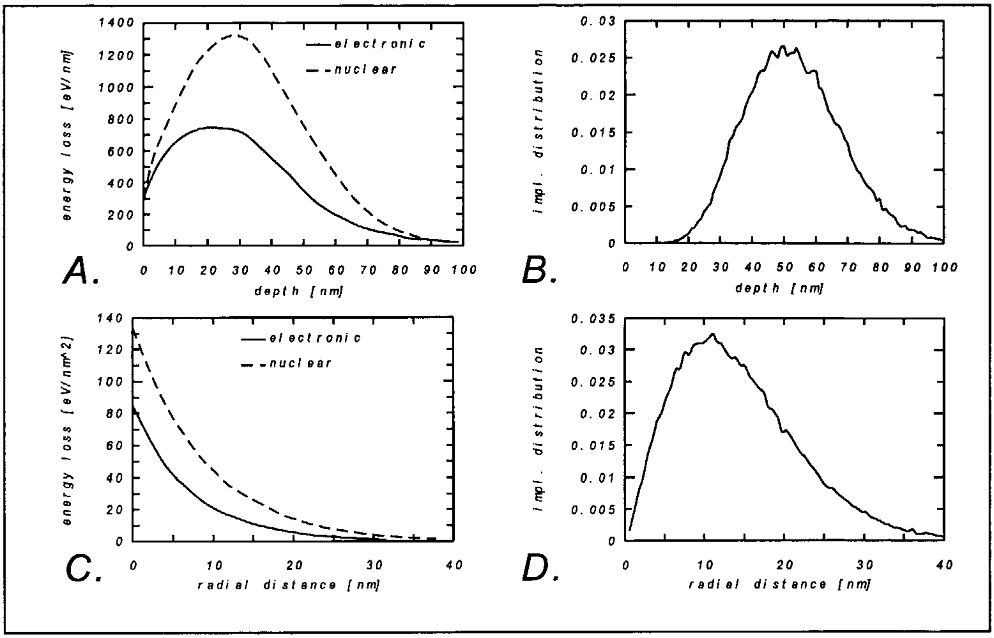

Fig. 3.1. *Energy loss during scattering and the implantation profile of 100 keV Sb ions in a Si substrate (a & b) depth, (c & d) lateral (Posselt, 1986) Implantation profile calculated using TRIM (Ziegler, 1985).*

The results of the calculation, using the program TRIM (TRansport of Ions in Matter) (Ziegler, 1985), can be compared with experimental implantation distributions. Since there is only little data available about low voltage ion implantation distribution, the experimental setup of the Delft Ion Beam Pattern Generator (IBPG) has been used to implant Ga ions in several samples.

This focused ion beam system has two lenses and is equipped with a liquid metal ion source for gallium. Three different types of samples have been used: 100 nm carbon on a silicon sample, pure silicon and 100 nm tungsten on a silicon sample. The adlayers are thick enough to assume that all gallium ions with energies lower than 15 keV are stopped in these layers.

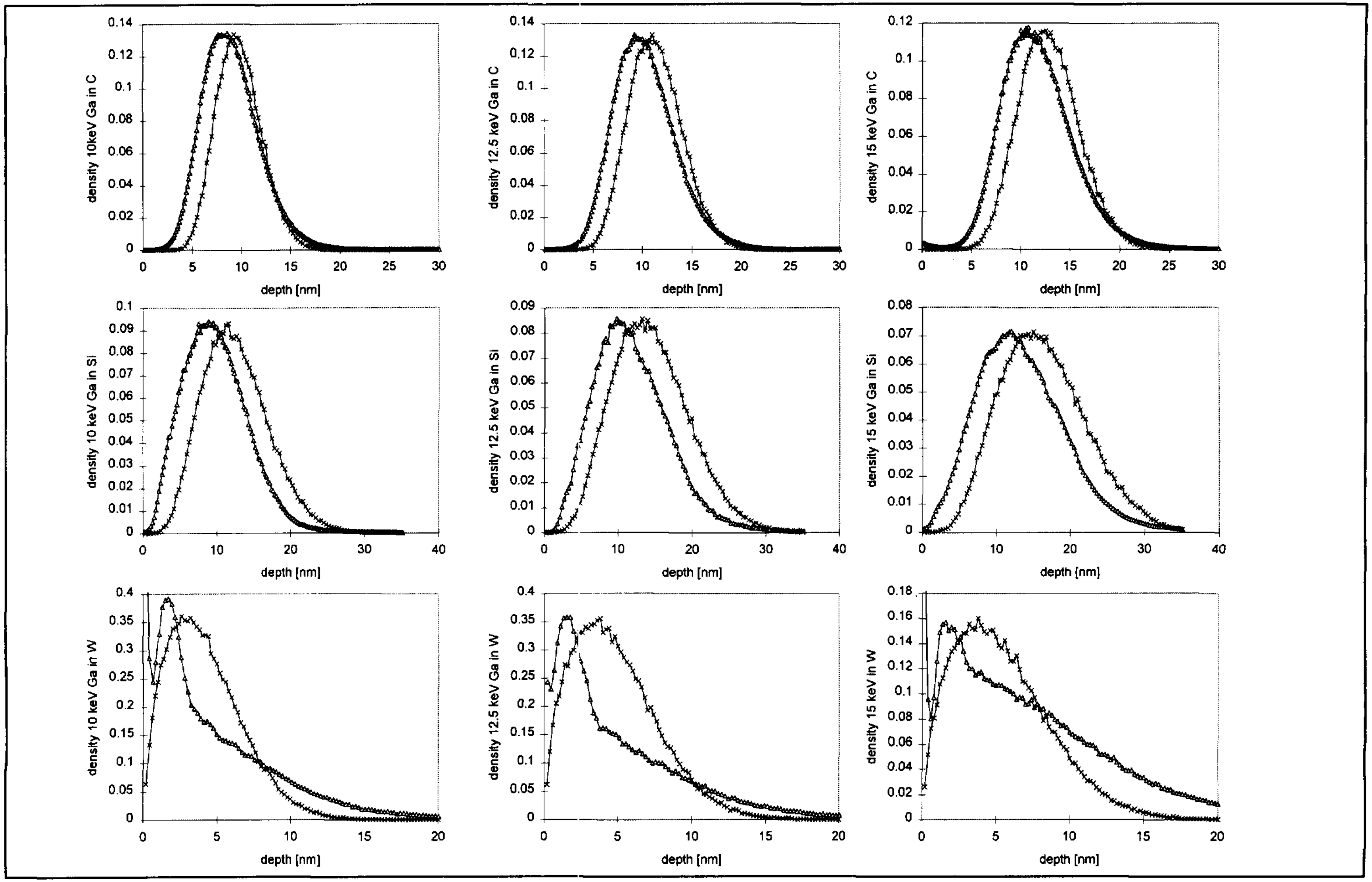

Fig. 3.2. *Comparison between simulated and experimental implantation distributions for different energies and substrates, "▲" SIMS results, "X" simulated results.*

An area of 500x500 μm has been bombarded with Ga ions at a relatively low dose of about 10^{-4} A/cm^2. This dose is chosen to avoid problems like dynamic change of the sample because of the implanted ions. This is called tailing and it is discussed below. The implanted samples have been analyzed using Secondary Ion Mass Spectroscopy (SIMS). For this analysis technique the sample is bombarded with low energy (< 2 keV) oxygen ions. They erode the sample and the emitted particles are detected. Since the oxygen ions penetrate deeper in the sample when the time proceeds, the detector signal as a function of time represents the implantation profile.

Figure 3.2 demonstrates this comparison for different specimens, carbon (C), silicon (Si) and tungsten (W), that are implanted with gallium (Ga) ions of energy 10, 12.5 and 15 keV. The concentration of ions is 10^{15} cm^{-2} in each figure. The area under the SIMS curves is normalized to unity, the curves obtained by simulations are scaled to equal maximum as the SIMS results. The experimental and simulated results show reasonable agreement for carbon and silicon even at these low energies. The shift in depth can be explained from an uncertainty in the starting position of the SIMS experiment. However for tungsten, where $\mu = M_1/M_2 < 1$, there is a significant difference between experiment and theory.

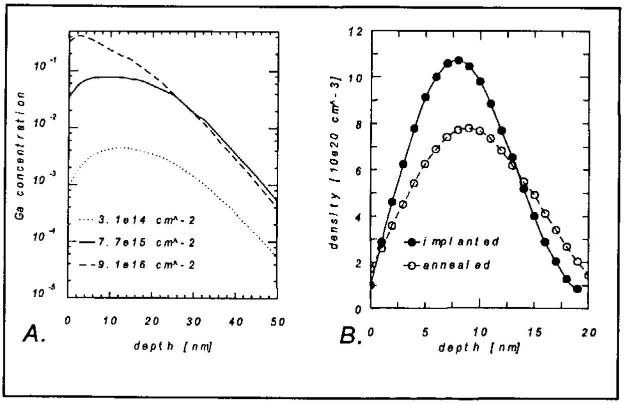

Fig. 3.3. *Effects on implantation distribution. (a) tailing to surface of 25 keV Ga ions in Si substrate(Gnaser, 1995), (b) thermal diffusion of K ions in Si substrate after annealing at 375°C for 209 hrs (Kalbitzer, 1992).*

This effect is called tailing (Kalbitzer, 1992). A deviation from a fast decaying Gaussian distribution is present and the distribution will change with increasing concentration of implantation material. It is the result of a change in the mean mass of the sample with increasing implantation concentration. For $\mu > 1$ it is far less pronounced than cases with μ<1 as regards tailing to the surface. When semiconductor layers of widely differing concentration levels are involved, tailing of free- energy implants may deserve thorough consideration. Figure 3.3a illustrates tailing for the case of a heavy ion, gallium, implanted into the lighter silicon substrate.

Another effect is thermally activated diffusion. The typical diffusion temperature of substitutional dopants in silicon is well above 1000 °C. This means that the activation annealing of the dopant impurities takes place at about 400 °C (Kalbitzer, 1992). If the temperature will be considerably lower than this temperature the above results for implantation profiles are valid, otherwise diffusion of the implanted ions has to be incorporated in the model. Figure 3.3b shows the effect of diffusion at 375 °C. The difference between the curves for gallium implantation shows some indication of a gallium depletion near the surface which is understandable in view of the lower surface binding energy of this specie (2.8 eV for Ga as compared to 4.07 eV for Si).

For different ion species that hit the substrate at various energies the implantation resolution has been calculated, the results are shown in figure 3.4 and 3.5. As a typical value for the resolution the median of the distribution is used. That is the area in which 50% of the total amount of ions is implanted. It can be seen from this last figure that implantation within a lateral area with radius sub 10 nm is possible with heavy ions and low energy, but these ions cannot be implanted deeper in the specimen than about 20 nm.

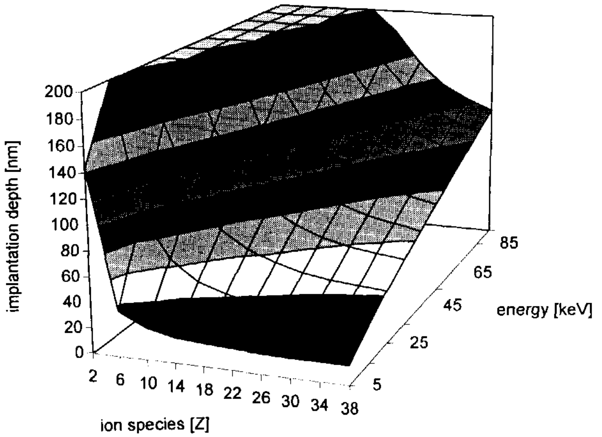

Fig. 3.4. *Median of the depth implantation distribution as a function of the atomic number and the energy of the incoming ions.*

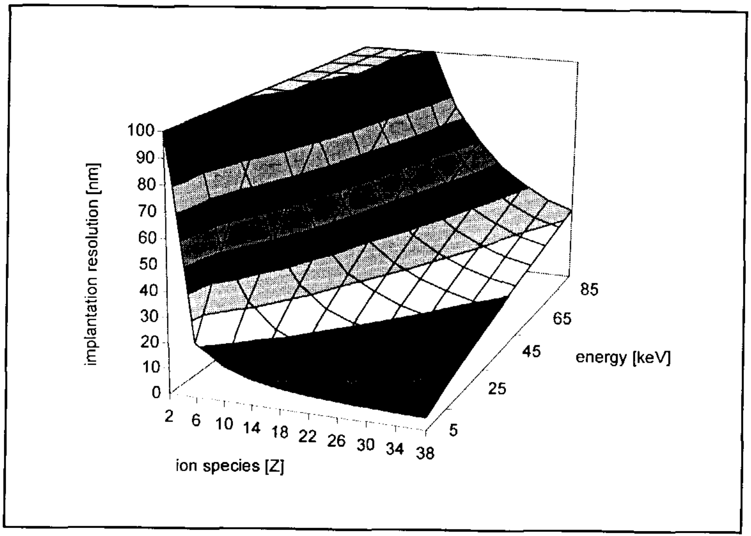

Fig. 3.5. *Median of the lateral implantation distribution as a function of the atomic number and the energy of the incoming ions.*

The resolution of structures made by implantation of Ar ions can be found by least-square fitting to the results depicted in figure 3.5

$$d_{impl} = 1.11 \left(\frac{U[eV]}{546} \right)^{0.816} [nm] \tag{3.2}$$

In the extreme case, at energies below 1 keV the focused ions are no longer implanted in the substrate but they are deposited on it. This method makes it possible to deposit patterned (metal) films directly on the substrate. The resistivities of structures made with this technique are much lower than those found in the technique of beam assisted metal deposition from organometallic vapors (Woodham, 1994), see also paragraph 3.3.

An important parameter is the sticking probability (Nagamachi, 1993 & 1994): the ratio between the number of deposited atoms and the number of incident ions. It can be seen in figure 3.6 that only at landing energies of approximately 100 eV the sticking probability is unity, allowing deposition on the surface. At higher energies an increasing number of the ions is implanted.

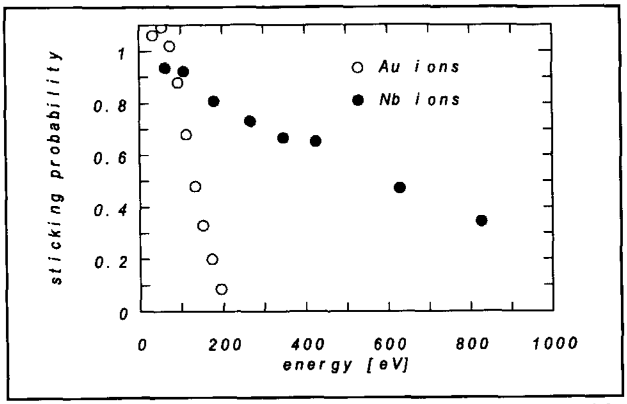

Fig. 3.6. *The sticking probability of Au and Nb ions as a function of the ion energy. The number of deposited atoms was estimated by the volume of the deposited film. Vacancies can result in a probability larger than one (Nagamachi, 1993 & 1994).*

Sub 5 nm islands deposited with this techniques have been reported (Woodham, 1994). Here also the resistance of 10 nm Au lines was reported to be 18 Ω compared with a calculated resistance of 5 Ω for bulk gold with this geometry. These values of resistance are close enough to be taken as evidence that the deposited film was of relatively high purity. This is probably because Au is chemically inactive. H_2O may be easily adsorbed and taken up by the gold film if the deposition rate becomes low. Therefore, in order to form very pure thin films directly by low-energy focused ion beam deposition, it may be necessary to combine a high deposition rate with very low background pressure inside the sample chamber (Yanagisawa, 1995).

3.2. Sputtering

Removal of atoms from the surface of a substrate is a way of fabricating structures on top of the specimen. Focused ion beams have drawn considerable interest as a tool for surface structure fabrication by sputtering. Sputtering of a target atom by energetic ions or recoil atoms is assumed to result from cascades of atomic collisions. In principle this method can be applied to every substrate material. But there is a strong dependence of the sputtering yield, the number of sputtered atoms per ion, on the substrate material as is shown in figure 3.7.

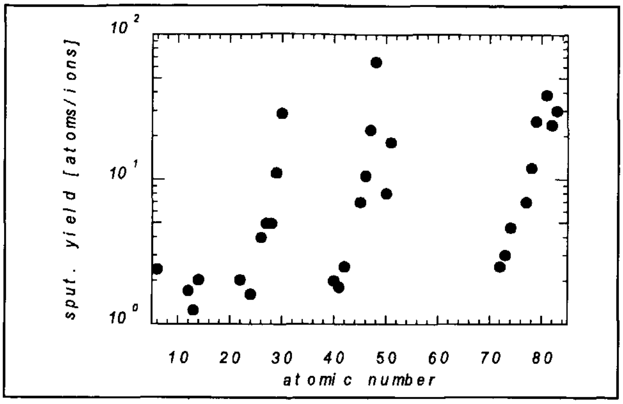

Fig. 3.7. *Sputtering yield as a function of the atomic number of the substrate after bombarding with Krypton ions with 45 keV energy (Almén, 1961).*

3.2.1. The yield

The sputtering yield of a specific substrate material, e.g. silicon, depends on the properties of the impinging ion. Figure 3.8 shows the trends in the total yield. It appears that the total sputtering yield varies rather smoothly with increasing ion energy U. This general shape is understood in a qualitative fashion (Wilson, 1973). The low energy region is controlled primarily by the increasing production of displaced lattice atoms. As the number of displaced atoms increases, more and more atoms have an opportunity to escape from the surface. Further increase in the incoming energy brings about an increase in the mean free-flight path. Thus the collisions, on the average, are occurring deeper in the specimen and the yield curve begins to form a plateau and even decreases at increasing energy.

The dependence of sputtering yield on ion type is fairly weak, especially at low energy, although it becomes slightly more pronounced for higher projectile energy and towards very light projectiles. This is in agreement with other simulations and experimental results (Auciello, 1984), where it is stated that the sputtering yield increases to a maximum value for increasing the incident atomic number.

The most successful attempt to analytically model these sputtering yields stems from Sigmund (Sigmund, 1969).

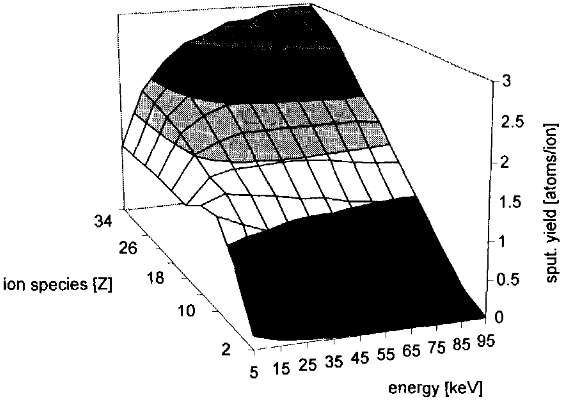

Fig. 3.8. *Sputtering yield of Si as a function of the atomic number and energy of the incoming ions.*

$$SY = K.\frac{(Z_1.Z_2)^{\frac{5}{6}}}{3.U_s}.S_n(E) = K.\frac{(Z_1.Z_2)^{\frac{5}{6}}}{3.U_s}.\frac{0.5.\ln(1+\epsilon)}{\epsilon+0.10718\ \epsilon^{0.375}} \tag{3.3}$$

$$\epsilon = \frac{a}{Z_1.Z_2}.\frac{M_2}{M_1+M_2}.U \tag{3.4}$$

$$a = \frac{0.8853\ a_0}{\sqrt{Z_1^{\frac{2}{3}}+Z_2^{\frac{2}{3}}}} \tag{3.5}$$

K= proportionality constant

This equation contains the reduced nuclear stopping power of equation (2.24).

In the computer program SUSPRE (Webb, 1987) a modified version of this equation is used in the form

$$SY = 0.042.\alpha.\frac{S_n(U)}{U_s}.\sqrt{1-\left(\frac{U_{th}}{U}\right)^2} \tag{3.6}$$

$\alpha.S_n(U)$= energy deposited at the surface

U_{th}= threshold energy below which negligible dynamic sputtering occurs

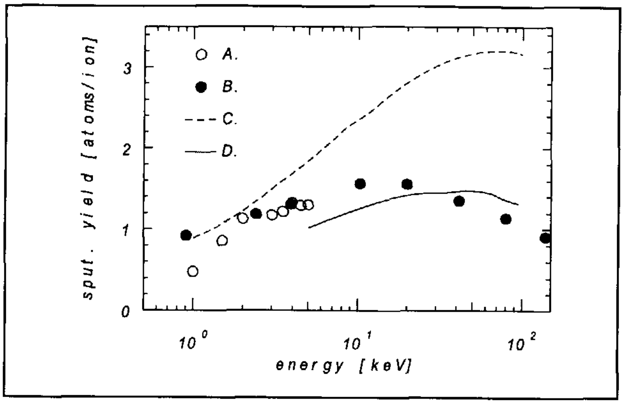

Fig. 3.9. *The sputtering yield of Ar ions on a Si sample. (a.) (Sigmund, 1969), (b.) (Zalm, 1994), (c.) (Webb, 1987), (d.) simulation.*

To check the Monte Carlo model described in chapter two with respect to the sputtering yield, its results are compared with the analytical model of equation (3.4) and experimental results. It is clear from figure 3.9 that these results agree within about 20 %.

Although this seems to be a large spread, also experimental results of sputtering differ largely. The sputtering yield of silicon using 30 keV gallium ions for example has been reported in literature: 1.8 atoms/ion (Young, 1993), 2.6 atoms/ion (Brodie, 1992), 3.1 atoms/ion (Yamaguchi, 1987). The Monte Carlo model gives a sputtering yield of 2.1 atoms/ion. These differences cannot be explained by a different behavior of specific silicon orientations: Si(100) and Si(111) behave alike (Pellerin, 1990). Deviations between simulation and experiment were observed however in cases of very dense collision cascades for heavy ions, which could be a consequence of nonlinear effects. Other deviations from experimental data occurred where the increased sputtering yields indicate a lower than normal binding energy under irradiation conditions possibly because of broken bonds (Biersack, 1987). In these results it is assumed that the ions impact normal on the specimen. The sputtering yield can be increased by a factor of 8 (Xu, 1992) in case of an angle of 70 degrees between the ion beam and the surface normal. At increasing angle the atoms have a larger probability of escaping. Above 70° there is a decreasing sputtering yield observed. This is presumably due to the fact that near grazing incidence also the incoming particles have a large probability of escaping.

3.2.2. The energy distribution

The energy distribution of sputtered atoms is well known from experimental results. Therefore it can be used to verify the Monte-Carlo model. The sputtered atoms have an energy distribution that is given by (Eckstein, 1987) (Sigmund, 1981)

$$f(U) = \frac{U}{(U+U_s)^{3-2.m}} \qquad (3.7)$$

U_s= surface binding energy, approximated by the heat of sublimation
m= constant potential parameter

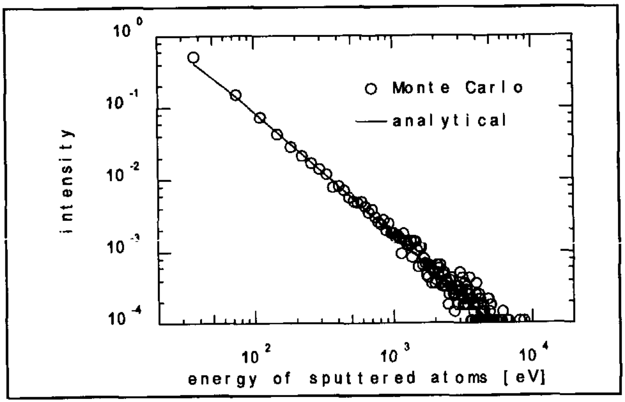

Fig. 3.10. *Energy distribution of sputtered Si atoms by 35 keV Ar ion impact from simulation and the least square fit of equation (3.11).*

if anisotropic effects are neglected and the ions have a normal incidence on the specimen. The potential parameter, m, for power interaction potentials is often chosen as zero or close to zero for the low energy region which is important in sputtering. Comparison of results from simulations with the analytical equation (3.7) give best agreement for a value m= 0.128, demonstrated in figure 3.10. This is in close agreement with m= 0.16 observed by Robinson (Robinson, 1983).

Figure 3.11 shows the median energy of the sputtered atoms for the ions discussed in this chapter. It is clear that the median energy is almost equal for these parameters except for low energy and low mass.

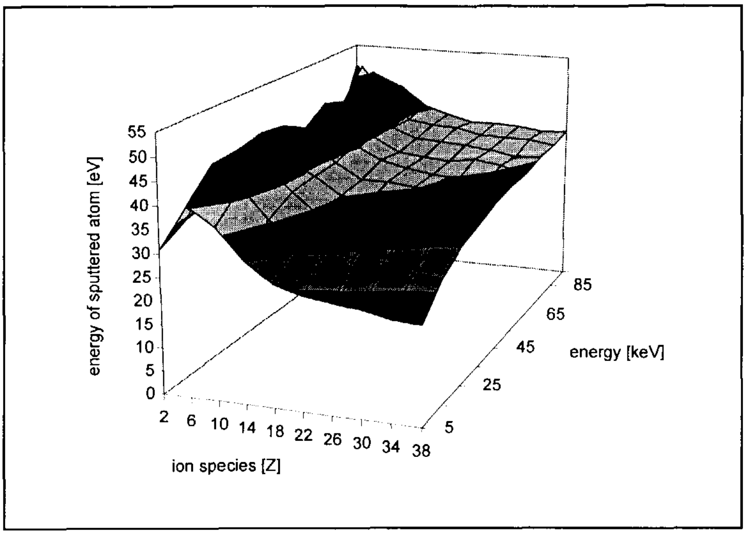

Fig. 3.11. *Median of the energy distribution of sputtered Si atoms as a function of the atomic number and energy of the incoming ions.*

3.2.3. The angular distribution

The angular distribution of sputtered atoms is well known from experimental results. Therefore it can be used to verify the Monte-Carlo model. Atoms that are sputtered from the sample, leave it with a certain angle with respect to the surface normal. The poloidal distribution follows a cosine law

$$\frac{dSY}{d\Omega}(\theta) = \frac{SY}{\pi}.\cos(\theta) \qquad \textbf{(3.8)}$$

The physical origin of the cos(θ)-distribution of emitted atoms is an isotropic distribution of moving atoms inside the solid. Anisotropic deviations from this law were shown (Waldeer, 1987) to lead to an overcosine distribution of sputtered particles. Here the particles are preferentially emitted near the target normal. The fact that these deviations are small led many authors to believe that additional effects, such as surface roughness or a modified surface potential, collaborate to establish the measured cosine or overcosine distributions.

Integration over the solid angle gives

$$\frac{dSY}{d\theta}(\theta) = \frac{SY}{\pi} \cdot \int_{0}^{2.\pi} \cos(\theta).\sin(\theta).d\phi = 2.SY.\sin(2.\theta) \tag{3.9}$$

This angular distribution model is compared with Monte Carlo simulation results of 15 keV Ar ions bombarding the Si sample, see figure 3.12.

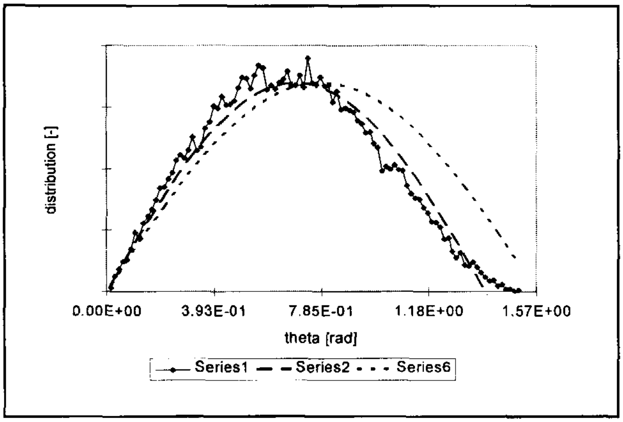

Fig. 3.12. *Angular distribution of sputtered Si atoms by 15 keV Ar ion impact from Monte Carlo simulation(series 1), a least square fit to the overconsine distribution (series 2) resulting in sin(2.27 theta) and a real cosine distribution (series 6).*

3.2.4. The resolution

The characteristic value for the resolution of a sputtered structure is its full width 50 % value, this is the median of the distribution of the emitted atoms. The result is shown in figure 3.13. It can be seen that a resolution of a few nanometers is possible with heavy ions at low energy.

The resolution of structures made by sputtering with Ar ions can be found by least-square fitting to the results depicted in figure 3.13

$$d_{sput} = 2.3 \ln\left(\frac{1 + 0.001\ U[eV]}{1.11\ 10^{5}}\right) + 26.9\ [nm] \tag{3.10}$$

One of the disadvantageous of fabricating structures by sputtering is that the sputtered atoms are partially redeposited at other locations on the specimen. This can result in generating defects in the patterned structure (Muller, 1986). Either this defect has to be (iteratively) repaired afterwards or it must be avoided by a special milling strategy, for example the large structures are generated at first and finally the small reticles are generated. For special combinations of ion and sample, like N_2^+ and C, chemical sputtering is possible (Hammer, 1996). Here the ion and the sample chemically react forming a volatile product like HCN. However this is not of general use for all sample materials.

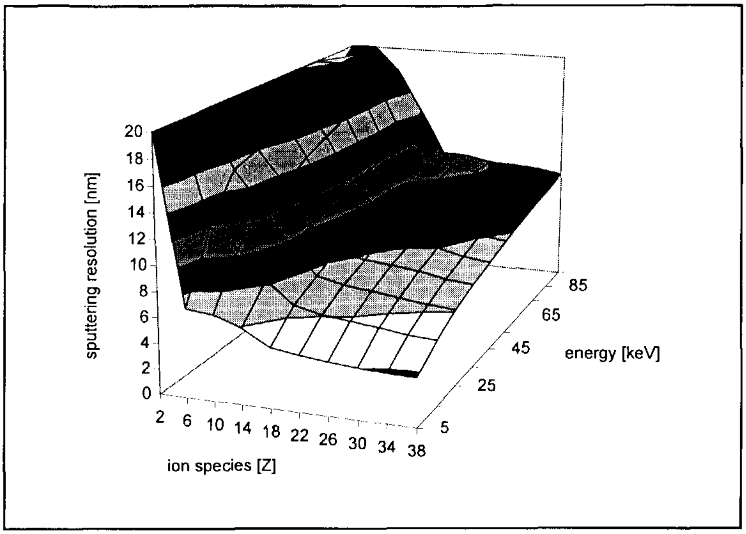

Fig. 3.13. *Median of the lateral distribution of sputtered Si atoms as a function of the atomic number and energy of the incoming ions.*

3.3. Beam induced pattern generation

Implantation and sputtering are direct techniques. This means that only the ions in the beam are used to fabricate the structures. Beam induced pattern generation is an indirect technique. Here the substrate is surrounded by a few millitorr of a precursor gas. Some of the gas molecules adsorb onto the substrate surface, see figure 3.14. In principle there is a reaction possible between the adsorbed gas molecule and the substrate that can result in deposition of an atom from the adsorbed molecule or in etching of the substrate. However, this reaction is endothermic. Therefore, simultaneously with the precursor introduction, a beam of energetic particles is incident on the substrate. The energy of each incident particle is deposited in the substrate through both nuclear and electronic excitations. This deposited energy results in the ejection of atoms through sputtering, but it can also result in locally overcoming the energy barrier for the chemical reaction.

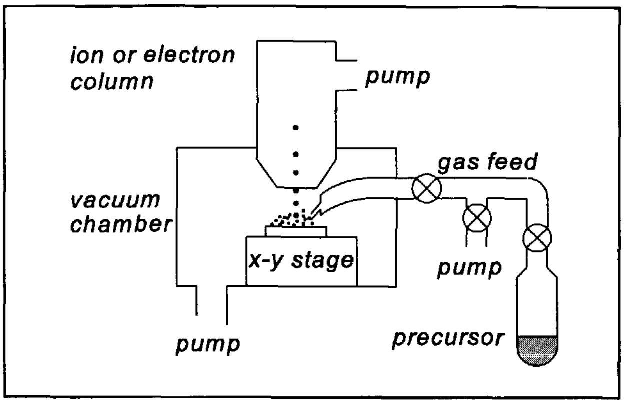

Fig. 3.14. *Angular distribution of sputtered Si atoms by 35 keV Ar ion impact from simulation and the consine distribution.*

The adsorbed molecules will fall apart because of this chemical reaction. In case of deposition, decomposition of the molecules results in a nonvolatile component being deposited and the volatile components leaving the surface. Net deposition occurs when the number of atoms added through deposition exceeds the number of atoms removed by sputtering. In case of etching, a volatile molecule is formed containing a specimen atom. It is immediately clear that the redeposition yield for etching is much smaller than in case of sputtering.

First in this paragraph a model is derived which gives the production yield of beam induced pattern generation as a function of the process parameters. Thereafter the model described in chapter 2 is used to calculate the production yield and the resolution as a function of the mass and energy of the impacting particle.

3.3.1. Model for beam induced pattern generation

When a focused ion beam is used to induce a chemical reaction, this beam will also have an eroding effect mainly through sputtering, as described in the former paragraph. Besides the sputtering effect and the ion beam parameters, the model for beam induced pattern generation also includes parameters such as precursor material and beam scanning speed.

Beam induced pattern generation is realized in a series of process steps. First the precursor molecule adsorbs on the specimen surface. Depending on the type of precursor this can be physisorption or chemisorption with a stronger binding to the specimen. If the adsorbed molecule does not desorb from the specimen before an energetic particle comes along it will be excited by this particle. For exited precursor molecules there are two possibilities: it can return to its ground state, called relaxation, or it can be part of a chemical reaction. Besides the process steps as described above there is also a possibility for a spontaneous reaction. In that case there is only a need for adsorption of a precursor molecule.

Table 3.1 shows the differential equations of each process step of induced pattern generation. The fields within the thick lines in this table are only of interest in the latter case: chemisorption. Seven process steps are incorporated in the model:

1. physisorption of precursor molecules

   This can only occur at free sites because the physisorbed molecule is only weakly bond to the surface. Physisorption on an already physisorbed site is unlikely. If the precursor material is introduced through a nozzle, as shown in figure 3.14, physisorption rate is given by

$$\frac{dN_{ps}}{dt} = g.F.\frac{N_f}{N_0} \qquad (3.11)$$

g= adsorption probability

F= gas flow per unit area per unit time

N_f= number of free sites per unit area

N_0= total number of sites per unit area

The adsorption probability gives the chance that a precursor molecule, that strikes the specimen at a free site, will adsorb on it. It is often assumed to be one. Another situation occurs if the sample is surrounded by an environmental cell. Adsorption from the gas in the cell is not the result of a directed gas flow but of a natural flow of molecules. In this case their velocity distribution is given by the Maxwell-Boltzmann distribution

$$f(v) = \left(\frac{m}{2.\pi.k.T}\right)^{\frac{3}{2}}.4.\pi.v^2.e^{\left(\frac{-m.v^2}{2.k.T}\right)} \qquad (3.12)$$

M= molecular mass of a precursor molecule

T= gas temperature

v= velocity

So, if the precursor material is introduced through a cell, the physisorption rate is given by

Table 3.1. *The partial differential equations for beam induced pattern generation*

	physisorption	desorption	chemisorption	excitation	relaxation	spontaneous reaction	induced reaction
dN_f/dt free sites	$-g.F.\left(\frac{N_f}{N_0}\right)$	$\frac{N_{ps,1}}{\tau_{des}}$	$-k_{chem}.N_f(N_{ps,1}+N_{ps,2})$				
$dN_{ps,1}/dt$ physisorbed sites	$g.F.\left(\frac{N_f}{N_0}\right)$	$-\frac{N_{ps,1}}{\tau_{des}}$	$-k_{chem}.N_f N_{ps,1}$				
dN_{cs}/dt chemisorbed sites	$-g.F.\left(\frac{N_{cs}}{N_0}\right)$	$\frac{N_{ps,2}}{\tau_{des}}$	$k_{chem}.N_f(N_{ps,1}+N_{ps,2})$				
$dN_{ph,2}/dt$ physisorbed sites	$g.F.\left(\frac{N_{cs}}{N_0}\right)$	$-\frac{N_{ps,2}}{\tau_{des}}$	$-k_{chem}.N_f N_{ps,2}$	$-m.s.J.\left(\frac{N_{ps,2}}{N_0}\right)$	$-k_e.N_e$	$-m.k_{r,2}.N_{ps,2}$	
dN_e/dt excited sites				$m.s.J.\left(\frac{N_{ps,2}}{N_0}\right)$	$k_e.N_e$		$-k_{r,1}.N_e$
dN_p/dt product sites						$m.k_{r,2}.N_{ps,2}$	$k_{r,1}.N_e$

$$\frac{dN_{ph}}{dt} = g.\frac{p}{\sqrt{2.\pi.M.k.T}}.\frac{N_f}{N_0} \tag{3.13}$$

p= gas pressure in cell

Table 3.1 shows two rows of physisorption. The first one, $N_{ps,1}$, will always occur whatever the precursor is. The second one, $N_{ps,2}$, will only occur in case of chemisorption. Some precursors, like Cl_2, chemisorb on the sample but that can be at maximum one monolayer. If a precursor molecule adsorbs on an already chemisorbed site, it will physisorb. This is called $N_{ps,2}$.

2. desorption of precursor molecules

Once a molecule is physisorbed it has a certain chance to evaporate. Surface evaporation or desoption is described by a characteristic surface residence time τ_{des}. The number of molecules leaving the surface of the vacuum system per time interval is equal to the total number of molecules on the surface times the frequency of molecules leaving the surface

$$\frac{dN_{ps}}{dt} = -\frac{N_{ps}}{\tau_{des}} \tag{3.14}$$

N_{ps}= number of molecules physisorbed per unit area
τ_{des}= mean remain time

Adsorbed molecules vibrate with frequencies of $10^{12}...10^{14}$ Hz. Therefore there is a chance for desorption every 10^{-13} seconds, this chance is given by the Boltzmann distribution. The mean time a molecules stays on the surface is equal to

$$\tau_{des} = 10^{-13}.EXP\left(\frac{U_B}{k.T}\right) \tag{3.15}$$

U_B= binding energy of a molecule on the surface

So the total number of molecules desorbing from the surface per second per unit area is

$$\frac{dN_{ps}}{dt} = -N_{ps}.10^{13}.\exp\left(-\frac{U_B}{k.T}\right) \tag{3.16}$$

This very simple model for desorption only takes into account desorption into the vacuum. A more sophisticated model also takes into account diffusion of an adsorbed molecule over the surface. This is described in chapter 9.

3. chemisorption

   For chemisorption both a physisorbed and a free site are necessary as the physisorbed molecule e.g. chloride (Cl_2), breaks and each individual atom is chemisorbed to an individual site. The chemisorption process is considered to be fast compared to the other reaction steps. Besides the bond strength is strong which makes desorption of the chemisorbed atom unlikely.

   $$\frac{dN_{cs}}{dt} = k_{chem}.N_f.N_{ps} \tag{3.17}$$

   k_{chem}= chemisorption constant

4. excitation

   The incident particle transfers a certain amount of energy to the adsorbed precursor molecule which transfers it to an excited state, the resonant frequency state. In this situation there is a large chance to change the chemical bonds. The excitation rate is given by

   $$\frac{dN_e}{dt} = m.s.J(t).\left(\frac{N_{ps}}{N_0}\right) \tag{3.18}$$

   N_e= number of excited molecules per unit area

   The factor m is the number of adsorbed molecules required to deposit one atom or to remove one substrate atom. J(t) is the particle density flux, which is shown as time dependent due to the beam scanning. The factor s is the number of excitations by a single particle, the excitation yield. It defines the maximum production yield. The details of the surface binding of reacted substrate atoms and energy deposition of the incident particle are included in the parameter s. Therefore it is this parameter which is mainly discussed in the next paragraphs. Here the effect of beam parameters, mass and energy, on resolution and production yield is described.

5. relaxation

   The excited state of the adsorbed molecule is assumed to be instable. Therefore there is a finite chance that the particle falls back into its ground state, this chance is given by k_e.

   $$\frac{dN_e}{dt} = -k_e.N_e \tag{3.19}$$

6. spontaneous reaction

   There is a finite chance for a spontaneous reaction which is not induced by the incident particles. In this case an adsorbed molecule is enough. The chance is given by the reaction constant $k_{r,2}$.

$$\frac{dN_p}{dt} = m.k_{r,2}.N_{ps} \tag{3.20}$$

   N_p= number of etched or deposited atoms per unit area

7. induced reaction

   There is a finite chance for a reaction of an excited molecule which is induced by the incident particles. In this case an excited molecule is necessary The chance is given by the reaction constant $k_{r,1}$. The sum of k_e and $k_{r,1}$ has to be equal to unity.

$$N_p = k_{r,1}.N_e \tag{3.21}$$

This description is in agreement with models for non-polar precursor molecules by other authors, (Takahashi, 1991) and (Harriott, 1993). An example is the deposition of copper from Cu(hfac)TMVS (copper hexafluoro acetylacetonate trimethylvinylsilane) (Della Ratta, 1993). The TMVS group acts to stabilize the copper oxidation state at room temperature. The normal deposition reaction is

$$2.Cu(hfac)TMVS\ (g) \rightarrow Cu(s) + Cu(hfac)_2(g) + 2.TMVS(g) \tag{3.22}$$

where the letters in parentheses indicate solid phase and gas phase respectively.

In case of a polar precursor molecule also the boxes within thick lines in the table are of importance: it can be chemisorbed. In this case e.g. chloride (a polar precursor molecule) does not react with a clean silicon surface but with SiCl, the etching mechanism consists of two steps

$$\begin{gathered} 2\ Si\ (s) + Cl_2\ (g) \rightarrow 2\ SiCl\ (s) \\ 2\ SiCl\ (s) + 3\ Cl_2\ (g) \rightarrow 2\ SiCl_4\ (g) \end{gathered} \tag{3.23}$$

The differential equations are not in agreement with a published model for polar precursor molecules (Gerlach-Meyer, 1981). In this article it is assumed that a chemisorbed site is excited, followed by physisorption of a molecule on the excited state. This is not a very probable model, as the excited situation can only exist for a very short time (about 10^{-13} seconds). Therefore it is assumed in the model described here that only those molecules on the surface can be excited that have been chemisorbed and on which another precursor molecule has been physisorbed.

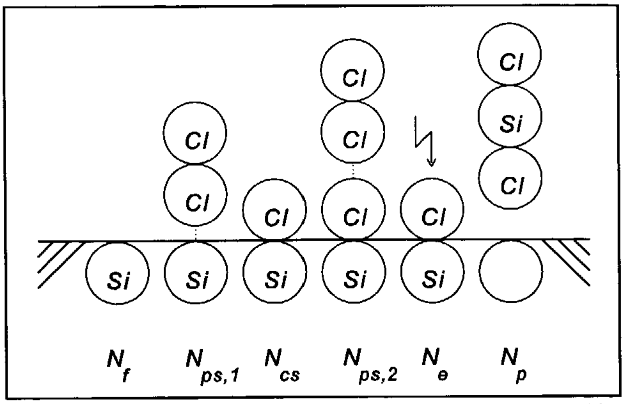

Fig. 3.15. *The etching of silicon with the polar precursor chloride.*

The production yield at equilibrium for beam induced pattern generation is given by

$$PY= \frac{1}{J}.\left[k_{r,1}.N_e+c_1.\left(1-\frac{N_{ps}}{N_0}\right).J.PY_s\right] \tag{3.24}$$

J= particle density flux in the probe of the ion or electron beam
c_1= +1 in case of etching, -1 in case of deposition
PY_s= sputtering yield

Where the second term within brackets describes the sputtering. This increases the production yield in case of etching because substrate atoms are removed. But it decreases the production yield in case of deposition because already deposited atoms are removed.

Equilibrium is obtained for dN/dt=0 for each row in table 3.1, resulting in an equilibrium density

$$\begin{aligned} N_{ps} &= \frac{g.F.N_0}{g.F+\dfrac{N_0}{\tau_{des}}+k_{r,2}.m.N_0+k_{r,1}.m.\dfrac{s.J}{k_e+k_{r,1}}} = \frac{gF}{Q_1} \\ N_e &= \frac{g.F.m.s.J}{\left(\dfrac{1}{\tau_e}+k_{r,1}\right).\left(g.F+\dfrac{N_0}{\tau_{des}}+k_{r,2}.m.N_0+k_{r,1}.m.\dfrac{s.J}{k_e+k_{r,1}}\right)} \\ &= \frac{g.F.m.s.J}{(k_e+k_{r,1}).N_0.Q_1} \end{aligned} \tag{3.25}$$

The production yield becomes at equilibrium

$$PY = \frac{k_{r,1}.g.F.m.s}{(k_e+k_{r,1}).N_0.Q_1} - c_1.\left(1-\frac{gF}{N_0.Q_1}\right).PY_s$$

$$Q_1 = \frac{g.F}{N_0} + \frac{1}{\tau_{des}} + k_{r,2}.m + \frac{k_{r,1}.m}{N_0}.\frac{s.J}{k_e+k_{r,1}} \qquad (3.26)$$

This equation simplifies if it is assumed that no relaxation from the excited state takes place (k_e=0), therefore every excited state results in a reaction ($k_{r,1}$=1) and that no spontaneous reactions and sputtering occur ($k_{r,2}$=0 and PY_s=0)

$$PY = \frac{g.F.m.s}{g.F + \frac{N_0}{\tau_{des}} + m.s.J} \qquad (3.27)$$

This is the model which is often used in literature (Koops, 1988).

But in general the system is not at equilibrium. Beam induced pattern generation is accomplished by raster scanning of the particle beam during the exposure of the sample surface to the gas flux. The beam is generally scanned in a pattern made of discrete points or pixels in multiple exposures to deliver the necessary total charged particle dose, see figure 3.16. It is assumed here that the probe in which the electrons or ions are focused is not changed during the exposure of the full pattern. However there are several exposure techniques that change the probe size during exposure, like variable shaped beam exposure (Koets, 1994) (Mulder, 1991).

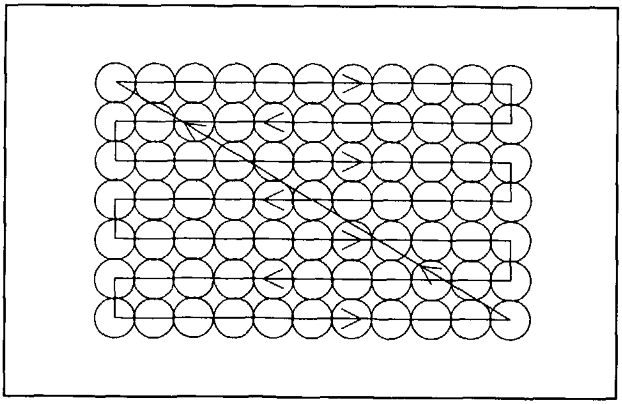

Fig. 3.16. *Beam raster scan illustrating dwell time (the exposure time of a pixel) and refresh time (the exposure time of the frame).*

In case of raster illumination each pixel is exposed to the beam for a time T_d, the dwell time, and then exposured again when the raster scan is repeated. Production only takes place at any given pixel during the dwell time. The dwell time is defined as

$$T_d = \frac{d}{v} \tag{3.28}$$

d= Full Width at Half Maximum (FWHM) of the particle beam
v= scan speed of the beam

The period of time between repeated pixel exposures, the refresh time T_r, allows for adsorption of additional gas molecules on the sample surface. The sum of dwell time and refresh time is called loop time T_l. The loop time is defined as

$$T_l = \frac{A}{[d.(1-R)]^2}.T_d \tag{3.29}$$

A= area to be exposed
R= overlap between the pixels

In the assumption that the ion flux is constant over a pixel during the dwell time, the production yield at raster scanning exposure for beam induced pattern generation is given by

$$\begin{aligned} PY &= \frac{1}{J.T_d}.\int_0^{T_d}\left[k_{r,1}.N_e + c_1.\left(1 - \frac{N_{ps}}{N_0}\right).J.PY_s\right]dt \\ &= \frac{m.s - c_1.PY_s}{N_0.T_d}.\int_0^{T_d} N_{ps}.dt + c_1.PY_s \end{aligned} \tag{3.30}$$

$$\frac{dN_{ps}}{dt} = g.F - N_{ps}.\left(\frac{g.F}{N_0} + \frac{1}{\tau_{des}} + \frac{m.s.J}{N_0}\right) \tag{3.31}$$

During dwell time the number of physisorbed sites is

$$\begin{aligned} N_{ps,d} &= \frac{g.F}{Q_2}.\left(1 - c_2.e^{-Q_2.t}\right) \quad 0<t<T_d \\ Q_2 &= \frac{g.F}{N_0} + \frac{1}{\tau_{des}} + \frac{m.s.J}{N_0} \end{aligned} \tag{3.32}$$

During refresh time the number of physisorbed sites is

$$
\begin{aligned}
N_{ps,r} &= \frac{gF}{Q_3}.\left(1 - c_3.e^{-Q_3.t}\right), \quad T_d<t<(T_d+T_r)\\
Q_3 &= \frac{g.F}{N_0} + \frac{1}{\tau_{des}}
\end{aligned}
\qquad (3.33)
$$

The integration constants c_2 and c_3 follow from the boundary condition that N_{ps} connect during the dwell time and the refresh time

$$
\begin{aligned}
N_{ps,d}(t=T_d) &= N_{ps,r}(t=T_d)\\
N_{ps,d}(t=0) &= N_{ps,r}(t=T_d+T_r)
\end{aligned}
\qquad (3.34)
$$

The production yield becomes at raster scanning exposure

$$
\begin{aligned}
PY &= \frac{m.s-c_1.PY_s}{T_d}.\frac{g.F}{N_0.Q_2}\\
&\quad .\left(T_d + \frac{Q_2-Q_3}{Q_2.Q_3}.\frac{[1-e^{-Q_2.T_d}].[1-e^{-Q_3.T_r}]}{1-e^{-Q_2.T_d}.e^{-Q_3.T_r}}\right) + c_1.PY_s\\
Q_2 &= \frac{g.F}{N_0} + \frac{1}{\tau_{des}} + \frac{m.s.J}{N_0}\\
Q_3 &= \frac{g.F}{N_0} + \frac{1}{\tau_{des}}
\end{aligned}
\qquad (3.35)
$$

Equation (3.35) is in agreement with the model described by Takahashi (Takahashi, 1991). But there is a slight disagreement with models described elsewhere (Harriott, 1993) and (Lipp, 1995). In these models it is assumed that there is no adsorption and desorption of precursor molecules during the exposure time, therefore equation (3.27) reduces to

$$
\begin{aligned}
N_{ps,d} &= c_2.e^{-Q_2.t}, \quad 0<t<T_d\\
Q_2 &= \frac{m.s.J}{N_0}
\end{aligned}
\qquad (3.36)
$$

The production yield becomes at raster scanning exposure

$$
\begin{aligned}
PY &= \frac{m.s - c_1.PY_s}{T_d} . \frac{g.F}{N_0.Q_2.Q_3} \\
&\quad . \left(\frac{[1-e^{-Q_2.T_d}].[1-e^{-Q_3.T_r}]}{1-e^{-Q_2.T_d}.e^{-Q_3.T_r}} \right) + c_1.PY_s \\
Q_2 &= \frac{m.s.J}{N_0} \\
Q_3 &= \frac{g.F}{N_0} + \frac{1}{\tau_{des}}
\end{aligned}
\qquad (3.37)
$$

Whether equation (3.35) or (3.37) describes the production yield more accurately strongly depends on the substrate temperature during exposure. If there is a large temperature rise adsorption is unlikely. The influence of particle beam parameters on temperature rise will be dealt with in the next paragraph. Figure 3.17 shows the time dependencies in case of beam induced deposition. In practice a typical dwell-time is 1 μs, while the total refresh time can be several seconds.

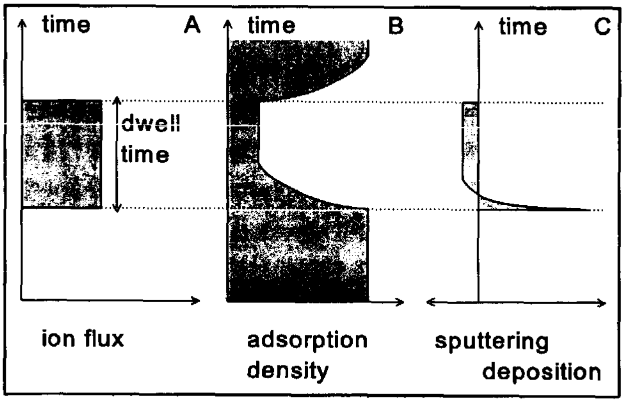

Fig. 3.17. *Time dependencies of (a.) ion beam, (b.) gas adsorption density and (c.) deposition and sputtering at an arbitrary point in the exposed area (Takahashi, 1991).*

3.3.2. The yield

In all equations for the production yield in the former paragraphs there is the parameter s, the number of excitations induced by a single incoming particle. This excitation yield is equal to the production yield if the yield is limited by the beam, so g.F>> m.s.J in equation (3.27). However it is this parameter that will be discussed in this and the following paragraph as it is the parameter through which the ion parameters act on the production yield and the resolution of beam induced pattern generation.

In fact the ion transfers energy to the sample during its collision cascade. Part of this energy releases as phonons and secondary electrons. The chemical reaction can occur through the temperature rise or the excitations by the secondary electrons.

There are several phenomenological models for the diffusion of heat transferred to a sample by energetic particles

$$(\mathit{Tandon},\ 1995) \qquad \Delta T = \frac{U.J}{8.\lambda_h} . \frac{d^2}{r} \tag{3.38}$$

U= energy of the ions
J= current density
λ_h= thermal conductivity
d= diameter of the probe
r= radial distance from the center of the probe

$$(\mathit{Arnold},\ 1995) \qquad \Delta T = T_{\max} . \left(1 - \frac{r^2}{w_T^2} \right) - T_\infty \tag{3.39}$$

T_{max}= maximum temperature
T_∞= temperature of substrate far away from probe
w_T= radius of localization of the temperature

For the impact of a probe of ions as will be discussed in chapter 4 (d= 2 nm, J= 0.32 A/cm^2, U= 25 keV) the temperature rise at the boundary of the probe in a Si sample (λ_h= 149 W/(m.K)) is 2.7 10^{-4} K according to equation (3.38). However this equation gives an average temperature rise over time assuming a uniform energy impact. Therefore the assumption is made that the diffusion process is slow compared to the rate of arriving of the ions. In the actual case of "the Fancier" the time interval between the arriving of two particles with a probe current of 10^{-14} A is 16 μs.

Figure 3.18a shows the temperature rise of the area directly under the beam of 25 keV Ar ions as a function of the time after impact of a single ion. It is the result of the calculation of the time and place dependent phonon diffusion through the sample, based on equation (2.51). The data for phonon energy have been obtained using the Monte Carlo program TRIM (Ziegler, 1985). It can be concluded that after less than 10 ps the sample has returned to its original temperature. So the assumption for equation (3.38) is not valid. Therefore the temperature rise is actually higher than calculated with the above equation.

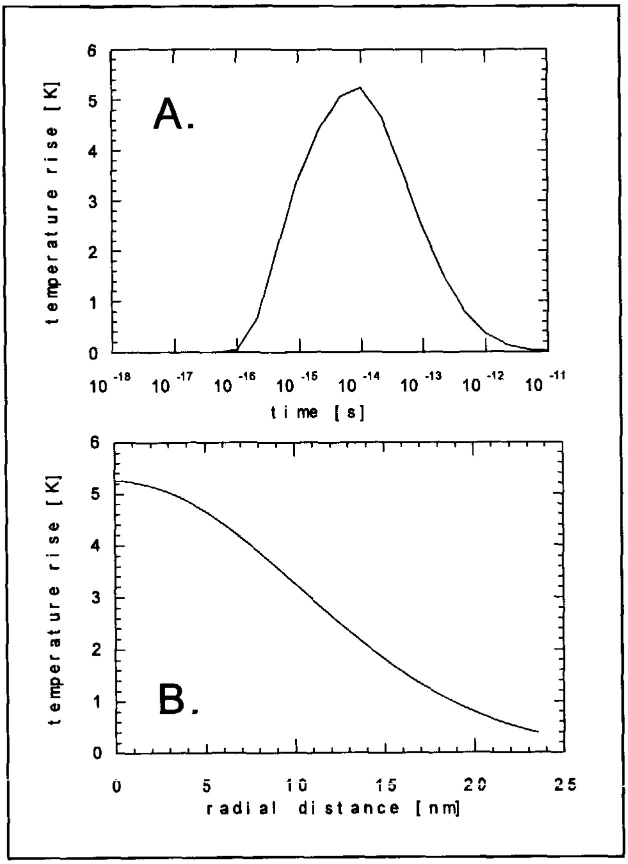

Fig. 3.18. *Temperature rise due to the impact of a 25 keV Ar ion on a Si sample (a.) time distribution, (b.) lateral distribution.*

Another time dependent temperature increase (Ishitani, 1995)

$$\Delta T = T_{\max}.\frac{2}{\pi}.\arctan\left(\sqrt{\frac{16.\lambda_h.t}{\rho.C_p.d^2}}\right) - T_\infty \tag{3.40}$$

shows that 95% of the maximum is reached after 4.6 10^{-13} s. This is in reasonable agreement with the Monte Carlo simulation. The lateral temperature rise for an infinitesimal small probe is depicted in figure 3.18b for the same ion parameters. This shows that the full width at half maximum of the temperature distribution at the surface is about 20 nm. Figure 3.19 shows the maximum temperature rise for different ion species and energies on a Si sample.

From this figure it can be seen that it is not very reasonable to assume that the chemical reaction is induced by the temperature rise. The activation energy is 1-5 eV for most of the precursors meaning that a excitations yield of 10-30 excitations per ion is only possible for a temperature increase of more than 10^3 K. In principle these values can be reached especially for very large current density in a large probe. Also the material of the substrate is of main importance especially through its thermal conductivity (Ishitani, 1995).

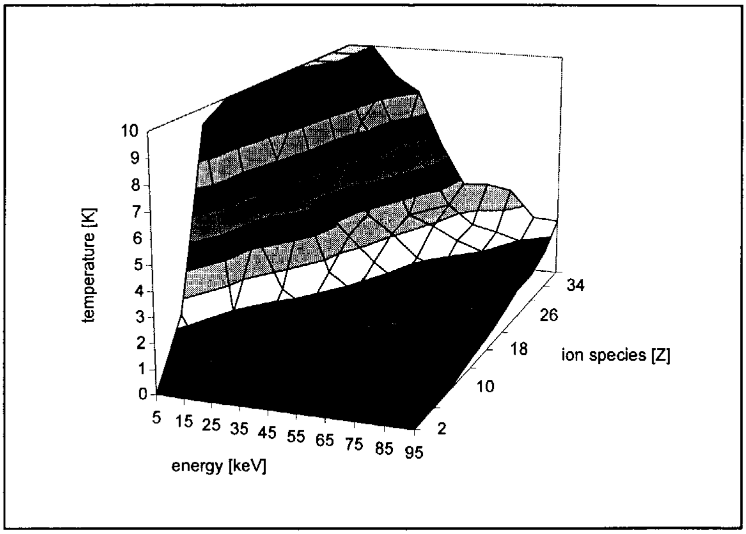

Fig. 3.19. *Maximum temperature rise of a Si sample as a function of the atomic number and energy of the incoming ions..*

The other possible origin, excitation by secondary electrons generated by the primary particle, is therefore the only reasonable explanation for beam induced etching and deposition at very high resolution. This is in agreement with other theoretical studies and experimental results. In a Monte Carlo simulation of the illumination process of PMMA-resist (Samoto, 1983) the results clearly indicate that the secondary electrons play the most important role in determining the energy dissipation profile in the vicinity of the point of incidence, being the significant source of broadening the energy dissipation profile.

Also the process of beam induced deposition by energetic electrons, secondary electrons are assumed to be of main importance. Experimental results (Kohlmann, 1993) show that the primary electron scattering cannot explain the observed growth. For that reason, the surface growth was correlated to the number of secondary electrons emitted by the primary beam considering the Gaussian intensity distribution of the electron beam and the angle dependence of the secondary electron yield. It was concluded (Kohlmann, 1993) that there is a linear relation between the number of secondary electrons and the surface growth. Therefore it is reasonable to assume that the chemical reactions are induced by the secondary electrons.

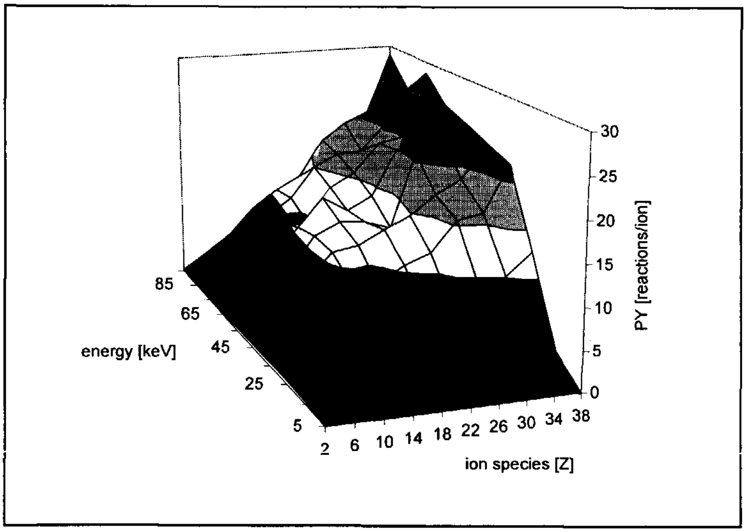

Fig. 3.20. *Production yield of deposition induced by sec. electrons as a function of the atomic number and energy of the incoming ions.*

Figure 3.20 shows the excitation yield for deposition of Al as a function of the beam parameters atomic number and energy. The Al atoms are deposited from the precursor $Al(C_4H_9)_3$. The activation energy for the dissociation is 0.95 eV, while the reaction rate coefficient is 10^9 reactions /(atom.s) (Granneman, 1991). For various precursors experimental results of the excitation yield are listed in table 3.2. If the results of this table are compared to the results of figure 3.20 it can be concluded that the results are of equal order of magnitude, assuming that the activation energy of most precursors is about a few eV. Furthermore it can be concluded that the removal rate of etching is more than one order of magnitude larger than of physical sputtering while it is also more effective because the redeposition is minimized.

Table 3.2. *The excitation yield of different precursors as a result of the impact of a beam of energetic particles.*

precursor	substrate	particle, energy	excitation yield, s [-/particle]	reference
$Al(CH_3)_3$	SiO_2	Ar, 50 keV	13	Gamo, 1984
$MeCpPt(Me)_3$	SiN	Ga, 25 keV	1	Puretz, 1992
$W(CO)_6$	SiO_2	Ga, 30 keV	222	Takahashi, 1991
$W(CO)_6$	Si	electrons, 5 keV	$1.39\ 10^{-3}$	Hoyle, 1993
Cl_2	Si	He, 1 keV Ne, 1 keV Ar, 1 keV	1 2 3.5	Gerlach-Meyer, 1981
Cl_2	Si	Ga, 5 keV Ga, 20 keV	36 47	Komuro, 1990
Cl_2	Si SiO_2 Au	Ga 30 keV	21 1.4 10-26	Young, 1993
I_2	Si	Ga, 30 keV	155	Lipp, 1995
XeF_2	Si	He, 1 keV Ne, 1 keV Ar, 1 keV	13 22 30	Gerlach-Meyer, 1981
XeF_2	SiO_2 W	Ga, 20 keV	5.1 29.5	Harriott, 1993
XeF_2	SiO_2	Ga, 20 keV	~100	Harriott, 1993

3.3.3. The resolution

The resolution of beam induced reaction techniques is defined as the lateral area on the surface in which 50 % of the reactions occurs. Figure 3.21 shows the distribution of the excitation yield over the surface. It has a maximum near the impact point of the incoming ion and a tail away from the impact point. The maximum is a result of the path of the primary beam in the first collisions into the sample: all energy is very localized. The broadening of the ion distribution after a lot of collisions makes the secondary electrons coming from a relative large distance from the impact point. This results in the tails of the excitation distribution. Similar results have been obtained for illumination of resist (Murata, 1990).

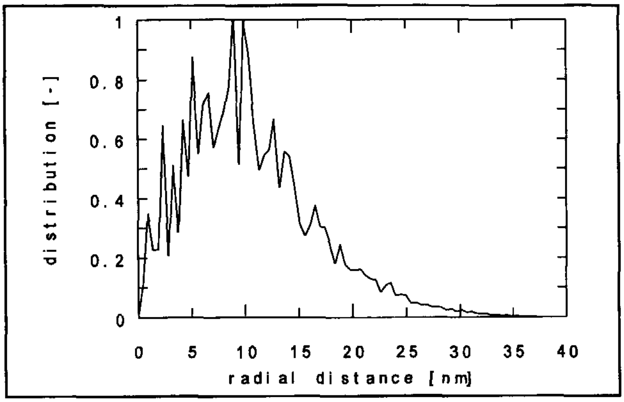

Fig. 3.21. *Lateral distribution of the excitation yield of 25 keV Ar ions for* $Al(C_3H_9)_3$ *precursor.*

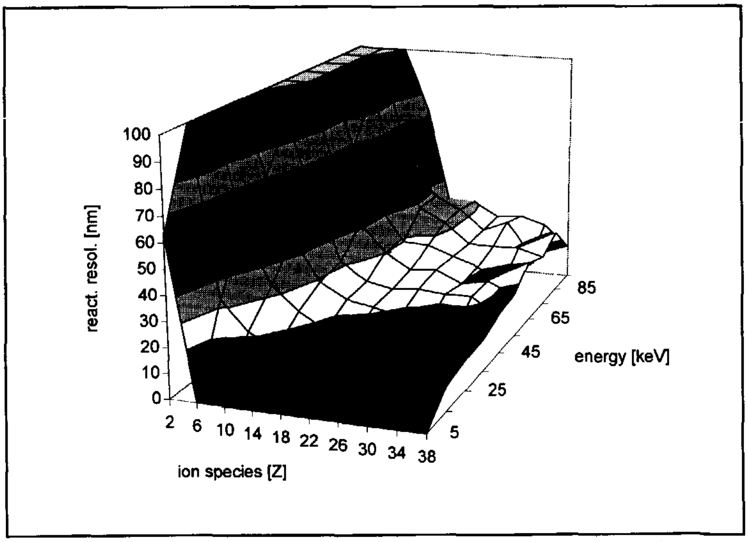

Fig. 3.22. *Resolution of Al induced deposition on Si as a function of the atomic number and energy of the incoming ions.*

Figure 3.22 depicts the resolution of the deposition of Al from $Al(C_3H_9)_3$. It again shows a decreasing resolution for increasing energy of the primary particle. This is similar to the proximity effect as known from electron beam lithography. The proximity range is given by (Schoranzer, 1995)

$$d = d_{sc} \cdot \left(\frac{U}{U_{sc}} \right)^{n} \tag{3.41}$$

d_{sc}= scaling range (1.94 for electrons in Si)
U_{sc}= scaling energy (20 keV for electrons in Si)
n= power factor (1.65 for electrons in Si)

Least-square fitting of this equation to the beam induced deposition resolution with Ar ions give d_{sc}= 2.151 nm, U_{sc}= 516 eV and n= 0.545.

3.4. Observation

When a beam of energetic particles impinges upon a solid, these primary particles lose energy through inelastic scattering. Part of this energy is transferred to the electrons in the specimen. Some excited electrons escape from the specimen and it is usual to define all electrons emitted from the target with a kinetic energy lower than 50 eV as secondary electrons.

Secondary electrons can be used to characterize solids with scanning electron microscopy. In a scanning electron microscope secondary electrons are used to image surface topography, see figure 3.23. Secondary electron imaging with high spatial resolution (<1 nm) has been achieved in a dedicated scanning transmission electron microscope (Bleloch, 1989).

Therefore, the most convenient way to observe the mesoscopic structures in a particle optics instrument is to measure the number of secondary electrons coming from the

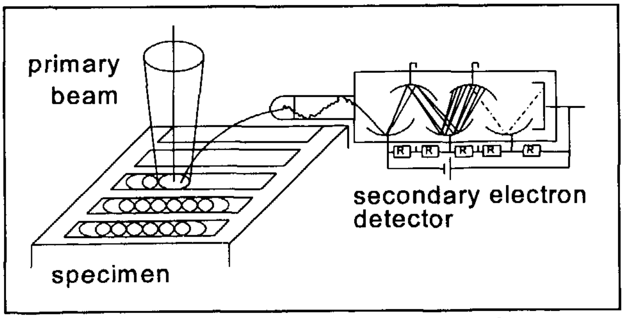

Fig. 3.23. *Secondary electron detector in a scanning electron microscope.*

specimen after bombarding with a primary beam in scanning mode. The primary particle can in principle be as well an electron as an ion, both give a certain amount of secondary electrons per impinging particle. This secondary electron yield will be discussed first and compared with results of the simulation. Thereafter the energy distribution and the angular distribution of secondary electrons is described. Finally the resolution of observation by secondary electron counting is simulated based upon the model of chapter 2.

3.4.1. The yield

The number of free secondary electrons above the sample, or the secondary electron yield, reflects three processes. Firstly there is the production of secondary electrons in the sample by the primary particle. Secondly these electrons start moving around in the sample and they have a finite chance to reach the surface. Thirdly the electrons can be emitted, if they have enough energy, resulting in a free secondary electron.

A very simplified model for free secondary electron emission has been described by Joy (Joy, 1987). Consider an electron traveling in a solid, the rate of production of secondaries can be assumed to be proportional to the average rate of energy loss during inelastic collisions, the electronic energy loss

$$\frac{dN(z,U)}{dz} = -\frac{1}{\epsilon}.\left(\frac{dU}{dz}\right)_e = -\frac{1}{\epsilon}.S_e \qquad (3.42)$$

z= depth in surface

ϵ= energy needed to produce a secondary electron with sufficient excess energy to allow escape from the target, approximately 50 eV/electron

S_e= electronic stopping power

If any effects of refraction and reflection are ignored the average escape probability for a secondary electron produced will be

$$W(z) = W_0 e^{-\frac{z}{L}} \qquad (3.43)$$

W_0= probability of electron escaping from the surface, approximately 0.5

L= characteristic attenuation length for the substrate material, approximately 1 nm

The total secondary electron yield is then

$$SEY = \int_{0}^{\infty} \frac{dN(z,U)}{dz}.W(z)dz = \int_{0}^{\infty} \frac{W_0}{\epsilon}.S_e.e^{-\frac{z}{L}}dz \tag{3.44}$$

In order to evaluate this equation for electrons and ions as primary particles, a specific description of the electronic stopping power has to be introduced.

For electrons the electronic stopping power is given by the Bethe equation (2.20). According to Reimer (Reimer, 1993) the ln(U/U_{nl})/U term in the Bethe equation can be approximated by $U^{-0.8}$ for electron energies between 5 keV and 100 keV. Besides it is stated here that equation (3.42) has to be separated in two regimes

$$\begin{aligned} \frac{dN(z,U)}{dz} &= \frac{A}{\epsilon}.U, \quad R \ll L \\ &= \frac{A}{\epsilon}.L.S_e, \quad R \gg L \end{aligned} \tag{3.45}$$

A= proportionality factor [m^{-1}]
R= electron range

When modifying an approach for SEY, both regimes can be combined in (Reimer, 1993)

$$SEY = 1.31\ \delta_m.\left(\frac{U}{U_m}\right)^{-0.8}.\left[1 - e^{-1.45\left(\frac{U}{U_m}\right)^{1.45}}\right] \tag{3.46}$$

d_m= maximum yield
U_m= energy of secondary electrons at maximum yield

In a slightly different approach (Joy, 1987) another equation is derived for the secondary electron yield for electrons as primary particles

$$SEY = 1.11\ \delta_m.\left(\frac{U}{U_m}\right)^{-0.35}.\left[1 - e^{-2.3\left(\frac{U}{U_m}\right)^{1.35}}\right] \tag{3.47}$$

For a silicon specimen δ_m is given to be 1.10 and U_m is 400 eV (Joy, 1987), while Weast (Weast, 1987) gives 1.10 and 250 eV respectively. According to Kanaya (Kanaya, 1972) the maximum yield is 0.73-0.85 at an energy of 290-300 eV.

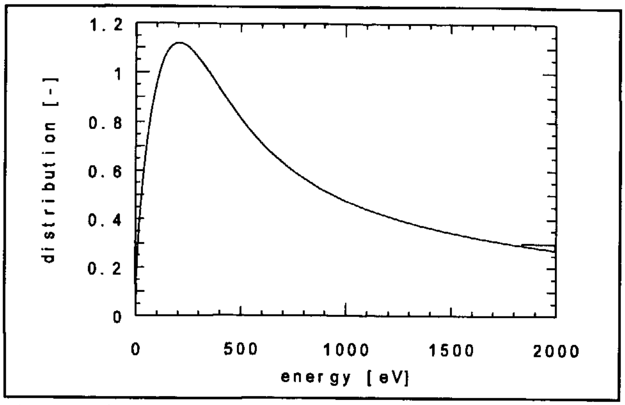

Fig. 3.24. *The secondary electron yield coming from a Si specimen after bombarding with electrons as a function of their energy after equation (3.46).*

Ions travel at much lower velocities, here the Bethe equation for the electronic stopping power is no longer valid, therefore the Lindhard-Scharff equation is used, see equation (2.18). Hence according to Beuhler (Beuhler, 1977)

$$SEY = \frac{W_0}{\epsilon}.\frac{N}{4.\pi.\epsilon_0}.\frac{8.\pi^2.a_0}{v_0}.\xi.\frac{(Z_1.Z_2)}{\left(Z_1^{\frac{2}{3}}+Z_2^{\frac{2}{3}}\right)^{\frac{3}{2}}} \cdot \int_0^{\infty}\sqrt{\frac{2.U(z)}{M_1}}.e^{-\frac{z}{L}}.dz \qquad (3.48)$$

It can be seen that if the energy does not change significantly as the projectile penetrates the thin surface layer from which secondary electrons can escape this equation reduces to

$$SEY = \frac{W_0}{\epsilon}.\frac{N}{4.\pi.\epsilon_0}.\frac{8.\pi^2.a_0}{v_0}.\xi.\frac{(Z_1.Z_2)}{\left(Z_1^{\frac{2}{3}}+Z_2^{\frac{2}{3}}\right)^{\frac{3}{2}}}.\sqrt{\frac{2.U(z)}{M_1}}.L \qquad (3.49)$$

Figure 3.24 and 3.25 show the secondary electron yield as a function of the mass and energy of the incoming particle calculated with equation (3.46) for electrons and equation (3.49) and Monte Carlo calculation for ions.

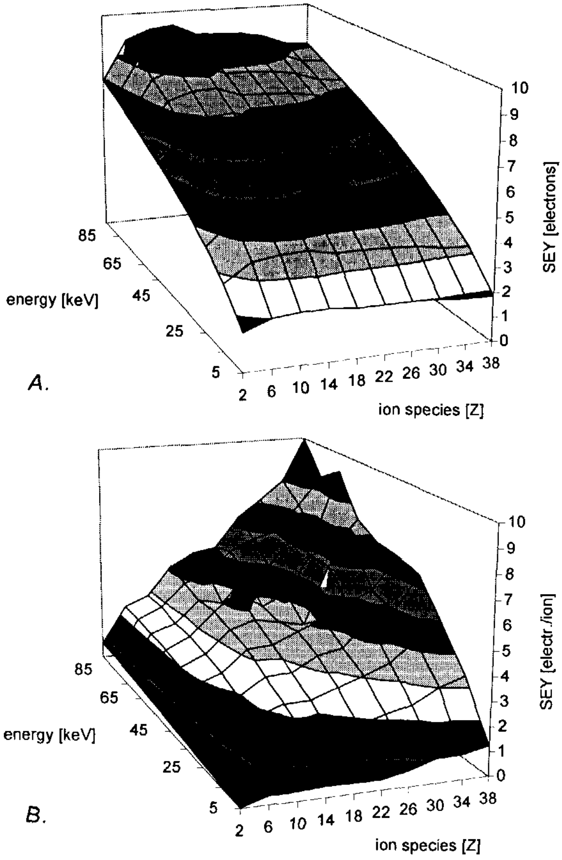

Fig. 3.25. *The secondary electron yield coming from a Si specimen as a function of the atomic number and energy of the incoming ions (a.) equation (3.49), (b.) Monte Carlo simulation.*

When an electron microscope works at a configuration where the total yield is unity we talk about a "non-Loading" condition. When the yield is lower than unity there a more electrons impinging on the specimen than electrons leaving the sample. The surplus charge must be drained off or the specimen charges up in case of a non-conductive specimen.

When electrons of a few keV are used as primary particles the process stabilizes. The surface will charge negatively. With this negative charge, the acceleration voltage with respect to the surface potential decreases and the emission yield increases neutralizing the specimen. If positive ions are used as primary particles the specimen always charges positively without any stabilization.

Therefore a (semi-)isolating specimen preferably has to be observed with electrons of a few keV energy (Mulvey, 1991).

3.4.2. The energy distribution

The energy distribution of electrons emitted from a specimen surface is a typical cascade distribution, modified by the refraction effect at the transition from the solid to the vacuum. The main features of electron spectra are, therefore, not so much determined by the primary excitation but by the development of the electron cascade. This is in agreement with the statement that the energy distribution of the emitted secondaries obtained in case in case of electrons and ions are fairly similar (Cailler, 1990). The distribution of emitted secondary electrons is given by

$$\frac{dN_{se}}{dU_{se}} \sim \frac{U_{se}}{\left(U_{se}+\phi_w\right)^2 . S_e(U_{se})} \qquad (3.50)$$

The electronic stopping power of low energy (order of eV) secondary electrons is obtained by Schou and given by equation (2.16) with $U_{se}+\phi_w$ as the internal energy in the specimen.

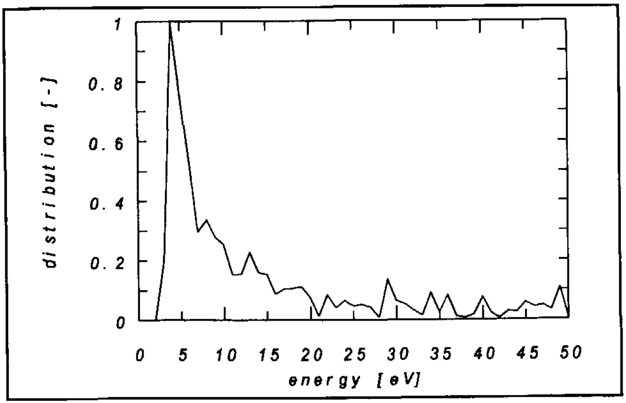

Fig. 3.26. *The energy distribution of secondary electrons coming from a Si sample at various energies of the incoming Si ions at 45 keV energy.*

$$\frac{dN_{se}}{dU_{se}} \sim \frac{U_{se}}{\left(U_{se}+\phi_w\right)^2 . \left(U_{se}+\phi_w\right)^{2.4}} \tag{3.51}$$

Compare this with the often used equation (Reimer, 1993)

$$\frac{dN_{se}}{dU_{se}} \sim \frac{U_{se}}{\left(U_{se}+\phi_w\right)^4} \tag{3.52}$$

This results in a most probable secondary electron energy $\phi_w/3$. Figure 3.26 shows the energy distribution of secondaries after impact of Si ions at 45 keV energy calculated by the Monte-Carlo simulation as described in chapter 2.

3.4.3. The angular distribution

In the regime of kinetic electron emission from amorphous or polycrystalline substrates, all investigations agree in that:

- the angular distribution is rotationally symmetric around the surface normal
- the azimuthal symmetry is independent of the angle of primary particles incidence if this angle is smaller than 60°

The poloidal distribution follows very closely a cosine law

$$\frac{dSEY}{d\Omega}(\theta) = \frac{SEY}{\pi}.\cos(\theta) \tag{3.53}$$

The physical origin of the cos(θ)-distribution of emitted electrons is an isotropic flux distribution of electrons inside the solid. All registered distributions conform a cos(θ)-law, despite the fact that for particles incidenting at low energy electron emission is due to potential emission. For potential emission, one would expect (Hofer, 1990) a distribution more peaked in the direction of the surface normal.

Integration over the solid angle gives

$$\frac{dSEY}{d\theta}(\theta) = \frac{SEY}{\pi}.\int_0^{2.\pi} \cos(\theta).\sin(\theta).d\phi = 2.SEY.\sin(2.\theta) \tag{3.54}$$

The angular distribution model, calculated by Monte Carlo simulation of Ar ions, shows a more uniform distribution than the above model. See figure 3.27.

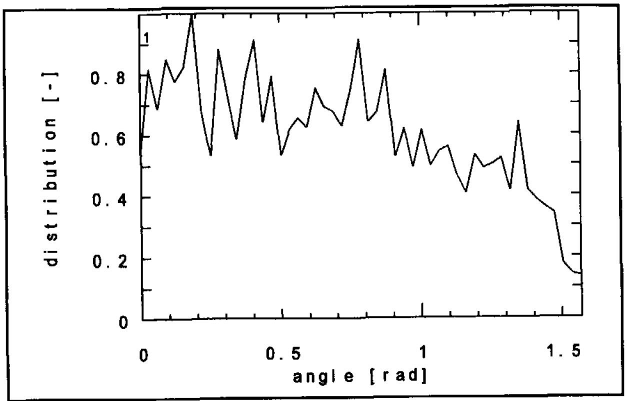

Fig. 3.27. *The angular distribution of secondary electrons emitted from a Si sample after bombardment of 25 keV Ar ions.*

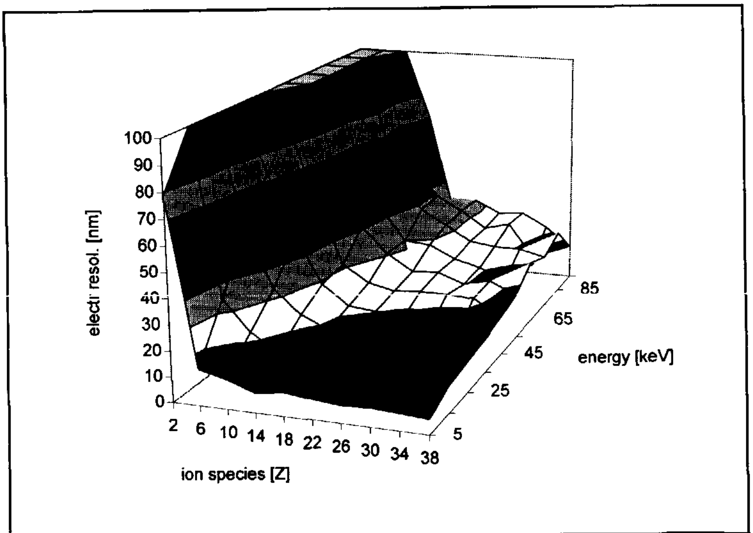

Fig. 3.28. *Resolution of Al induced deposition on Si as a function of the atomic number and energy of the incoming ions.*

3.4.4. The resolution

The resolution of secondary electron imaging with an infinitesimal small beam of primary particles is defined as the lateral area on the surface from which 50% of the secondary electrons are emitted. This definition is chosen since in the Monte-Carlo model the specimen is assumed to be homogeneous. Therefore a regular definition for resolution cannot be used here.

Figure 3.28 depicts the resolution of secondary imaging according to the above definition. As with the fabrication techniques the resolution is improved if the primary particles have a higher mass and lower energy.

3.5. Comparison of fabrication techniques

With the help of the Monte Carlo simulation model, discussed in chapter 2, the properties have been discussed of pattern generation and observation with energetic particles as a function of their mass and energy. The simulations have been compared with experimental results and other models for yield, energy and angular distribution. It can be concluded that the Monte Carlo model is in sufficiently good agreement with these results. Based on the same model, the resolution is calculated that can be obtained with the fabrication techniques, direct implantation, sputtering and beam induced pattern generation.

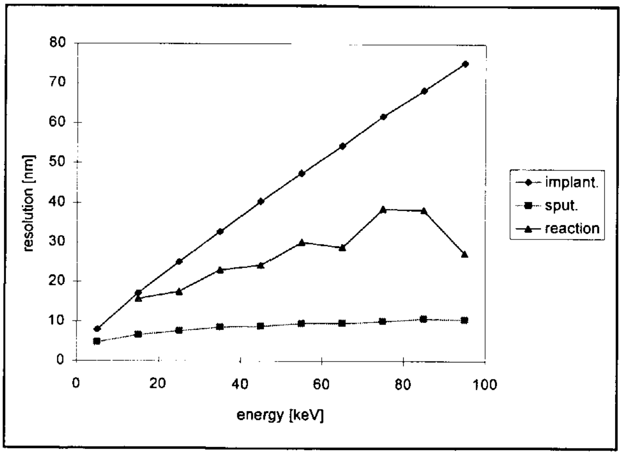

Fig. 3.29. *Resolution of fabrication with Ar ions (series 1) direct implantation, (series 2) sputtering, (series 3) beam induced pattern generation.*

In general it can be concluded that the best resolution is obtained for high mass, low energy particles. The explanation is that these particles are stopped very effectively in a specimen keeping the interaction between the ions and the sample very localized. It will be shown in the next chapter that this trend is opposite to minimizing the interactions between the particles in the beam. Figure 3.29 summarizes the resolution of an Ar ion beam with infinitesimal small lateral probe size for these techniques.

This shows that the highest resolution is achieved for pattern generation by sputtering.

Although this conclusion is probably valid for a wide range of samples and beam induced reactions, it is to be expected that it is not of general use. Further away from the point of impact there is less energy available. Therefore the specific surface binding energy or the chemical reaction energy can influence the resolution of sputtering and beam induced pattern generation respectively. If more energy is necessary the resolution will increase but also the production yield will decrease.

3.6. Comparison of imaging with ions and electrons

Once the nanostructures have been created, they need to be observed. The most convenient method is to measure the secondary electron yield coming from the specimen after bombarding with a primary beam in scanning mode. With the same Monte-Carlo model, discussed in chapter 2, the generation and transport of secondary electrons through the sample have been calculated and compared with experimental and analytical results. It shows that there is significant difference between these results. However several conclusions can be made based on these calculations.

For one pixel of an image 10^4 secondary electrons are needed for a reasonable signal-to-noise ratio (Herrmann, 1984). Unfortunately, it is not only secondary electrons that are emitted after bombarding with ions, also emission of sputtered atoms will occur. This will erode the specimen. One can calculate the minimum number of sputtered monolayers that results from observation of a surface with a surface density of 13.2 atoms per nm^2 (Si). The ratio of sputtering yield and secondary electron yield, as calculated in paragraph 3.2 and 3.4, is depicted in figure 3.30 for different primary particles incident on a Si sample. Based on these data the number of eroded monolayers is calculated for impact of 25 keV particles, see figure 3.31. If it is required that at most one monolayer may be removed, only electrons can be used to observe the structures with a resolution better than 1 nm. This conclusion is in agreement with other authors (Orloff, 1996).

Therefore "the Fancier" will combine two beams: an ion beam for fabrication and an electron beam for observation of the nanostructures. In the next chapters the design of this instrument will be discussed. There the results of this chapter will be used as they are of main influence defining the actual resolution of pattern generation.

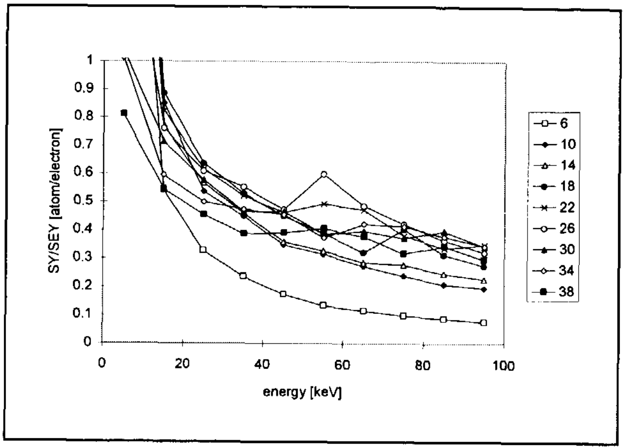

Fig. 3.30. *Ratio of the sputtering yield and the secondary electron yield as a function of the energy of the primary particles.*

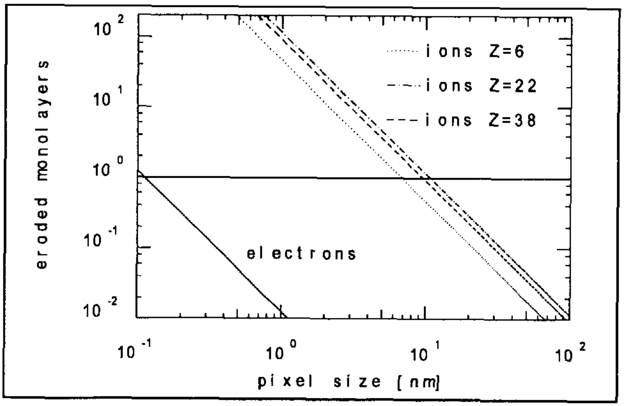

Fig. 3.31. *Number of sputtered monolayers after observation of a Si structure with different particle beams as a function of the pixel size.*

References

Almen, O. and G. Bruce , Nuclear Instruments and Methods 11, 1961, pp257

Arnold, N., *On the spatial confinement in energy beam microprocessing*, Journal of Applied Physics 78(7), 1995, pp. 4805-4807

Auciello, O. and R. Kelly, *Ion Bombardment Modification of Surfaces - Fundamentals and Applications* -, Elsevier, Amsterdam, 1984, pp. 44-53

Beuhler, R.J and L. Friedman, *A model of secondary electron yields from atomic and* *polyatomic ion impacts on copper and tungsten surfaces based upon stopping-power calculations*, Journal of Applied Physics 48(9), 1977, pp. 3928-3936

Biersack, J.P., *Calculation of projected ranges- analytical solutions and a simple general algorithm*, Nuclear Instruments and Methods 182/183, 1981, pp. 199-206

Biersack, J.P., *Computer simulation of sputtering*, Nuclear Instruments and Methods B 27, 1987, pp. 21-36

Bleloch, A.L., *Secondary electron spectroscopy in a dedicated scanning transmission electron microscope*, Ultramicroscopy 29, 1989, pp. 147-152

Brodie, I. and J.J. Muray, *The physics of micro/nano-fabrication*, Plenum Press, New York, 1992

Cailler, M. and J.P. Ganachaud, *Secondary electron emission from solids I.*, Scanning Microscopy Supplement 4, 1990, pp. 57-79

Della Ratta, A.D., J. Melngailis and C.V. Thompson, *Focused ion beam induced deposition of copper*, Journal of Vacuum Science and Technology B11(6), 1993, pp. 2195-2199

Eckstein, W., *Energy distribution of sputtered particles*, Nuclear Instruments and Methods B 18, 1987, pp. 344-348

Gamo, K., N. Takakura, N. Samoto, R. Shimizu and S. Namba, *Ion Beam Assisted Deposition of Metal Organic Films Using Focused Ion Beams*, Japanese Journal of Applied Physics 23(5), 1984, pp. L293-L295

Gerlach-Meyer, U., *Ion enhanced gas-surface reactions: a kinetic model for the etching mechanism*, Surface Science 103, 1981, pp. 524-534

Gnaser, H., C. Kallmayer and H. Oechsner, *Focused ion beam implantation of Ga in elemental and compound semiconductors*, Journal of Vacuum Science and Technology B 13 (1), 1995, pp. 19-26

Granneman, E.H.A., *Deposition methods in IC technology*, ASM International, Delft, 1991

Hammer, P. and W. Gissler, *Chemical sputtering of carbon films by low energy* N_2^+ *ion bombardment*, Diamond and Related Materials 5, 1996, pp. 1152-1158

Harriott, L.R., *Digital scan model for focused ion beam induced gas etching*, Journal of Vacuum Science and Technology B11(6), 1993, pp. 2012-2015

Herrmann, K.H., *Detection systems*, in: J.N. Chapman, *Quantitative electron microscopy*, The Scottish Universities Summer School in Physics, 1984, pp. 119-139

Hofer, W.O., *Ion-induced electron emission from solids*, Snanning Microscopy Supplement 4, 1990, pp. 265-310

Hoyle, P.C., M. Ogasawara, R.J.A. Cleaver and H. Ahmed, *Electrical resistance of electron beam induced deposits from tungsten hexacarbonyl*, Applied Physics Letters 62(23), 1993, pp. 3043-3045

Ishitani, T. and H. Kaga, *Calculation of local temperature rise in focused-ion-beam sample preparation*, Journal of Electron Microscopy 44, 1995, pp. 331-336

Joy D.C., *A model for calculating secondary and backscatter electron yields*, Journal of Microscopy 147, 1987, pp.51-64

Kalbitzer, S., *Ion beams in semiconductor physics and technology*, Nuclear Instruments and Methods B 63, 1992, pp. 1-13

Kanaya, K. and H. Kawakatsu, *Secondary electron emission due to primary and backscattered electrons*, Journal of Applied Physics D5, 1972, pp. 1727-1742

Koets, E., P. Kruit and T. Chisholm, *Optimum switching time for a beam-size switch (250 nm ↔ 1000 nm) in a vector scan electron beam lithography machine*, Microcircuit Engineering 23, 1994 pp. 77-80

Kohlmann-von Platen, K.T., J. Chebek, M. Weiss, K. Reimer, H. Oertel and W.H. Brünger, *Resolution limits in electron-beam induced tungsten deposition*, Journal of Vacuum Science and Technology B11(6), 1993, pp. 2219-2223

Komuro, M., N. Watanabe and H. Hiroshima, *Focused Ga Ion Beam Etching of Si in Clorine Gas*, Japanese Journal of Applied Physics 29(10), 1990, pp. 2288-2291

Koops, H.W.P., R. Weiel, D.P. Kern and T.H. Baum , *High-resolution electron-beam induced deposition*, J. Vac. Sci. Technol B 6(1), 1988, pp. 477-481

Lipp, S., L. Frey, G. Franz, E. Demm, S. Petersen and H. Ryssel, *Local material removal by focused ion beam milling and etching*, Nuclear Instruments and Methods B106, 1995, pp. 630-635

Matsui, S. and Y. Ochiai, *Focused ion beam applications to solid state devices*, Nanotechnology 7, 1996, pp. 247-258

Mulder, E.H., *On the throughput optimization of electron beam lithography systems*, thesis, Delft, 1991

Muller, K.P., U. Weigmann and H. Burghause, *Simulation of focused ion beam milling*, Microelectronic Engineering 5, 1986, pp. 481-489

Mulvey, T. and C.J.R. Sheppard, *Advances in optical and electron microscopy*, Academic Press, London, 1991

Murata, K., *Monte Carlo simulation of electron scattering in resist film/substrate* *targets*, Electron Beam Interactions with Solids, AMF O'Hare, Chicago, 1990, pp. 311-329

Nagamachi, S., Y. Yamakage, H. Maruno, M. Ueda, S. Sugimoto and M. Asari, *Focused ion beam direct deposition of gold*, Applied Physics Letters 62 (17), 1993, pp.2143-2145

Nagamachi, S., Y. Yamakage, M. Ueda, H. Maruno, K. Shinada, Y. Fuijyama and M. Asari, *Focused ion beam direct deposition of superconductive thin film*, Applied Physics Letters 65 (25), 1994, pp. 3278-3280

Orloff, J., L.W. Swanson and M. Utlaut, *Fundamental limits on imaging resolution in focused ion beam systems*, Journal of Vacuum Science and Technology B14(6), 1996, pp.3759-3763

Pellerin, J.G., D.P. Griffis and P.E. Russell, *Focused ion beam machining of Si, GaAs and InP*, Journal of Vacuum Science and Technology B 8 (6), 1990, pp. 1945-1950

Petroff, P. M., Z. Xu, Y.J. Li, M. Miller and M. Wassermeier, *Focused ion beam processing of mesoscopic quantum structures*, Instrumentation Physics Conference Series 127, 1992, pp. 85-93

Posselt, M. and J.P. Biersack, *Influence of recoil transport on energy-loss and damage profiles*, Nuclear Instruments and Methods B 15, 1986, pp. 20-24

Puretz, J. and L.W. Swanson, *Focused ion beam deposition of Pt containing films*, Journal of Vacuum Science and Technology B10(6), 1992, pp. 2695-2698

Reimer, L., *Image formation in low-voltage scanning electron microscopy*, SPIE, Washington, 1993

Reinelt, M. and S. Kalbitzer, Journal of Physics Coll. 4 supplement 10 (42), 1981, pp. 843

Robinson, M.T., *Computer simulation of the self-sputtering of uranium*, Journal of Applied Physics 54, 1983, pp. 2650-2659

Samoto, N. and R. Shimizu, *Theoretical study of the ultimate resolution in electron beam lithography by Monte Carlo simulation, including secondary electron generation: Energy dissipation profile in polymethylmethacrylate*, Journal of Applied Physics 54(7), 1983, pp.3855-3859

Schmoranzer, H. and M. Reisser, *Spatial energy deposition distribution by a keV-electron beam in resist layers for electron-beam lithography*, Nuclear Instruments and Methods B105, 1995, pp. 35-41

Shukuri, S., e.a., *Submicron channel mosfet using focused boron ion beam implantation* *into silicon,* Japanese Journal of Applied Physics 23 (8), 1984, pp. 543-545

Sigmund, P., *Theory of sputtering I. Sputtering yields of amorphous and polycrystalline targets*, Physics Review 184 (2), 1969, pp. 383-416

Sigmund, P., *Sputtering by ion bombardment: theoretical concepts*, In: *Sputtering by particle bombardment I.*, R. Behrisch, Springer Verlag, Berlin, 1981

Steckl, A.J., H.C. Mogul and S. Mogren, *Localized fabrication od Si nanostructures by focused ion beam implantation*, Applied Physics Letters 60 (15), 1992, pp. 1833-1835

Takahashi, Y., Y. Madokoro and T. Ishitani, *Focused ion beam induced deposition in the high current density region*, Japanese Journal of Applied Physics 30 (11B), 1991, pp. 3233-3237

Tandon, U.S. and W.S. Khokle, *Patterning of Material Layers in Submicron Region*, John Wiley & Sons, New York, 1995, pp. 40-63

Waldeer, K.T. and H.M. Urbassek, *On the angular distribution of sputtered particles*, Nuclear Instruments and Methods B18, 1987, pp. 518-524

Webb, R.P., *Manual of SUSPRE, Surrey University Sputter Profile Resolution*, 1987

Woodham, R.G. and H. Ahmed, *Fabrication of atomic-scale metallic microstructures by retarding-field focused ion beams*, Journal of Vacuum Science and Technology B12 (6), 1994, pp. 3280-3284

Wilson, R.G. and G.R. Brewer, *Ion beams with applications to ion implnatation*, John Wiley & Sons, New York , 1973

Xu, X., A.D. Della Ratta, J. Sosonkina and J. Melngailis, *Focused ion beam induced deposition and ion milling as a function of angle of ion incidence*, Journal of Vacuum Science and Technology B10(6), 1992, pp. 2675-2680

Yamaguchi, H., *Line dose dependence of Silicon and Gallium Arsenide removal by a focused gallium ion beam*, Journal de Physique C6 (11), 1987, pp. C6.165-C6.170

Yanagisawa, J., K. Kito and K. Monden, *Low-energy focused ion beam system and direct deposition of Au and Si*, Journal of Vacuum Science and Technology B 13 (6), 1995, pp. 2621-2624

Young, R.J., J.R.A. Cleaver and H. Ahmed, *Characteristics of gas-assisted focused ion beam etching*, Journal of Vacuum Science and Technology B 11 (2), 1993, pp. 234-241

Zalm, P.C., *Secondary ion mass spectroscopy*, in: *Surface science techniques*, J.M. Walls and R. Smith, Pergamon, UK, 1994

Ziegler, J.F., J.P. Biersack and U. Littmark, *The stopping and range of ions in solids*, Pergamon Press, 1985

4. Optical design of a combined ion and electron beam system for nanotechnology: "the Fancier"

Introduction

Ion beams are widespread tools in microtechnology, but their applicability for nanotechnology is not straightforward. However, they can be used in several unique fabrication techniques for nanostructures such as direct implantation, direct deposition, sputtering and beam induced etching and deposition. For the observation of the structures the use of ions is limited due to their erosion effect.

The usual way to observe the structures is to measure the secondary electron yield coming from the specimen after bombarding it with a charged particle beam in scanning mode. For one pixel of an image 10^4 *secondary electrons are required for a reasonable signal-to-noise ratio (Herrmann, 1984).While collecting these secondary electrons in order to observe a specimen at nanometer resolution with ions, several monolayers are sputtered, see former chapter. This means that the ions would destroy the nanostructures completely. However, when using electrons the erosion effect is much smaller.*

The aim of "the Fancier" is to fabricate and analyze structures with typical line sizes in *the order of a nanometer. Therefore an instrument is developed that combines the best of both worlds: an ion and an electron beam can be focused on the specimen with a probe size less than the typical structure size for fabrication and observation respectively. To realize this a charged particle optical instrument has to be built which is able to focus both an ion and an electron beam at the same position on the specimen with a probe size less than the typical structure size. The optical design of this system will be discussed in this chapter.*

4.1. System design

Commercially available electron microscopes are able to focus an electron beam to within a probe of subnanometer size, while commercial ion beam instruments can reach a resolution of about 50 nm by the start of this project. It is advantageous to use an electron microscope as basic instrument, because an ion beam pattern generator as basic instrument would mean improving both the ion and the electron beam optical system.

The project start with a Philips Scanning Transmission Electron Microscope (STEM) EM 420, figure 4.1, to do research both with thin and thick specimens. Thin specimens can be analyzed in transmission mode using the complete microscope. For the collection of surface sensitive information a Secondary Electron Detector (SED) is incorporated in the microscope, which is then used as a Scanning Electron Microscope (SEM). Here only the illumination part of the microscope is functional.

As an ion beam has to be added to this microscope it has to be investigated how this can be realized. Three alternative principles will be discussed. To compare the alternative principles, some criteria will be developed first.

The first criterium deals with the flexibility of research. The combination of the ion and the electron beam can limit the fabrication or observation techniques that "the Fancier" can be used for. This is called the flexibility of research. For example a specific combination of both beams can mean that the impact energy of the ions has to be high which would mean that the direct deposition fabrication technique, as discussed in chapter 3, cannot be realized. It is concluded in chapter 3 that the highest resolution of the fabrication techniques are obtained at low beam energy. Therefore the system has to be able to operate at energies less than 30 keV.

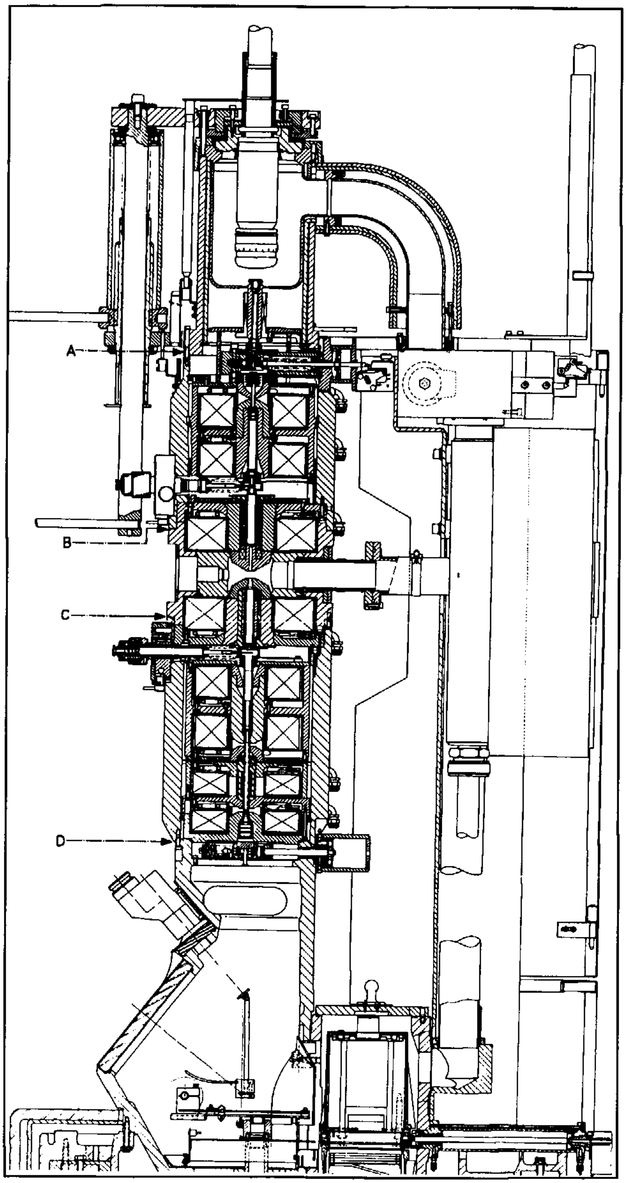

Fig. 4.1. *The Philips EM420 Scanning Transmission Electron Microscope (STEM).*

When a switch is made from electrons to ions or "vice versa", some settings in "the Fancier" has to be modified too. It takes some time to realize and stabilize these modifications. This time is called the switching time, the second criterium. In principle there is no strong demand on this switching time, because the speed of production with the ion beam can be calibrated which makes analysis with the electron beam during the fabrication with the ion beam unneeded. The analysis after the fabrication does not have a strong time limit too. However, it is advantageous to be able to switch fast from one beam to another. Therefore it is required that no mechanical and as less as possible high tension changes have to be carried out during the switching. This is because the speed of the first type of changes is very hard to improve, while the electrical settings can be improved using computer control. Even then it takes some time for the high tension to stabilize.

However, the most important criterium is the ion beam resolution, which has to be about a nanometer. In general the resolution of a probe forming system is a combination of the geometrical and the aberration contribution. The resolution is expressed as the full width of the beam that contains 50 % of the particles.

$$d=\sqrt{\left(\left(d_s^4+d_\lambda^4\right)^{\frac{1.3}{4}}+d_g^{1.3}\right)^{\frac{2}{1.3}}+d_I^2+d_c^2} \qquad (4.1)$$

d= total probe size, full width 50 %
d_s= probe contribution of spherical aberration
d_λ= probe contribution of diffraction
d_g= geometrical probe contribution
d_I= probe contribution of Coulomb interaction
d_c= probe contribution of chromatic aberration

The above equation (Barth, 1996), combines the different probe contributions. The probe current is only defined by the geometrical disc

$$d_g=\frac{2}{\pi.\alpha}.\sqrt{\frac{I}{B.U}} \qquad (4.2)$$

I= current
B= reduced brightness
U= energy of the ions
α= opening angle

It seems reasonable to assume that the aberration disc of an ion optical system is dominated by the Coulomb interactions, the chromatic aberration and/or the spherical aberration. Coulomb interactions origin from the forces between individual charged particles. Ions travel relatively slow compared to electrons which, in general, make Coulomb interactions a serious resolution limiting factor (Jansen, 1988) (de Jager, 1994). The effect of Coulomb interactions is divided in two regimes separated by a small aperture. This aperture will be called the mass selecting aperture in figure 4.13. The main effect of Coulomb interactions will be between the source and this aperture, it is to be expected that the system will be in the Holtzmark regime here. This means that the probe enlargement is proportional to the angular current density of the beam. The effect of Coulomb interactions in this regime is treated as an enlargement of the source size.

Behind the aperture the current will be limited enough to describe the Coulomb interactions by the equations of the Pencil beam regime. The contribution of Coulomb interactions to the aberration disc can here be approximated from (Kruit, 1997):

$$d_I = 0.143\ \frac{M_1^{3/2}}{e^{7/2}.\epsilon_0}.\left[S_c^3+(1-S_c)^3\right].\frac{I^3.\alpha.L^3}{U^{5/2}} \qquad (4.3)$$

M_1= mass of the particles in the beam
S_c= geometrical factor, about 0.5

An ion source based on field emission, like a Liquid Metal Ion Source (LMIS) (Orloff, 1991), seems to be advantageous: a wide variety of elements can be emitted with relative high brightness compared to other source types. For systems which are equipped with a liquid metal ion source the importance of chromatic aberration on the final spot size has been shown (Liebl, 1983). The chromatic aberration contribution to the probe size is given by

$$d_c = 0.34\ C_c.\alpha.\frac{\Delta U}{U} \qquad (4.4)$$

C_c= coefficient of chromatic aberration
ΔU= Full Width at Half Maximum (FWHM) energy spread of the ions

Besides the Coulomb interactions and the chromatic aberration, the spherical aberration can contribute to the ion probe.

$$d_s = 0.18\ C_s.\alpha^3 \qquad (4.5)$$

C_s= coefficient of spherical aberration

In general the system resolution can also be limited by the diffraction

$$d_\lambda = 0.54\,\frac{\lambda}{\alpha} = 0.54\,\frac{h}{\alpha.\sqrt{2.M.U}} \tag{4.6}$$

λ= wavelength of the particles
h= Plancks constant
M= mass of the particles

As the mass of the ions is relatively high the diffraction can be neglected, but it is of importance in a high resolution electron beam system.

The focused ion beam part of "the Fancier" will comprise many lenses. In order to determine which lenses are causing probe size contributions by aberrations, one has to determine magnification and acceptance angle of each lens, combine those with the aberration coefficients and refer them to the specimen plane in order to compare the contributions of the lenses to the probe size at the specimen.

In general however, aberrations of the objective lens, the final lens above the specimen of such a system are dominant. This is caused by the fact that the objective lens demagnifies, thus it thereby demagnifies all previous aberration contributions. Therefore the parameters in equation (4.4) and (4.5) can be taken as those of the objective lens (Slingerland, 1988).

The coefficients of chromatic and spherical aberration for a good objective lens are typically about 3 and 30 times the focal length respectively. A typical value of the focal length is 20 mm. At a typical beam energy of 30 keV, an energy spread of 5 eV, a source brightness of 10^6 A.m^{-2}.sr^{-1}.V^{-1} and an opening angle of 5 mrad the contributions from Coulomb interactions, chromatic and spherical aberration are respectively 1.2 nm, 17 nm and 9 nm.

It is clear from these numbers that a proper design of the objective lens is not enough to end up with a nanometer ion probe. One or more parameters in the above equations have to be decreased as a result of the system setup. This can not only be the opening angle as it has a quadratic influence on the probe current

$$I = \frac{\pi^2}{4}.\alpha^2.d_g^2.B.U \tag{4.7}$$

So for a two times smaller opening angle the spherical aberration decreases eight times, the chromatic aberration two times but the probe current four times. This means that limiting the chromatic aberration by the opening angle would decrease the current density in the probe. Therefore the other parameters in equation (4.4) are discussed in the three alternative system designs that will be described here.

4.1.1. Without integration

The optical setup of the principle of combining both beams without integrating them on the same optical axis is depicted in figure 4.2. Only at the specimen both beams are on the same point.

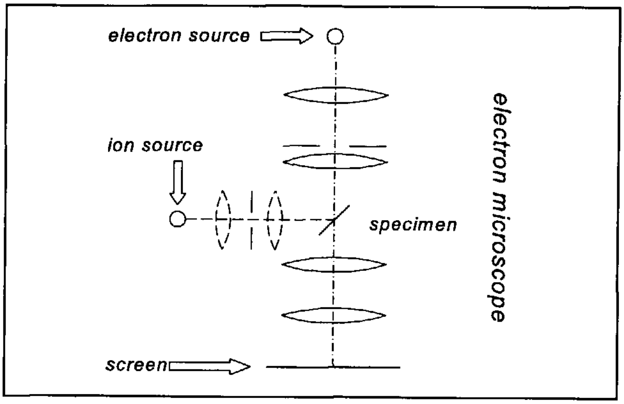

Fig. 4.2. *Combining the ion and the electron beam without integration.*

This means that the sources and the optical elements for the ion and the electron beam are totally separated, giving maximum flexibility of research and the possibility to optimize both systems independently. On the other hand the limited space around the objective lens in the electron microscope makes it hard to add an extra lens there. This means that a choice has to be made between two solutions.

First the lens can be positioned relatively far away, resulting in a large focal length of several tens of mm (Swens, 1988). If more elements are necessary close to the specimen, it can be 100 mm. Therefore a chromatic aberration disc of 57 nm will result with the other parameters as described above. Several commercial available combinations of a scanning electron microscope with a Focused Ion Beam (FIB) system are based on this combination principle, like those from Philips/FEI and Jeol. The resolution can be improved by an energy filter in the ion beam column that stops ions which have an energy to far from the mean energy of the beam. With for example a Wien filter (Andersen, 1970), which is a combination of electrostatic and magnetic deflectors, the energy spread and therefore the resolution can be improved.

In the second solution the specimen is moved from the ion column to the electron column or "vice versa". The two columns are really separated to enable short focal lengths for both systems. This means for sure a mechanical movement of the specimen followed by a time consuming repositioning.

4.1.2. Partial integration

In figure 4.3 a schematic drawing is given of the principle of partial integration. The ions follow the same optical axis as the electrons from a certain position between the electron source and the specimen. This means that the sources are separated but also that a part of the optical system coincides. For example it will be necessary to develop an objective lens that is able to focus both the ion and the electron beam. This will be a combined electrostatic and magnetic lens because the focusing properties of the magnetic lens of the electron microscope are too weak for the ions. Besides a combined lens offers the possibility to influence both beams individually.

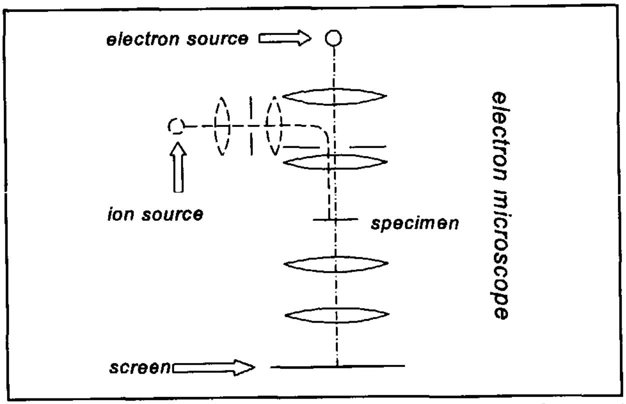

Fig. 4.3. *Combining the ion and the electron beam with partial integration.*

The flexibility of the research is not influenced at the source because the ion source can be chosen conform its application without taking care of the electron source. Probably the combined optical system will give some limitations, e.g. with respect to the ion energy. This will certainly be the case if the switching time has to be eliminated to do "in situ" analysis. However, if mass and energy of the ions and the electrons differ sufficiently it is possible to manipulate both beams independently using a combination of electrostatic and magnetic optical elements.

Obviously an optical element is needed to bring the ion beam on the optical axis of the microscope. The ion beam is deflected in stead of the electron beam, as is done in a similar combination of an ion and an electron beam (Sawaragi, 1990) for two reasons. First, the energy of the ions will be lower than of the electrons which makes it easier to bend the ion beam. Second, besides the primary aim of this combining element it can also be used to improve the resolution of the ion system by reducing C_c or ΔU from equation (4.4). Two alternatives for the combining element are an electrostatic mirror and a 90°-deflector.

1. Electrostatic mirror

   C_c can be minimized by optimizing the objective lens. If this is not enough an element with negative C_c can be introduced. Such an element is a mirror. Figure 4.4 shows a 90° deflection mirror based on old optical ideas (Zworykin, 1945).

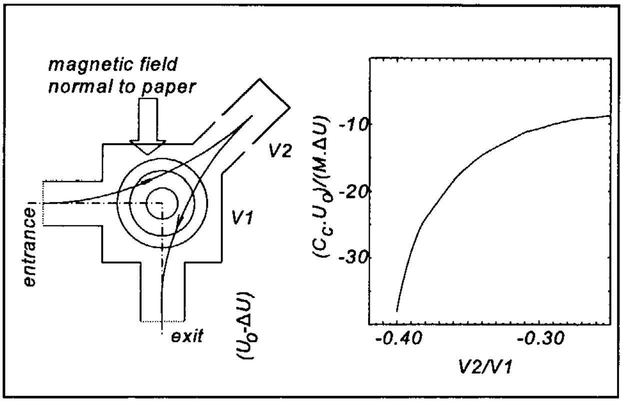

Fig. 4.4. *Principle and axial chromatic aberration of a converging electron mirror.*

From the fact that the converging action of an electrostatic mirror increases quite generally when its positive electrode, V2, is made less positive it follows that the faster ions, penetrating deeper into the mirror field, are refracted more strongly by the field than the slower ions. The sign of the chromatic aberration of the ion mirror is normally opposite to that of the ion lens. Figure 4.4 shows the calculated variation of the coefficient with the ratio of the potentials of the electrodes for an electrostatic mirror consisting of two cylinders of equal diameter, the potential of the positive electrode being throughout sufficiently low so that the mirror acts as a converging system. It is clear that the correction strength can be varied by changing the mirror potential

This method introduces additional Coulomb interactions, because the ions are stopped in the mirror. The influence of interactions on the beam quality gets worse in case the energy of the particles is smaller, see equation (4.3). Another note about this method is that the filtering is based on the idea of making a small coefficient C_c by subtracting the two large C_c's of the mirror and the objective lens. Relative small changes in one of these will influence the result drastically.

2. 90°-deflector

   ΔU is defined initially by the choice of the ion source, as mentioned before. If ΔU is too large to reach the resolution as a result of this choice, energy filtering with a dispersive element can be a solution. Figure 4.5 shows a 90°-deflector in chromatic mode.

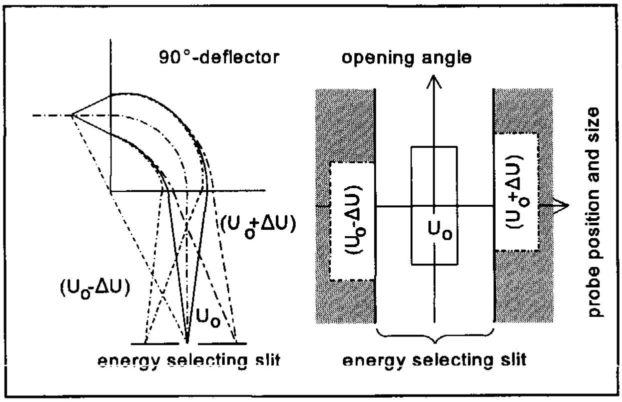

Fig. 4.5. *Principle of energy filtering with a 90°-deflector.*

Particles with more or less energy than the central energy are deflected over an angle which is, respectively, smaller or larger than 90 degrees (Wollnik, 1967). To realize enough dispersion the deflector has to separate the phase diagrams of the energies which have to be filtered, such that they can be selected with a slit. By varying the slit size the filter strength can be varied. The energy spread after filtering is then given by

$$d_{sl} = \frac{\Delta U}{U}.L_l \tag{4.8}$$

d_{sl}= width of the slit
L_l= length over which the dispersion appears

In general an electrostatic mirror has no influence on the probe current as no ions are stopped or filtered out. A 90°-deflector influences the probe brightness, and therefore the probe current (equation (4.7)), according to

$$B_p = B_s.\frac{\Delta U_p}{\Delta U_s} \tag{4.9}$$

B_s= reduced brightness of the ion source
B_p= reduced brightness of the ion beam at the specimen
Δu_s= FWHM energy spread of the ions at the source
Δu_p= FWHM energy spread of the ions at the specimen

Both methods are as effective in reducing the aberration contribution to the probe. However the effect of Coulomb interactions is larger in the electrostatic mirror as the ions are stopped. Therefore a 90°-deflector is more attractive.

4.1.3. Total integration

The principle of total integration is based on the idea that both the ion and the electron beam are totally on the same optical axis, as shown in figure 4.6. As a result of this a source has to developed that is able to emit as well ions as electrons.

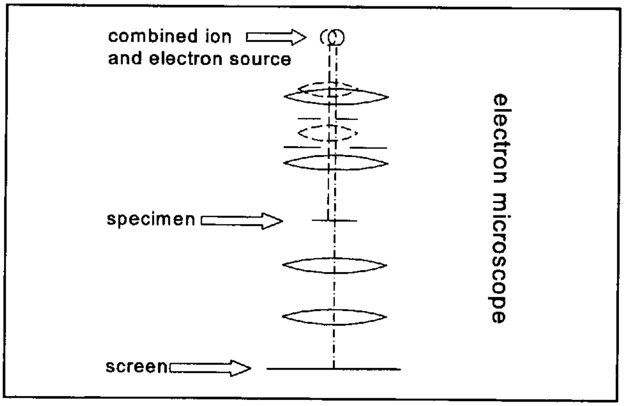

Fig. 4.6. *Combining the ion and the electron beam with total integration.*

It seems to be realistic to assume that the emission principle of this source is field emission, here switching is possible by changing the polarity of the extraction field (Rao, 1989). For the ions this means a liquid metal ion source or a gas field ion source. Both types can in principle be used for electron emission, but a liquid metal ion source will probably have a lower brightness for electron emission than a stand alone electron field emitter. The reason for this is that the brightness is strongly influenced by the radius of the needle which has to be about a micrometer to obtain stable ion emission from the liquid metal ion source. Typical radii for electron field emitters are in the order of nanometers. On the other hand a gas field ion source, with sharper tip, strongly limits the flexibility of the research with "the Fancier": emission of species which are of interest for implantation is not possible because of unacceptable high temperatures to bring these materials in the gas phase.

The switching between electrons and ions has to be made in the source already. This means the switching of high tension, taking some time to stabilize. Another problem is the resolution of the ion beam in this principle. The ion optical axis is a straight line, this means that an element like a 90°-deflector cannot be used to improve the resolution. Therefore there is only one parameter of freedom left: the beam energy of the ions. To reach the nanometer resolution with the ion beam the beam energy has to be at least more than 100 keV which makes a combined electrostatic and magnetic optical system very complicated.

Based on the above arguments the decision is made to realize the combination of the ion and the electron optical system by means of partial integration. Compared to totally separated columns the resolution can be better at a shorter switching time. In principle it is possible to have both beams on the specimen at the same time. This is impossible in the case without integration, with separated columns, and in the case of total integration where both beams come from the same source.

In case of partial integration the 90°-deflector is chosen. It offers a good filtering system by means of energy band passing. In principle a mirror can give more probe current at a given resolution in case of a chromatic and Coulomb interaction dominated probe, but the stopping of the ions in the mirror makes it probable that the interaction between the ions gets important. This is unattractive.

A possible switching strategy between ion and electron beam can consist of on/off switching of the excitation of the 90°-deflector and the extra optical elements that are added to the microscope for the ion beam. When these excitations are switched off the column behaves like a standard EM420 microscope. The ions hit the wall of the deflector. Mutatis mutandis that will happen with the electrons if these elements are excited. The ions are focused on the specimen with the extra optical elements. The settings of the magnetic lenses in the microscope are conserved, it only means adding some weak lenses to the ion optical system and it avoids adjustment effects of the magnetic lenses. The switching time is defined by the time to settle the excitations of the 90°-deflector and the extra optical elements in the microscope.

In principle it is possible to counterbalance the effect of the 90°-deflector on the electrons by a magnetic pre-deflector. If the settings of the microscope elements are adapted to the excitations of the extra lenses "in situ" observation of the fabrication with the ion beam is possible with the electron beam.

Therefore a partial integrated ion beam system with a 90°-deflector as connecting and energy dispersive element is concluded to be the optimum alternative for the combination of the ion and the electron system in "the Fancier".

4.2. Optical and physical design of electron system

The optical system of a Transmission Electron Microscope (TEM), like the Philips EM420, consists of two parts (see figure 4.7): the illumination system and the imaging system. The aim of the illumination system is to illuminate that part of the specimen that has to be imaged. For example the electrons are focused in a small spot in case of Scanning Electron Microscope (SEM) imaging of thick specimens, while a larger part of a thin specimen is illuminated in low magnification TEM imaging.

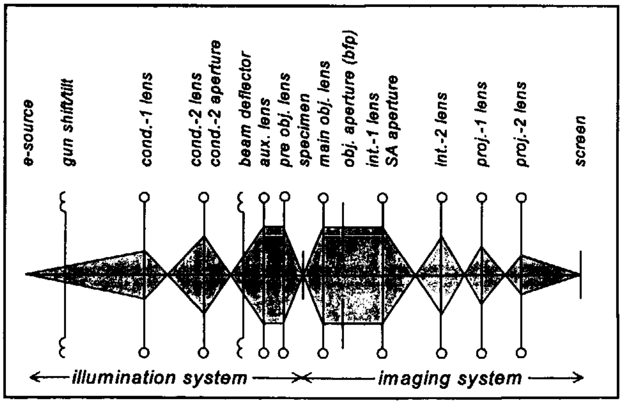

Fig. 4.7. *The optical setup of a Transmission Electron Microscope with illuminating and imaging system.*

The illumination system consists of an electron source, two magnetic condenser lenses, the objective lens and an angle limiting aperture in the second condenser lens. To reach the high level demands of imaging and analysis a twin lens has been developed, a condenser-objective lens is supplemented with an auxiliary lens. The specimen is positioned in the center of the objective lens at the symmetry plane between the upper and the lower pole piece. This makes it possible to position detectors like a backscatter detector near the specimen at minimal gap width.

Three modes of operation of the illumination system can be distinguished: TEM-Microprobe, TEM-Nanoprobe and Scanning Transmission Electron Microscope (STEM) mode. The TEM-Microprobe mode can be used for both high resolution imaging and diffraction use of the imaging system. In this mode of operation the auxiliary and condenser-objective lens form a telefocal system. This results in an illumination equal to the traditional coherent TEM illumination. Figure 4.8 shows the TEM-Microprobe modes for coherent and focused illumination.

In the TEM-Nanoprobe mode the auxiliary lens is switched off. This does not mean that

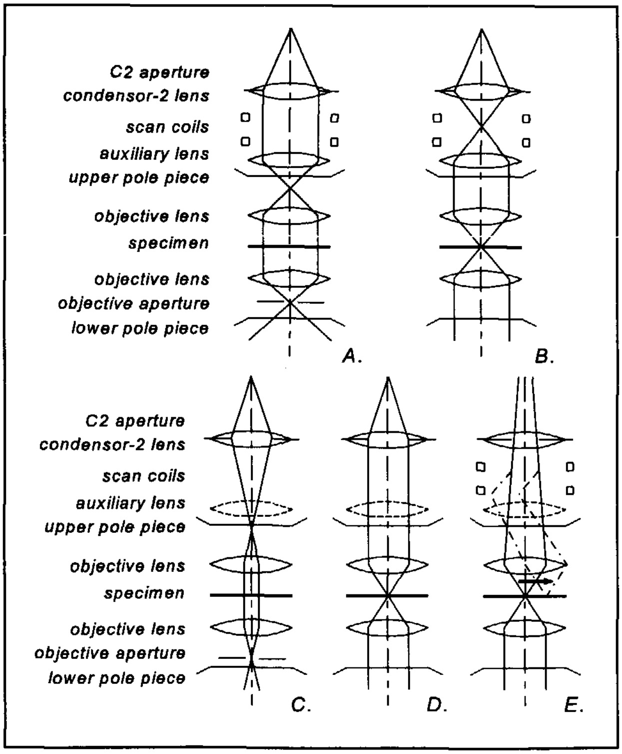

Fig. 4.8. *Modes of operation. A. TEM-Microprobe coherent illumination, B. TEM-Microprobe focused illumination, C. TEM-Nanoprobe coherent illumination, D. TEM-Nanoprobe focused illumination, E. STEM.*

the current supply is switched off but its lens effect is minimized by reversing the current (Thompson, 1983). This mode of operation enables high electron currents at reasonable smaller probes than in case of traditional illumination. With the decreasing probe size the illumination angle increases which improves the conditions for a convergent beam. This mode of operation is advantageous for analysis.

In the standard STEM mode there is no flexibility of the second condenser lens. Also in this mode of operation the auxiliary lens is optically switched off. In practice the dynamic TEM modes are used more often than the static STEM mode for direct observation of the part of the specimen under the beam.

From the above it is clear that the TEM-Nanoprobe and the STEM mode can best be used to observe thick specimens equal to a SEM. These modes offer also the possibility to fabricate structures with the electron beam. However some changes to this standard illumination system are necessary to combine the ion and the electron beam. It seems to be possible to remove the auxiliary lens to create space for the objective lens for ions. This auxiliary lens is not necessary in both modes of interest.

Table 4.1. *Optical parameters of four electron sources (Reimer, 1984), (Mul, 1992)*

	tungsten emitter	LaB6 emitter	Schottky emitter	cold field emitter
source size [nm]	20.10^3-50.10^3	10.10^3-20.10^3	20-50	5-10
brightness [$A/m^2.sr.V$]	1.10^4-5.10^4	20.10^5	1.10^7-1.10^8	2.10^7-2.10^8
energy spread [eV]	1-2	0.5-2	0.7	0.2-0.4

Another change deals with the source. At least the distance between the source and the first condenser lens has to be increased to position the 90°-deflector for the ions. Besides it is advantageous to incorporate also a field emission electron source: it is brighter and the source size is smaller than for the standard tungsten emitter. Table 4.1 shows these data for different electron sources.

The focal length and aberration coefficients of a magnetic condenser lens are given by

$$f = \frac{\sqrt{S^2+D^2}}{\theta.\sin(\theta)}$$
$$\theta = 0.78\ B.S.\sqrt{\frac{q}{8.M.U}}\ ,\quad B = \frac{\mu_0.N.I}{S} \tag{4.10}$$

$$C_s = k_s.\left(2.4\ \frac{f^3}{S^2+D^2}\right),\quad C_c = k_c.f \tag{4.11}$$

S= distance between the upper and lower pole piece
D= diameter of the bore in the pole pieces
μ_0= magnetic permeability
N= number of turns of the magnetic coil
I= current through the magnetic coil

Together with their “new” position and the data of the lenses, as listed in figure 4.14, the electron probe size at the specimen can be calculated. Figure 4.9 shows the probe size and probe current in the focused TEM-Nanoprobe and the STEM mode for a tungsten emitter. The setting of the C2 aperture is chosen such that the current density in the probe is optimized.

It is clear from this figure that a resolution better than 1 nm can be obtained. With a tungsten emitter the best resolution is 0.65 nm, while in TEM-Nanoprobe mode 1.2 nm can be reached at a probe current of 4.6 10^{-14} A and 2.5 10^{-13} A respectively. Therefore it can be concluded that in principle no further changes have to be made to the optical system for the electrons to be able to reach a resolution better than 1 nm. However it would be advantageous to have a Schottky emitter. In this case the flexible TEM-Nanoprobe mode can be used at a resolution better than 1 nm, while also more current in the probe can be obtained resulting in a higher signal-to-noise ratio in the image or a faster imaging of the specimen. This is because it takes less time to collect the needed 10^4 secondary electrons for a pixel in the image (Herrmann, 1984) with a larger probe current.

The imaging system does not have to be changed. The lenses in this system can be explained as follows. In a microscope the specimen and the screen are fixed. Therefore an imaging system of only one lens has a fixed magnification. With a second lens, the projector lens, varying magnification is possible while the objective lens is used to focus.

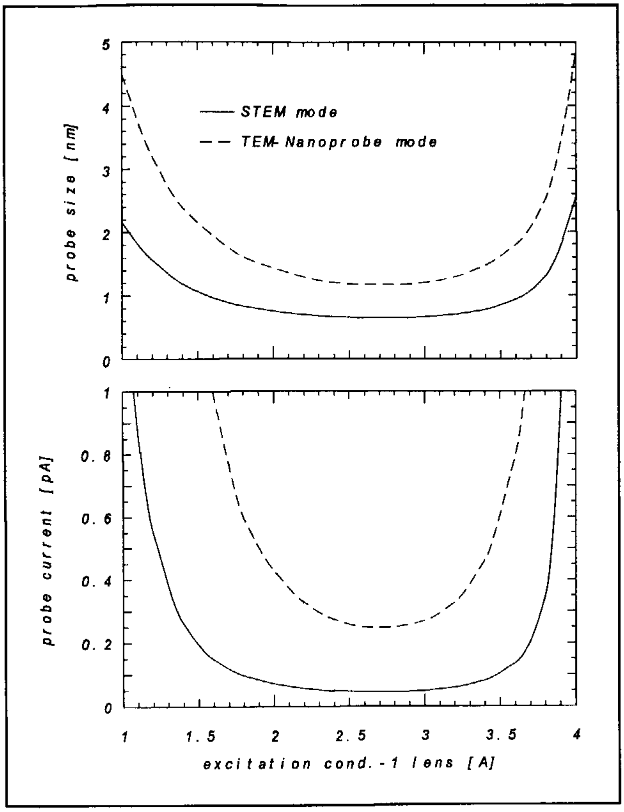

Fig. 4.9. *The probe size and probe current as a function of the excitation of the first condenser lens for two modes of operation with a hot tungsten emitter.*

A varying objective lens excitation is not advantageous. A fixed excitation always results in an image at the same position. With an aperture at that position, the Selected Area (SA) aperture, only the electrons can pass that come from the area on the specimen that can be seen through the aperture regardless the other lens settings. An extra lens is now necessary to focus the image at a fixed objective excitation: the intermediate lens.

Finally the range of magnifications is enlarged by adding a second projector lens. It is now also possible to reach a specific magnification in different ways, this enables to choose the setting with least aberration contribution to the final electron probe size.

4.3. Optical design of ion system

A partially integrated ion beam system with a 90°-deflector as connecting and energy dispersive element is concluded to be the optimum system for the combination of the ion and the electron system in "the Fancier". In this paragraph seven alternatives for the optical setup of the ion column based on this system will be discussed and compared. To compare these some demands on the system are defined first.

The ion source has to be based on field emission. This is advantageous because a wide variety of elements can be emitted with relatively high brightness compared to other source types. A liquid metal ion source (Orloff, 1991) emits ions from a Taylor cone in liquid material on a metal tip. This source type can emit dopant material for direct implantation in Si, e.g. from a PdBAs alloy (Clark, 1987) on the tip. Also emission of Au for direct deposition is possible (Swanson, 1994). Another field emission ion source is a gas field ion source (Sakatia, 1992). The optical parameters of this source are even better, but it can only emit ions from the gas phase by bringing this gas close to a metal tip. For beam induced etching and deposition noble gas ions, like Ar, are preferable: they have less deterioration effect on the specimen than e.g. Ga ions. The application of these sources differ in such a way that it has to be possible to use both sources in the system. But the calculations will be based on the use of a liquid metal ion source, this origins from the worst case approach. It has a source size of 40-50 nm, a source reduced brightness of 1.10^6 A/(m^2.sr.V) and a source energy spread of about 4.5 eV. A source lens typically magnifies the source size 5 times to limit the influence of motions of the source module with respect to the system.

The energy of the ions after emission from the source during their transport through the system is chosen to be 30 keV. It was demonstrated in the former chapter (de Jager, 1996) that nanofabrication with energies above 30 keV is unrealistic as the scattering in the specimen gets important in defining the structure size. Lower energies seems even more preferable from this point of view, but Coulomb interactions and external stray fields gets important at lower energies. To obtain lower energies the specimen can be used as a decelerating electrode (Kasahara, 1988). This means that the ions travel at 30 keV energy through the system, but they are decelerated in the last few millimeters before they impact on the specimen to an energy which is reasonably smaller than the transport energy.

All lenses in an optical system contribute to the final probe size through their chromatic and spherical aberration. However, usually all other contributions can be ignored compared to the influence of the objective lens. This was already mentioned in this paragraph. It is assumed that only the aberrations of the objective lens contribute to the probe size as the contributions of the other lenses are demagnified. The parameters of the electrostatic objective lens, which will be discussed in chapter 7, are: minimal focal length 14.9 mm, chromatic aberration coefficient 49.5 mm and spherical aberration coefficient 1247 mm (de Jager, 1996). The relatively large focal length arises from the requirement to combine this electrostatic lens with the magnetic objective lens of the microscope.

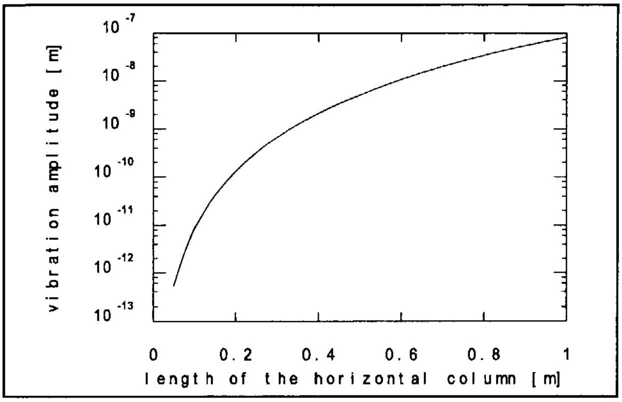

Fig. 4.10. *Influence of vibrations as a function of the length of the horizontal column.*

One of the external influences as mentioned before are vibrations. Due to the finite stiffness of the construction the optical elements vibrate with respect to each other. The size of an intermediate image is the integral over time of the vibrating image. Therefore the amplitude of the vibration has to be smaller than the size of this geometrical image. Figure 4.10 depicts the vibration amplitude of the horizontal column as a function of its length. It is assumed that the horizontal column is constructed from stainless steel tube of 60 mm inner diameter and 2 mm wall thickness. The vibrating source acceleration is 10^{-3} m/s^{-2}, a typical value for a laboratory. It is clear from this figure that the horizontal column can be about 350 mm at maximum to have less than 1 nm vibration. This equals about 5 % of the expected probe size at this position.

Another demand originates from the microscope. The distance from where the ion beam enters the column towards the specimen along the axis of the microscope is 451.5 mm. On this axis the position to insert an aperture for both the ions and the electrons is at 118 mm above the specimen.

Table 4.2. *Parameters and their numerical values as will be used in the comparison of the different alternative optical setups.*

parameter	numerical value	argumentation
source size	45 nm	the virtual source size of a Liquid Metal Ion Source (LMIS) (Komuro, 1983)
	1 nm	the virtual source size of a Gas Field Ion Source (GFIS) (Dudnikov, 1996)
brightness	1.10^6 A/(m^2.sr.V)	the brightness of a Liquid Metal Ion Source (LMIS) (Konuro, 1983)
	2.10^9 A/(m^2.sr.V)	the brightness of a Gas Field Ion Source (GFIS) (Dudnikov, 1996)
emission energy	5 keV	a reasonable extraction potential
energy	30 keV	a reasonable compromise between scattering in the specimen and Coulomb interactions
FWHM energy spread	4.5 eV	the energy spread of a LMIS at an emission current less than 2 μA (Mühle, 1992)
	1 eV	the energy spread of a GFIS (Dudnikov, 1996)
object distance of source lens	2.73 mm	practical value of the source lens in chapter 5
magnification of source lens	5	practical value to enlarge the source to be less sensitive for vibrations
minimal focal length	10 mm	practical value of an electrostatic Einzel lens
minimal distance between center of lenses	50 mm	practical value of an electrostatic Einzel lens
radius of 90°-deflector	30 mm	practical value of an electrostatic 90°-deflector
focal length of objective lens	14.9 mm	value of lens discussed in chapter 5
C_c of objective lens	49.5 mm	value of lens discussed in chapter 5

C_s of objective lens	1247 mm	value of lens discussed in chapter 5
maximal length of horizontal column	321.6 mm	practical value to limit the effect of vibrations
length vertical column	451.5 mm	distance from a typical point in the microscope where the 90°-deflector can be positioned to the specimen
distance from aperture to specimen	118 mm	distance in the microscope from the C2 aperture to the specimen

With the parameters, as argued above and summarized in table 4.2, the optical behavior of the alternatives depicted in figure 4.12 and 4.13 is calculated. First the position and strength of the lenses, E1, E2 and E3 in these figures, is determined by the requirement of a demagnified source at the specimen of 0.5 nm with the shortest possible column in the assumption that the focal length of the lenses is at least 10 mm. The results are listed in table 4.3. Secondly the maximum current in a certain ion probe can be calculated using the equations (4.1) and (4.2). The result is 1.10^{-14} A probe current or a current density of 1.38 A/cm^2, the corresponding energy spread is 0.9 eV and the half aperture angle of the beam at the specimen is 1.11 mrad.

These parameters have to be realized with respectively the energy spread limiting slit of size s1 and the angular limiting aperture of size d1 as indicated in figure 4.12 and 4.13.

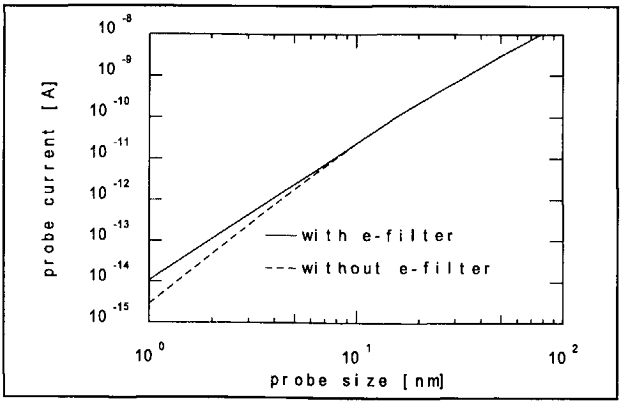

Fig. 4.11. *Probe current versus probe size. The difference between the dotted line and the solid line indicates the effect of energy filtering.*

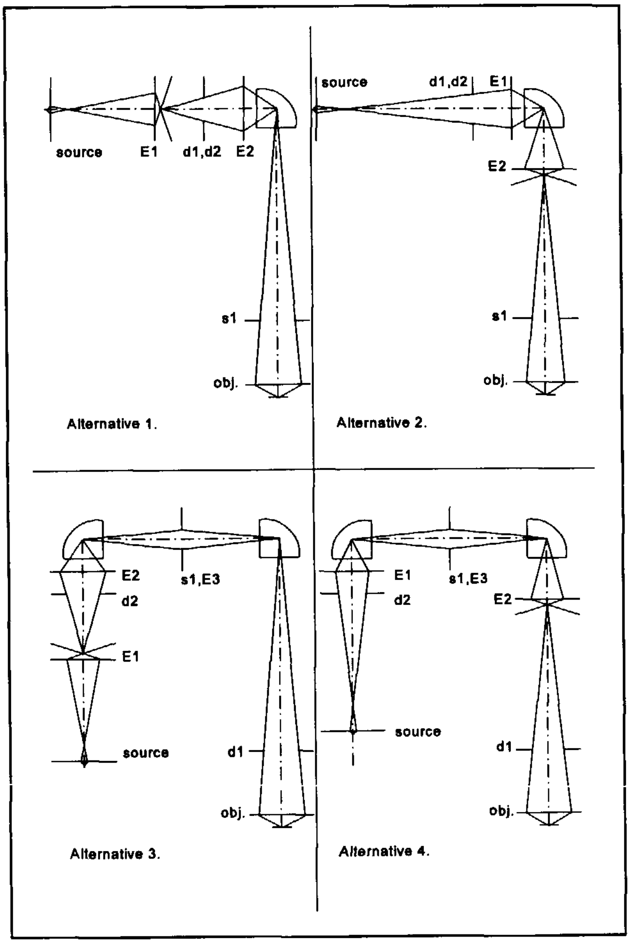

Fig. 4.12. *Alternatives based on angular dispersion with lenses E1, E2 and E3, apertures d1, d2 and slit s1.*

The alternatives can be divided in two groups differing in the use of the 90°-deflector: angular dispersive (figure 4.12) or position dispersive (figure 4.13). In case of angular dispersion the ions with different energies leave the 90°-deflector under different angles with the optical axis. To distinguish between ions with different aperture angles and equal energy and ions with different energies transferred into different angles, the aperture angle has to be limited in front of the energy spread limiting slit. It is clear from table 4.3 that a straightforward angular dispersive system (alternative 1 and 2) results in an unacceptable small size of this d2 aperture. It is hard to make and would erode very fast.

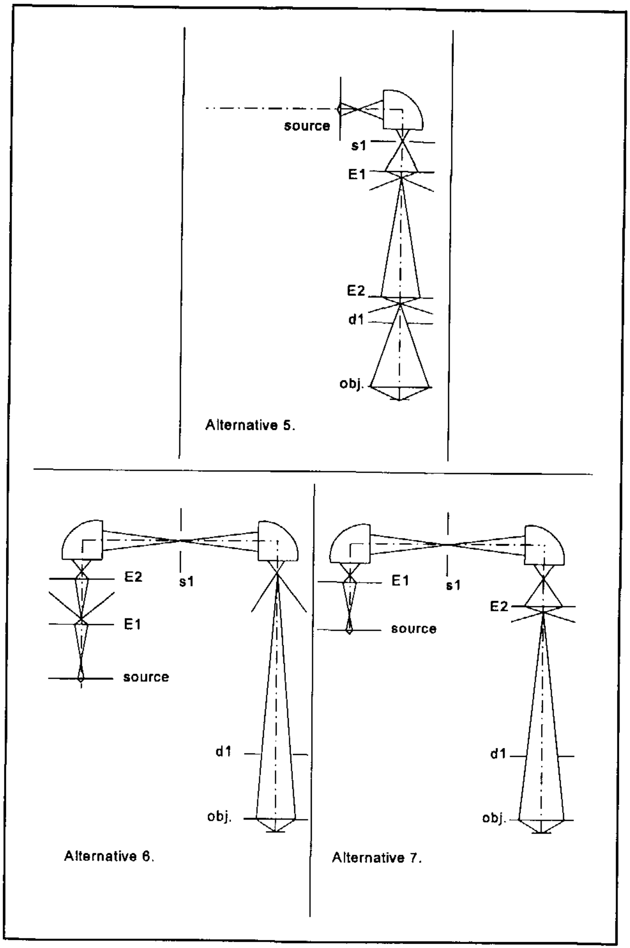

Fig. 4.13. *Alternatives based on position dispersion with lenses E1 and E2, apertures d1 and d2 and slit s1.*

In case of position dispersion the ions with different energy end up at different positions in the imaging plane. This means that in general a non-circular-symmetric image is passed through the energy spread limiting slit. However this is not wanted as this can result in highly different line sizes in perpendicular directions. Therefore also a straightforward position dispersive system (alternative 5) is not desired.

The alternatives 3, 4, 6 and 7 combine two 90°-deflectors. Both deflectors are energy dispersive, but the effect of the first one is balanced by the second one to make the total system achromatic. The energy spread limiting slit is positioned in the center between the two deflectors. For the angular dispersive alternatives 3 and 4 this means that the aperture angle at the specimen does not have to be defined by an aperture in front of the energy filter. There is a separate aperture angle limiting aperture in the microscope. This aperture enables in principle an extra degree of freedom to optimize the current density at the probe but it is still necessary to have a very small angular limiting aperture in front of the first deflector. This is a fundamental disadvantage of angular dispersion in this setup.

For the position dispersive alternatives 6 and 7 the extra 90°-deflector means that a round spot is possible as the second deflector compensates the effect of the first one. The

Table 4.3. *The total column length, l, from source to specimen is the sum of the individual contributions from the lenses: source lens, E1-E3 lens and objective lens. The size of the opening angle limiting apertures d1 and d2 and the size of the energy spread limiting slit s1 for the alternative optical designs depicted in figure 1.*

	altern. 1	altern. 2	altern. 3	altern. 4	altern. 5	altern. 6	altern. 7
v1 [mm]	98.0	78.0	98.0	78.0	50.0	51.0	28.8
b1 [mm]	11.1	50.0	11.1	50.0	12.5	12.4	15.3
v2 [mm]	87.8	218.0	87.8	218.0	89.0	51.0	200.0
b2 [mm]	50.0	10.5	50.0	10.5	11.3	12.4	10.5
v3 [mm]	-	-	160.8	160.8	-	-	-
b3 [mm]	-	-	160.8	160.8	-	-	-
vobj [mm]	436.5	208.0	436.5	208.0	213.8	399.6	189.0
bobj [mm]	15.0	15.0	15.0	15.0	15.0	15.0	15.0
l [mm]	734.6	615.7	1056.2	937.3	547.8	973.0	890.2
d1 [μm]	2.73	0.261	25.4	16.8	17.2	24.8	15.2
d2 [μm]	0.536	0.510	0.536	0.510	-	-	-
s1 [μm]	10.0	65.4	4.82	4.82	1.80	4.82	4.82

images in front of the first deflector and behind the second deflector are equal except for the effect of energy spread of the ions, disregarding aberrations of the deflectors. The difference between alternative 6 and 7 is mainly the position of the second lens. In alternative 6 it is not positioned inside the microscope column. This is advantageous as there is very limited space in this column. However the extra length of the column outside the microscope makes the probe size more sensitive to vibrations. It is assumed that this can be minimized by making the construction sufficiently stiff. Based on the above arguments alternative 6 is preferred. If the assumption is not valid alternative 7 should be used.

Until here only the lenses and the 90°-deflectors are incorporated in the design but other optical elements will be necessary too, like a mass filter, deflectors and stigmators. For direct implantation the ion source has to emit dopant material. This dopant material is often part of an alloy, see for more details the next chapter. Therefore the ion source will emit several species of which only one has to be selected: the dopant specie. This can be realized with a mass filter. The mass filter is positioned right after the source to stop the unwanted material shortly after emission. In this setup the effect of Coulomb interactions is minimized.

Deflectors and stigmators have to be added to the above design to align the ion beam with respect to the optical axis of the lenses. Although in general (de Pierre, 1994) one element can fulfill this demand if it is positioned in front of every two optical elements, some more will be added, especially around the 90°-deflectors. Finally a double stigmator/deflector is introduced above the objective lens to position the probe on the target while the beam goes through the center of the objective lens. This way of illuminating the sample minimizes the aberrations of the objective lens.

Figure 4.14 gives an overview of the elements to manipulate the ion beam.

4.4. Physical design of ion system

In this section the optical design of combining the ion and electron beam system with two position dispersive 90°-deflectors will be converted to a physical design, taking into account the above-mentioned demands. Also the resolution of fabricated structures will be discussed. Figure 4.15 shows the actual realization of the combined ion and electron system.

The ion source can be either a Gas Field Ion Source (GFIS), which is able to emit noble gas ions, or an LMIS, which is able to emit dopant material for implantation, e.g. from a PdBAs alloy. In this case the ion source will emit several species of which only one has to be selected: the dopant species. This can be done with a mass filter for example directly after the source. The different source types are described in chapter 5.

The electrostatic 90°-deflectors have spherical electrodes. This results in a double focusing system meaning that the focal lengths are equal in the dispersive and the non-dispersive direction. Therefore the intermediate images made by these deflectors are real which is convenient for the alignment procedure of the system. The design of the 90°-deflectors is discussed in chapter 6.

Deflectors have to be added to the above design to align the ion beam with respect to the optical axis of the lenses. All deflectors are constructed as eight poles to allow stigmation by these elements too. The eight pole at the exit plane of the second 90°-deflector is used as a quadrupole to correct the angular dispersion there. This is possible without influencing the probe shape because there is an intermediate image in the pivot point of the eight pole. The effect is a larger current density in the probe at the specimen as energy selective stopping of ions by the angular limiting aperture is minimized.

The energy spread limiting slit is positioned such that its size and position in the symmetry plane between the deflectors can be adjusted, as is described in greater detail in chapter 6. This enables easy replacement of the knife edges that form the slit after part of the knife edges has been eroded by the impacting ions.

Table 4.4. *The size and opening angle at the different cross-overs in the ion beam system of "the Fancier"*

cross-over name	size [nm]	angle [mrad]
vitual source size	45	0.0304
between source and E-cond.-1 lens	225	0.00248
between E-cond.-1 and E-cond.-2 lens	45	0.0124
between E-cond.-2 lens and 90°-deflector	13.3	0.0418
at energy selecting slit	58.2	0.00959
between 90°-deflector and objective lens	13.3	0.0418
probe at specimen	0.9	1.11

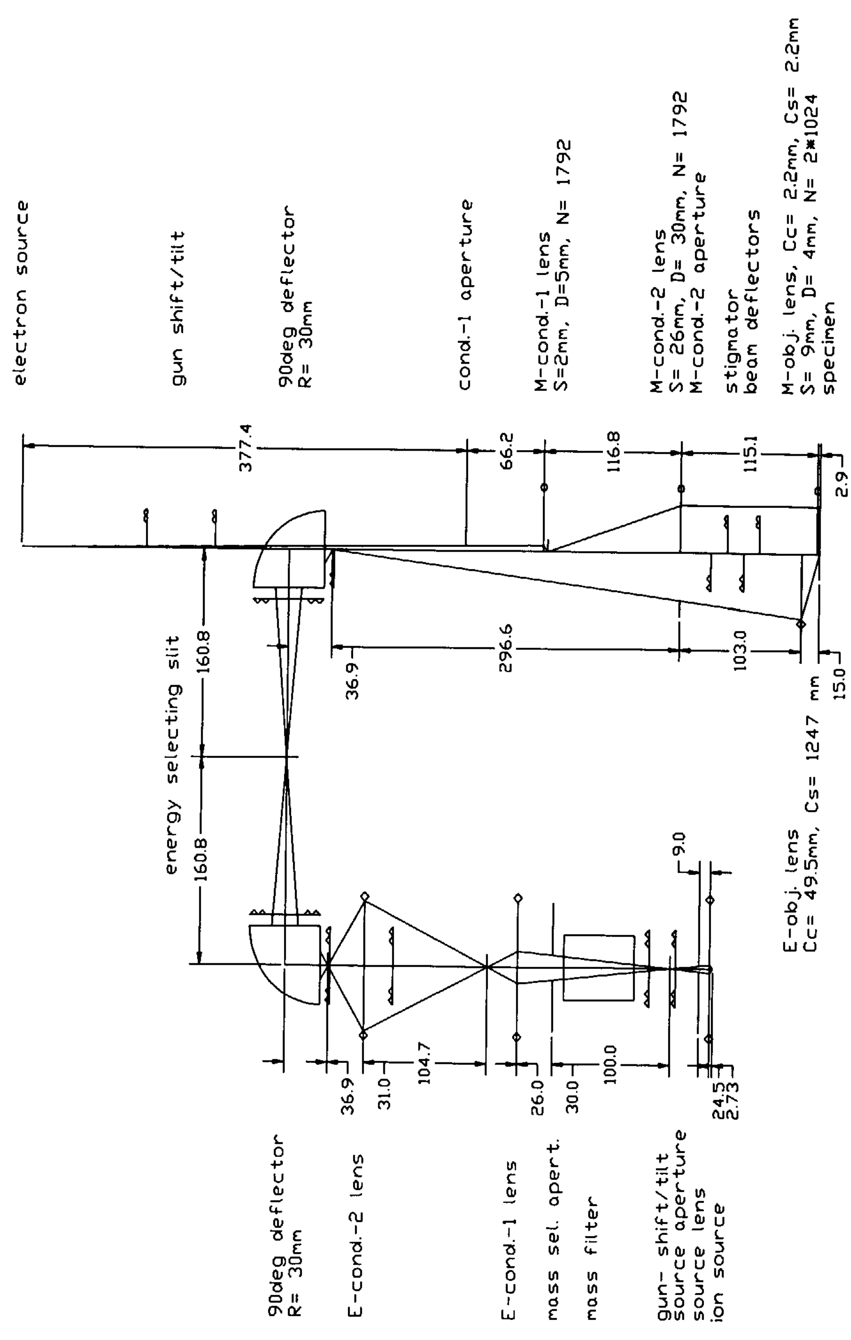

Fig. 4.14. *The optical system for the ion beam.*

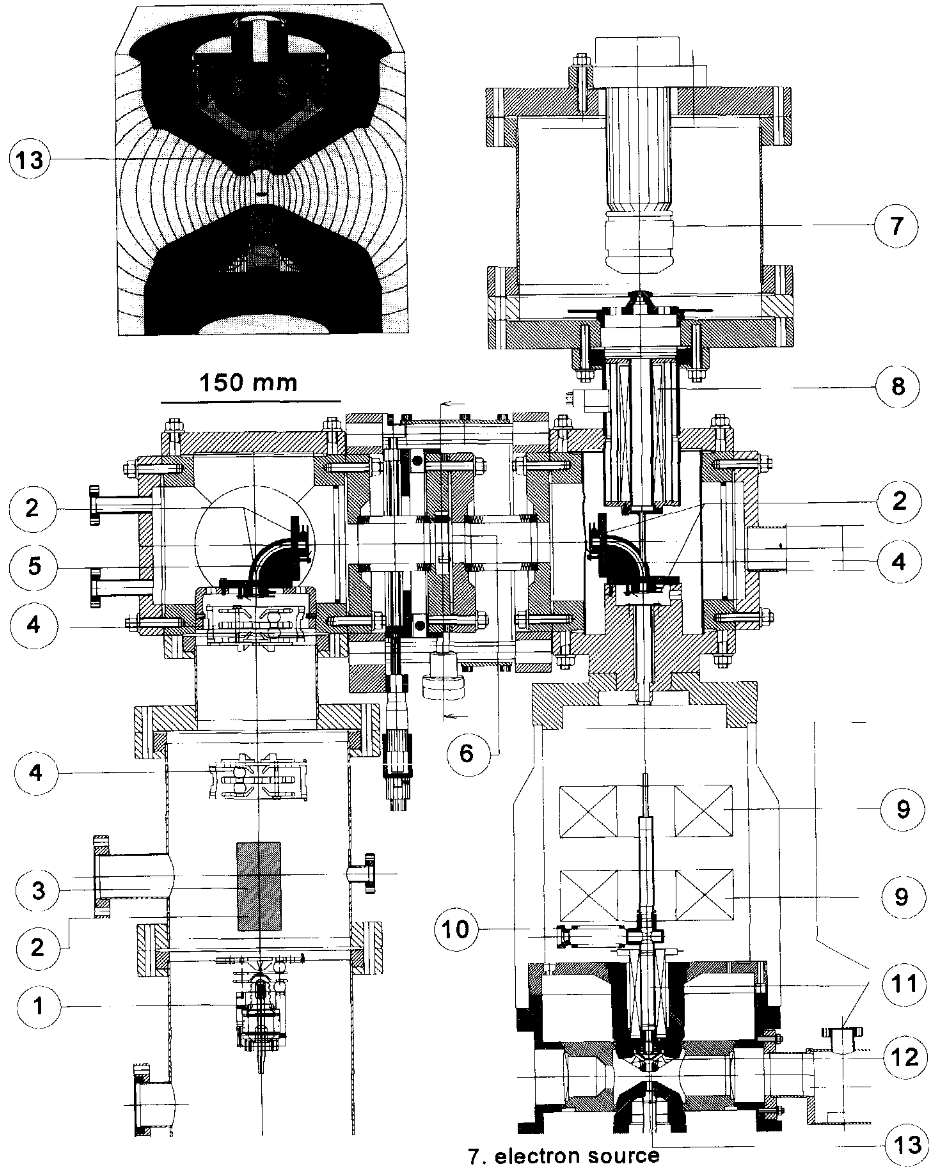

1. ion source
2. deflector / stigmator
3. mass filter
4. ion condenser lens
5. 90°-deflector
6. energy spread limiting slit
7. electron source
8. electron pre-deflector
9. electron condenser lens
10. angular limiting aperture
11. pattern generation deflector
12. combined ion and electron objective lens
13. target

Fig. 4.15. *The physical design of the combined ion and electron optical instrument.*

A double stigmator/deflector is inserted above the objective lens to position the probe on the specimen for pattern generation keeping the beam centered in the objective lens. This way of illuminating the sample minimizes the effect of the objective lens aberrations on the probe size as results from a simulation in chapter 9.

The objective lens is a combined electrostatic and magnetic lens to focus both the ions and the electrons. The integration of both lenses is realized by using the upper pole piece of the magnetic lens as the third electrode of an electrostatic Einzel lens, see chapter 7 for details. The aberration coefficients of the magnetic lenses are not changed significantly by adding the electrostatic lens. Taking into account the aberrations of this lens a probe size of 0.6 nm for electrons can be obtained and 1 nm for ions. The secondary electron detector, which is an integrated part of this lens, is dealt with in chapter 8.

The achievable size of the fabricated structures is the convolution of the probe size and the area over which an infinitesimal small ion probe should have effect on the structure fabrication. The last contribution originates from the scattering of the ions in the specimen, as presented in chapter 3. For sputtering a structure in Si with Ar ions this contribution, d_{scat}, to the structure size as a function of the impact energy, U_p of the ions on the specimen is given by

$$d_{scat}\ [nm] = 2.3\ .\ln\left(\frac{1+0.001\ U_p}{1.11\ 10^5}\right)+26.9 \qquad \textbf{(4.12)}$$

This equation is found by least square fitting on simulation results depicted in figure 3.13 in the energy range from 5 keV to 100 keV. This equation only describes the resolution in case of sputtering, but for other fabrication techniques similar equations can be derived.

In general, decreasing the ion energy is beneficial to minimize this contribution, but it increases the probe size through the Coulomb interactions. Figure 4.16 shows the probe size as a function of the beam energy. The calculation of the Coulomb interactions is performed with the program ANALIC (Jiang, 1996). The effect of Coulomb interactions comprises three parts: the space charge effect, the trajectory displacement and the Boersch effect. In a first order approximation the space charge effect only causes a defocusing because it is a broadening of the beam caused by the average charge density. This effect can be corrected. The latter two, a spatial broadening and an energy spread broadening due to statistical two particle collisions, cannot be corrected.

To minimize the influence of Coulomb interactions two apertures are used to limit the beam current: a 30 μm aperture in the source and a 20 μm aperture at a plane just in front of the first condenser lens. As follows from the simulations the Coulomb interactions have the largest effect in front of the energy filter, because the current density is largest there. Therefore the Boersch effect has negligible effect on the probe size but it decreases the probe current. This leaves only the effect of trajectory displacement on the probe size.

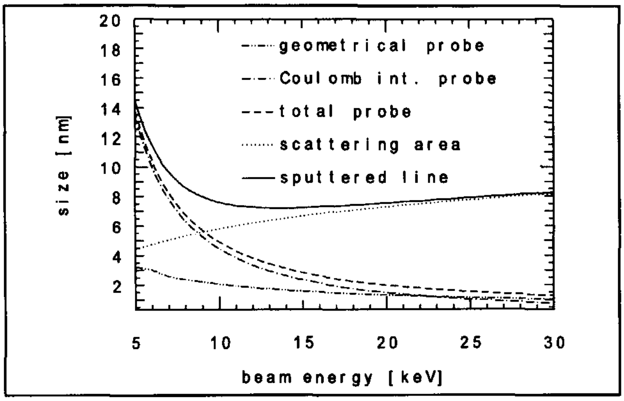

Fig. 4.16. *Size of structure in Si sputtered with Ar ions (10^{-14} A probe current) as a function of the energy of the ions. The probe size, a combination of the geometrical probe contribution (demagnified source size, chromatic and spherical aberration) and the probe contribution from Coulomb interactions, is depicted as well as the scattering area of the ions in the specimen.*

The final structure size is a combination of the scattering in the specimen (equation (4.12)) and the total probe size (equation (4.1)). At 14 keV beam energy the combination of interactions in the beam and in the specimen, which behave opposite as a function of beam energy, results in a minimum sputtered structure size of 7 nm at 1.10^{-14} A probe current. The geometrical probe size and the probe current are calculated using the equations (4.1) to (4.6). The probe size can still be decreased by further demagnification at the cost of current or a Coulomb tube in the first part of the system or a decelerating specimen.

In case of a decelerating specimen (Kasahara, 1988) the ions travel at a certain energy through the system but they are slowed down in the last few millimeters before they impact on the specimen to an energy which is reasonably smaller than the transport energy. In this case the scattering area can be decreased. However, if the ions are decelerated by the substrate, their optical properties will change. The opening angle will change according to (Narum, 1988)

$$\alpha_d = \alpha . \sqrt{\frac{U_t}{U_p}} \tag{4.13}$$

α_d= opening angle for decelerating specimen
α= opening angle for uniform energy
U_t= transport energy
U_p= energy of the decelerated ions

To calculate the effect of decelerating the ions on chromatic and spherical aberration, the substrate can be considered as part of the final lens. The aberration coefficients change now according to (Narum, 1988)

$$\begin{aligned} C_{c,r} &= C_c . \left(\frac{U_p}{U_t} \right) \\ C_{s,r} &= C_s . \sqrt{\frac{U_p}{U_t}} \end{aligned} \tag{4.14}$$

The consequence is that the chromatic contribution to the probe size decreases (according to equation (4.4)) while the spherical contribution increases (according to equation (4.5)).

The retarding method using a sample at high tension does not influence the Coulomb interaction contribution significantly. This is because the decelerating range is short with respect to the total length from source to specimen. This is just a rough estimation since the Coulomb interaction is not uniform over the column, but it will be of more influence at cross-overs and other places where the interionic distance is lowered. But the effect will still be so small that Coulomb interactions are treated equally in the uniform system and in the system with a decelerating specimen.

The sputtered structure size with a decelerating specimen is depicted in figure 4.17 for equal parameters as in figure 4.16. The opening angle, energy and energy spread at the specimen are optimized to give minimal structure size with 10^{-14} A probe current. This results in a smallest structure size of about 3 nm for 30 keV transport energy and 790 eV probe energy.

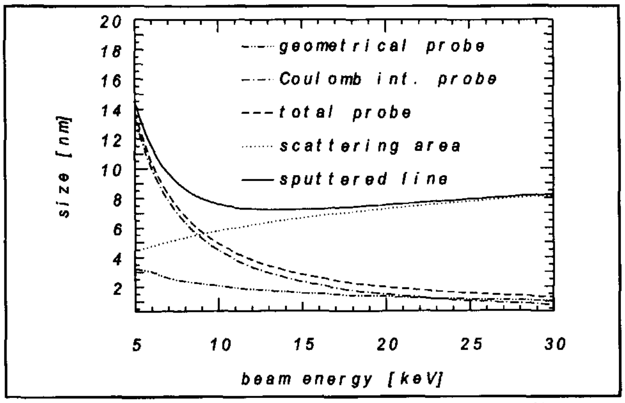

Fig. 4.17. *Size of structure in Si sputtered with Ar ions (10^{-14} A probe current) as a function of the transport energy of the ions with optimized probe energy. The probe size, a combination of the geometrical probe contribution (demagnified source size, chromatic and spherical aberration) and the probe contribution from Coulomb interactions, is depicted as well as the scattering area of the ions in the specimen.*

4.5. Summary

It is argued that nanostructures can in principle be fabricated using ion beams. A combined ion and electron beam instrument is designed for writing and inspection of nanostructures. The basic instrument is a Transmission Electron Microscope with a resolution of 0.65 nm after slightly modifying it. These modifications are necessary to add the ion beam system by means of partial integration. The optical systems for both beams partially coincides. In the ion beam system an energy filter is integrated to limit the energy spread of the ions from a Liquid Metal Ion Source and therefore to limit the chromatic contribution to the probe size.

The minimal structure size in case of sputtering in Si with Ar ions is 7 nm. This size results from a convolution of the ion probe size and the scattering area of the ions in the specimen. The probe size is minimized to 2 nm by reducing the chromatic aberration contribution with an energy filter based on two position dispersive 90°-deflectors. Compared to commercially available combined ion and electron beam instruments with non-coincident beams, this means a significant improvement of the probe size of magnitude at equal current density.

With a decelerating specimen the resolution of the sputtered line can even be improved to 3 nm. Although this is not a major improvement, it leaves open the fabrication technique of direct deposition where the landing energy of the ions has to be less than 1 keV.

References

Andersen, W.H.J., J.B. le Poole, *A double Wienfilter as a high resolution, high transmission electron energy analyser*, Journal of Physics E 3, 1970, pp. 121-126

Barth, J.E. and P. Kruit, *Addition of different contributions to the charged probe size*, Optik 101(3), 1996, pp. 101-109

Clark, W.M. and L.W. Swanson, *Long-lifetime, reliable LMIS for Boron, Arsenic and Phosphorus*, Journal of Vacuum Science and Technology B5(1), 1987, pp. 197-202

Dudnikov, V.G., *Review of high brightness ion sources for microlithography*, Review of Scientific Instruments 67(3), 1996, pp. 915-920

Herrmann, K.H., *Detection systems*, in: J.N. Chapman e.a., *Quantitative electron microscopy*, The Scottish Universities Summer School in Physics, 1984, pp. 119-139

Jager, P.W.H. de and L.J. Vijgen, *Beam interactions in a Focused Ion Beam system with a Liquid Metal Ion Source*, Microelectronic Engineering 23, 1994, pp. 107-110

Jager, P.W.H. de, C.W. Hagen and P. Kruit, *The influence of ion beam parameters on pattern resolution*, Microelectronic Engineering 30 ,1996, pp. 353-356

Jager, P.W.H. de, M.C.W. Kelder and P. Kruit, *A combined objective lens for electrons and ions*, Microelectronic Engineering 30, 1996, pp. 427-430

Jansen, G.H., *Coulomb Intercations in Particle Beams*, thesis, Delft, 1988

Jiang, X.R. and P. Kruit, *Comparison between different imaging modes in focussed ion beam instruments*, Microelectronic Engineering 30, 1996, pp. 249-252

Kasahara, H., H. Sawaragi, R. Aihara, K. Gamo, S. Namba and M. Hassel Shearer, *A 0-30 keV low-energy focused ion beam system*, Journal of Vacuum Science and Technology B6(3), 1988, pp. 974-976

Komuro, M. e.a., *Measurements of virtual crossover in liquid gallium ion source*, Applied Physics Letters 42(10), 1983, pp. 980-910

Liebl, H, *Ion optics of ion microprobe instruments*, Vacuum 33(9), 1983, pp. 525-531

Mühle, R, *High-field ion sources and applications*, Review of Scientific Instruments

63(5), 1992, pp. 3040-3049

Mul, P.M., B.J.H. Bormans and M.T. Otten, *Design of the CM20 FEG*, Philips Electron Optics Bulletin 130, 1992, pp.53-62

Narum, D.H. and R.F.W. Pease, *A variable energy focused ion beam system for in situ micro fabrication*, Journal of Vacuum Science and Technology B6(3), 1988, pp. 966-973

Narum, D.H. and R.F.W. Pease, *Applications of a variable energy focused ion beam system*, Journal of Vacuum Science and Technology B6(6), 1988, pp. 2112-2119

Orloff, J, *Focused Ion Beams*, Scientific American, October 1991, pp. 74-79

Rao, K.A. e.a., *A combination electron/ion field emission source*, Journal of Vacuum Science and Technology B7(6), 1989, pp. 1793-1799

Reimer, L., *Transmission Electron Microscopy, Physics of Image Formation and Microanalysis*, Springer-Verlag, Berlin, 1984, pp. 88

Sakatia, T. e.a., *Helium field ion source for application in a 100 keV focused ion beam system*, Journal of Vacuum Science and Technology B10(6), 1992, pp. 2842-2845

Sawaragi, H., R. Mimura, H. Kasahara, R. Aihara, W. Thompson and M. Hassel Shearer, *Performance of a combined focused ion and electron beam system*, Journal of Vacuum Science and Technology B8(6), 1990, pp. 1848-1852

Slingerland, H.N., *A fast ion beam pattern generator*, thesis, Wibro, Helmond, 1988, pp. 34-41

Swanson, L.W., *Use of the Liquid Metal Ion Source for Focused Beam Applications*, Applied Surface Science 76(1-4), 1994, pp. 80-88

Swens, J.J., *Design of an ion optical system for probe forming and sputtering*, Delft, 1988

Thompson, M.N., *The design of the EM 420 and its applications*, Philips Electron Optics Reporter 30(1), augustus 1983

Wollnik, H., *Electrostatic prisms*, in: Septier, A., *Focusing of charged particles II*, Academic Press, New York, 1967, pp. 163-202

Zworykin, V.K., *Electron optics and the electron microscope*, John Wiley & Sons, London, 1945, pp. 641-647

5. Ion source and condenser system

This chapter has been realized in close cooperation with M.S.H. Bauer and M.J. Fransen, as part of their master research.

Introduction

For the different fabrication techniques, as discussed in chapter 3, different types of ions are necessary. For example a noble gas ion source is favorable for sputtering and beam induced etching and deposition, because the implanted ions do not change the electrical behavior of the substrate significantly. However this is the aim in case of the implantation technique itself. So for direct deposition and implantation specific ion species are necessary. All these ion species cannot be emitted from the same source but there are common factors that need to be fulfilled.

A high brightness ion source with low energy spread is a necessary but not sufficient condition for a high performance focused ion beam system. It is argued in chapter 4 that 10^{-14} *A probe current in the nanometer probe can be obtained with a source brightness of* 10^6 $A.sr^{-1}m^{-2}.V^{-1}$ *and an energy spread of 4.5 eV. This can best be achieved with a field emission ion source (Bell, 1990). In this source a large potential difference is applied between a sharp tip and an extractor. This leads to an electric field at the tip of a few volts per nanometer, see figure 5.1. Under the influence of this electric field, optionally with the assistance of thermal excitation atoms on the needle or in the neighborhood of the needle can be ionized, because valence electrons move towards the needle. The extractor pulls the ions away. Three types of ion sources are based on this principle:*

1. *ionization of the tip material itself*
2. *ionization of a gas in the neighborhood of the tip: a Gas Field Ion Source*
3. *ionization of a liquid with which the tip is wetted: a Liquid Metal Ion Source*

It will be argued in the following paragraphs that for sputtering and beam induced etching a Gas Field Ion Source can be used, while a Liquid Metal Ion Source can perform as an ion source when direct deposition or implantation has to be realized.

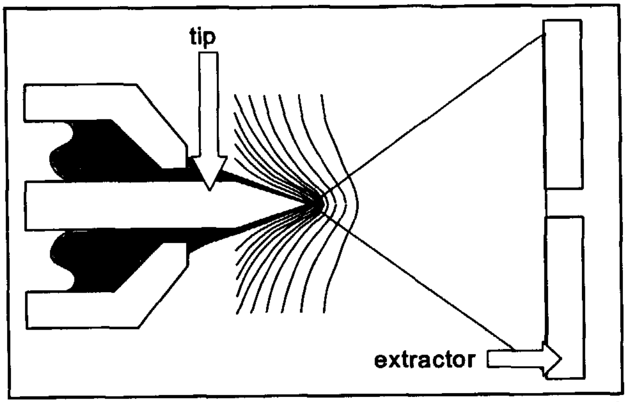

Fig. 5.1. ***Liquid Metal Ion Source based on field emission with equipotential curves near the tip.***

Besides the demands on brightness and energy spread there is also a need for stable emission. In fact the probe current is a certain fraction of the emission current. So instable emission at the source results in modulation of the dose with which the specimen is illuminated. This can only be allowed to a maximum of 5 % of the emission current over a time period of one hour. For practical reasons there is also a demand on the life time. It should work properly for at least 200 hours. In principle field emission can fulfill these demands.

The area from where the ions are emitted is in general larger than the probe size that is aimed for in "the Fancier". Therefore the emitted ion beam has to be condensed with (demagnifying) lenses. The first lens is already near the source. It will be discussed in paragraph 5.3 after a description of the different ion sources that are needed in "the Fancier" in paragraph 5.1 and 5.2. The other condenser lenses are dealt with in paragraph 5.4. For these lenses two types of electrostatic lenses will be compared: quadrupole lenses and rotationally symmetric lenses.

5.1. Ion source for sputtering and beam induced etching and deposition

For three of the fabrication techniques, as discussed in chapter 3, the ion species are not of direct importance. This is because the ion beam is used only to transfer energy from the ion to the target. With this energy the atomic bonds of a surface are broken which results in sputtering or the activation of a chemical reaction resulting in beam induced etching and deposition. However, the ions transfer their energy meaning that they are slowed down and stopped in the specimen. This is why the atomic species are of indirect importance. The implanted ion may not alter the properties of the specimen. This is best achieved if the ions are of the same species as the specimen or if they are inert gas ions. The specimen will be a silicon substrate which would recommend the use of Si ions. However these ions will also end up in, for instance, the deposited layer. This layer is made of conductive material like Gold and Platinum, which would recommend the use of these elements as ions. Therefore it is advantageous to use ion species which result in minimal effects in general; inert gas ions can fulfil this demand.

In chapter 4 the effect of the mass of the ions has been discussed. It turned out that low mass ions, like He, result in small interactions in the beam but in large scattering areas in the specimen. The opposite is valid for heavy ions, like Xe: large beam interactions and small scattering areas. So both low and high mass ions give rise to low resolution structures. The optimum is achieved for medium mass ions. Therefore an Ar gas field ion source would be the best to achieve sputtering and beam induced pattern generation.

5.1.1. Theory of a Gas Field Ion Source

Field ionization of gas atoms can take place near the apex of the tip. The essential mechanism is equal to the one of field electron emission but of opposite sign: electrons tunnel from the gas atom into the tip. In this way the gas atom is ionized. The theory of electron emission from a metal due to an electric field was developed by Fowler and Nordheim (Fowler, 1928). More recent descriptions are given by Gomer (Gomer, 1961) and Modinos (Modinos, 1984). However a simplified version will be given here, as it is of importance for the development of the ion source.

In figure 5.2 the potential energy diagram of a 1s electron of a H atom is shown in front of a metal tip. In the figure the energy levels of the metal can be seen, up to a maximum given by the Fermi level U_F. The energy required to raise the energy from the Fermi level up to the vacuum level is commonly called work function, denoted by ϕ_w. On the horizontal axis the distance is taken with the zero at the apex of the tip. The originally symmetric potential is tilted due to the external field. On one side the potential barrier has become finite and the electron can tunnel through the barrier if the field is high enough. Close to a metal-vacuum interface the barrier becomes even smaller, due to the image charge which builds up in the metal.

The shape of the potential barrier, where electrons may tunnel through, can be understood from the following three effects:

1. the electrons in the metal itself will cause an image charge in the bulk of the metal, leading to a potential curve as depicted by the broken line
2. the Coulomb potential, seen by the electron, due to a positive ion of charge e located at a distance z_i from the metal as shown by the dotted line
3. the applied electric field will tilt the initially zero potential level as shown by the broken-solid line.

Assuming a zero potential inside the metal occupying the half-space from z= -∞ to z= 0, the vacuum potential is given by

$$V(z) = -\frac{e^2}{16.\pi.\epsilon_0.z} - \frac{e^2}{16.\pi.\epsilon_0.|z-z_i|} + e.E.z \tag{5.1}$$

This potential field has a minimum a few Å from the surface, leading to the result that ionization will occur beyond a critical distance z_c. Because the metal does not have empty states below the Fermi level the field must raise the tunneling electron to the Fermi level U_F. At distances further away from the tip than the minimal distance z_c, the energy levels

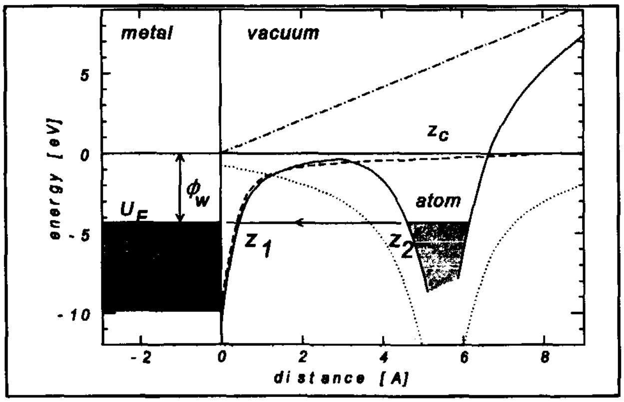

Fig. 5.2. *The potential energy distribution of an 1s electron of a H-atom in the vicinity of a metal tip.*

of the H atom will be higher than in the metal. So here tunneling is possible. However the probability decreases as z gets larger, since the potential barrier gets broader.

The field strengths that enable ionization near the metal surface, are in the order of 0.6-0.8 V/Å. Fields with this strength can be realized most practically by forming the cathode as a wire, ending in a sharp tip. At the apex of the tip the field will be high enough to overcome the potential barrier. Due to this geometry, field emission will be confined to a small area on the tip. Although the basic mechanism seems simple in itself, there are some operation modes to be distinguished:

1. *Operation at high fields.*

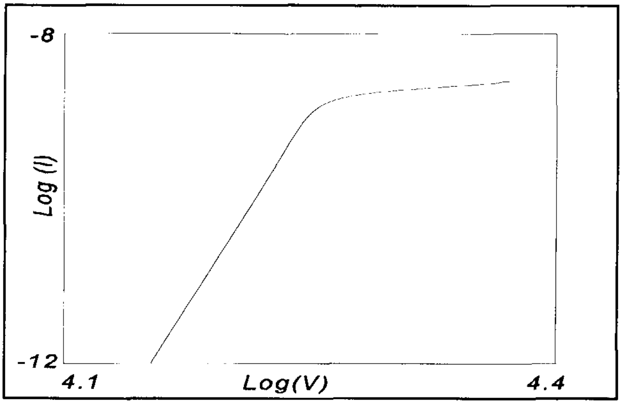

Fig. 5.3. *Current-voltage characteristic of a Gas Field Ion Source with low and high current regime.*

In this case all gas atoms arriving at the tip are ionized while they are still far from the tip. The ion current will only depend on the gas supply function, in other words: the number of gas atom coming in the vicinity of the tip in a certain time interval. Calculation of the ion current will give even higher results than expected at first sight. This is because the polarization forces near the tip will have an additional attraction effect. As a consequence from the high field, the emitting area and the energy spread will be relatively large.

2. *Operation at low fields.*

In this regime neutral gas atoms can come closer to the tip. The ionization probability cannot be taken now as unity. The only place where ionization can happen is very close to the apex of the tip, starting at the critical distance z_c, given approximately by $(U_{nl} - \varphi_w)/ E_0$, with U_{nl} the ionization potential of the gas atom, E_0 is the field at the tip surface, elsewhere the electric field is given by $E = E_0(r_t/r)^2$ and a factor k is introduced to correct for the field at a sphere: $E_0^{tip} = E_0^{sphere}/k$. The value for k is approximately 5. The ionization potential for Ar is about 15.76 eV, leading to a distance of 3.0 Å from a tungsten tip, when a field of $3.8 \cdot 10^{10}$ V/m is applied. In this regime the brightness of the source will be better than in the first case, because the emitting area is better defined, although the total emission current can be low.

It is possible to come to a more quantitative description for each of the two regions. A general expression for the ion current is given by (Gomer, 1961)

$$I = e.k_i.N_t = e.k_i.\frac{Z_{sup}}{k_d+k_i} \tag{5.2}$$

k_d= rate constant describing diffusion
k_i= rate constant describing ionization
N_t= number of trapped gas molecules near the surface
Z_{sup}= gas supply function

Mode 1 operation is valid if $k_i >> k_d$, while mode 2 operation is only valid when $k_i << k_d$; in other words

$$I_{high} = e.Z_{sup} \ , \quad I_{low} = e.\frac{k_i}{k_d}.Z_{sup} \tag{5.3}$$

If both regimes are characterized by rate constants (Gomer, 1961), the following distinction can be made: the rate constant k_d describes the diffusion rate, in other words: the number of atoms that leave the tip area without being ionized:

$$k_d = \frac{(2.k_B.T)^{\frac{3}{2}}}{\sqrt{M_e}.\alpha_p.E_0^2.r_t} \tag{5.4}$$

where α_p is the polarizability of the gas atom and r_t the radius of the tip. The ionization rate, k_i, is given by

$$k_i = \frac{4.\alpha_p}{3.k_B.T.r_s}.\sqrt{\frac{E_o^5.\Delta z^3.e}{U_{nl}-\Phi_w}.\frac{J(E,T)}{e}}.\exp\left[-\frac{4.\alpha_p.E_o.(U_{nl}-\Phi_w)}{3.r_s.k_B.T.e}\right] \tag{5.5}$$

r_s= radius of the emitting tip

Δz= half the distance z_2-z_1 in figure 5.2

J(E,T)=~current density according to Fowler-Nordheim (Miller, 1953)

The gas supply function describes the number of gas molecules arriving at the tip. This is a result of natural gas flow and the polarization force due to the electric field around the tip (Southon, 1963)

$$Z_{sup} = 4.\pi.r_s^2.\frac{p_{gas}}{\sqrt{2.\pi.M_{gas}.k_B.T_{gas}}}.\sqrt{\frac{2.\pi.\alpha_p.V^2}{k_B.T_{gas}.\left(r_s.\frac{lnR}{r_s}\right)^2}} \tag{5.6}$$

In order to fulfil the condition for low current mode (k_i<<k_d), it is most effective to maximize the exponent, *id est* by lowering both the temperature and the tip radius. Cooling of the tip will also improve the emission current as the residence time of the gas atom in the ionization region is extended by thermal accommodation (Müller, 1957). Gas atoms arrive at the emitter tip in nearly normal direction due to the high dipole attraction. This makes it more plausible to assume that mostly the rebound atoms are ionized. The only really interesting situation is the one of repeatedly hopping image gas atoms. Three situations can appear when an atom strikes the tip while it has an energy which is a sum of thermal energy and polarization energy, see figure 5.4.

a. *no thermal accommodation.* The gas collides almost elastically with the tip. This is because the polarization energy is smaller than the thermal energy. However, the

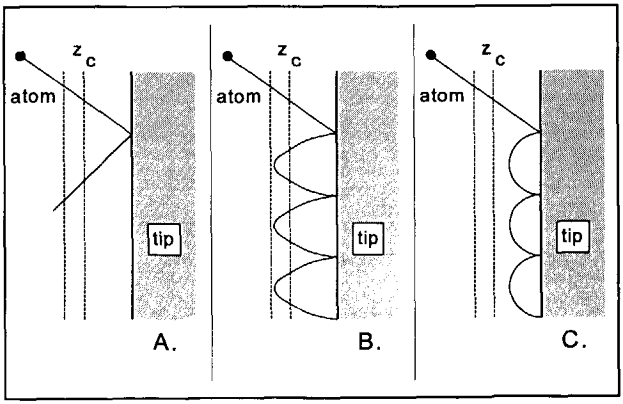

Fig. 5.4. *Thermal accommodation of gas atoms at the tip (a.) no accommodation , (b.) optimum accommodation and (c.) too strong accommodation.*

chance to get ionized is small due to the limited residence time of the atom.

b. *optimum thermal accommodation.* When the polarization energy is higher than the thermal energy, an atom striking the tip is trapped and will perform a series of hops until it is ionized or diffused away from the tip. It is favorable to have the hopping trajectory such that the particle exceeds the critical distance, z_c. The ionization probability will be higher and the ion current only depends on the gas supply function when the probability is unity. The effect is stronger when the tip is cooled, because in that case accommodation of the atom to the tip temperature is possible so that the trapping requirement is easier to fulfill.

c. *too strong thermal accommodation.* When the temperature is too low, the thermal accommodation will be too strong and the particles diffuse out of the tip region without being ionized. This is because they don't exceed the critical distance, z_c.

These effects have been shown (Müller, 1957) for a tungsten emitter with a radius of 50 nm and He atoms. By cooling from 20 K to 4 K the emission current is reduced by a factor fifty, probably by going from regime b to regime c. When mode 2 operation, low emission current, is fulfilled the total emission current is given by

$$\begin{gathered} I = 2.\pi.e.r_t^2.z_c.c_t.k_i \\ c_t = c_g.f\left\{\frac{T_g}{T_t}\right\}.\exp\left[\frac{-V(E)}{k.T_t}\right] \;,\; f\left\{\frac{T_g}{T_t}\right\} = \sqrt{\frac{T_g}{T_t}} \end{gathered} \tag{5.7}$$

c_t= gas concentration near the tip

All g-subscripts refer to gas parameters, the t-subscript describe the tip. The maximum distance where f in equation (5.7) is valid, is about the average hopping height of the gas atoms. It is approximated by unity elsewhere.

From the same model it is possible to derive an expression for the energy spread of the ions as it originates from the position of ionization. An ion formed at the tungsten surface of the emitter has an energy equivalent to the full accelerating voltage when it reaches the extractor. An ion having originated at a distance x away from the surface has an energy equal to the full acceleration voltage reduced by an amount

$$\int_0^x e.E(z).dz \tag{5.8}$$

The smallest distance at which ionization can take place is the critical distance. The difference between the highest energetic ions (originated at the critical distance) and the ions originated at a distance x from the surface then becomes

$$\Delta U = \int_{x_c}^{(x-x_c)} e.E(z).dz \tag{5.9}$$

For several gases measurements of the energy distribution half width have been done. For argon the distribution half width appears to be about 0.8 eV(Gomer, 1961). This corresponds to an ionization zone of 0.42 Å.

5.1.2. Design considerations in Gas Field Ion Source development

Based on the above theory a Gas Field Ion Source is developed for Ar. An important item in the design of this Gas Field Ion Source is the supply and control of the gas pressure. In the solution that has been chosen, the emitter tip is installed in a sharp stainless steel needle. The gas will flow through the needle and will leave it with an opening angle of about 30° (Kohlmann, 1992). This setup gives good supply to the emitter tip while the needle does not alter the electric field as it is circular symmetric around it. The flow of gas results from the conductivity of the needle and the driving force, the pressure difference between the gas reservoir and the vacuum chamber. The gas supply reservoir is very similar to the one for precursor gasses that will be described in chapter 9.

The pressure is regulated with a servo valve. The Ar gas has to be very pure (~5 ppm contamination) since this influences the stability of the emission. If contaminations have a higher ionization energy than the basic element they stay on the tip since they are attracted to it but not ionized (Börret, 1988). The tip is cooled by liquid nitrogen. The influence of the tip temperature, the origin of thermal accommodation, on the emission current is measured. The result is shown in figure 5.5 for a reservoir pressure of 7.1 10^{-3} mbar and an extraction potential of 25 kV.

Although it is a preliminary result, it is clear from this measurement that there are a few maxima in the total ion current. The largest one appears at about 150 K. However this maximum is also visible in the background pressure. It is probably the result of desorption of gas atoms from the copper that is in the neighborhood of the tip. The gas has accummulated on these elements since the experiment started at 80 K. Another maximum is at 100 K and is not visible in the background pressure. This is probably the result of thermal accommodation of Ar on the tungsten tip, which is likely at this temperature. Left from the maximum the ion current drops to about 5 pA and right from this maximum the ion current drops to 10 pA.

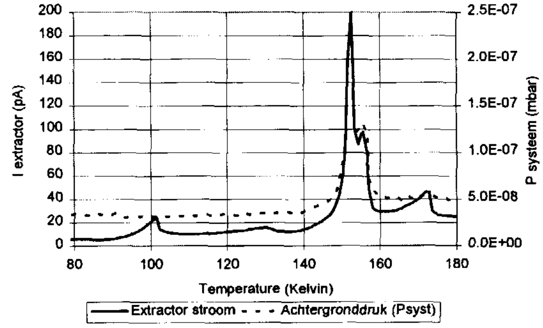

Fig. 5.5. *Temperature dependence of the emission current (Bauer, 1997).*

Another design consideration is the angular current density. It is very low, 0.5 μA/sr (Bell, 1990) compared to a Liquid Metal Ion Source (10 μA/sr). A proposal for a practical Gas field Ion Source with high angular current density suggests a protrusion on top of a conventional tip (Börrect, 1988). This protrusion, casually denoted as supertip, is created on a tip with a sharpness of a few hundred nanometers by cathode sputtering (Jousten, 1988). These supertips have a field enhancement of 30-50 % relative to the average field strength of the tip. They confine the beam to about 1° at total currents of a few nanoamperes since the regular tip has a lens effect on the emitted ions. Angular current densities of 20 μA/sr are reported for He and even higher values for H_2 (Bell, 1990). However this is not of main importance for "the Fancier", only if the area of emission is limited at the same time the brightness will increase. But it is doubtful wether a supertip is necessary to reach the desired brightness of 10^6 $A.sr^{-1}.m^{-2}.V^{-1}$ since the virtual source size is only about 2 nm for a normal tip (Bell, 1990).

5.2. Liquid Metal Ion Source

Both direct deposition and implantation have direct demands on the ion species. In the

Next project transport phenomena are mainly of interest. This means that the structures should be conductive. Therefore metal ions have to be deposited directly on the specimen. This requires an ion source that emits metal ions like gold (Au).

For implantation the interest is mainly in dopant material. The substrate material is Si, an element of the fourth group of the periodic table of the elements. This means that donor and acceptor implantation materials are elements of the third and fifth group respectively. These elements like boron (B) and arsenic (As) have to be emitted form the source for implantation.

The heat of sublimation of the direct deposition and implantation materials does not allow a Gas Field Ion Source as described in the former paragraph. Lower temperatures of operation are sufficient in a Liquid Metal Ion Source. Therefore an elegant method to come to a high brightness source can be realized by covering a metal tip with the liquid of the material to be ionized. The electric and hydrostatic forces on the liquid film will balance, leading to a cone, which ends in a small tip.

5.2.1. Theory of Liquid Metal Ion Source

The principle of a Liquid Metal Ion Source is not equal to that drawn in figure 5.2. This would suggest that atoms from the liquid are evaporated from the tip and are ionized when they have diffused to a position equal or further away from the tip than the critical distance z_c. This model of field ionization, including the evaporation, is not likely. It is found (Mair, 1980) (Mair, 1981) that it is impossible to develop a self-consistent model giving an adequate area at a high enough temperature to provide the required flux of thermally evaporated neutral atoms for subsequent field ionization.

A more likely model is field evaporation. In field evaporation the ionization of a surface atom (in this case an atom in the liquid) takes place by lowering the activation energy for ionization Q, with the aid of a high electric field. In equation (Mühle, 1992):

$$Q = H_0 + U_{nl} - \Phi_w - 1.2\sqrt{E} \qquad \textbf{(5.10)}$$

H_0= heat of evaporation [eV]
U_{nl}= ionization energy [eV]
E= field strength [V/nm]

This barrier Q is now to be overcome with thermal activation. In this manner the atom escapes from the surface as an ion, leaving an electron in the bulk. A sufficient increase of the electric field strength at the surface will lower the activation energy. This principle is depicted in figure 5.6. For a sufficiently low activation energy Q, an electric field strength of about a few V/nm is necessary.

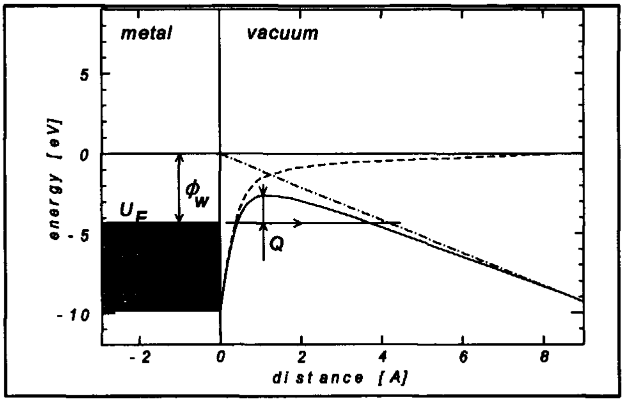

Fig. 5.6. *The potential energy distribution of the ion at the liquid metal-vacuum interface with activation energy Q (Swanson, 1983).*

In fact the liquid at the vertex of the needle is a droplet. From Taylor (Taylor, 1964) it can be gathered that a droplet in an electric field develops an apparently conical end which usually oscillates. Since the curvature of the conical surface is inversely proportional to the distance from the vertex, the stress normal to it, which balances the surface tension, must also be inversely proportional to the distance from the vertex. Since the fluid will be assumed to be conducting the conical surface must be equipotential. To balance the surface tension the potential gradient there must be proportional to $r^{0,5}$ where r is the radial coordinate, see figure 5.7a.

The electric field expressed in spherical coordinates which satisfies the stress condition has a potential

$$V(r)=V_v+A.r^{0,5}.P_{1/2}(\cos\ \theta) \qquad \textbf{(5.11)}$$

V_v= potential at the vertex
A= constant
r= radial coordinate
$P_{1/2}(\cos\theta)$= Legendre function of order $_{½}$
θ= angle of the cone, θ=0 or θ=π is the axis of the cone

The potential at the liquid should be equal at all regions of the surface for a stable situation, so V must equal V_v and thus $P_{1/2}(\cos\theta)$= 0. $P_{1/2}$ has only one zero in the range

$0<\theta<\pi$ at $\theta = \theta_0 = 130{,}7099^0$. So the only positive electric field which can exist at equilibrium with a conical fluid surface is that external to a cone of semivertical angle $\alpha = \pi - \theta_0 = 49{,}3^0$. This cone is called the Taylor cone. The electric field at the apex is given by

$$E = \frac{V}{\sqrt{R_o . r_t}} \tag{5.12}$$

V= extraction potential

R_0= form factor of the order of the electrode spacing, assumed 0.1 cm (Gomer, 1979)

r_t= radius of the apex

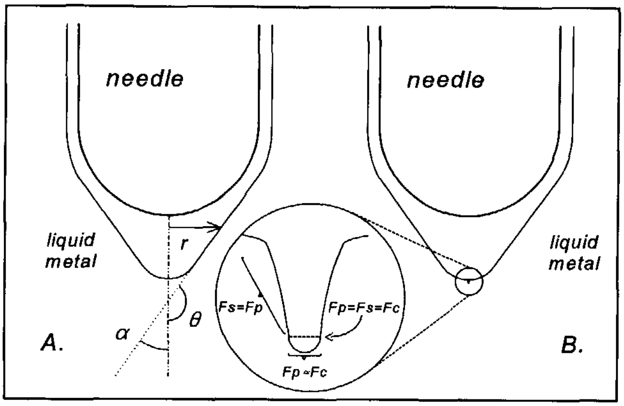

Fig. 5.7. *Emission area of a Taylor cone (a) hemispherical cone, (b) jet-on-cone.* F_e= *electric force,* F_h= *hydrodynamic force,* F_c= *critical force.*

Measurements show a spherical apex at the end of the Taylor cone with a radius of 1 μm. For a typical extraction potential of 3.5 kV this will result in a maximum field strength of 0.11 V/nm. This is not sufficient to initiate ionization. It has been shown (Kang, 1984) that it is impossible to have a high enough field strength at the emitter apex for currents larger than 2 μA due to space charge suppression. Therefore the hemispherical cap on the Taylor cone has to be adapted. Most accepted is an elongation near the apex of the Taylor cone, also known as the jet-on-cone model (Kang, 1984). A rise of the electric field will lead to ion emission as soon as the force due to the electric field, F_e, the hydrodynamic force, F_h, and the critical force necessary to move atoms far enough from the bulk to start ionization, F_c, balance as indicated in figure 5.7b. The Taylor cone with micro protrusion has been observed in-situ (Benassayag, 1985). The dimensions of the micro protrusion are in the order of 3 nm diameter and up to approximately 30 nm long. Therefore the radius of the apex of the jet is about one nanometer. For the same extraction potential and form factor as described above a field strength of 3.5 V/nm results, high enough to explain ion emission.

The length of the micro protrusion will change as a function of the emission current: there is a feedback from the space charge to the field strength at the tip. The space charge screens part of the field. When a source starts to emit ions, a space charge will arise in front of the micro protrusion. As a result the micro protrusion will bend and emission will occur "along" the space charge cloud. This process will repeat itself making it probable that the micro protrusion will rotate over the Taylor cone, creating a helix shaped space charge cloud.

Another effect is the origin of constrictions as a result of the surface tension. Constrictions have been described for water emitted from a nozzle (van de Sande, 1974). Although the situation is not completely identical, the given equation is

$$L_b = 12.\frac{e.I.M}{\pi.r^2.\rho}.\sqrt{\frac{8.\rho.r^3}{\sigma}} \qquad \textbf{(5.13)}$$

L_b= break length
I= emission current
M= mass of the ions
r= radius of the micro protrusion
ρ= density
σ= surface tension

For emission current less than 1 μA the break length according to this equation, is 5 nm. As this is shorter than the length of the micro protrusion for stable emission the constriction can be a reasonable explanation why liquid metal ion sources so not emit stable below a certain emission current. Due to the lower emission current the velocity of the liquid in the micro protrusion is decreased which can result in breaking before emission appears. The minimal emission current has also been observed experimentally (Beckman, 1996)

In literature different equations can be found that describe the emission current as a function of the process parameters. Based on the theory of field evaporation it can be written as (Forbes, 1982) (Forbes, 1992)

$$I= C.A_n.N_n.\exp\left(-\frac{Q}{k_B.T}\right) = C.\tau.\pi.r_t^2.\exp\left(\frac{S.(E-E_0)}{E_0}\right) \qquad (5.14)$$

C= constant
τ= frequency factor (10^{-12} á 10^{-13} s^{-1}) for a bonded electron
S= semi-logarithmic field sensitivity of the evaporation rate constant
E_0= threshold field strength

This relation shows a linear relation between the emission current and the area of the emitting surface of the jet-like micro protrusion. This is in agreement with a model (Kingham, 1984) (Thompson, 1984) that is based on the force balance as described above

$$I= C.\pi.r_t^2.\sqrt{\frac{1}{2}.\epsilon_0.E^2-\frac{2.\gamma}{r_t}} \qquad (5.15)$$

γ= surface tension

Due to the tiny jet the emission site is very small. Therefore it is very reasonable that space charge effects will influence the emission characteristics. A model including these effects is given for a needle in capillary source as depicted in figure 5.1 (Mair, 1984) (Mühle, 1992)

$$I= 3.\pi.\sqrt{\frac{2.e}{M}}.\gamma.R.\cos(\theta).\frac{V-V_x}{V_x^{1.5}}$$

$$V_x= \sqrt{2.K.R.\gamma.\frac{\cos(\theta)}{\epsilon_0}}\ ,\quad V_x= \sqrt{\frac{\gamma.r_t}{\epsilon_0}.\ln\left(\frac{a.h}{r_t}\right)} \qquad (5.16)$$

R= outer ratio of the capillary
V_x= threshold or extinction voltage
K= geometrical factor
a= needle form parameter, often: 2 (Mair, 1986)
h= distance from tip to extractor

Because of these space charge effects the emission site is enlarged to a virtual source size of about 50 nm (Komuro, 1983). The contents of the beam will change during the raising of the emission current. At small emission current ions will be emitted, at larger emission currents the beam contains charged clusters of atoms (Bhaskar, 1989), while at very large emission currents emission of droplets appears (Vladimirov, 1992) (Wagner, 1981). This is a result of the instability of the flow of material to the protrusion at larger emission currents.

The energy spread of a liquid metal ion source is constant at low emission currents in the order of some μA's and is about 4.5 eV. An explanation for this minimal value is mostly sought in collisions of atoms with ions, heating of the tiny jet due to the large electron current that flows back towards the tip and instabilities of the jet itself. At higher currents the energy spread becomes larger. The minimal energy spread achievable with a liquid metal ion source determines the limitation of the optical system: it will be limited by the chromatic aberration. This increase in the value of ΔU is almost certainly a direct consequence of the broadening of the distribution as a result of Coulomb interaction in the beam.

Besides metals, like Ga, non-metallic materials or metal with a high vapor pressure at its melting temperature can be emitted by including them in a conductive alloy. A widely used example is the eutectic AuSi with a melting temperature of 310 °C. It is used as a gold source suitable for direct deposition.

5.2.2. Design consideration in Liquid Metal Ion Source development

Successful development of a liquid metal ion source depends upon the satisfactory confluence of several design considerations. The desirable properties of the alloy and substrate cannot be fully and simultaneously satisfied. In the following some of these considerations will be discussed (Bozack, 1986). If some of the considerations cannot find express in the design, this results in short lifetime or unstable emission of the element of interest.

1. Low melting temperature

   The needle must be covered with the material to be ionized in liquid phase. The melting temperature of this material must not only be considerably lower than the tip material, it also influences reactions between the material and the tip which lowers the lifetime. Besides a high working temperature raises the energy spread, so it lowers the brightness.

   A convenient way to come to ion emission of elements that do not meet these requirements is the use of an alloy of some elements with a low melting point, a binary or ternary eutectic composition. This gets interesting when the ion source is used for implantation, like boron. Pure boron has a melting temperature of 2077 °C. A mass-separating device makes the selection of the desired ion species possible.

2. High relative bulk concentration of ion species of interest

   A desirable property of the alloy is that it possess a high relative bulk concentration of the intended ionizing element.

It is the bulk concentration, and not the surface concentration, of the element that is important because the steady state emission characteristics of the liquid metal ion source reflect the bulk stoichiometry of the material. Besides the current of ion species X is linearly dependent upon the fractional bulk concentration of the atom X, assuming the field evaporation mechanism of ions to be valid.

3. Congruent ion formation

When the stoichiometry of the beam reflects the stoichiometry of the liquid alloy producing the ions it is said that we have congruent ion formation. It is not possible to operate a non-congruent ion forming liquid metal ion source for long time stable emission because:

1. when using an eutectic alloy it will no longer be eutectic and so solid precipitations will be formed,
2. the source reservoir composition will change and this will change the beam composition,
3. local concentration gradients will appear near the tip resulting in emission instability.

4. Low solubility of alloy in substrate

The rate and extent of diffusion and reaction of alloy components into the substrate material must be minimal. This process is the major lifetime-limiting mechanism for contact systems composed of liquid metal alloys of B wetted to refractory metal substrates. So, much attention must be paid to the choice of the tip-material.

5. Low partial vapor pressure

Low volatility is necessary to conserve the liquid film supply and promote long life. Several elements cannot be used for a liquid metal ion source because they have high vapor pressures at their melting points and would volatilize completely if operated at this temperature for any significant period of time.

A general rule of thumb is that component partial pressures greater than 10^{-7} mbar are unacceptable. Here a Gas Field Ion Source is preferable.

6. Good wetting

To facilitate liquid flow from the reservoir to the apex tip where emission occurs good wetting of the needle is necessary. So for a stable emission good wetting has to be provided (Prewett, 1985). In principle wetting of the needles is realized by dipping them in a reservoir with the over layer material, the material to be ionized.

Figure 5.8a shows a simplified situation of the needle which is partially covered with the overlayer material. A striking atom can occupy locations A,B and C. The energy effects occupying these locations can be calculated

$$\begin{aligned}\Delta\gamma_A &= \gamma_s-\gamma_o-\gamma_i \\ \Delta\gamma_B &= \gamma_o-\gamma_o = 0 \\ \Delta\gamma_C &= -2.\gamma_o\end{aligned} \tag{5.17}$$

γ_i= free energy per unit area at the overlayer-substrate interface
γ_o= free energy per unit area at the overlayer-vacuum interface
γ_s= free energy per unit area at the substrate-vacuum interface

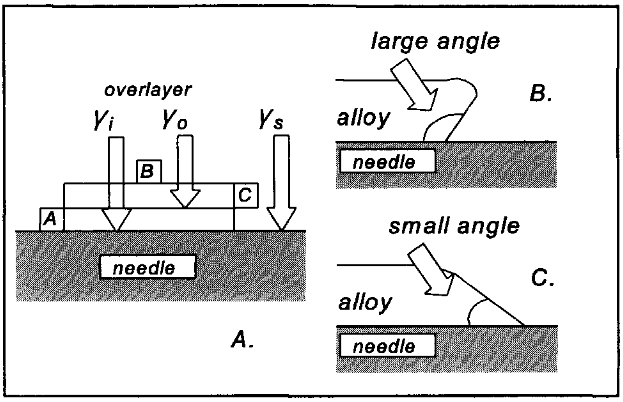

Fig. 5.8. *Wetting of the needle with the material to be ionized (a.) principle, (b.) bad wetting and (c.) good wetting.*

From this equation the Bauer criterium (Zangwill, 1990) can be derived: when $\Delta\gamma_A > \Delta\gamma_B$ position A is more advantageous and complete wetting occurs. Droplet growth takes place when $\Delta\gamma_A < \Delta\gamma_C$. In the intermediate regime, $\Delta\gamma_C < \Delta\gamma_A < \Delta\gamma_B$, the wetting is not perfect because a large contact angle between layer and needle. However no droplets are formed. So sufficient wetting can be defined as a contact angle considerably less than 90 degrees, see figure 5.8b and 5.8c. The contact angle can be calculated with the equation of Young (Tabor, 1979)

$$\gamma_s = \gamma_i + \gamma_o.\cos(\chi) \tag{5.18}$$

χ= contact angle

These equations are only a qualitative estimation because any anisotropic effect of the surface tension is neglected. However it can be seen that the Bauer criterium for perfect wetting is fulfilled if $\gamma_s > \gamma_i + \gamma_o$. Therefore it is preferable to have an over layer material with low surface tension. Although material like tungsten can fulfill this demand its surface tension can be lowered due to impurities and oxides (Rieck, 1967). Note that the overlayer surface tension, γ_o, will be significantly lower when it is covered with an oxide layer (Filand, 1968) or incorporates impurities (Foster, 1968). This causes the appearance of wetting without an enthalpy decrease at the interface but with incorporation of unwanted materials. This can result in a higher temperature to get the overlayer in the liquid phase.

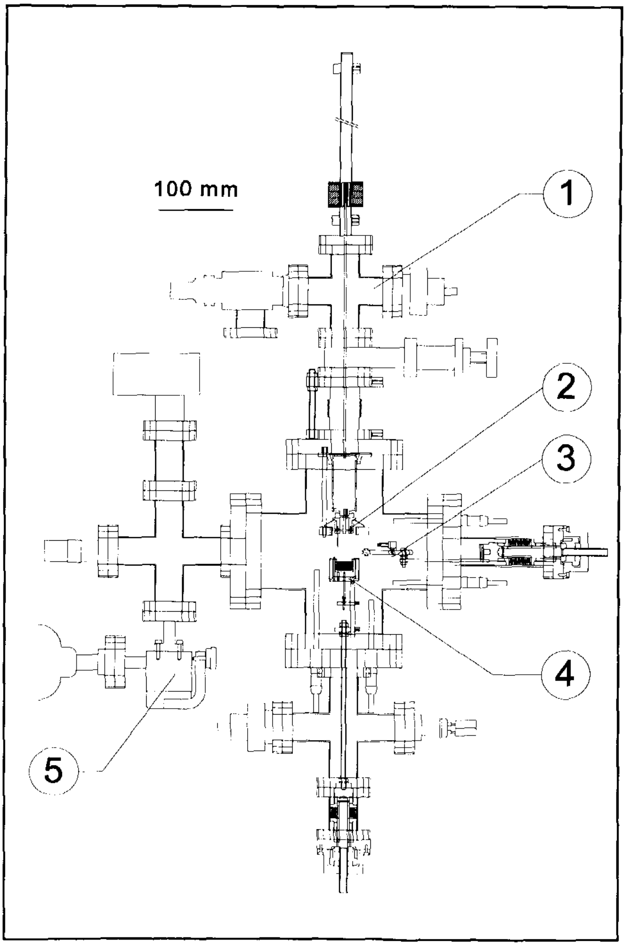

Fig. 5.9. *Overview of the wetting system. 1. needle load lock, 2. needles in holder, 3. needle heater, extractor and shutter, 4. Ga reservoir with heater and 5. Argon inlet (Fransen, 1994).*

Therefore it can be concluded that both the needle and the overlayer have to be free of impurities and oxides before they are brought into contact with each other. An ultra high vacuum system has been built to realize this, see figure 5.9. This system is in agreement with other systems that are used to cover the needles with overlayer material (Swanson, 1979). Both the tip and the reservoir with the material to be ionized can be heated to a sufficiently high temperature that all unwanted materials have been dissociated. This system can be used for wetting needles with materials like Gallium (Ga).

Table 5.1. *Alloys for emission of metal ions and dopant elements for Si. The subscripts indicate the mass fraction in the bulk.*

alloy	melting temperature [K]	lifetime [hr]	beam composition	energy spread [eV]	reference
$Pd_{40}Ni_{40}B_{10}As_{10}$	900-1000	10	As~ 10% B< 10%		Wang, 1981
$Cu_{36}P_7Pt_{33}B_{24}$	1150-1200	30		P: 12 B: 12	Umemura, 1986
$Pd_{40}Ni_{40}B_{10}As_{10}$			no B		Clark, 1987
$Pd_{70}B_{16}As_{14}$	1100-1150	150	B: 7% As: 20%	As: 17 B: 8	Clark, 1987
$Pd_{30}Ni_{30}B_{20}As_{20}$	1050	20		15	Fukuda, 1987
$Ni_{58}B_{22}As_{20}$	1100-1200		B: 15% As: 8%		Umemura, 1988

In an attempt to satisfy as many as possible design considerations, several alloys have been developed for emitting the elements of interest: metals for direct deposition and elements of the third and fifth group of the periodic table of elements as dopant material for implantation in Si. Table 5.1 shows several alloys and their properties. Based on these data the decision is made to use an AuSi alloy for Au deposition and a PdBAs alloy for direct implantation. The argumentation is mainly the relatively long lifetime. However it will be hard to realize the demands on optical properties as listed in table 4.2. Firstly, the energy spread is larger. This means that the energy filter will stop more ions resulting in lower probe current. Secondly, the brightness is lower because the elements of interest are only a fraction of the total emitted current. This makes a mass filter necessary. Such a filter has been developed for the Delft Ion Beam Pattern Generator (Bohlander, 1987).

5.3. Ion source optics

Directly behind the emitting needle there will be a source lens. It has two functions. Firstly it has to generate the electric field necessary for field emission. The second function is to focus the ion beam. The most often used form of source optics for a field emission ion gun is the tetrode system, schematically shown in figure 5.10. In this arrangement both current and image distance can be regulated independently by, respectively, the extraction voltage and the lens electrode voltage. The potential difference between the tip and the ground electrode defines the beam energy of the ions.

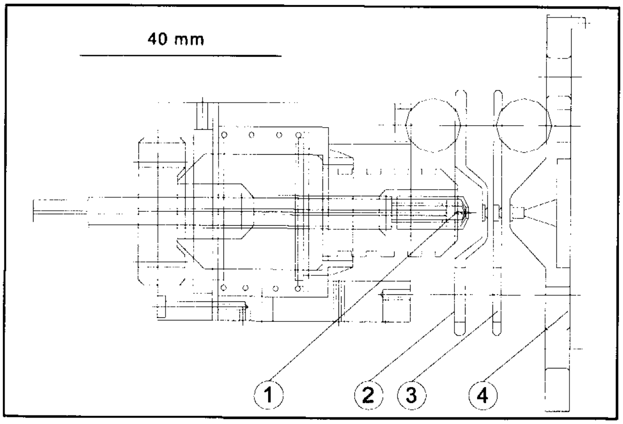

Fig. 5.10. *Principle drawing of a source module with source optics. 1. emitter tip, 2. extractor electrode, 3. lens electrode and 4. ground electrode.*

Some aspects concerning the source optics will be discussed separately:

1. lens quality

   The image of an ion beam system with a (liquid metal) field ion source is generally limited by the chromatic aberration (Slingerland, 1984). Therefore the chromatic aberration coefficient of the source optics, C_c, is an important parameter. With the parameters of table 4.4 it can be calculated that the chromatic aberration coefficient of the source optics has to be smaller than 5 m to limit the contribution to the final probe size to less than 5 %.

With the scaling of an optical instrument $C_c.f^{-1}$ (with f the focal length) will obviously be a constant. Therefore the optimization of the source optics, only taking into account the aberrations, is mainly achieved by scaling the tetrode system. For a first approximation of the performance, the focal length is considered

$$f = \frac{16}{3}.d.\left[\frac{(k_1-1)^2}{k_1^{5/4}} + \frac{(k_2-1)^2}{k_2^{5/4}}\right]^{-1}, \quad k_1 = \frac{U_1}{U_0}, \quad k_2 = \frac{U_2}{U_1} \qquad (5.19)$$

U_0= beam energy in front of the lens
U_1= beam energy in the middle electrode
U_2= beam energy after the lens
d= distance between the lens electrodes

For best results the lens working of this system has to be achieved by accelerating the ions rather than by decelerating. This can be understood by inspecting the ion energy along the axis: $\Delta U/U_0$ is smaller in the accelerating mode. Furthermore the ion trajectories are bound more closely along the axis, thus giving smaller aberrations. Unfortunately this leads to unacceptably high voltages. Therefore the decelerating mode is chosen. Simulation of the performance of this lens can be done with the finite difference program ELSTAT (van der Mast, 1988). The results are depicted in figure 5.11 for different focal lengths of the lens. The dimensions of the lens are minimized to the limit given by the need for acceleration of the ions to 30 keV.

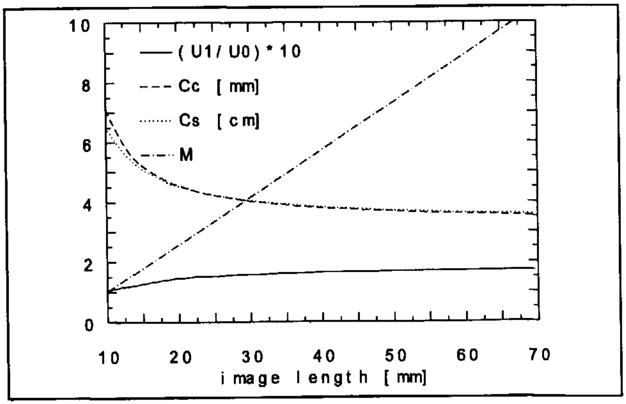

Fig. 5.11. *Properties of the source lens: energy in lens relative to beam energy, chromatic and spherical aberration and magnification.*

In the simulated lens the holes in the electrodes are assumed to be thick and all of the same diameter. Further improvement of the lens quality is possible by optimizing these diameters resulting in lower coefficients of chromatic aberration (8 %) and spherical aberration (22 %).

2. alignment

   Ions are emitted from the tip with a large opening angle of 60 degrees. Therefore these ions are relatively far from the optical axis or close to the lens electrodes. This makes the beam sensitive to the alignment of the electrodes with respect to each other and with respect to the tip.

   A good alignment has been achieved using Al_2O_3 balls both as insulators and for alignment (Slingerland, 1988). But it is very hard to position the individual apertures in the center of each electrode. This can result in a spot by the source lens which is larger than could be expected based on the aberrations (Vijgen, 1994). A better technique is to machine the holes in all electrodes at the same time. Now the electrodes are fixed first, before the central hole is machined. The result is an aligned optical axis through all three electrodes. Consequently all holes have the same diameter. It is realized in the actual source module used, depicted in figure 5.12.

3. Coulomb interactions

   The minimum emission current from a liquid metal ion source is about 1 μA. These ions all origin from the very small area of the micro protrusion. Therefore it is very likely that interactions between the ions take place. That can be space charge effects but also statistical interactions which cannot be corrected. In general a virtual source size is measured taken into account these interactions. Consequently, in calculations of system properties the parameters of the virtual source are used disregarding the Coulomb interactions. The virtual source for a liquid metal ion source is about 45 nm in diameter (Komuro, 1983) and is found 50 μm in front of the real source position (Vijgen , 1994). So the field near the tip must be about spherical. Because the point of the tip is placed in the extractor electrode, this is a comprehensive result. This virtual source size can be used independent of the beam energy because of the fixed extraction voltage and therefore accelerating field in the area in the vicinity of the tip.

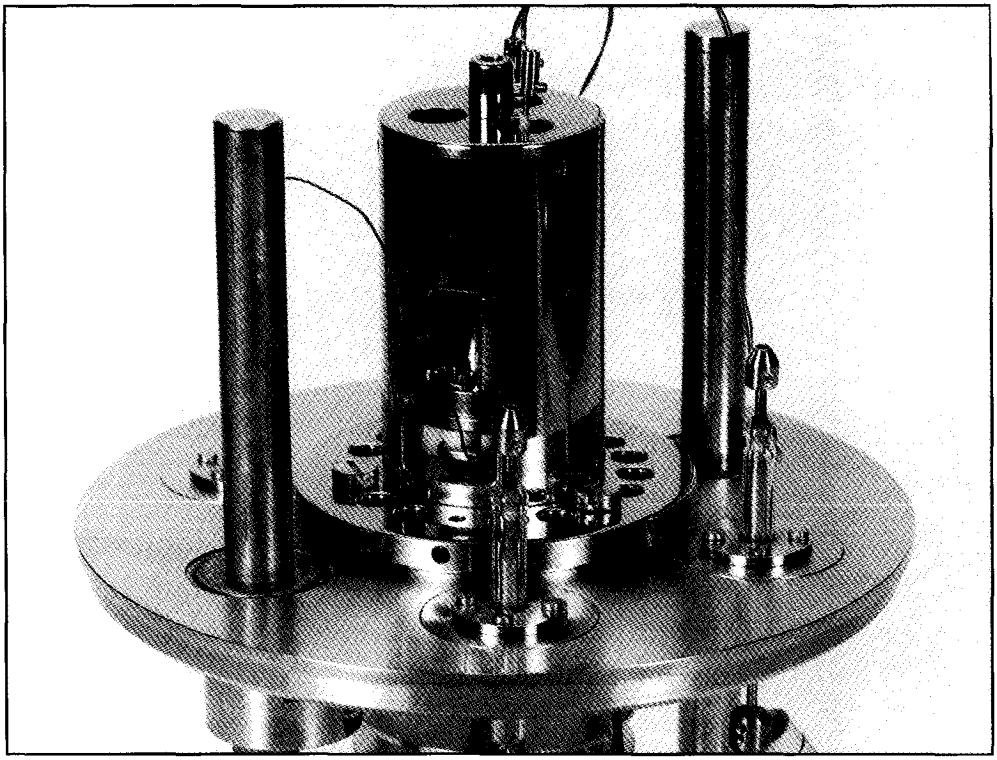

Fig. 5.12. *The source module with source optics.*

However these parameters take only into account the Coulomb interactions directly in front of the tip, but if the beam is focused additional Coulomb interactions will appear. It is most likely that the system is in the Holzmark regime. Therefore it is not effective to limit the current here with an aperture since that does not change the angular current density. Only a very small aperture will bring the system into the Pencil beam regime. Here limiting the current is very effective in reducing the Coulomb interaction contribution to the probe size, see equation (4.3). This is possible with an aperture in the source optics. It stops ions which are further off-axis than a certain distance. So only those ions are stopped that have a large opening angle. They would be stopped anyway further in the system as their opening angle is too large to come to the desired probe size. But as long as they are part of the ion beam they will deteriorate its brightness through the Coulomb interactions on those ions that have to be transferred to the probe. Therefore the interactions between the ions inside the lens should be calculated.

4. aperture erosion

   The beam limiting aperture can in principle be positioned on or near every electrode of the source lens. However it cannot be positioned in the extraction electrode because the emitting tip is positioned in this electrode. Placing of the beam limiting aperture in the lens electrode implies the limitation as soon as practically possible which is beneficial to limit the effect of Coulomb interactions. Another advantage of this position is that the ions hit the specimen with low energy. The ion energy is here only some 5 keV instead of 30 keV elsewhere, this means a sputtering yield of 4.10 atoms/ion compared to 6.28 atoms/ion at 30 keV (Ziegler, 1985). The overall effect is a longer lifetime of the beam limiting aperture.

   However the large field at the aperture implies a large spherical aberration coefficient unless the aperture is screened from the field. Therefore a thick lens electrode is used, enabling the aperture to be in a more or less field free region. Also the alignment of the aperture is more sensitive when it is positioned in the lens electrode than at the ground electrode.

   Therefore, although the lifetime of the aperture is smaller at the ground electrode and the Coulomb interactions can act for a longer time, the beam limiting aperture is positioned at the ground electrode mainly to avoid problems because of miss alignment by placing it in a field free region.

It is clear from the above discussion that the design of the source optics change considerably depending on which aspect is expected to be of main importance. In the actual source optics, depicted in figure 5.10, the accent is put on the sensitivity for alignment (the holes in the electrodes are made after assembling) and, in a smaller measure, to the lens aberrations. As a result, the beam limiting aperture is at the ground electrode.

If the interactions are expected to be of importance this design has to be reconsidered, especially the place of the aperture. This will be the case primarily for the liquid metal ion source as it has a minimal emission current. For the gas field ion source the alignment of the tip with respect to the extractor electrode seems to be an important parameter. Vibrations, due to the flow of cooling liquid, can change the position of the tip dynamically. This can be limited by making a stiff construction in which the tip is connected to the electrodes, while the cooling is flexibly connected to the tip.

Although no practical solutions have been reported for a gas field ion source, three different configurations of the basic source of a liquid metal ion source are known. Figure 5.13 shows these sources. Both the hairpin (Swanson, 1979) and the ribbon heater or

Hughes type (Wang, 1981) are directly heated sources in which the source material is maintained in the liquid phase by the passage of a heating current through the body of the source itself. This makes the source suitable for materials with a high melting temperature. In the Culham type (Prewett, 1981) (Prewett, 1985) a larger more substantial reservoir is employed and the source temperature is maintained by the use of a separate resistive heater assembly. The heater filament is not in contact with the liquid metal or alloy. This needle-in-capillary source type is mostly used for materials like gallium, which has a melting temperature of only 26 °C. The actual source module can be operated with a hairpin and a needle-in-capillary.

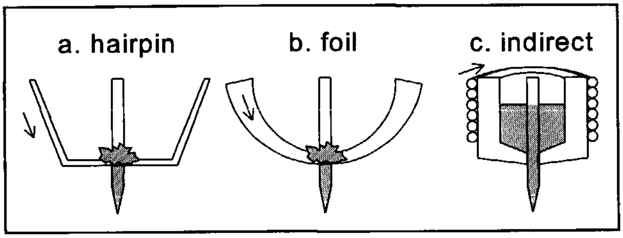

Fig. 5.13. *Three different forms of a liquid metal ion source: (a.) hairpin filament source, (b.) Hughes type and (c.) needle-in-capillary or Culham type.*

5.4. Condenser optics

Between the source and the objective lens some demagnifying power is necessary in "the Fancier" to reach the required resolution of the ion beam at the specimen. This demagnifying power can be delivered by condenser lenses. It is concluded in paragraph 4.3 that two condenser lenses are needed if a minimum focal length of these lenses of 10 mm (see table 4.2) can be reached.

These two lenses will be positioned in front of the energy filtering system. However it is concluded that one of the condenser lenses has to be positioned in the microscope column if the construction is too sensitive for vibrations. Therefore some attention will be paid to the design of a condenser lens for the 30 keV ion beam that has to fit within the linertube of the microscope with inner diameter of 10 mm. For the ion beam magnetic lenses are normally too weak (see also chapter 7), so two types of electrostatic condenser lenses will be discussed: quadrupole lenses and rotationally symmetric lenses.

The general solution of the Laplace equation in cylindrical coordinates is described as

$$V_n(r,\phi,z)=\sum_{m=0}^{\infty}\frac{(-1)^m.n!.2^n}{m!.(n+m)!.a^n}.\left(\frac{r}{2}\right)^{n+2m}.\left(\frac{d^{2k}V_a(z)}{dz^{2k}}.\cos(n.\phi)\right) \qquad (5.20)$$

$V_n(r,\phi,z)$= potential at a position r, ϕ, z
n= order of the field
$V_a(z)$= distribution along the optical axis of the potential at a radius a from the optical axis, see figure 5.14

For simplification the sin-terms are disregarded as they would have equal effect but rotated over 90 degrees.

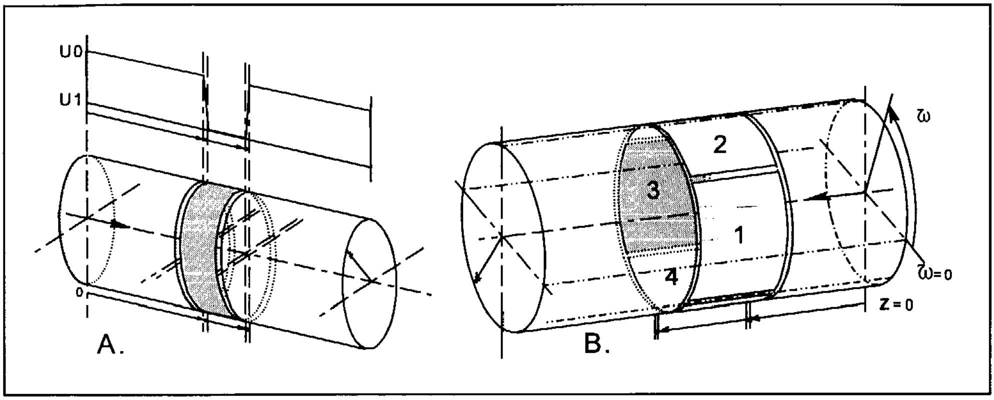

Fig. 5.14. *Two types of electrostatic lenses (a) rotational symmetric lens and (b) quadrupole lens with the potential distribution $V_a(z)$.*

Only the even numbers of the order of the field are of interest for a pure lens effect as the odd numbers would give rise to unwanted deflection effects. Therefore the first potential distribution of interest are n=0 (rotational symmetric lens effect) and n=2 (quadrupole lens effect). Near the optical axis of the system the lower powers of r give a satisfactory description

$$\begin{aligned} V_0(r,\phi,z) &= V_a(z)-\frac{r^2}{4}.\frac{d^2V_a(z)}{dz^2}+O(r^4) \\ V_2(r,\phi,z) &= \frac{r^2}{a^2}.V_a(z).\cos(2.\phi)+O(r^4) \\ V_2(x,y,z) &= \frac{x^2-y^2}{a^2}.V_a(z) \end{aligned} \qquad (5.21)$$

In an electrostatic field it is the field strength E, the derivative of the potential distribution, which acts on the ions. The acting force is q.E, where q is the charge of the ions. Therefore the ray equation of the ion beam in the electrostatic field can be written as

$$\frac{d^2r}{dz^2}=\frac{1}{2.U_0}.\left[1+\left(\frac{dr}{dz}\right)^2\right].\left[\frac{dV}{dr}-\frac{dr}{dz}.\frac{dV}{dz}\right] \tag{5.22}$$

In the assumption dr/dz<<1 the paraxial ray equation is derived. This means for a rotational symmetric lens and the quadrupole lens respectively

$$\begin{gathered}\frac{d^2r}{dz^2}=\frac{-q}{2.U_0}.\left(\frac{r}{2}.\frac{d^2V_a(z)}{dz^2}+\frac{dV_a(z)}{dz}\right)\\ \frac{d^2x}{dz^2}=\frac{x.q}{a^2.U_0}.V_a(z)\ ,\quad \frac{d^2y}{dz^2}=\frac{-y.q}{a^2.U_o}.V_a(z)\end{gathered} \tag{5.23}$$

Two important conclusions can be drawn from this equation. Firstly, the focusing action of a rotationally symmetric lens does not depend on the electrostatic field but only on its variations along the optical path. Secondly, the focusing action of a quadrupole lens is opposite in two perpendicular directions. This means that the ion beam is focused in one direction (y-direction) while it is defocused in the other direction (x-direction) in equation (5.23)

$$\begin{gathered}x=A.\cosh\left(\sqrt{\frac{q.V_a}{U_0}.\frac{z}{a}}\right)+B.\sinh\left(\sqrt{\frac{q.V_a}{U_0}.\frac{z}{a}}\right)\\ y=C.\cos\left(\sqrt{\frac{q.V_a}{U_0}.\frac{z}{a}}\right)+D.\sin\left(\sqrt{\frac{q.V_a}{U_0}.\frac{z}{a}}\right)\end{gathered} \tag{5.24}$$

This means that several quadrupoles are needed to have a real lens action. (Regenstreif, 1967). Table 5.2 summarizes the focusing effect of these quadrupole sets.

It is clear from this table that at least a full triplet is needed if stigmatic focusing with free focal length is required. However in that case a strong lens can be created with relatively small excitation on the electrodes, see figure 5.15. The excitation of the three quadrupoles are respectively 200 V, 235 V and 400 V. Particles on the x-axis at a distance from the optical axis feel the influence of a diverging, converging and diverging field while particles on the y-axis at a distance from the optical axis feel the influence of a converging, diverging and converging field. The resulting focal length is 60 mm.

Table 5.2. *Properties of a set of quadrupoles. The set consists of 1, 2, 3 or 4 quadrupoles with equal radius and length. For different degrees of freedom in the excitation the effect on focal length and principle plane is given. $\exists$= there is, $\forall$= for every, f= focal length, z_H= position principle plane, M= magnification*

set	V1	V2	V3	V4	focal length	principle plane	note
singlet	V1	-	-	-	$\exists V1: f_x=-f_y$	$z_{Hx} \neq z_{Hy}$	not stigmatic
doublet	V1	V1	-	-	$f_x=f_y$	$z_{Hx} \neq z_{Hy}$	not stigmatic
	V1	V2	-	-	$\forall V1: \exists V2: f_x=f_y$	$\exists(V1,V2): z_{Hx}=z_{Hy}$	stigmatic fixed f fixed M
triplet	V1	V2	V1	-	$\forall V1: \exists V2: f_x=f_y$	$\exists(V1,V2): z_{Hx}=z_{Hy}$	stigmatic fixed f fixed M
	V1	V2	V3	-	$\forall(V1,V2): \exists V3: f_x=f_y$	$\forall V1: \exists(V2,V3): z_{Hx}=z_{Hy}$	stigmatic free f fixed M
quad.	V1	V2	V2	V1	$\forall V1: \exists V2: f_x=f_y$	$\exists(V1,V2): z_{Hx}=z_{Hy}$	stigmatic fixed f fixed M
	V1	V2	V3	V1	$\forall(V1,V2): \exists V3: f_x=f_y$	$\forall V1: \exists(V2,V3): z_{Hx}=z_{Hy}$	stigmatic free f fixed M
	V1	V2	V3	V4	$\forall(V1,V2,V3): \exists V4: f_x=f_y$	$\forall(V1,V2): \exists(V3,V4): z_{Hx}=z_{Hy}$	stigmatic free f free M

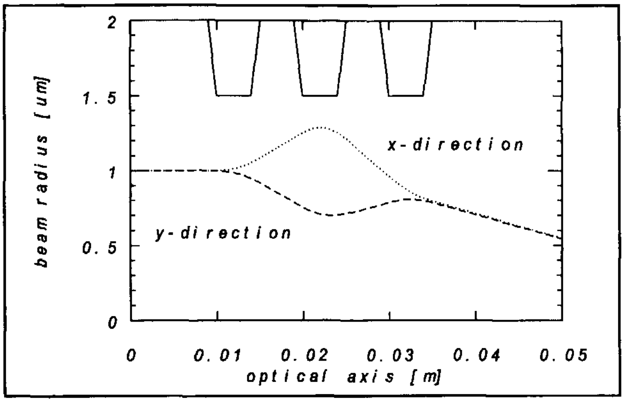

Fig. 5.15. *The focal length of a triplet of quadrupoles as a function of the excitation.*

Although this is a large focal length it can be concluded that the excitation of the quadrupole lens is relatively small compared to that needed for a rotationally symmetric lens. However for a real lens with free focal length and free magnification a combination of four quadrupoles is needed.

A frequently used version of a rotationally symmetric lens is a unipotential Einzel lens. It consists of three electrodes: the outer electrodes are at ground potential while the middle electrode is at high tension. The focal length of such a lens can be calculated from equation (5.19) with $k=k_1=k_2^{-1}$, it is given by

$$f=\frac{16}{3}.\frac{k^{5/4}}{(k-1)^2.(\sqrt{k}+1)}.d\ ,\quad k=\frac{U_l}{U_0} \tag{5.25}$$

U_0= potential of the ion beam outside the lens
U_l= potential of the ion beam in the lens
d= bore of the electrode

Short focal lengths can be reached for k<<1 or k>>1, which is called a decelerating and an accelerating lens (Harting, 1976). Although the focal length can be the same in the two configurations there are some differences. The most important is that an accelerating lens needs a potential on the middle electrode of at least several times the beam energy, so in this case at least -120 kV for a 30 keV ion beam. A decelerating lens functions optimal for a potential on the middle electrode close to the beam energy, e.g. 28 kV for 30 keV ion beam. Therefore it can be concluded that a decelerating lens is more of practical use, since the potential to be applied is lower. However there are specific applications where accelerating rotational symmetric lenses are beneficial.

An intermediate summary gives two lens types that can give the needed short focal length (10 mm) for a 30 keV ion beam: a quadruplet quadrupole lens and a decelerating rotational symmetric Einzel lens. Both lenses have specific advantageous. As lower excitations are required in a quadrupole lens this lens can easier be installed at places where space is a problem. This is the case if a condenser lens has to be installed in the linertube of the microscope. It will be very hard to insulate a typical potential of 30 kV needed for the Einzel lens at this position.

If space is not the most important limitation, the Einzel lens is more beneficial. Only one excitation is needed while a quadrupole needs at least eight excitations. It is assumed that the aberration contribution of the condenser system are not important in defining the resolution of the ion beam probe at the specimen. This is because these contributions are demagnified by the objective lens.

The decision is made to realize a decelerating Einzel lens as the condenser lenses are positioned between the source and the energy filtering system. If electrostatic lenses in the microscope are required this decision has to be reconsidered.

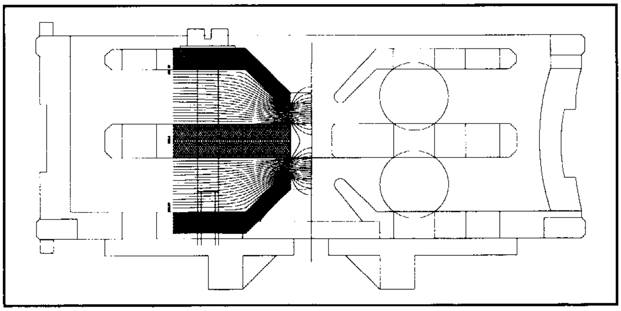

Fig. 5.16. *Schematic drawing and equipotential lines of the 30 kV condenser.*

Figure 5.16 shows the RZ-plot of the actual lens used, after a design of Slingerland (Slingerland, 1988). Ions move on or near the axis while the lens electrodes are assumed to be rotationally symmetric. The lens is merely designed to withstand 30 kV which is the maximum deceleration needed in this lens. A very useful insulator is the ceramic ball that can be used to position the electrodes with respect to each other as well. If the diameter of the hole in which the ball rests is less than the radius of the ball, the field distribution around the ball prevents electron multiplication over its surface. An Al_2O_3 ball of 10 mm diameter can withstand voltage differences of 30 kV reliable (Slingerland, 1988).

The performance of the Einzel lens is calculated by the computer program Electrostatic Lens Design (ELD) (Lencová, 1992). The minimal focusing distance is 5.47 mm. The middle electrode potential, relative to beam energy, needed for other focal lengths is depicted in figure 5.17. The chromatic aberration coefficient is linear with the focal length apart from some offset. The C_c value as a function of the focal length f [mm] can be interpolated above 9 mm by

$$C_c(f) = 16.4 + 2.36\, f \quad [mm] \tag{5.26}$$

Below 9 mm C_c is about 36 mm, as can be seen in figure 5.17. Here the spherical aberration coefficient C_s is depicted too. It is approximated by the following third order curve fitted equation (f>6mm)

$$C_s(f) = 23.6 - 2.65\, f + 0.333\, f^2 + 0.0647\, f^3 \quad [mm] \tag{5.27}$$

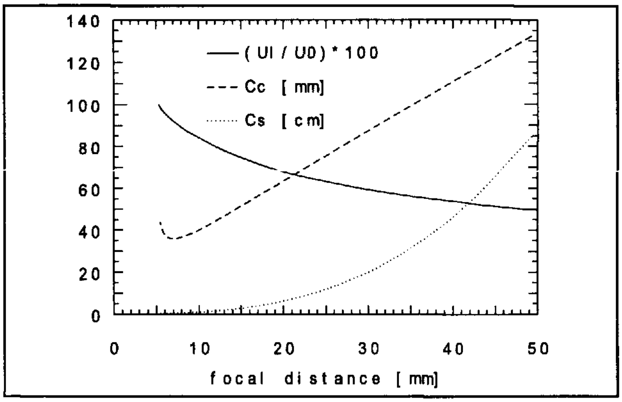

Fig. 5.17. *Properties of the condenser lens (a.) lens voltage relative to beam energy, (b.) chromatic [mm] and (c.) spherical [cm] aberration coefficient.*

The coefficients are calculated at infinite magnification. It can be concluded from the simulation that at short focal length the separation between the principle planes is about 5 mm while it is less than 1 mm for focal lengths of 17 mm (Adriaanse, 1987). This is in agreement with the assumption that a lens can be treated as thin lens when the bore is smaller than the focal length. The electrodes of the 30 kV lens have a 3 mm bore radius, which is less than the focal distance in the latter case.

The assumption has been made that these condenser lenses do not contribute to the aberration contribution in the final lens significantly. It turns out that this assumption is valid for the above mentioned data of the aberration coefficients.

5.5. Summary

Different ion sources are necessary for the different fabrication techniques. For sputtering and beam induced pattern generation an Ar Gas Field Ion Source is chosen. These fabrication techniques make use of the energy of the ions but the ion species is not of direct importance. Inert gas ions are used to prevent deterioration of the electrical properties of the specimen by the implanted ions. In a Gas Field Ion Source the gas is introduced locally near the sharp tip of a needle that is at a high electric field. The inert gas atom is ionized when an electron tunnels from the atom to the tip. This is only possible if the gas atom is only a few nanometers away from the tip. The emission current can be improved by cooling the tip to a desired temperature. At this temperature the adsorbed gas atoms start hopping on the needle because of thermal accommodation. During every hop there is a chance for ionization because the atoms come into the ionization zone. Above this temperature the thermal accommodation is too weak to start hopping, while at a lower temperature the height of the hops decreases until the atoms only migrate over the surface without being ionized.

First experiments in a test setup show that the brightness of a Gas Field Ion Source is high enough for "the Fancier". Sources with comparable brightness but a wider energy distribution are Liquid Metal Ion Sources. In this source the material to be ionized in is the liquid phase on the needle. By thermal activation an ion overcomes the surface barrier. As the material to be ionized only has to be heated to its melting temperature, a wider range of ions can be emitted, like Au for direct deposition of metal lines and B and As for implantation of dopant material in Si.

These elements are part of an alloy (AuSi, PdBAs) to prevent operating of the ion source at a very high temperature. It would induce unwanted chemical reactions with the tip. An important parameter for stable emission from a Liquid Metal Ion Source is good wetting of the needle with the overlayer, the material to be ionized. It is realized in a separate Ultra High Vacuum system where the needle and the overlayer material are cleaned before they are brought in contact with each other.

Both source types need source extraction optics. This can be a tetrode sytem where the emission current and focal length can be set independently. In the design an optimum has to be found between lens aberrations (they can be of importance as the source lens is magnifying), alignment of the electrodes (the particles are emitted with a large opening angle and therefore they are far off-axis), Coulomb interactions (the current density is very high in the source region) and aperture erosion (the current is large in the source region).

Behind the source optics, the condenser optics are positioned to demagnify the beam. Two types of lenses are considered: rotationally symmetric and quadrupole lenses. The advantage of a quadrupole lens is its lower excitation energy. But for a lens which gives a stigmatic image with arbitrary focal length and magnification four quadrupoles have to be combined. The conclusion is drawn that a rotationally symmetric lens is preferable if there is enough space available. The designed condenser lens has a minimal focal length of 6 mm. Its aberration coefficients are small enough to make the assumption valid that they can be disregarded compared to the aberration contributions of the objective lens.

References

Adriaanse, J.P., *Design of a control program for an ion beam pattern generator*, thesis, Delft 1987

Bauer, M.S.H., *Argon Gas Field Ion Source for the Fancier*, master thesis, Delft, 1997

Beckman, J.C., T.H.P. Chang, A. Wagner and R.T.W. Pease, *Energy spread in liquid metal ion sources at low currents*, Journal of Vacuum Science and Technology B14(6) , 1996, pp. 3911-3915

Bell, A.E., K. Jousten and L.W. Swanson, *High field ion sources*, Review of Scientific Instruments 61(1), 1990, pp. 363-368

Benassayag, G., P.Sudraux and B. Jouffrey, *In situ high voltage TEM observation of an electro-hydro-dynamic (EHD) ion source*, Ultramicroscopy 16, 1985, pp. 1-8

Bhaskar, N.D., C.M. Klimcak and R.P. Freuholz, *Liquid metal ion source for cluster ions of metals and alloy: design and characteristics*, Review of Scientific Instruments 61(1), 1990, pp. 366-368

Bohlander, J.H., H.N. Slingerland, E. Koets and K.D. van der Mast, *An achromatic massfilter employing permanent magnets for the Delft Ion Beam Pattern Generator*, Microelectronics Engineering 7(1), 1987, pp. 6189

Börret, R, K. Jousten, K. Böhringer and S. Kalbitzer, *Long time current stability of a gas field ion source with supertip*, Journal of Physics D 21, 1988, pp. 1835-1837

Bozack, M.J. e.a., *Materials considerations in LMIS development*, Journal de Physique 47, 1986, pp. C2.95-C2.100

Clark, W.M. and L.W. Swanson, *Long-lifetime, reliable LMIS for Boron, Arsenic and Phosphorus*, Journal of Vacuum Science and Technology B 5(1), 1987, pp. 197-202

Filand, M.A. and E.I. Simenosa, *Handbook of rare metals; trace elements and light elements*, Metal Institute USSR, London, 1968

Fink, H.W., *Point source for ions and electrons*, Phys. Scr. 38, 1988, pp. 260-263

Forbes, R.G. and G.L.R. Mair, *Arguments about emitter shape for a liquid-metal-field-ion emission source*, Journal of Applied Physics D 15, 1982, pp. L153-L158

Forbes, R.G. and N.N. Ljepojevic, *Liquid-metal ion source theory: electro-hydrodynamics and emitter shape*, Surface Science 266, 1992, pp. 170-175

Foster, L.M., in: C.A. Hample, *The encyclopedia of chemical elements*, Reinhord Book Cooperation, New York, 1968, pp. 231

Fowler, R.H. and L. Nordheim, *Electron Emission in Intense Electric Fields* ,Proceedings of the Royal Society London A119, 1928, pp 173-181

Fukuda, H., *Characteristics of liquid metal ion source for Boron and Arsenic*, Journal de Physique C 6, 1987, pp. C6.153-C6.158

Fransen, M.J., *Field emission particle sources*, master thesis, Delft, 1994

Gomer, R., *Field emission and field ionization*, Harvard monographs in Applied Science 9, Harvard University Press, Cambridge, 1961

Gomer, R., *On the mechanism of liquid metal electron and ion sources*, Applied Physics 19, 1979, pp. 365-375

Harting, E. and R.F. Read, *Electrostatic lenses*, Elsevier, Amsterdam, 1976

Jousten, K., K. Böhringer, R. Börret and S. Kalbitzer, *Growth and current charactersitics of stable protrusions on tungsten field ion emitters*, Untramicroscopy 26, 1988, pp. 301-312

Kang, N.K. and L.W. Swanson, *Computer simulation of LMIS optics*, Applied Physics A30, 1989, pp. 95-104

Kingham, D.R. and L.W. Swanson, *Shape of a LMIS: a dynamic model including fluid flow and space charge effects*, Applied Physics A 34, 1984, pp. 123-132

Kohlmann, K.T., M. Thiemann and W.H. Brünger, *E-beam induced X-ray mask repair* *with optimized gas nozzle geometry*, Microelectronic Engineering 13, 1991, pp. 279-282

Komuro, M., e.a., *Measurements of virtual cross-over in liquid gallium ion source*, Applied Physics Letters 42(10), 1983, pp. 908-910

Lencová, B. and G. Wisselink, *Electrostatic Lens Design program package*, licensed by Delft Particle Optics Foundation, 1992

Mair, G.L.R., *Emission form liquid metal ion sources*, Nuclear Instruments and Methods 172, 1980, pp. 567-576

Mair, G.L.R. and A. von Engel, *Mass transport in liquid Gallium ion beam sources*, Journal of Physics D: Applied Physics14, 1981, pp. 1721-1728

Mair, G.L.R, *Theoretical determination of current-voltage curves for liquid metal ion sources*, Journal of Physics D: Applied Physics 17, 1984, pp. 2323-2330

Mair, G.L.R. and T. Mulvey, *Some aspects of liquid metal ion sources*, Journal of Microscopy 142, 1986, pp. 191-200

Mast, K.D. van der, *Programs for the calculation of potential fields of systems with rotational symmetry and the properties of electrostatic lenses*, Delft, 1988

Miller, S.C. and R.H. Good, *A WKB-type approximation to the Schrödinger equation*, Physics Review 91, 1953, pp 174-179

Modinos, A., *Field, Thermionic and Secondary Electron Emission Spectroscopy*, Plenum Press, New York and London, 1984

Mühle, R., *High-field ion sources and applications*, Review of Scientific Instruments 63(5), 1992, pp. 3040-3049

Müller, E.W., Journal of Applied Physics 28(1), 1957

Oostrom, A.G.J. van, *Validity of the Fowler-Nordheim model for field electron emission*, Dissertation, Unversity of Amsterdam, 1965

Prewett, P.D., D.K. Jefferies and T.D. Cockhill, *Liquid metal source of gold ions*, Review of Scientific Instruments 52, 1981, pp. 562-566

Prewett, P.D. and E.M. Kellogg, *Liquid metal ion sources for FIB microfabrication systems- Recent advances*, Nuclear Instruments and Methods B6, 1985, pp. 135-142

Regenstreif, E., *Focusing with quadrupoles, doublets and triplets*, in: A. Septier, *Focusing of charged particles Volume 1*, Academic Press, Orlando, 1967, pp. 353-410

Rieck, G.D., *Tungsten and its compounds*, Pergamon Press, Oxford, 1967

Sande, E. van de, *Air entrainment by plunging water jets*, Delft, 1974

Slingerland, H.N., *Optimization of a chromatically limited ion microprobe*, Microelectronic Engineering 2, 1984, pp. 219-226

Slingerland, H.N., *A fast ion beam pattern generator*, thesis, Wibro, Helmond, 1988

Swanson, L.W., G.A. Schwind, E.A. Bell and J.E. Brady, *Emission characteristics of gallium and bismuth liquid metal field ion sources*, Journal of Vacuum Science and Technology 16(6), 1979, pp. 1864-1867

Swanson, L.W., *Liquid Metal Ion Sources: machanism and applications*, Nuclear Instruments and Methods 218, 1983, pp 347-353

Tabor, D.,*Gases, liquids and solids*, Cambridge university press, Cambridge, 1979, pp. 253

Taylor, G., *Disintegration of water drops in an electric field*, Proceedings of the Royal Society A 280, 1964, pp. 383-397

Thompson, S.P. and P.D. Prewett, *The dynamics of liquid Metal Ion Sources*, Journal of Physics D: Applied Physics 17, 1984, pp. 2305-2321

Umemura, K. e.a., *Boron and phosphorus ion emissions from a Cu-P-Pt-B LMIS*, Japanese Journal of Applied Physics 25, 1986, pp. L885-887

Umemura K. e.a., *Development of an arsenic Liquid Metal Ion Source*, Nuclear Instruments and Methods in Physics Research B 37/38, 1988, pp. 208-211

Vladimirov, V.V., V.E. Badan and V.N. Gorshkov, *Microdroplet emission and instabilities in liquid-metal ion sources*, Surface Science 266, 1992, pp. 185-190

Vijgen, L.J., *Coulomb Interactions in Focused Ion Beam Systems*, thesis, DUP, Delft, 1994

Wagner, A., T. Venkatesan, P.M. Petroff and D. Barr, *Droplet emission in liquid metal ion sources*, Journal of Vacuum Science and Technology 19(4), 1981, pp. 1186-1189

Wang, V. e.a., *A mass-seperating focused-ion-beam system for maskless ion implantation,* Journal of Vacuum Science and Technology 19(4), 1981, pp. 1158-1163

Zangwill, A., *Physics at surfaces*, Cambridge University Press, Cambridge, 1990, pp. 428-432

Ziegler, J.F., J.P. Biersack and U. Littmark, *The stopping and range of ions in solids*, Pergamon Press, 1985

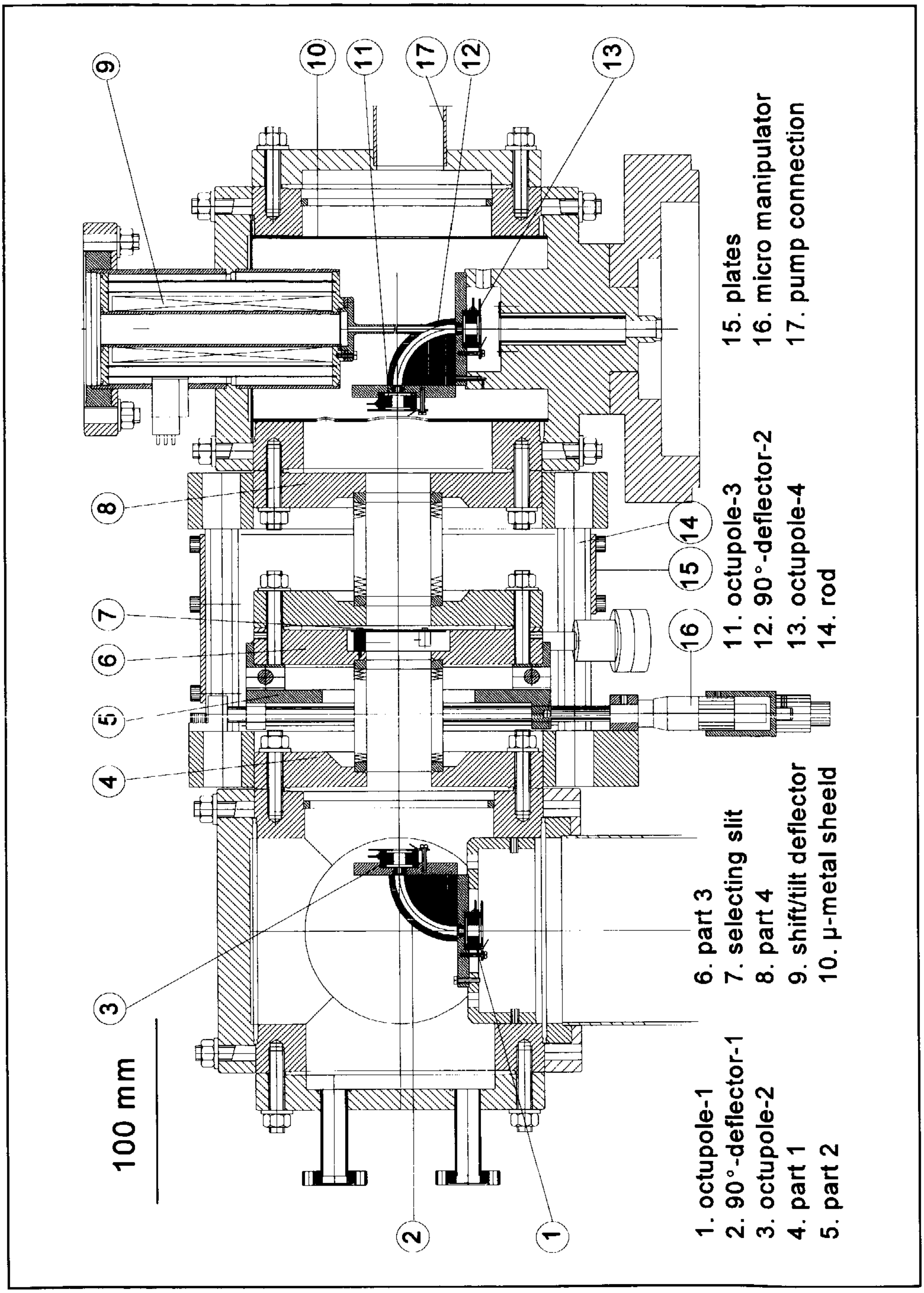

Fig. 6.1. *The energy filtering system.*

6. The energy filtering system

Introduction

The horizontal column of “the Fancier” is a transport section meaning that the image near the entrance plane (at the end of the condenser system) and exit plane (at the beginning of the probe forming system inside the microscope) are in principle just the same except for the energy spread that has been limited. Figure 6.1 shows the mechanical setup of this column. It consists of a combination of two 90°-deflectors. This combination is achromatic meaning that the position of the ions in the image at the exit plane is not influenced by their energy. But the image between the deflectors is chromatic, so the ions with different energies are separated in this plane. Therefore a slit is positioned here to stop the particles that have an energy which is too far from the mean energy of the beam.

It can also be seen in figure 6.1 that the second deflector has a function in the electron beam system. It has to pass the electron beam with minimal disturbance of this beam. If the deflector excitation can be switched off this is less a problem, than in case of in-situ observation. Because here both beams have to be transferred to the specimen meaning that the electron beam has to pass an excited 90°-deflector.

The design of the energy dispersive element, the 90°-deflector, and the energy selecting element, the slit, will be discussed separately.

6.1. The energy dispersive element

Electrostatic and magnetic prisms have proven to be useful tools for the deflection and the analysis of charged particles as in an energy analyzer (Rose, 1992) (Ross, 1994) or in combination in a mass spectrometer because the deflecting angle is energy and mass dependent. However they can also be used to bring two beams on the same optical axis (Seybel, 1995) or to separate two beams that are on the same axis (Bleeker, 1991). The basic form of a prism consists of two plates, in between which the particles move. Large deflection angles are easily obtained by, for example, cylindrical shaped electrodes in case of an electrostatic prism. The particles move on parabolic trajectories if the electrodes of this electrostatic deflector are spherical The electrostatic and magnetic field strength on the middle surface between the electrodes must be adjusted to a value that enables particles to move on the circular main path between the electrodes having a radius R_0.

$$\textit{electrostatic} \quad R_o = \frac{2.U}{E}, \quad E = \frac{V}{S} \tag{6.1}$$

$$\textit{magnetic} \quad R_o = \frac{\sqrt{2.\frac{M}{q}.U}}{B}, \quad B = \frac{\mu_0.N.I}{S} \tag{6.2}$$

R_o= radius of curvature of the central beam
q= charge of the particle
M= mass of the particle
U= energy of the particle
S= gapwidth between the electrodes
V= potential difference between the electrodes
μ_o= magnetic permeability
NI= excitation of the coil

To realize a specific radius of curvature it can be calculated which type of field is beneficial for practical reasons. A figure of merit is now the ratio of the electrostatic and magnetic excitation.

$$\frac{2.U_o.S}{q.V} = \frac{\sqrt{2.m.U_o}.S}{q.\mu_o.N.I} \Rightarrow \frac{V}{N.I} = \mu_o.\sqrt{\frac{2.U_o}{m}} \tag{6.3}$$

The assumption is made that a smaller number for this figure of merit indicates that the electrostatic excitation (=V) can be realized easier than the magnetic excitation (=NI), although there is not a linear relation. In the case of a small radius of the circular main path electrostatic fields can be applied relatively easier as a result of saturation of the magnetic field. Also for a large radius there is a difference, here the magnetic fields can be applied relatively easier because of flash-over.

For 30 keV helium and gallium ions this relation is 1.10 and 4.59 respectively while it is 779 for 120 keV electrons. This results in the following conclusion:

> Both ion species can be deflected by an electrostatic deflector much easier than electrons. However, the perturbation of the electron beam by the deflector has to be small: this beam has to go straight through. It influences the electron beam much less than a magnetic field would do, while it is effective for ions.

Now that the choice is made to realize an electrostatic deflector, the question has to be answered which shape the electrodes must have. In general there are four different types of electrostatic deflectors, see figure 6.2. They differ in the radii of the electrodes in the deflection direction and perpendicular to that direction.

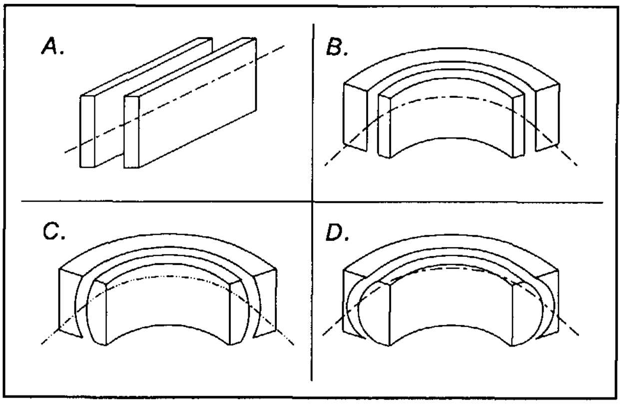

Fig. 6.2. *Four types of an electrostatic deflector.*

1. flat plate electrodes
   properties: only deflection over small angles
2. cylindrical electrodes
   properties: single focusing; only imaging in one direction
3. spherical electrodes
   properties: double focusing; real imaging
4. toroidal electrodes with different curvature in perpendicular directions
   properties: double focusing with second order correction if the inner and outer electrodes have different radii of curvature

The deflector has to be used for deflection over 90 degrees. This means that the flat plate deflector cannot be used: it does not allow such large deflection angles. The three types left differ in the shape of the image. A cylindrical and a toroidal deflector have different focal lengths in each perpendicular direction meaning that the image position is different in two perpendicular directions along the optical axis. For a cylindrical deflector this is a disadvantage: it is impossible to make a real image of the object in front of the deflector. For a toroidal deflector with different radii of curvature for the two electrodes this can be an advantage: it is possible to correct second order aberrations of the deflector or of elements elsewhere in the system. However it is assumed that the second order aberrations are not of main importance. Therefore a toroidal deflector will not be used either. This multipole stigmator can also be used to make a cylindrical deflector double focusing meaning that a real image is possible at the image plane. Figure 6.3 depicts this optical scheme. This double focusing is a standard property of an electrostatic deflector with spherical electrodes. Therefore two configurations will be worked out in greater detail: a cylindrical deflector with a multipole stigmator and a spherical deflector.

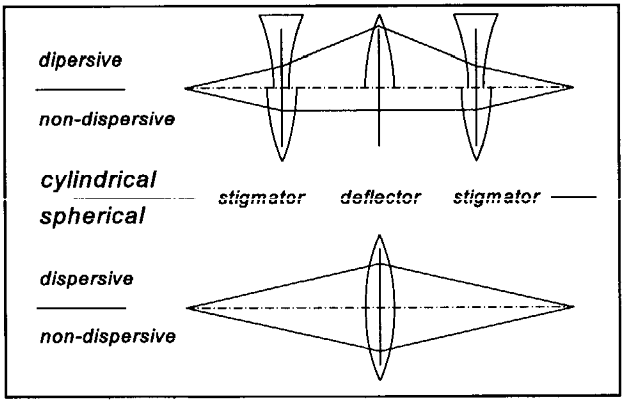

Fig. 6.3. *Double focusing systems (a) cylindrical deflector with multipole stigmator, (b) spherical deflector.*

Figure 6.4 shows the realization of the deflector at the microscope side schematically, while in the other deflector the vertical exit for the electrons is missing. Here are also the parameters indicated which have to be dimensioned. The subjects will be discussed which are, wanted or unwanted, effects of the 90°-deflector. At the end they will be combined to come to a decision on the electrode shape and to come to a practical design.

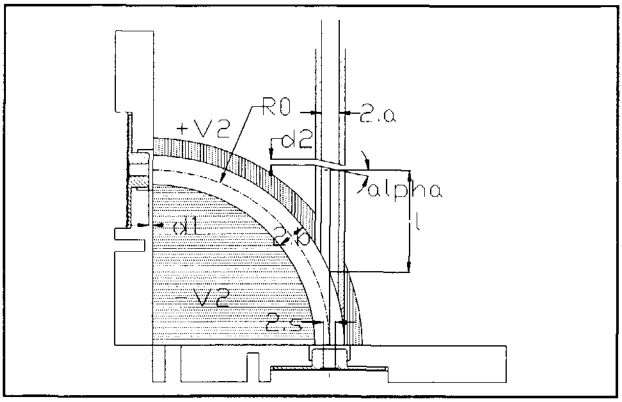

Fig. 6.4. *Schematic drawing of the 90°-deflector at the microscope side.*

1. Deflection of ions over 90 degrees

   This is the main aim of the deflectors. The electrostatic field strength on the middle equipotential surface must be adjusted to a value that enables ions of energy U_0 to move on the mentioned circular main path.

$$R_0 = \frac{2.U_0.S}{2.V_2} \tag{6.4}$$

   R_0= radius of the main path of the deflector
   U_0= mean energy of the ions
   S= distance between the electrodes
   V_2= potential of an electrode of the deflector

   The equation expresses the fact that the centrifugal force is just compensated by the electrostatic force. The charge of the ions is positive. Therefore the outer electrode is at $+V_2$, retarding the ions, while the inner electrode is at $-V_2$, attracting the ions. This means that the potential difference between the electrodes is $2V_2$ and that the circular main path is at the electrical symmetry plane.

2. Focusing the ions

   An electrostatic 90°-deflector will act as a lens. The transfer from object to image can be written for cylindrical (equation (6.5)) and spherical electrodes (equation (6.6)) as (Wollnik, 1967) *cylindrical*

$$\begin{pmatrix} x_i \\ \alpha_i \end{pmatrix} = \begin{pmatrix} 1 & l_2 \\ 0 & 1 \end{pmatrix} . \begin{pmatrix} C_x & \frac{1}{g}.S_x \\ g.S_x & C_x \end{pmatrix} . \begin{pmatrix} h_2 & \frac{R_0}{\sqrt{2}}.h_1 \\ -\frac{\sqrt{2}}{R_0}.h_1 & h_2 \end{pmatrix} . \begin{pmatrix} 1 & l_1 \\ 0 & 1 \end{pmatrix} . \begin{pmatrix} x_o \\ \alpha_o \end{pmatrix}$$

$$\begin{pmatrix} y_i \\ \beta_i \end{pmatrix} = \begin{pmatrix} 1 & l_2 \\ 0 & 1 \end{pmatrix} . \begin{pmatrix} C_y & \frac{1}{g}.S_y \\ -g.S_y & C_y \end{pmatrix} . \begin{pmatrix} 1 & R_0 \\ 0 & 1 \end{pmatrix} . \begin{pmatrix} 1 & l_1 \\ 0 & 1 \end{pmatrix} . \begin{pmatrix} y_o \\ \beta_o \end{pmatrix} \qquad \textbf{(6.5)}$$

$$g = \frac{2}{d}.\sqrt{\frac{V_1}{U}}$$

$$S_x = \sinh(g.l_3),\ C_x = \cosh(g.l_3),\ S_y = \sin(g.l_3),\ C_y = \cos(g.l_3)$$

$$h_1 = \sin\left(\frac{\pi}{\sqrt{2}}\right),\quad h_2 = \cos\left(\frac{\pi}{\sqrt{2}}\right)$$

spherical

$$\begin{pmatrix} x_i \\ \alpha_i \end{pmatrix} = \begin{pmatrix} 1 & l_2 \\ 0 & 1 \end{pmatrix} . \begin{pmatrix} 0 & R_0 \\ -\frac{1}{R_0} & 0 \end{pmatrix} . \begin{pmatrix} 1 & l_1 \\ 0 & 1 \end{pmatrix} . \begin{pmatrix} x_o \\ \alpha_o \end{pmatrix}$$

$$\begin{pmatrix} y_i \\ \beta_i \end{pmatrix} = \begin{pmatrix} 1 & l_2 \\ 0 & 1 \end{pmatrix} . \begin{pmatrix} 0 & R_0 \\ -\frac{1}{R_0} & 0 \end{pmatrix} . \begin{pmatrix} 1 & l_1 \\ 0 & 1 \end{pmatrix} . \begin{pmatrix} y_o \\ \beta_o \end{pmatrix} \qquad \textbf{(6.6)}$$

x_0, y_0= distance from the optical axis in the dispersion direction at the entrance plane
x_i, y_i= distance from the optical axis in the dispersion direction at the exit plane
α_0, β_0= angle with respect to the optical axis in the dispersion direction at the entrance plane
α_i, β_i= angle with respect to the optical axis in the dispersion direction at the exit plane
l_1= distance from the object to the deflector
l_2= distance from the deflector to the image
l_3= length of the quadrupole
d= distance between the poles of the quadrupole
V_1= excitation of the quadrupole
R_0= radius of the main path of the 90°-deflector

The first, practical, problem is to form an image at the slit from the object in front of the 90°-deflectors. The cylindrical deflector can only make an image in one direction, so to form a real image the quadrupole has to be excited too. Only one specific excitation of the quadrupole results in a real image. In general this image does not have equal magnification in the two perpendicular directions. With the spherical deflector a real image can be made without other optical elements, since this deflector is double focusing.

3. Energy dispersion of the ions with a chromatic 90°-deflector

The energy spread of the ions is to large, therefore the bandwidth of energies has to be decreased by stopping ions outside a slit. The position of the ions on the slit depends on their energy and the dispersion of the 90°-deflector. The second function of the 90°-deflector is to filter the energy spread of the ions in a band-pass way. According to Wollnik (Wollnik, 1967) the matrix of the 90°-deflector in equation (6.5) and (6.6) can be extended in the dispersion direction to

$$\textit{cylindrical} \quad \begin{pmatrix} x_i \\ \alpha_i \\ \delta \end{pmatrix} = \begin{pmatrix} h_2 & \frac{R_0}{\sqrt{2}}.h_1 & \frac{R_0}{2}.(1-h_2) \\ -\frac{\sqrt{2}}{R_0}.h_1 & h_2 & \frac{1}{\sqrt{2}}.h_1 \\ 0 & 0 & 1 \end{pmatrix} . \begin{pmatrix} x_o \\ \alpha_o \\ \delta \end{pmatrix} \tag{6.7}$$

$$\textit{spherical} \quad \begin{pmatrix} x_i \\ \alpha_i \\ \delta \end{pmatrix} = \begin{pmatrix} 0 & R_0 & R_0 \\ -\frac{1}{R_0} & 0 & 1 \\ 0 & 0 & 1 \end{pmatrix} . \begin{pmatrix} x_o \\ \alpha_o \\ \delta \end{pmatrix} \tag{6.8}$$

δ= relative energy spread, $\Delta U/U_0$

The dispersion of a spherical deflector at the slit position, which is equal to the image plane is equal to

$$\textit{spherical} \quad \Delta x_{i,d} = (R_0 + l_2).\delta \tag{6.9}$$

Figure 6.5 shows the dispersion as a function of the length of the horizontal column with halfway the energy selecting slit distance from the deflector to the slit. This is calculated for 0.9 eV Full Width at Half Maximum (FWHM) energy spread in a 30 keV beam as was concluded in paragraph 4.3 to give optimum current density in a nanometer probe. It can be concluded from this figure that the cylindrical deflector has about 40% more dispersion than the spherical one.

The energy distribution after the slit for a spherical deflector and a column length of 321.6 mm is depicted in figure 6.6. To obtain a FWHM energy spread of 0.9 eV the slit size is 4.82 μm. The different curves in the upper figure show the distribution for several sizes of the image at the slit. It can be seen that the nice spot condition is obtained if the image size is half the slit size. The nice spot condition is of importance if the image at the energy selecting slit is used directly to make a probe at the specimen. If the nice spot condition is not fulfilled a line spot will result or the energy selection will not function properly. But in "the Fancier" there is a second 90°-deflector that brings all ions back in one probe. The set of two 90°-deflectors is achromatic. Therefore the nice spot condition is not of importance.

The image at the slit is 58.2 nm, this means that an almost uniform distribution results from the Gaussian energy distribution at the source.The Full Width at Half Maximum (FWHM) energy spread is 0.9 eV.

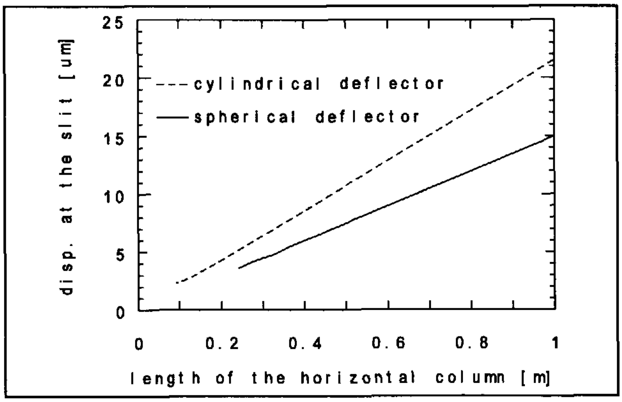

Fig. 6.5. *Dispersion of the 90°-deflector as a function of the length of the horizontal column for 0.9 eV energy spread in an ion beam with 30 keV energy.*

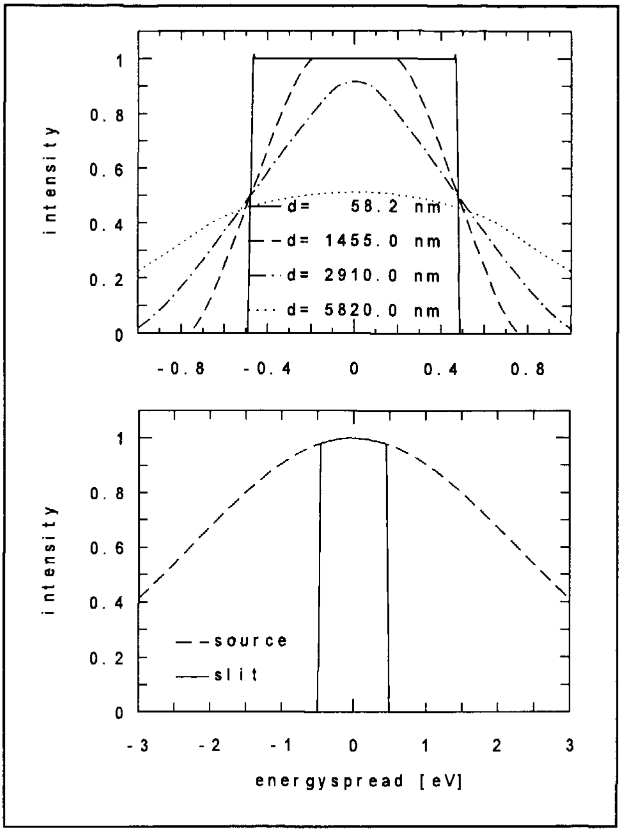

Fig. 6.6. *Energy distributions (a) after the energy filtering slit for different sizes of the image at the slit based on uniform source distribution, (b) of the source and after the slit based on a Gaussian source distribution with 4.5 eV FWHM energy spread.*

4. Rest dispersion of the ions with a chromatic 90°-deflector

It was mentioned before that the combination of two 90°-deflectors can transport the object from the entrance of the horizontal column to the image in the microscope column achromatically. This means that no position dispersion is left here. Unfortunately the angular dispersion is increased by this combination. See figure 6.7. This means that it is possible to form an achromatic image but slight changes in optical settings will bring this angular dispersion to the front. Figure 6.8 shows the rest angular dispersion at the image in the microscope column. It can be concluded from this figure that the cylindrical deflector has about three times more rest dispersion than the spherical one.

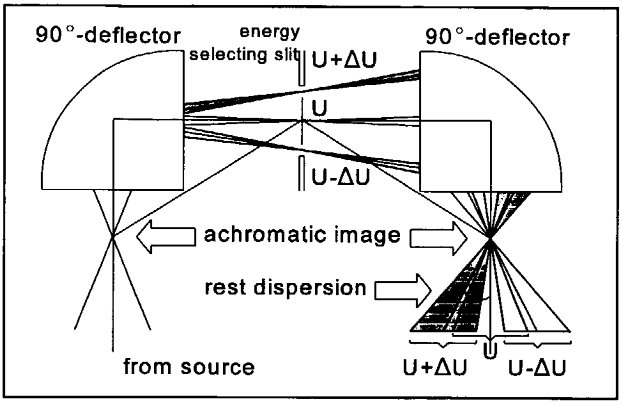

Fig. 6.7. *Rest angular dispersion at the image plane behind the second deflector.*

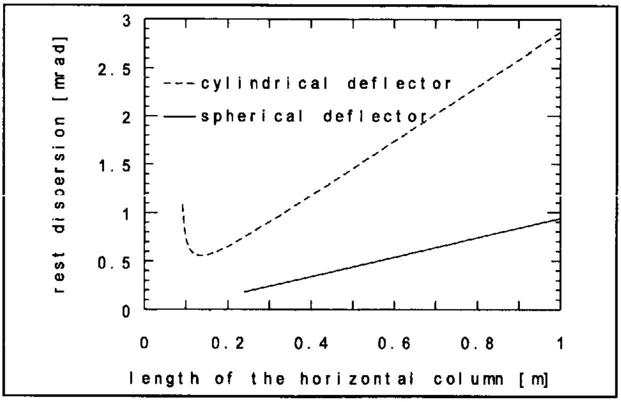

Fig. 6.8. *Rest angular dispersion at the image plane behind the second deflector as a function of the length of the horizontal column for 0.9 eV energy spread in an ion beam with 30 keV energy.*

The rest angular dispersion can be a serious problem if there is an aperture behind the second 90°-deflector (the cond.-2 aperture in figure 4.14). The purpose of this aperture is to limit the opening angle at the specimen. As there is now a relation between the energy of the ions and their angle with respect to the optical axis, this aperture will also act as energy selecting aperture. However it stops ions that were transferred through the real energy selecting slit between the 90°-deflectors. So it limits the probe current unnecessarily.

This effect of the cond.-2 aperture can be corrected with a quadrupole at the image plane behind the second 90°-deflector. This quadrupole does not influence the position of the ions but it influences their angle. So it can be used to pass more ions through the aperture by concentrating them in the dispersive direction. But the half opening angle of the beam is 1.69 mrad, so it is only a serious problem if the rest dispersion is larger.

5. Magnification of the ion probe at the energy selecting slit

The paraxial size of the image at the entrance and exit slit of the horizontal column is about 13 nm, see table 4.4. This image is magnified to the slit. For a spherical deflector the radial magnification will be

$$\textit{spherical} \quad M = \sqrt{\frac{l_2}{l_1}} \qquad \textbf{(6.10)}$$

Figure 6.9 shows the magnification of the 90°-deflector as a function of the distance from the deflector to the slit. It can be concluded from this figure that the magnification of the cylindrical deflector is about two times larger than of the spherical one. Since the best distribution after filtering is a uniform one, the smallest spot at the energy selecting slit is preferable.

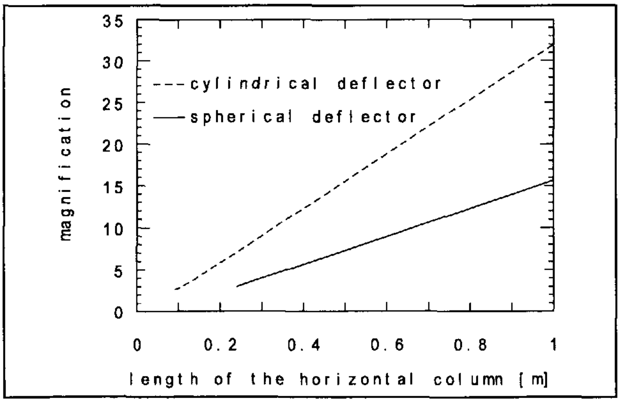

Fig. 6.9. *Magnification of the 90°-deflector as a function of the length of the horizontal column.*

6. Second order aberrations of the ion image

The deflector is not circular symmetric seen from the optical axis, therefore the first aberrations that will come in are proportional to the second order of position and/or angle. The transfer from entrance to exit plane including these aberrations is given

$$\begin{pmatrix} \dfrac{x_2}{R_o} \\ \alpha_2 \\ \delta \end{pmatrix} = \begin{pmatrix} 0 & 1 & 1 & -1 & -1 & 2 & 0 & 2 & 0 & 0 & 1 & -0.5 \\ -1 & 0 & 1 & 0 & -1 & 1 & -1 & 1 & 0 & -0.5 & 1 & 0 \\ 0 & 0 & 1 & 0 & 0 & 0 & 0 & 0 & 0 & 0 & 0 & 0 \end{pmatrix} . \begin{pmatrix} x_1.R_o^{-1} \\ \alpha_1 \\ \delta \\ \left(x_1.R_o^{-1}\right)^2 \\ x_1.R_o^{-1}.\alpha_1 \\ x_1.R_o^{-1}.\delta \\ \alpha_1^2 \\ \alpha_1.\delta \\ \delta^2 \\ \left(y_1.R_o^{-1}\right)^2 \\ y_1.R_o^{-1}.\beta_1 \\ \beta_1^2 \end{pmatrix} \tag{6.11}$$

$$\begin{pmatrix} \dfrac{y_2}{R_o} \\ \beta_2 \\ \delta \end{pmatrix} = \begin{pmatrix} 0 & 1 & 0 & 0 & -1 & 0 & 0 & 1 & 1 \\ -1 & 0 & 0 & 1 & 0 & 0 & -1 & 0 & 1 \\ 0 & 0 & 1 & 0 & 0 & 0 & 0 & 0 & 0 \end{pmatrix} . \begin{pmatrix} y_1.R_o^{-1} \\ \beta_1 \\ \delta \\ y_1.x_1 R_o^{-2} \\ y_1.R_o^{-1}.\alpha_1 \\ y_1.R_o^{-1}.\delta \\ \beta_1.x_1.R_o^{-1} \\ \beta_1.\alpha_1 \\ \beta_1.\delta \end{pmatrix} \tag{6.12}$$

Figure 6.10 shows the images at the slit position an at the exit plane of the deflector in the microscope. The opening angle at the entrance of the first 90°-deflector is 4.18 10^{-2} mrad, see table 4.4. Second order aberrations do not spread out the beam significantly at the slit or at the exit plane of the second 90°-deflector in the microscope. Therefore it is true that second order aberrations do not influence the system behavior negatively, as is assumed earlier.

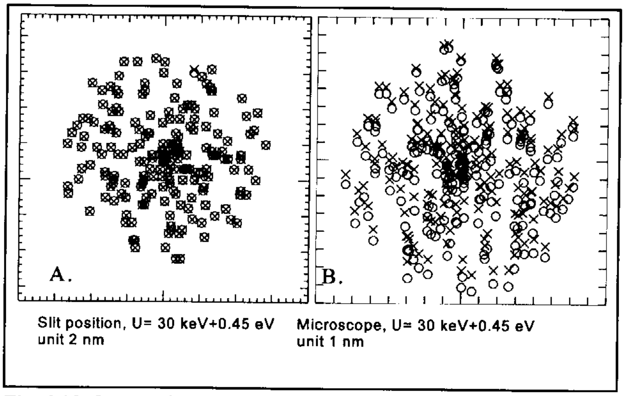

Fig. 6.10. *Intermediate images. (a) at the slit position, (b) the image in the microscope behind the second 90°-deflector. (x)= without second order aberrations, (o)= with second order aberrations.*

7. <u>Fringing fields of the deflector</u>

Inside the deflector the fieldlines will be straight and radial between the electrostatic electrodes but at the entrance and exit plane they will be bend outside the deflector. This causes extra, unwanted, effects. In order to narrow the fringing field region, shielding apertures are used, see figure 6.11a. The fringing field distribution of such a shielded parallel plate condenser can be obtained from Herzog (Herzog, 1940).

The fabrication of the electrodes is more complicated in case η in figure 6.11a is non-zero, because this means that the entrance and exit plane of the electrodes are not perpendicular to each other (see figure 6.4) When η is taken to be zero both for the thick and thin fringing apertures curves can be obtained which show when the effect of fringing fields is minimized. These curves are depicted in figure 6.11b. These fringing apertures will be insulated from the system to enable current measurements. For the fitting of the apertures with an outer diameter of 3.04 mm, 2.s has to be smaller.

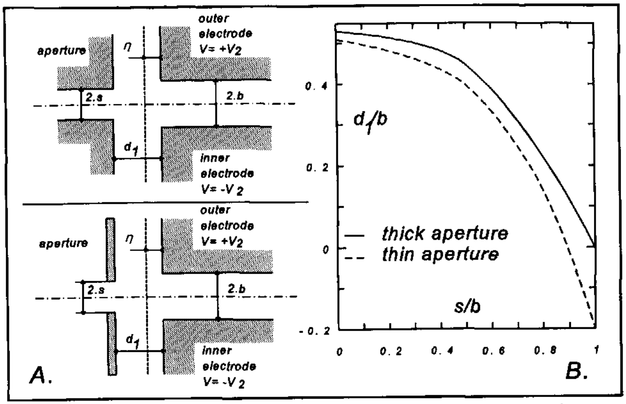

Fig. 6.11. *(a.) Thick and thin apertures for shielding of the fringing field, (b.) Relations between the fringing parameters to minimize fringing effects (Herzog, 1940).*

8. Effect of electron entrance

Both 90°-deflectors are in principle equal except for the fact that the deflector at the microscope side has to transfer the electrons. This hole in the upper electrode will have an effect on the ions. The electrostatic equipotential lines bend into this hole and will introduce aberrations of the ion beam.

Without further calculations, it is assumed that this effect is negligible if the length of the tube, l, is at least 5 times larger than its diameter, 2a.

9. Transfer of the electron beam through the 90°-deflector

It was mentioned earlier: the entrance of the electrons in the deflector will have an effect on the ions. Therefore it has to be made as small as possible, but it may not be beam limiting. In equation

$$2.a > 2.\alpha_d.l = 2.(\alpha_t.M).l \tag{6.13}$$

α_d= opening angle of the electron beam in the deflector
α_t= opening angle of the electron beam at the target (9.29 mrad)
l= distance from the entrance of the cylinder to the next image (226.9 mm)
M= magnification of the condenser and objective lenses of the electron system ($8.51\ 10^{-5}$)

This means 2.a> 0.4 μm

10. Deflection of the electron beam by the 90°-deflector

The electron beam is deflected by the 90°-deflector if it is excited. This is necessary if in situ observation is wanted. Here both the ion and the electron beam are focused on the specimen: the ions fabricate the structures while the electrons observe the fabrication. Therefore the deflection effect on the electron beam has to be minimized and/or compensated by pre-deflection. The angle of deflection of the electrons can be calculated using

$$\tan\gamma_1 = \frac{V_e.l_e}{2.U_e.d_e} = \frac{2.V_2.\sqrt{(R_0+b)^2-R_0^2}}{2.U_e.2.b} = \frac{V_2}{2.U_e}.\sqrt{1+\frac{2.R_0}{b}} \qquad \textbf{(6.14)}$$

This angle can be compensated by a slightly angled entrance for the electrons. The angle that results from this is

$$\tan\gamma_2 = \frac{V_e.l_e}{2.U_e.d_e} = \frac{V_2.\dfrac{2.a}{\tan\alpha}}{2.U_e.2.a} = \frac{V_2}{2.U_e.\tan\alpha} \qquad \textbf{(6.15)}$$

α= angle with respect to optical axis of the tube for the electron

The optimum situation, complete compensation, is realized if $\gamma_1=\gamma_2$

$$\frac{1}{\tan\alpha} = \sqrt{1+\frac{2.R_0}{b}} \qquad \textbf{(6.16)}$$

This is a fixed compensation, but additional deflection can be realized with the magnetic gun shift/tilt unit that will be above the 90°-deflector.

11. Lens effect on the electron beam of the 90°-deflector

The cylinders at the entrance of the deflector for the electrons are at different potentials: they will act as a two cylinder lens on the electrons. The focal length for this lens is given by Harting (Harting, 1976)

$$\frac{f}{2.a} = \frac{\dfrac{q.V_2}{U_e}.\sum_{i=0}^{5} A_i.\left(\dfrac{q.V_2}{U_e}\right)^i}{\left(\dfrac{q.V_2}{U_e}-1\right)^2} \qquad \textbf{(6.17)}$$

The focal length in units of the tube diameter is depicted in figure 6.9 for 100 keV electrons. It can be concluded that $f \approx 2.a.10^4$ for a potential difference between the electrodes of 5 kV.

12. Construction

The two deflector modules are about the same from a construction point of view except for the electrodes. For a cylindrical deflector two cylindrical electrodes are needed which are relatively easy to construct. For a spherical deflector two ball elements are needed as electrodes. This is more complicated to machine, especially with small tolerances. CNC techniques, however, make this easier.

13. High voltage insulation

The electrodes of the 90°-deflector will be at high tension. In general this means that there is a chance of break down, because locally at the surface of the insulator the field strength will be much higher than inside it. See also Shannon (Shannon, 1965) or Latham (Latham, 1981). As a rule the field strength at which break down will occur in case of macor insulators is

$$E = \frac{10}{\sqrt{d}} \left[\frac{kV}{mm}\right] \tag{6.18}$$

In the three actual situations this equation can be written as:

electrodes to each other: $V_2 < 158.10^3.(2.b)^{0.5}$

electrode to fringing aperture: $V_2 < 316.10^3.(d_1)^{0.5}$

electrode to electron entrance: $V_2 < 316.10^3.(d_2)^{0.5}$

14. System housing

The deflectors have to be built in a vacuum housing. This has to be UHV compatible and has to have entrances and exits for both beams. This makes a Conflat-cube advantageous. If e.g. a CF100 cube is used the central radius of the deflector can be 30 mm at maximum.

Table 5.1. *Comparison between a cylindrical and a spherical 90°-deflector system. The numbers are relative to the values for the spherical deflector.*

	cylindrical deflector	spherical deflector
focusing	-	+
energy dispersion	1.4	1
rest angular dispersion	3.5	1
magnification	2	1
construction	+	-

The energy dispersion and construction of a cylindrical 90°-deflector are favorable. But quadrupoles are necessary in case of a cylindrical 90°-deflector with an excitation of 3.8 kV when they have a plate distance of 6 mm. Other parameters that make the spherical deflector more beneficial are better focusing, rest dispersion, magnification and sensitivity. The last point is of importance as the total column length has to be smaller than 350 mm to minimize the effect of vibrations (see figure 4.10). Therefore a spherical 90°-deflector will be realized.

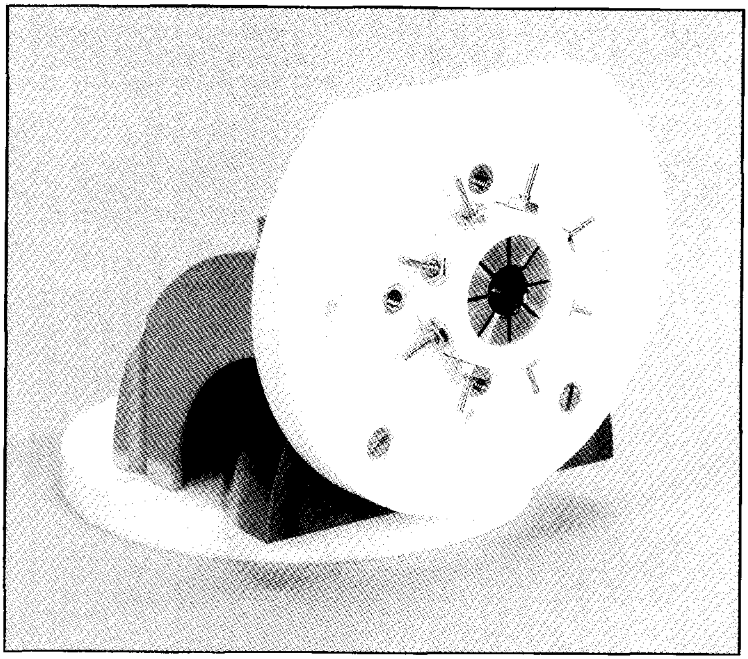

Fig. 6.12. *The 90°-deflector with spherical electrodes and stigmotor.*

Based on the subjects "energy dispersion" and "system housing" the radius of the central axis is chosen to be maximal: $\mathbf{R_0}$ is **30 mm**. This means with the subject "deflection over 90 degrees" that V_2= 2.b.10^6 [V] for a beam of 30 keV. The distance between the electrodes, 2.b, has to be a few mm to prevent ion beam limitation. Therefore $\mathbf{V_2}$ is taken to be **5 keV**, this results in **2.b** is **5 mm**.

From the subject "high voltage insulation" it can be concluded that V_2 has to be smaller than 11 keV to prevent break down between the electrodes. From the same subject it can be concluded that d_1 and d_2 may not be smaller than 0.25 mm. Because of practical reasons and high tension overdimensioning $\mathbf{d_1}$ and $\mathbf{d_2}$ are taken **1 mm**. It is now possible to decide about the fringing aperture. In figure 6.11 it can be seen that for d_1/b is 0.4 s/b needs to be 0.58, which means 2.s is 2.9 mm. This is too large to mount the fringing apertures. Therefore $\mathbf{d_1}$ is taken **1.1 mm**, so **2.s** will be **2.3 mm**. Figure 6.1 shows a picture of the 90°- deflector on the microscope. For an image length of 160.8 mm an ion beam with an energy spread of 0.9 eV and an energy of 30 keV will be dispersed over a distance of 4.8 μm.

The electron transfer can now be dimensioned. The optimum inclination angle of the electrode follows from equation (6.15): **α** is about **12°**. The diameter of the cylinder can be calculated: 2.a must be larger than 8 μm. In the system **2.a** is chosen **3 mm**. Finally the length of the cylinder which is connected to the upper electrode is **15 mm** to screen the effect of the hole in this electrode.

These parameters have been implemented in the design, the result is depicted in figure 6.1. It can be seen that the two deflectors are nominally the same: both get spherical electrodes with the same radius of curvature of the main path.

It is necessary to adjust the position of the ion beam and its inclination relative to the electrostatic 90°-deflector. Therefore, a multipole is added close to the entrance and exit plane of each 90°-deflector to align the beam as indicated in figure 6.1. The multipoles have eight electrodes, this enables not only deflection in an arbitrary direction but also stigmation in an arbitrary direction.

6.2. Energy selecting element

Between the two 90°-deflectors which act as energy dispersive elements, there has to be an element that stops these ions that have an energy that differs to much from the mean energy of the beam. Two knife edges with a slit in between function as a band-pass filter for the energy. High energy ions are stopped by the knife edge above the optical axis, low energy ions by the one below the optical axis in figure 6.1.

The width of the slit and the position of the knife edges has to be very flexible:

1. The distance between the central axis of the beam and an ion at the slit plane, is linearly proportional to the difference in energy of that ion from the mean energy of the beam (see equation (6.9)). From the point of view of the filtering element this means that the distance between the knife edges is linearly proportional to the width of the energy band that is passing the filter.

   For high resolution application this width has to be small to limit the chromatic aberration contribution to the final probe size. It is demonstrated in paragraph 4.3 that the optimum energy spread in a 30 keV beam is 0.9 eV to give maximum probe current in a probe of 1 nm. The size of the slit needed to limit the energy spread to the desired value depends on the length of the horizontal column as can be seen in figure 6.5. A longer column results in a larger slit size. However, the unwanted vibrations also increase with a longer column as is depicted in figure 4.10. The length of the horizontal column is designed as 321.6 mm, the needed slit size is 4.8 μm. The vibration amplitude is limited to less than 1 nm. This can be allowed with a spot size at the energy selecting slit of 13 nm.

At lower resolution the slit may be wider to increase the probe current. This makes a setting of the width of the slit during operation necessary from 4.8 μm to over 100 μm for total beam transfer with a resolution of 1 μm.

2. The optical axis of the beam is fixed: it is defined by the two 90°-deflectors. Therefore the slit has to be positioned symmetrically around this optical axis to have maximum passing current for a given energy band width.
3. It is already mentioned at the beginning of this paragraph that part of the ions have to be stopped by the knife edges. The ions that impact, will scatter in the upper

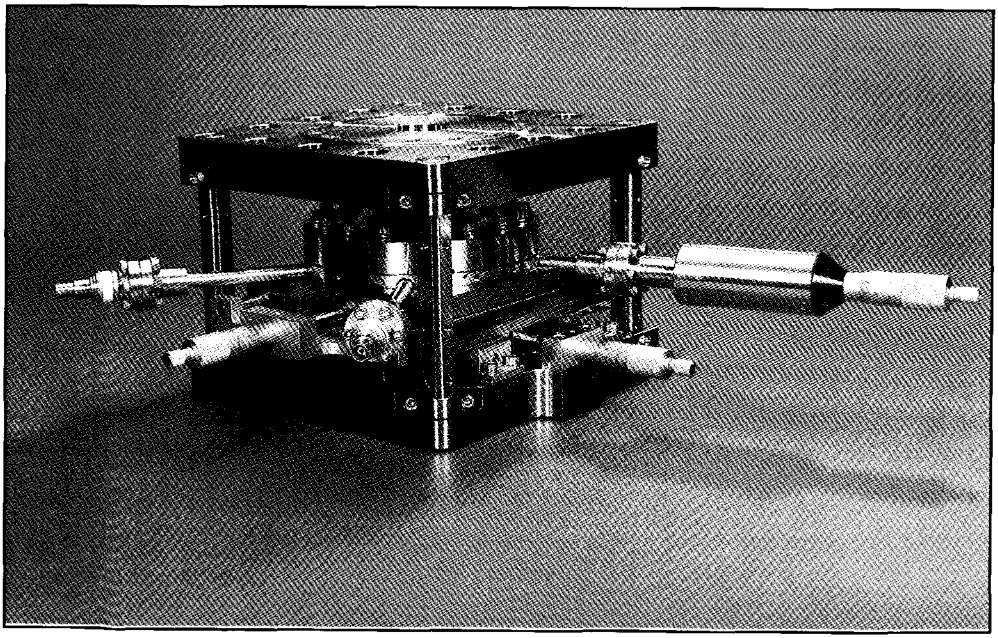

Fig. 6.13. *The energy selecting element.*

layers of the material resulting in erosion of the knife edges mainly because of sputtering. A detailed description of the physical process of sputtering is given in chapter 2 and 3. Here it is mentioned that the sputtering yield of 30 keV Ga ions on a stainless steel substrate (71 % Fe, 18 % Cr, 10 % Ni) is 3.19 Fe atoms/ion, 0.799 Cr atoms/ion and 0.445 Ni atoms/ion (Ziegler, 1985). The erosion speed is then

$$v_e = \frac{J.SY.M_2}{q.\rho} \tag{6.19}$$

v_e= erosion speed
J= ion beam current density
SY= sputtering yield
q= charge of the ions, $1.6\ 10^{-19}$ C
M_2= mass of a substrate atom
ρ= density of the substrate, the knife edges, $7.8\ 10^3$ kg/m^3

So, Ga ions with 30 keV beam energy have a sputtering yield of 0.0522 nm^3/ion on the knife edge. The typical beam current density of $1.4\ 10^4$ A/m^2 is decreased at the slit to 33.8 A/m^2 because of the dispersion. This means digging about 11 nm/sec or 50 μm (the thickness of the knife edge) in 75 minutes.

This time can be enlarged by spreading out the beam in the non-dispersive direction. Both for the cylindrical and the spherical deflector this can be realized by exciting the multipole as a quadrupole.

4. The two 90°-deflectors have to be exactly equal. One of the results of this mirror symmetry is that the intermediate image between the deflectors has to be exactly at the mirror plane. But the energy selecting slit has to coincide with this plane because selection on position is used.
5. During the refreshing of the slit, mentioned at point 3, the slit size and position in the dispersive direction may not change. Therefore the knife edges have to be parallel and the slit has to be parallel to the refreshment axis.

The central part of the technical solution is a hole-hinge construction (Koster, 1992) as can be seen in figure 6.14. The slit size can be adjusted with a linear motion feedthrough with micrometer precision. The knife edges move now symmetrically around the central line of the slit, the alternative linkage is also drawn in figure 6.14. Slit sizes from 0 to 500 μm can be set with an accuracy of less than 1 μm. With the equation of van der Hoek (Pistecky, 1995) the dimensioning of the hole hinge construction can be made.

$$\frac{\sigma}{E} = 0.58\ \phi.\sqrt{\frac{h}{D}} \tag{6.20}$$

σ= coefficient of conductivity of the plate material
E= modules of elasticity of the plate material
ϕ= maximal angle of rotation of the hole hinge
h= wall thickness
D= diameter of the hole

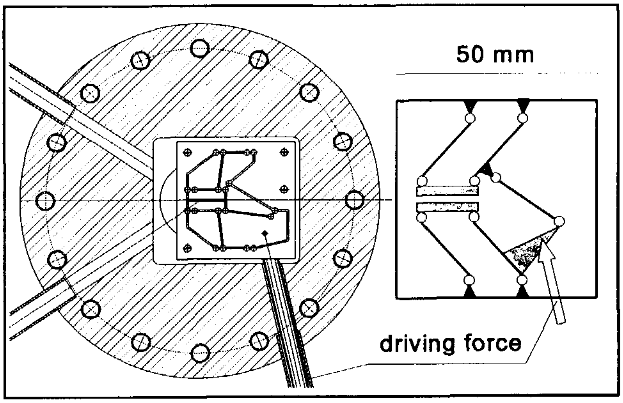

Fig. 6.14. *The hole hinge construction that defines the size of the energy selecting slit.*

Based on the design in figure 6.14, the maximum angle of rotation is 21 mrad for a slit size of 500 μm. The plate deformation parameter, σ/E, gets 3.85 10^{-3} for h and D respectively 0.3 mm and 3 mm. This parameter combined with the need for positioning in vacuum results in the selection of the plate material: beryllium-copper or phosphor-brons. It has a maximum deformation parameter of 7.7 10^{-3} and 4.5 10^{-3} respectively (Pistecky, 1995). Larger deformations result in plastic or inelastic deformations. Figure 6.15 shows the distance between the knife edges for different positions of the driving force. It is clear that there is a linear relation between these parameters.

The knife edges are electrically isolated from the system. This enables the measurement of the current on each knife edge independently for monitoring the position of the slit with respect to the beam. The actual positioning of the slit in space is realized by an xy-table which is connected to the central flange, drawn in figure 6.14. This is indicated in figure 6.1 as part 3. Part 2 can move in vertical direction with respect to part 3 and 4, the fixed outer flanges. On the other side moves part 3, connected to the central flange, in horizontal direction with respect to part 2. The flexible vacuum connection is realized

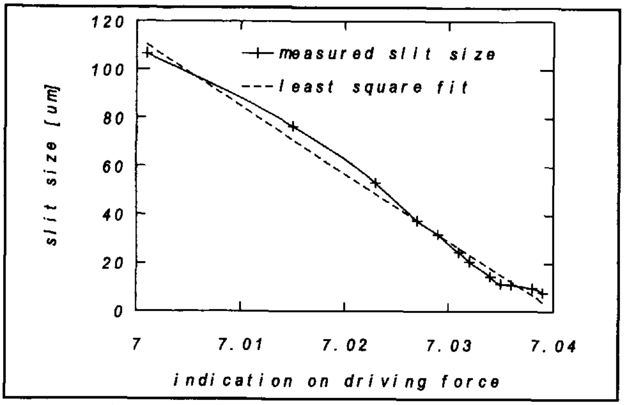

Fig. 6.15. *The size of the slit measured as a function of the position of the micrometer indicator that is connected to the driving force in figure 6.12.*

using etch welded bellows.

Finally a stiff connection is made between the two outer flanges using four rots and plates as can be seen in figure 6.1 and figure 6.13. The differential equation of the elastic line is given by:

$$E.I.\frac{d^2w}{dz^2} = -M(z) \tag{6.21}$$

E= modules of elasticity
I= moment of inertia
w= bending
z= optical axis
M(z)= moment of bending as a result of external force F

The moment of inertia is given by:

$$\begin{aligned} I &= \int x^2.dA \\ &= 4.\left[\frac{\pi}{4}.(\frac{d_r}{2})^4+\pi.(\frac{l}{2})^2.(\frac{d_r}{2})^2\right]+ \\ &\quad +2.\left[\frac{2}{3}.d_p.l^3\right]+2.\left[2.d_p.l^3+2.l^2.d_p^2+\frac{2}{3}.l.d_p^3\right] \\ &= \frac{\pi}{16}.d_r^4+\pi.(l.d_r)^2+\frac{16}{3}.d_p.l^3+4.l^2.d_p^2+\frac{4}{3}l.d_p^3 \end{aligned} \tag{6.22}$$

d_r= diameter of the rot (20 mm)

d_p= thickness of the plates (5 mm)
l= distance from central axis to center of rot (92.5 mm)

The moduli of inertia is $3.28*10^7$ mm^4. This exceeds the value that is used to calculate the effect of vibrations in figure 4.10. So the assumption is valid that the effect of vibrations will not be of more importance than the results presented there.

6.3. Summary

Although an energy filter decreases the probe current by a factor two when the energy spread is halved, it seems to be the optimum solution to achieve a nanometer probe. The main parts of the horizontal column are two 90°-deflectors and a slit, together this is the energy filter. The first 90°-deflector separates the ions with different energies. They end up at different positions at the energy selecting slit. The width of the slit defines the energy spread of the ion beam that is transferred to the specimen. The second 90°-deflector brings all ions, that have passed the energy selecting slit, together at the same point near the exit plane of this deflector. This makes the horizontal column achromatic, which means that the images near the entrance plane of the first 90°-deflector and near the exit plane of the second 90°-deflector are equal except for the energy spread of the ions in these images that has been limited. The 90°-deflectors have spherical electrostatic electrodes with a mean radius of curvature of 30 mm. This is decided mainly to make it easy to tune the system as a spherical deflector is double focusing. So a real image is formed at the slit position. At the slit ions with an energy that differs too much from the central energy of the beam, are stopped because they end up at a larger distance from the central axis than the slit width. However other effects than energy spread can bring the ions off-axis too, like vibrations of the system. As a result of the optimization between length of the horizontal column and the slit size the system behavior is not dominated by vibrations. The slit has to be adjusted with micrometer accuracy; for the calculated optimum energy spread the slit size is 4.8 μm.

For the alignment of the system multipoles are positioned at the entrance and exit slit of the 90°-deflectors, while the position of the slit can be adjusted. Also the part of the knife edges in front of the beam can be adjusted to refresh them as they are eroded by the ion beam.

References

Bleeker, A.J., *Optical and mechanical design for 1 nm resolution Auger spectroscopy in an Electron Microscope*, thesis, Delft, 1991, pp. 4.1-4.22

Harting E. and F.H. Read, *Electrostatic lenses*, Elsevier, Amsterdam, 1976

Herzog, H., *Elektronenoptische Zylinderlinsenwirkung der Streufelder eines Kondensators*, Zeitschrift fur Physik 41, 1940, pp. 18-26

Koster, M.P., *Constructie principes voor het nauwkeurig bewegen en positioneren*, Enschede, 1992

Latham, R.V., *High voltage vacuum insulation*, Academic Press, London, 1981

Pistecky, P.V., *private communication*, 1995

Rose, H. and Preikszas, *Outline of a versatile corrected LEEM*, Optik 92(1), 1992, pp. 31-44

Ross, A.W., L.K. Smith, C. Xie, L.H. Theusen, M. Fink and H.F. Wellenstein, *Design of a 90 degree spherical analyzer*, Journal of Electron Spectroscopy and Related Phenomena 69 , 1994, pp. 189-195

Seybel, S.J., *An instrument for positron microanalysis*, thesis, Delft, 1995, pp. 107-112

Shannon, J.P. e.a., *Insulation of high voltage across solid insulators in vacuum*, Journal of Vacuum Science and Technology 2, 1965, pp. 234-239

Wollnik, H., *Electrostatic prisms*, in Septier, A., Focusing of charged particles II, Academic Press, New York, 1967, pp. 163-202

Ziegler, J.F., J.P. Biersack and U. Littmark, *The stopping and range of ions in solids*, Pergamon Press, 1985

7. The combined objective lens for ions and electrons

This chapter has been realized in close cooperation with M.C.W. Kelder as part of his master research.

Introduction

Both the ion and electron beam need to be focused by an objective lens. This chapter will explain what choices have been made with respect to the lens configuration to fulfil the function of focusing the ion and electron beam into a very small probe onto the specimen.

From the point of view of the objective lens the preceding system produces a spot on the optical axis, with a certain size and at a certain place in front of the objective lens. This spot is called the geometrical spot and it can be seen as the object that will be imaged by the objective lens. The imaging function of the objective lens can be divided into two subfunctions. The first is to demagnify the geometrical spot at the object side and the second is to vary the strength of the lens in order to position the image exactly onto the specimen. The probe size that results is a combination of the demagnified geometrical spot and the spherical and chromatic aberration contributions of the objective lens. In general also Coulomb interactions and diffraction can contribute to the probe at the specimen. This can be seen in the general equation (4.1) that presents the size of the imaged spot as a function of the most significant contributions. From the equations (4.2) to (4.6) it can be seen that C_c *and* C_s *are important parameters. These chromatic and spherical aberration coefficients, defined at the specimen side of the objective lens,* *depend on the geometry of the objective lens. They are often used to express the quality of the lens in a certain situation.*

Much attention will be paid in this chapter to minimize these aberration coefficients both for the ion and the electron objective lens.

7.1. Optical properties of an objective lens

To form a small probe at the specimen the objective lens needs to be placed as close as possible to the specimen. There are two arguments that support this statement. The first is that the objective lens needs to demagnify the geometrical probe contribution. The second reason is that C_c and C_s, and therefore the aberration contributions, strongly depend on the working distance. The shorter the working distance the smaller the aberration coefficients will be. In case of large demagnification it follows that the focal length, f, is approximately equal to the working distance. This means that a strong lens effect, so short focal length, is required to give minimal probe size.

For charged particles two types of lenses are known. Lenses which make use of magnetic fields and lenses which make use of electrostatic fields. In principle for the electron beam, the standard magnetic objective lens of the Philips EM420 microscope, the basic instrument, can be used to function in "the Fancier", because it is of high quality. But integrating an ion lens causes this choice to be reconsidered as a consequence of the limited space in this region. Therefore all possible combinations of the type of objective lenses in "the Fancier" will be discussed. They are given in table 7.1.

Table 7.1. *The possible lens type combinations in the dual beam instrument.*

configuration:	A	B	C	D
electron obj.lens:	magnetic	electrostatic	electrostatic	magnetic
ion obj.lens:	magnetic	magnetic	electrostatic	electrostatic

Option A seems to be the easiest way to focus ions as well as electrons if one would be able to use the standard magnetic objective lens for ions. The strength and thus the focal length of the objective lens for ions must be the same as for electrons because the image length stays the same and the object distance is also large compared to the image distance. In order to see if that is possible, the focusing properties of the magnetic objective lens will be examined, followed by a discussion of an electrostatic lens.

1. The magnetic lens

   Figure 7.1 shows the basic action of a magnetic lens. In order to understand the action the magnetic field in the gap, as a result of the current through the coil, is divided into a homogeneous part where the field is parallel to the axis of the lens and the end sections, where the field is radial.

   Because of the radial field an incoming electron at a distance r_0 from the central axis receives such a tangential impulse that the radius of curvature in the constant field area is $r_0/2$. At the field exit the tangential impulse is compensated, while the radial impulse remains. This is then the net lens effect.

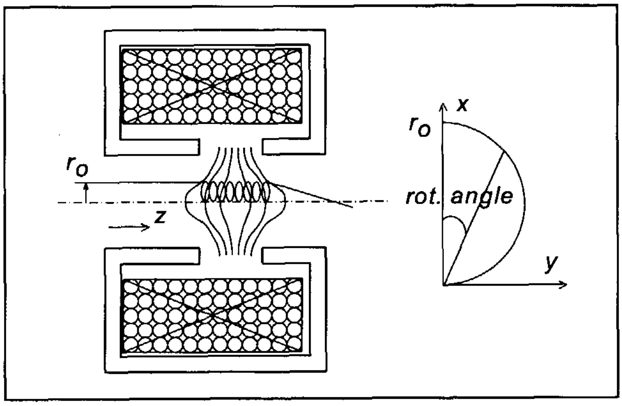

Fig. 7.1. *A magnetic lens.*

In the assumption of a block field the focal length of the magnetic objective lens for charged particles can be written as:

$$f_{obj}=\frac{\sqrt{S^2+D^2}}{\theta}$$
$$\theta=0.78\ B.S.\sqrt{\frac{q}{8.M.U}}\ ,\quad B=\frac{\mu_0.N.I}{S} \tag{7.1}$$

S= distance between the upper and lower pole piece
D= diameter of the bore in the pole pieces
B= magnetic field strength
μ_0= magnetic permeability
N= number of turns in the magnetic coil

I= current through the magnetic coil

In the assumption of a block field the strength of a magnetic lens is proportional to $\theta.\sin(\theta)$ which reaches a maximum for θ= 2.03 rad (see equation 4.11). One should distinguish between a lens used as a projector or an objective lens. In the case of a projector lens the whole magnetic field forms the image and only the asymptotic direction of the rays is of interest. In a lens used as an objective the object is near the real cross-over inside the lens field and the strength will be proportional to θ. The difference is shows in figure 7.2.

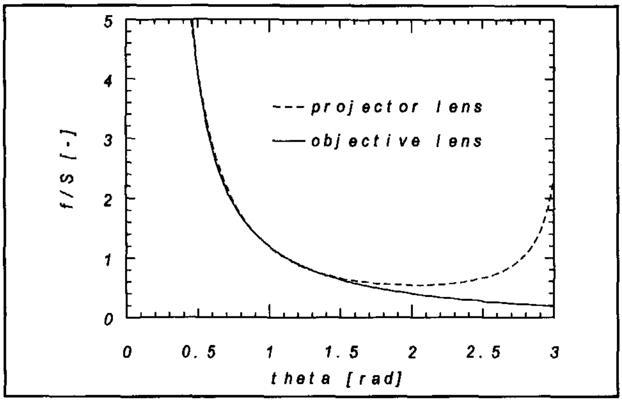

Fig. 7.2. *The focal length of a magnetic projector lens and a magnetic objective lens.*

Equation (7.1) shows that f_{obj} is proportional to the square root of the mass and the acceleration voltage of the particle. Therefore it is important to look at the particle properties of the ions compared to those of the electrons. In "the Fancier" heavy ions like Gallium will be used for the ion beam. The energy to which these ions are accelerated is determined to be 30 kV at maximum. The magnetic objective lens is designed for 120 keV electrons. However, the mass of an electron is $9.11\ 10^{-31}$ kg while the mass of the Gallium ion is about $1.15\ 10^{-25}$ kg.

Consequently the focal length of the magnetic objective lens will be 180 times larger for Gallium ions than for electrons at equal magnetic field. The only way to counteract this increase in focal length is to increase the magnetic field in the gap 180 times, because f_{obj} is proportional to the inverse of the magnetic field strength B. B depends on the current I through the objective coils, but also on the conductance of the magnetic circuit. Especially the magnetic resistance of the gap plays an important role. It shows that B can be increased solely by increasing the current through the objective coils, because the other parameters, N and S, are embedded in the design of the instrument. And the aim is to switch from one beam to another without interference of any mechanical part as mentioned in chapter 4.

However, increasing the current through the coils by a factor of 180 will not have the desired effect because such a high magnetic field cannot be held inside the magnetic circuit of the lens. At a certain level the metal will saturate and no more fluxlines will be conducted through the magnetic circuit. Then the magnetic field in the gap cannot be increased any further. This will already occur when the flux density increases by a factor of about two compared to the flux density in the objective lens in normal operation.

2. The electrostatic Einzel lens

The second lens type is an electrostatic lens. Only the axial potential distribution of the lens configuration plays a role in the focusing properties. This can be seen in the paraxial ray equation for the motion of charged particles traveling near the axis of a cylindrically symmetrical electrostatic lens, paragraph 5.4. Its focal length can be given by

$$f = \frac{16}{3} . \frac{k^{5/4}}{(k-1)^2 . (\sqrt{k}+1)} . d \ , \quad k = \frac{U_l}{U_0} \tag{7.2}$$

d= bore of the electrode
U_l= potential of the ion beam in the lens
U_0= potential of the ion beam outside the lens

The axial potential distribution depends only on the charge of the particle and the potentials on the electrodes of the lens with respect to the energy of the particle.

The lens effect of electrostatic lenses is induced by increasing or decreasing electrostatic fields of a rotationally symmetric form. Most common is the Einzel lens (figure 7.3), which consists of three electrodes with a hole, placed above each other. The focal length given in equation (7.2) is actually the one of an Einzel lens. The middle electrode is put at a high voltage while the outer electrodes remain at earth potential. There are accelerating and decelerating electrostatic lenses. The strength of a lens increases if the accelerating or decelerating electric field increases (Rempfer, 1985). However, the decelerating lens becomes a mirror if the decelerating electrode potential equals the potential of the beam. Little below this value the decelerating lens works at its best; the working distance is shortest and consequently

C_c and C_s as well. Because f has the lowest value at the same time this means that in this setting the lens can form the smallest probe and demagnifies maximal. Comparing the quality of the decelerating lens with the accelerating lens, it is known that the accelerating is better, so lower spherical and chromatic aberration coefficients, if the particle will be accelerated to more than its own energy in the beam. This means that the acceleration potential for a 30 keV ion beam should be several times minus 30 kV. But even in deceleration mode the middle electrode has a positive potential of little less than 30 kV to perform optimally. This brings about practical insulation problems. In vacuum, the field strength must not exceed 10-15 kV/mm to avoid disruptive discharges. The maximum field strength along the surface over an insulator is even a few times lower to prevent flash overs. In order to reduce the field strength between the electrodes some space is required.

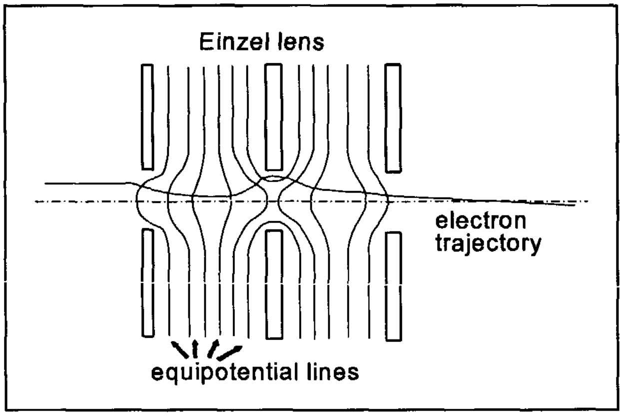

Fig. 7.3. *A decelerating electrostatic Einzel lens.*

As a result the standard magnetic objective lens cannot be used for ions and therefore option A and B remain possible only if a new kind of magnetic lens for ions can be designed. However, in practice it will appear almost impossible to generate such a high magnetic field on the axis and therefore both options are excluded. A better way to focus the ions is an electrostatic lens. The reason is that this type of lens works independent of the mass of the particle.

The space for a combination of two separate electrostatic lenses for the ion and electron beam respectively, as suggested by option C, can be created by removing the magnetic objective lens. However, if two electrostatic lenses are used, one will always be further away from the specimen than the other. The quality of the most distant lens will probably be too low, due to the longer working distance. So this is not a good alternative. However, if a single electrostatic lens can be used to focus the electron beam as well as the ion beam, this would allow the working distance for both objective lenses to be smaller. This 'one-lens' configuration can be made by putting the middle electrode at a decelerating potential of about minus 120 kV for electrons which is at the same time an accelerating potential for 30 kV ions. In this design the electrodes of the combined lens would have to be placed at least 12 mm away from each other. Consequently the focal length will be in the same order of magnitude. The present focal length of the magnetic objective lens is 2.9 mm. Therefore the demagnification will be about 4 times lower and because the aberrations also depend strongly on the focal length, the total aberration spot increases as well. So for electrons the standard objective lens would be preferred, compared to the one-lens configuration. For the 30 kV ions a much smaller lens is possible and to be preferred, since its quality will be much better as a result of the smaller focal length, even in decelerating mode. This configuration has been developed by Cleaver (Cleaver, 1985) as well. It is stated that the apparent simplicity of the solely electrostatic form of this lens is offset by its operational inflexibility, since the focusing conditions cannot be set up independently without changing the energy of the beams. A way to overcome this problem is the superposition of a magnetic field for the electron beam to compensate the focusing conditions. But then the standard objective lens should stay in the EM 420 and consequently a combination of an electrostatic and a magnetic lens is designed.

As a result the only option left is option D. It is obvious that the standard magnetic objective lens, which is of high quality, should be used to focus the electron beam, instead of designing a new one. This will be discussed in the next paragraph. Accordingly an electrostatic objective lens for the ion beam must be integrated near the specimen as will be described in paragraph 7.4. To avoid high voltage problems in the limited room for this lens it is best to use a decelerating lens.

7.2. The standard objective lens of the EM420 microscope.

Before any changes will be made to implement the ion optical elements near the objective lens for electrons, the working of the standard objective lens must be known in greater detail in order to be able to estimate the effects of alterations of different parts.

Figure 7.4 shows the magnetic circuit of the TWIN objective lens as it is situated in the standard EM 420. This picture has been made with the Magnetic Lens Design (MLD) computer program (Lencová, 1992), which is able to calculate the magnetic field and flux density of magnetic lenses. Because MLD assumes a lens design to be cylindrical symmetric it only gives an ZR-plot of the longitudinal cross section of a lens. In this figure the electrons come from the right, along the Z-axis, and are focused on the specimen which is positioned in the gap, right between the upper and the lower pole piece.

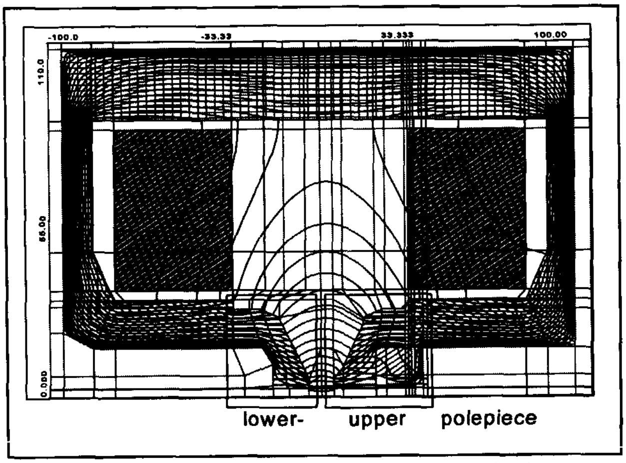

Fig. 7.4. *The ZR-plot of the MLD input of the standard magnetic objective lens with 7500 At through objective coils.*

The objective lens effect is induced by a current through two large, coupled coils. On the outside of the coils the magnetic field is conducted by a soft iron yoke. Towards the inner side the center yoke which is made of nickel-iron fits to the outer yoke. The center yoke conducts the magnetic fluxlines to the upper and lower pole piece in the middle made of cobalt-iron. Between the two pole pieces the fluxlines must cross a gap of 9 mm. The form of the magnetic field in the gap between the upper and lower pole piece brings on a lens effect for charged particles. The strength of the lens can be varied by changing the current through the coils.

For microscopy in TEM-Microprobe mode (see figure 4.8) an auxiliary lens, fitted in the upper pole piece, is used (see figure 7.6a). The small magnetic gap for the auxiliary lens is formed by a ring of non-magnetic material which has been soldered on the upper pole piece. The ring is positioned at the inner side of the auxiliary coil where it is closest to the axis and in the strongest part of the field induced by the coil. On top of the non-magnetic ring a small center yoke, made of cobalt-iron, is soldered to conduct the fluxlines to the gap for the auxiliary lens. The flat ring above the auxiliary coil is able to conduct fluxlines from the center yoke of the objective lens to the center yoke of the auxiliary lens. This magnetic ring is fixed to the auxiliary coil and to the shift- and tilt element above it. This part is fitted in a chamber at atmospheric pressure and can be removed as a whole if necessary. At the lower side of the auxiliary gap the upper pole piece itself conducts the fluxlines around the auxiliary coil until the center yoke of the objective lens is reached.

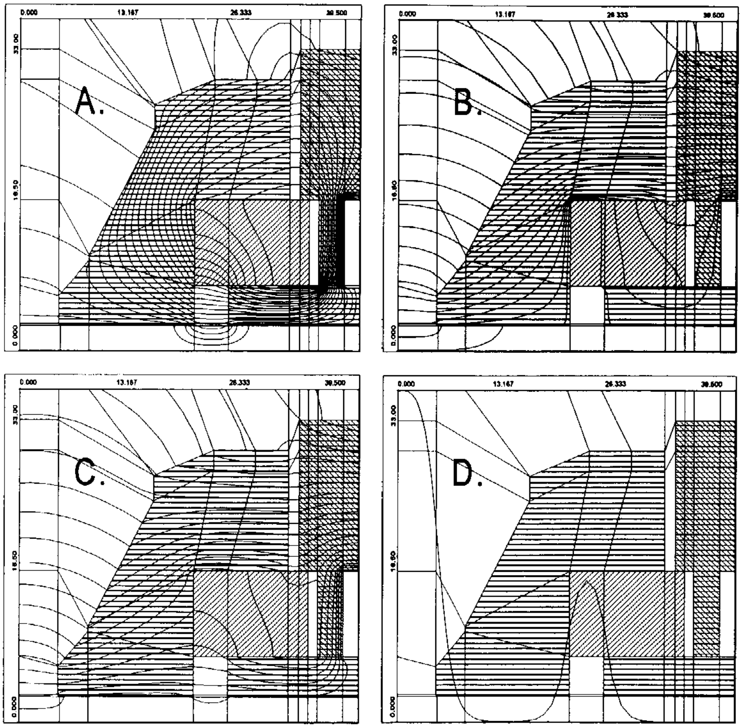

Fig. 7.5. *The ZR-plot of the auxiliary lens. (a.) obj. lens off, aux. lens on , (b.) obj. lens on, aux. lens off, (c.) obj. lens on, aux. lens on, (d.) axial potential with objective and auxiliary lens on.*

The form of the magnetic field which is caused only by the excitation of the coil for the auxiliary lens, is shown in figure 7.5a (ZR-plot). The strength of the auxiliary lens will increase if fluxlines of the main objective coils can be diverted via the magnetic conducting material above and at the inner side of the auxiliary coil, through the gap of the auxiliary lens and back into the upper pole piece. However, if the upper pole piece is connected directly to the center yoke of the objective lens, no fluxlines will be found in this alternative route because of the higher magnetic resistivity of the auxiliary gap compared to the direct route into the pole piece. Therefore the upper pole piece is shifted away (1.2 mm) from the center yoke resulting in a threshold for fluxlines that go directly into the upper pole piece. This causes both routes to have a certain magnetic resistance.

This means that by turning on the objective coils only, the auxiliary lens will be partially activated as well. By activating the auxiliary coil, with its ampere*turns directed opposite to the objective coils, the magnetic field in the auxiliary gap can be neutralized, so as to turn the auxiliary lens "off". On the other hand if the current is reversed, the magnetic field in the auxiliary gap will be doubled resulting in the setting: "auxiliary lens on". Figures 7.5b and 7.5c show the flux lines around the upper pole piece for both settings.

MLD is able to calculate the strength of the magnetic field on the axis, see figure 7.5d. This information can be used to calculate the lens properties in a certain optical situation. For the EM 420 in scanning mode, thus with auxiliary lens off, the objective lens has a C_s of 2.18 mm and a C_c of 2.16 mm. Philips claims both C_s and C_c of the objective lens to be about 2 mm, so the design in MLD is assumed to be accurate enough. With the simulations it will be possible to adapt the standard objective lens and predict its quality in a situation in which the optical elements for the ion beam have been integrated.

7.3. The objective lens for ions

The simple Einzel lens with three electrodes is well suitable to function as the ion objective lens since the electrostatic field has been restricted between the outer electrodes. The high voltage only needs to be applied to the middle electrode in order that the rest of the instrument can be kept at earth potential. The next step is to find a place near the specimen where the Einzel lens can be placed. In figure 7.6a the standard pole pieces are depicted in between which the specimen is inserted.

The auxiliary lens will not be used in "the Fancier". It is argued in paragraph 4.2 that the interesting modes of operation are TEM-Nanoprobe and STEM mode. In both modes the auxiliary lens is optically switched off. Therefore the auxiliary coil can be removed to create space. The small center yoke of the auxiliary lens doesn't conduct any magnetic flux of the magnetic objective lens in the original scanning mode and that is why this part can be removed as well without influencing the quality of the magnetic objective lens. At the cylindrical space of ⌀30mm and about 15mm high 3 electrodes can be placed. But it can be seen that the topside of the pole piece has the same shape and potential as the lowest electrode and therefore can be used as third electrode. This configuration is shown in figure 7.6c.

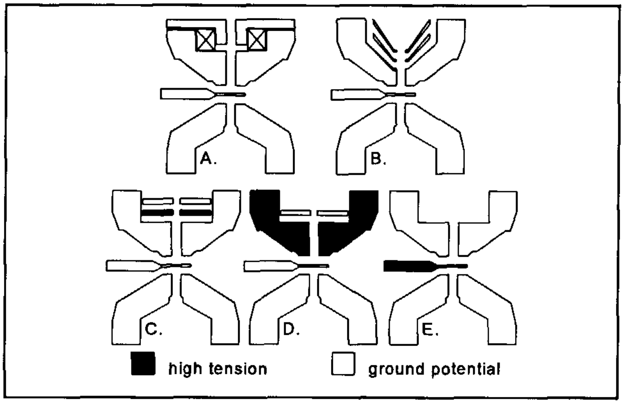

Fig. 7.6. *(a.) the standard objective lens, (b.) maximum material removed from upper pole piece, (c.) Einzel lens above the specimen, (d.) upper pole piece as central part of the Einzel lens, (e.) immersion lens.*

In the attempt to place the ion objective lens closer to the specimen a configuration like in figure 7.6d can be thought of. In this setup the upper pole piece functions at the same time as the middle electrode of the electrostatic lens. The outer electrodes are placed above the upper polepiece and just below it, but still above the specimen. The practical problem introduced by this configuration is the electrical insulation of the upper pole piece from the rest of the instrument. The pole piece which is of cobalt-iron is mounted with high accuracy in a round fitted hole, which will make good electrical contact. In principal this problem could be overcome by a very stiff fit of insulating material. However, in "the Fancier" the upper pole piece also makes contact (electrical as well) to the nickel iron center yoke to conduct the magnetic fluxlines. It is the removal of the auxiliary lens which causes the necessity of a threshold for fluxlines to be canceled. In other words the original gap of 1.2 mm needs to be closed by magnetic conducting material. Since the conduction of fluxlines at the necessary high flux implies electrical conductivity, it is not possible to put the upper pole piece at high voltage while the rest of the instrument remains at earth potential.

The last alternative for the integration of an electrostatic ion objective lens is the immersion lens, in which the ion beam is focused by a decelerating field between the specimen and the upper pole piece. Figure 7.6e shows a schematic drawing of the intended configuration. Again this can be seen as a sort of 'in lens' focusing at the middle electrode plane. The field immersion lens has a very short focal length and because of that low aberrations. On the other hand is has two side effects. When a high voltage is applied to the specimen, the energy with which the ions arrive at the specimen will be diminished largely due to the decelerating field. This is beneficial for most of the fabrication techniques as the resolution improves with lower impact energies as discussed in chapter 3. But an immersion lens makes it impossible to apply the direct implantation technique with the ion beam. Compare this to a standard three electrode Einzel lens. Here the 3rd electrode is at earth potential, the ions are accelerated again before they leave the lens. Therefore the energy of the particles in the ion beam is the same before and after the lens. So focusing and impact energy on the specimen are independent. Another effect of an immersion lens is an increase of the opening angle of the ion beam at the specimen, compared to a standard Einzel lens. As it is demonstrated at the end of paragraph 4.4 this will compensate the low aberration coefficients and causes the aberration spot to increase with stronger decelerating by the specimen. However it is calculated there, the best fabrication resolution of structures can be obtained using the specimen as decelerating electrode as is the case with an immersion lens.

Comparing the various alternatives it will be clear that the least of problems can be expected if the electrostatic lens is placed above the upper pole piece as in figure 7.6c. In order to see if it is able to function properly in this configuration, the quality of such a lens must be determined.

The ion objective lens is still relatively far away from the specimen. It would be better if the electrodes could be placed closer to the specimen. Therefore it is necessary to remove more material of the upper pole piece. To what extend this can be allowed, can be estimated by looking at the lower pole piece. In order not to disturb the conduction of fluxlines only a slanted side to the optical axis can be made. By making the electrodes in a bowl shape as well, the holes in the electrodes come closer to the specimen. This will result in a better objective lens quality. Figure 7.6b shows this configuration.

The ion objective lens in this configuration has now been positioned as close as possible to the specimen while remaining above the upper pole piece. It is clear that the pole piece in the region above the specimen is the limiting factor for the integration of the ion lens.

The shape as it is sketched in figure 7.6b is of minimal proportions in order to conduct the fluxlines without saturation occurring.

Since only the rough position and shape of the electrodes has been determined it is useful to optimize the geometry first. The computer program Second Order Electrode Method (SOEM) (van der Steen, 1992) has been used for this purpose. SOEM is able to optimize a geometry for a lens in various user modes. These are expressed in merit functions. Each merit function has certain design parameters fixed while others remain variable. The computer program searches for an optimum in the merit function. The merit function which was used for the ion objective lens was merit function number 3. This function optimizes the chromatic and spherical aberration coefficients of the ion objective lens for a given opening angle. This was taken because the C2-aperture which determines the opening angle at the specimen is not supposed to be removed during the working with the ion beam. Also the position of the ion objective lens is more or less fixed and therefore need not to be optimized. Because the diffraction aberration is almost negligible, when using the relatively heavy ions, a very small opening angle α at the specimen can be chosen as a fixed parameter. The angle in the optimization was taken 1 mrad. SOEM version 1 was used for the calculation.

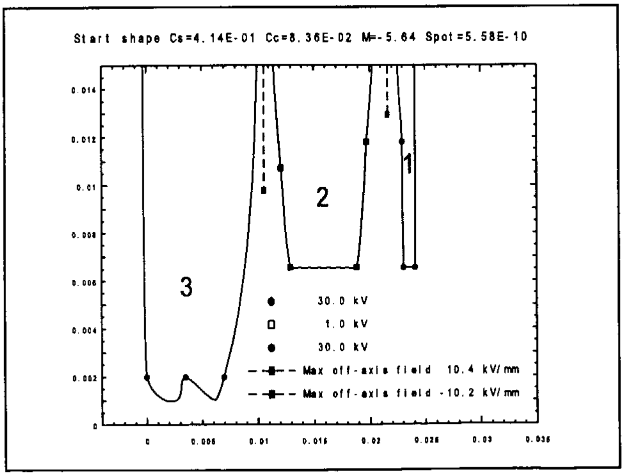

Fig. 7.7. *The initial shape of the electrostatic objective lens.*

The input geometry for SOEM is shown in figure 7.7. The program supposes a circular symmetric shape and therefore displays the configuration in a RZ-plot. The 3 electrodes of the ion objective lens like in figure 7.6b should be recognized in it. Number 1 is the upper electrode. Number 2 is the middle electrode, which is on high voltage. Number 3 is the upper pole piece. As stated in the previous section its shape should not be changed, which is imported in the program by means of 3 fixed points. It determines the thickness of the upper pole piece on 7mm at a radius of 2mm. The minimum thickness of the 2 other electrodes has been set on 1mm.

Figure 7.8 shows the same calculation results but now for the optimized electrostatic lens configuration. The output reflects the shift of the 2 upper electrodes;

- towards the optical axis,
- as close as possible to the upper pole piece,
- and the thickness of the electrodes being as thin as possible.

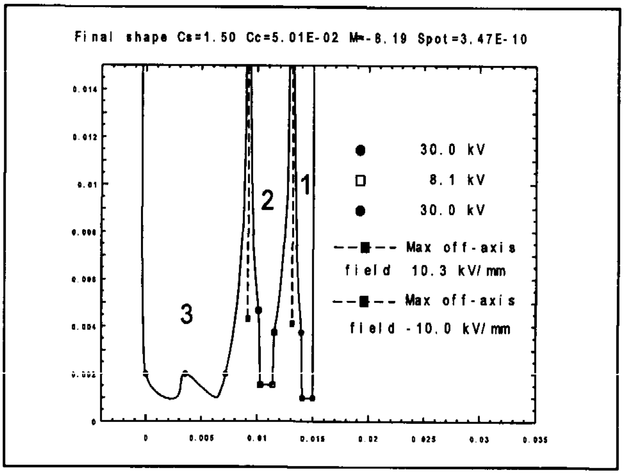

Fig. 7.8. *The final shape of the electrostatic objective lens.*

With these results a final shape for the ion objective lens can be determined:

- The holes in the middle and upper electrode are both chosen to be ⌀2mm. This choice mainly depends on the demands for the secondary electron detector.
- The distance in the Z-direction between the 3 electrodes is 3mm. At the slanted sides, further away from the axis, the distance between the electrodes will be less, but at least more than 2mm. Figure 7.8 shows that the potential on the middle electrode should be a little over 20kV to focus the ions on the specimen. Thus field strengths of more than 10kV/mm will be avoided to prevent disruptive discharges.
- To make the electrodes stiff enough a minimum thickness of 1mm has been chosen.

The lens properties of this electrostatic objective lens have been calculated with the Electrostatic Lens Design (ELD) computer program (Lencová, 1992). This program is able to calculate the focal distance, the (de)magnification, the applied potential to the middle electrode and the chromatic and spherical aberration coefficients. Among the input parameters for the calculation were the design as shown in figure 7.9, the potential on the outer electrodes (1 and 3) and a distance of the object at 414.6 mm from the specimen.

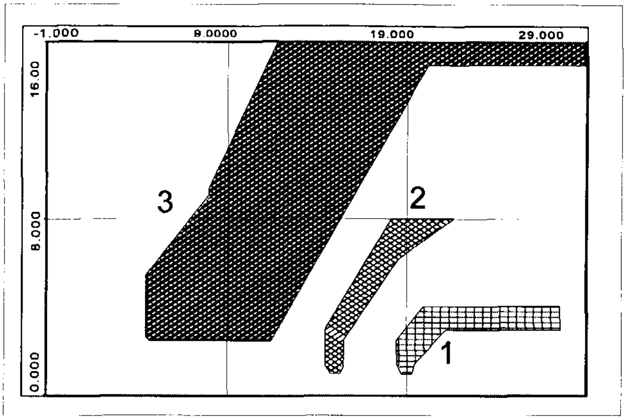

focal length	14.88 mm
middle elec. pot.	19.06 kV
demagnification	-26.64
coefficient C_c	49.5 mm
coefficient C_s	1247 mm

Fig. 7.9. *The input geometry for ELD calculation.*

7.4. The objective lens for electrons

In the EM 420 microscope a magnetic objective lens is used for electrons as was discussed in paragraph 7.2. The demand for sub-nanometer resolution with the electron beam in "the Fancier" can be achieved with this lens. On the other hand the quality of the lens system and thus the magnetic objective lens is not allowed to be deteriorated by the adaption of the electrostatic lens. This means that the upper pole piece may not saturate in the new situation. With the MLD calculations the conduction of fluxlines through the adapted upper pole piece has been examined, as well as the optical properties of the magnetic objective lens.

In order to make place for the ion objective lens and to be able to place its electrodes as close as possible to the specimen, a part of the inner side of the upper pole piece will be removed. This will increase the flux density in the material, for the same amount of fluxlines will have to go through less material. If the flux density in the material of the pole piece exceeds the saturation level, the surplus of fluxlines will have to leave the material since there will be no room for them anymore inside the pole piece. In this

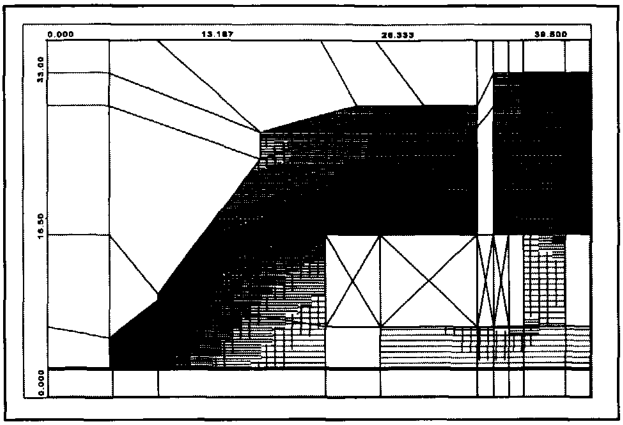

Fig. 7.10. *Fluxdensity in standard upper pole piece with auxiliary lens off, maximum magnetic induction 1.75 Tesla .*

situation the conduction of fluxlines to the gap is at its maximum. If saturation of parts of the upper pole piece occurs before the required field strength has been obtained in the gap, the focal length will be too long or the magnetic field will deform. In both cases the quality of the objective lens will deteriorate and so will the resolution of the image.

Consequently it is necessary to estimate the effect of the removal of an amount of material from the inner side of the pole piece in order to predict if saturation of the pole piece in the new situation will occur. The magnetic fluxlines through the upper pole piece

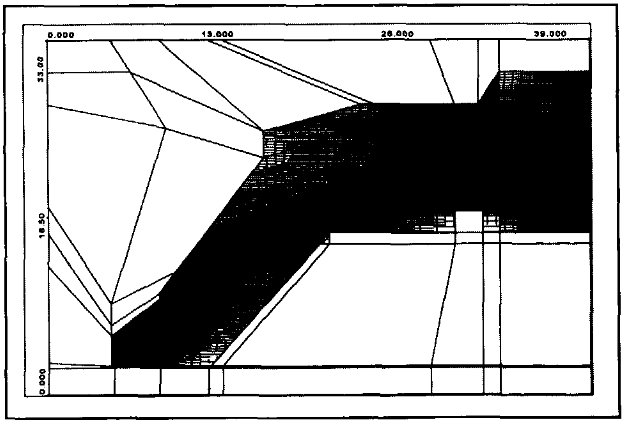

Fig. 7.11. *Fluxdensity in the adapted upper pole piece, maximum magnetic induction 1.87 Tesla.*

for the standard microscope in scanning mode, thus with auxiliary lens off, are drawn in figure 7.5b. MLD is also able to calculate the flux density at every position in the lens design. In figure 7.10 the same upper pole piece is displayed but now the areas with different flux density are reflected. The number of Ampere*turns through the objective coils is 7500 and through the auxiliary coil -825. This setting makes sure that no magnetic field exists at the auxiliary gap.

In the new situation the auxiliary lens has been removed from the pole piece. The auxiliary coil plus center yoke and nonmagnetic ring have made place for the electrodes of the ion objective lens. And in order to place the electrodes near to the specimen the pole piece now has a topside which follows the contours of the outside. The gap of 1.2 mm between the upper pole piece and the center yoke has been filled up because the auxiliary lens has been removed as well. This design has been put in MLD and the flux density has been calculated. The outcome is shown in figure 7.11, which gives the flux density in the upper pole piece in its new form. The number of Ampere*turns through the objective coils is the same as in the calculation of the standard situation, namely 7500 At. The saturation level of the Cobalt-iron of which the pole piece has been made is 2.4 Tesla. It can be seen that the flux density stays below this value in both cases. On the basis of this calculation alone, the conclusion would be that the adaptation of the upper pole piece doesn't have a significant effect on the conduction of fluxlines through the pole piece.

However, MLD is not able to simulate the effect of the holes in the pole piece for the standard Secondary Electron Detector (SED). Although only one of them is used for the SED, four holes have been made in the pole piece to obtain an octupole effect, which has a smaller effect on the shape of the electron beam than a lower multipole effect. Nevertheless the holes affect the conduction of the fluxlines. The influence of the holes will be larger when there is less material around them to conduct the fluxlines. At maximum 55% of the conducting material is removed for the holes on a section through the optical axis. So all fluxlines should go through 45% of the material left, at the position off the holes. It is shown in figure 7.11 that the average flux density at the position of the holes is about 1 Tesla. This results in a flux density of 2.2 Tesla if the holes are included, which is just below the saturation level.

The current through the objective coils in the new situation is 7500 Ampere*turns, just like in the simulation with the objective lens in Scanning mode (auxiliary lens "off" = -825 At through the auxiliary coil). The position of image on the specimen and the position of the geometrical spot in front the objective lens are the same in both calculations. MLD calculates the magnetic field in the objective lens and subsequently the energy of the particle, required to focus the particles at the desired plane. The 7500 At through the objective coils have been chosen to come close to the real situation in which 120 kV electrons are focused by the objective lens. When MLD has found the energy with which the particle can be imaged as specified, it calculates at the same time the aberration of the objective lens in this situation. In the original STEM mode the objective lens has a C_c of 2.16 mm and a C_s of 2.18 mm, for electrons with a relativistic energy of 111,675 eV (see paragraph 7.2). This means the electron must have been accelerated with a potential of about 101.5 kV. In the objective lens with adapted pole piece as shown in figure 7.11 the C_c is 2.16 mm and C_s is 2.19 mm, for electrons with a relativistic energy of 137,575 eV. The real acceleration voltage for this relativistic energy must be 122.8 kV.

From these results the conclusion can be drawn that the quality of the objective lens with adapted pole piece for the electrostatic objective lens is the same as in the original situation. The lens is even able to focus electrons with a higher energy for the same excitation of the objective coils. This effect can be explained by the fact that the gap between the upper pole piece and the center yoke has been closed in the new situation. As a result the total resistance of the magnetic circuit has been reduced.

Table 7.1. *Lens properties of the standard magnetic objective lens and of the magnetic objective lens with electrostatic lens off and on.*

	Optical mode of the magnetic objective lens.		
Properties:	stnd.magn.obj.lens	Elec.stat. lens off	Elec.stat.lens on
No. of Amp*turns	7500 A*t	7335 A*t	7318 A*t
Demagnification	-85.7	-85.7*	-84.3*
Focal length	2.87 mm	2.87 mm	2.92 mm
C_s	2.18 mm	2.19 mm	2.20 mm
C_c	2.16 mm	2.16 mm	2.18 mm

Also the effect of the electrostatic objective lens on the primary electron beam must be examined. Firstly because it would allow both beams to be switched rapidly or even to be operational at the same time. The switching time is limited mainly by the magnetic lenses, which need time for the magnetic field to be stabilized. And secondly because the high voltage on the middle electrode will also be used for the secondary electron detector as will be discussed in the next chapter. In order to compare the magnetic objective lens properties, in a situation with the electrostatic ion objective lens turned on or off, the computer program LENSPROP (Chmelik, 1989) has been used. Table 7.1. shows the lens properties for both situations. The standard magnetic objective lens is included in this table as well.

From C_s and C_c the conclusion can be drawn that the quality of the magnetic objective lens does not deteriorate significantly. The focal length decreases slightly which results in a negligible change in demagnification. And since the electrostatic lens also focuses the electron beam a little, it is obvious that the magnetic objective lens should focus a little bit less. This results in a lower excitation of the objective coils.

7.5. The design configuration

This paragraph will deal with the realization of the principle solution of the functions which have been derived in the previous paragraphs. An exploded view of the design is shown in figure 7.12a. It includes the adapted upper pole piece, the middle electrode, the Macor frame that holds the electrodes, the upper electrode, the lid for the vacuum sealing and a ring that conducts the magnetic field and that will be used at the same time to clamp the lid on the upper pole piece.

Figure 7.12b shows the configuration when the parts are fitted together. The outside has the same shape as the original pole piece, except the space for the auxiliary coils has been filled. This means that the complete configuration can be assembled outside the microscope and inserted like the exchange of an upper pole piece.

The central part is the Macor frame. It will fix the positions of the upper and middle electrodes of the electrostatic objective lens. On the other hand the Macor frame will be fixed with respect to the upper pole piece. However Macor is a hard and brittle glass ceramic. Consequently the surface is not suitable to function as one of the sliding surfaces of the fit. Therefore a metal ring has been fixed around it. It is made of non-magnetic stainless steel to avoid interference with the magnetic field.

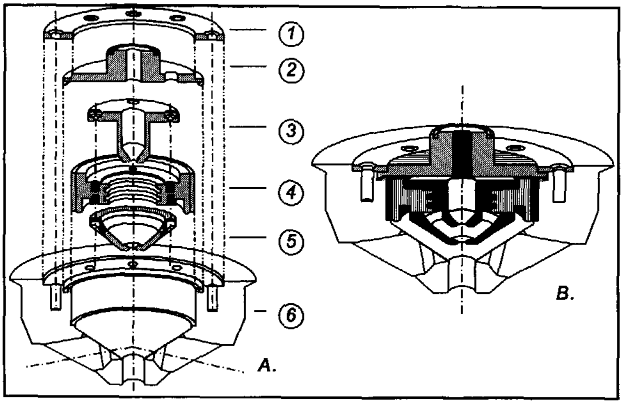

Fig. 7.12. *The integrated magnetic and electrostatic objective lens in exploded view and assembly. 1. cobalt-iron clamp ring, 2. vacuum lid, 3. upper electrode, 4. Macor frame, 5. middle electrode, 6 upper pole piece.*

The second function is the insulation of the high voltage on the middle electrode of the electrostatic lens. This determines the shape of the frame the most. The maximum flash-over voltage depends on the type of insulating material used. Macor consists mainly of a mix of oxides, including SiO_2 (46%), Al_2O_3 (16%), MgO (17%) and K_2O (10%). The maximum applicable field strength is given by

$$E = \frac{C}{\sqrt{d}} \tag{7.3}$$

d= distance [mm]
C= material factor, macor: 10 [$kV.mm^{-0.5}$]

It is clear that the distance by the way of the surface of the Macor between middle and outer electrodes can be made larger by groves in the Macor as shows in figure 7.12. The important thing is to shape surfaces such that the field strength is directed to the vacuum, in order to prevent secondary electrons, created by the leakage current, from falling back on the surface and starting a small avalanche of secondary electrons, headed to the middle electrode, resulting in flash-over.

The shape of the upper and middle electrodes is equal to the one drawn in figure 7.9. The material from which these electrodes have been made is titanium. For vacuum purposes the whole lens should be heated to over 100°C. However if the separate parts have different expansion coefficients, the heating will lead to material stress in the connected parts. It is not desired that the electrodes will end up at different positions after the heating procedure due to hysteresis effects. In the temperature range from 20 to 100°C titanium has a linear thermal expansion coefficient varying from 8.6 to 9.4 μm/(m.°C). The coefficient for Macor in the temperature range from 20 to 400°C is 9.4 μm/(m.°C), which is practically the same as for titanium. Another reason why titanium has been chosen is that it is non-magnetic. This is important for a proper working of the magnetic objective lens.

The most important element in this magnetic objective lens, the upper pole piece, does have a function in the electrostatic objective lens, as lower electrode. The electrostatic field between the middle electrode and the upper pole piece should be rotationally symmetric for a pure lens effect. There are two factors which could disturb the symmetry of this field near the optical axis.

1. There are four holes in the standard pole piece for the secondary electron detector. This will have an octupole effect on the primary beam . To minimize this effect the position of the holes is designed not to intersect with the bore of the pole piece. This means that the bore is still rotational symmetric which leads to a better field around the optical axis.

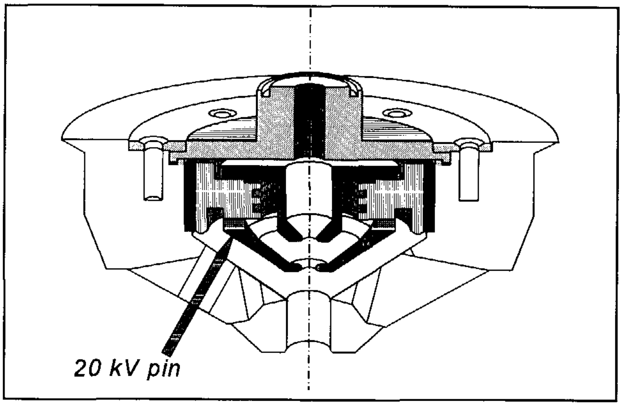

Fig. 7.13. *The high voltage feedthrough construction.*

2. The high voltage wire leading to the middle electrode will influence the beam if it is visible by the particles on the axis. To avoid disruptive discharges the high voltage wire needs to be fed through one of the four holes as discussed above.
   To reduce the effect of the part of the high voltage feedtrough that can be seen by the beams, the standard hole should be filled with non-magnetic metal. This reduces the distance of the middle electrode and the upper pole piece, which causes the field of the high voltage pin to lose strength in the direction of the optical axis. In the

metal a smaller hole can be machined for the actual feedthrough. The construction is shown in figure 7.13.

In the standard pole piece the auxiliary coil is situated in a small space at air pressure. On the side of the pole piece the specimen is positioned in a vacuum surrounding. Therefore the upper pole piece is a part of the partition of the vacuum at the specimen and the air pressure. The dividing line goes from the O-ring, around the outer side of the pole piece, to the indium sealing which connects the linertube to the pole piece. In the new situation, shown in figure 7.14, the O-ring is at the original position. But the material of the upper pole piece which previously led to the connection of the linertube, has been removed to make place for the electrostatic objective lens. Therefore an extra sealing part is required, which will provide the partition of vacuum and air between the end of the liner tube and the upper pole piece. This part is the vacuum lid that is connected with an indium sealing to the upper pole piece. To preserve the quality of the sealing a constant pressure on it should be maintained. This is realized with a cobalt-iron clamp ring.

After assembling the elements, the whole combined objective lens can be mounted like the exchanging of an upper pole piece.

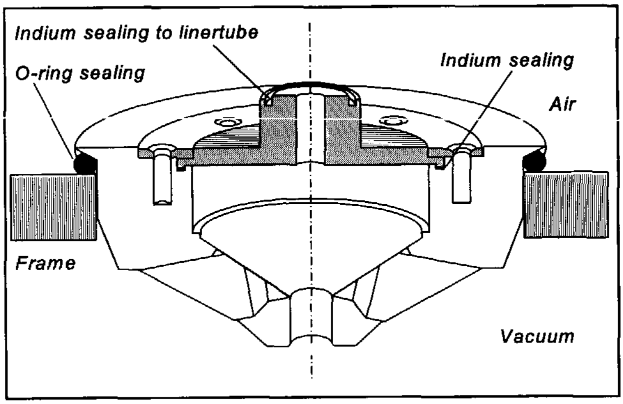

Fig. 7.14. *The vacuum sealing assembly.*

7.6. Summary

A high resolution particle beam instrument that combines an ion and an electron beam on the same optical axis, needs at least one combined lens: the objective lens. To obtain the smallest aberration contribution to the probe the final lens has to be close to the specimen.

Only in case of a combined lens this can be achieved for both beams. For the electron beam the standard magnetic lens can be used. An electrostatic Einzel lens has been integrated with the magnetic lens, because the magnetic lens is too weak to focus the ion beam properly. The upper pole piece functions as part of the magnetic lens and as third electrode of this electrostatic Einzel lens.

The quality of the magnetic lens has not been deteriorated. It still has a spherical and chromatic aberration coefficient of 2.2 mm. The new electrostatic lens has a spherical and chromatic aberration coefficient of 1247 mm and 49.5 mm respectively. These parameters allow the resolutions of fabrication and observation as discussed in chapter 4. The construction is made such that the integrated lens can be mounted in the instrument in the same way as a standard upper pole piece.

References

Chmelik, J., *Internal Report of Institute of Scientific Instruments of the Czechoslovak Academy of Sciences*, 1989, not published

Cleaver, J.R.A. and H. Ahmed, *A combined electron and ion beam lithography system*, Journal of Vacuum Science and Technology B3(1), 1985, pp. 144-147

Kelder, M.C.W., *Design and Fabrication of an Objective lens for ions, with an integrated Secondary Electron Detector, for a Scanning ion- and electron beam instrument*, Delft, 1994

Lencová, B. and G. Wisselink, *Electrostatic Lens Design program package*, licensed by Delft Particle Optics Foundation, 1992

Lencová, B. and G. Wisselink, *Magnetic Lens Design program package*, licensed by Delft Particle Optics Foundation, 1992

Rempfer, G.F., *Unipotential electrostatic lenses: Paraxial properties and aberrations of focal length and focal point*, Journal of Applied Physics 57(7), 1985, pp. 2385-2401

Steen, H.W.G. van der, *Program package for the optimization of electrostatic lenses*, licensed by Delft Particle Optics Foundation, 1992

8. The secondary electron detector

This chapter has been realized in close cooperation with M.C.W. Kelder as part of his master reserach.

Introduction

When the ion or the electron beam is on the specimen, it is needed the know where it is located. It is also needed to obtain information about the structure of the specimen. A secondary electron detector can fulfil these demands. A primary particle of the ion or electron beam that hits the specimen, can lose its energy by inelastic collisions with the atoms near the surface. Consequently electrons belonging to these atoms will be excited and they will be able to leave the material if they have enough energy. This subject is discussed in greater detail in chapter 2 and 3. All escaping electrons with an energy below 50 eV are defined as secondary electrons.

The number of secondary electrons depends on the material of the specimen and the energy of the primary beam. The energy distribution and the angular distribution with which the electrons are emitted from the specimen are given in figure 8.1 (Reimer, 1985). Also the surface structure is reflected in the number of secondary electrons that can escape from the specimen, because secondary electrons that are emitted from a location at the backside of the detector are less effectively collected by this detector.

To obtain the best information as many as possible secondary electrons should be detected. This can be realized with a Secondary Electron Detector (SED). In general it *has two functions: collecting secondary electrons coming from the specimen and amplifying the collected current. The first aim can be optimized by the place and shape of the collector, while for the second aim the type of detector can be chosen.*

The type and place of the detector in "the Fancier", in order to collect as many as possible secondary electrons without disturbing the primary beam, will be discussed in this chapter. Also the detector efficiency will be discussed.

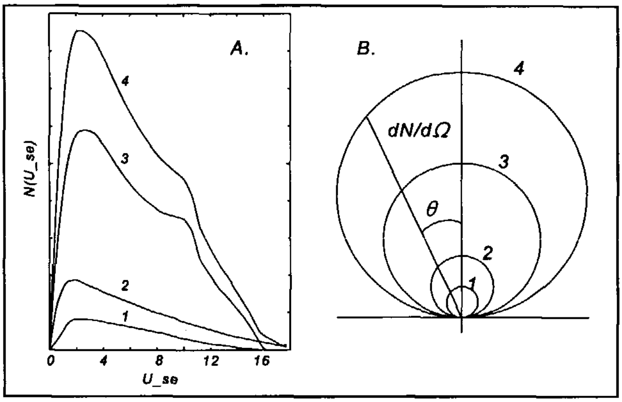

Fig. 8.1. *(a) Energy and (b) angular distribution of secondary electrons. Contributions come from: 1. core electrons, 2. electron-electron scattering, 3. plasmon decay and 4. shows the total distribution (Reimer, 1985).*

8.1. The type of the Secondary Electron detector

In principle the secondary electrons coming from the specimen can be seen as a very small current. If the electrons are collected on a metal conductor the current can be detected and electronically amplified. With this signal it is possible to construct an image of the specimen. However the probe current of the ion beam is only 10^{-14} A (see chapter 4). This means a secondary electron current of 10^{-14} A if a secondary emission coefficient of one is assumed. The secondary emission coefficient is the ratio between the secondary electron current and the current of the primary beam. For these currents the noise of the electronics, compared to the relatively small number of secondary electrons, make electronic amplification an inaccurate method for detection.

Therefore the secondary electron current needs to be pre-amplified in a natural process.

Two processes will be discussed in greater detail: a channeltron detector and a scintillator detector.

8.1.1. A channeltron detector

An electron channel is a type of electron multiplier tube. Earth alkali oxides (e.g. ZnO-TiO_2), the material the channeltron is made off, has a secondary emission coefficient larger than one. This electron current amplification can be used to magnify the small secondary electron current (Hughes, 1967) (Murata, 1996). The electrons collide in vacuum with the entrance of the channeltron tube. This current is amplified with the secondary emission coefficient (2.5 for ZnO-TiO_2) and then collected. This process is repeated about 100 times in the tube, which makes an amplification factor of 10^8 possible. Figure 8.2a shows the principle. The multipliers take the form of a tube about 1 mm in inner diameter. A bias of about 4.5 kV causes a continuous voltage drop along the high resistive inner wall of the tube and secondary electrons can be generated and accelerated, thus forming a cascade.

The impulse rise time is 2.0±0.3 ns for 4.5 kV bias voltage. This is the time that is needed to rise the impulse from 10% to 90% of its maximum. A fast rise time means a high detection efficiency and it is therefore important.

This detector has an extremely high signal to noise ratio as it is in principle meant for single electron counting but it is sensitive for the vacuum conditions. Hydrocarbons in the residual gas cause considerable contamination on the tube. This can change the secondary emission coefficient significantly and therefore the amplification factor.

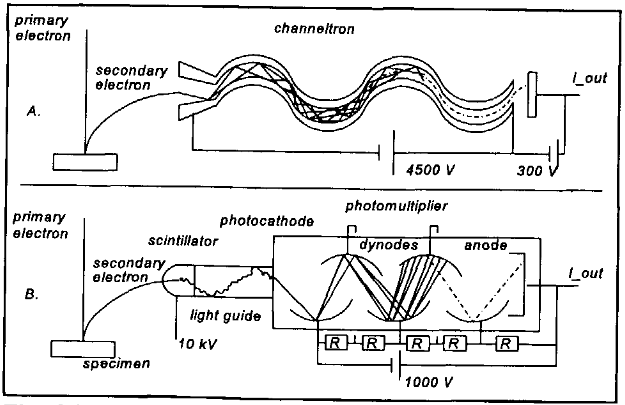

Fig. 8.2. *Secondary electron detection with (a) channeltron detector and (b) Everhart-Thornley detector.*

8.1.2. A scintillator detector

A widely used detector for secondary electrons is the scintillator-photo multiplier combination often known as the Everhart-Thornley detector (Reimer, 1985). It is depicted in figure 8.2b. The secondary electrons are accelerated to the scintillator with a bias of 10 kV at the conductive coating, which can be a thin evaporated film of aluminum of the order of a few tens of nanometers thick. The accelerated electrons penetrate this metal coating but the latter is thick enough to reflect and absorb light quanta. The secondary electrons, accelerated to 10 keV can produce a large number of electron-hole pairs inside the scintillator as the mean energy to produce an electron-hole pair is 2.21 eV for YAG (Daberkow, 1991), a specific scintillator material.

The recombination of electron-hole pairs in luminescence centers generates light quanta. They are guided by reflection at the metal coating and by total reflection in the light guide to the photo multiplier. For a typical system of the order of 1-10 photo electrons will be generated per secondary electron that arrives at the scintillator. Though this detector system is inefficient in the conversion of electron-hole pairs into light quanta and light quanta into photo electrons, it shows a high signal-to-noise ratio.

As the decay time of the scintillator material is less than 100 nanoseconds, the time constant will be limited by the drift time of electrons through the photo multiplier which is of the order of 10 nanoseconds. This detector system therefore forms a wideband amplifier which converts all spatial frequencies into a video signal even when working at TV scan rates.

8.2. The position and shape of the Secondary Electron detector

In general electrons in a homogeneous magnetic field circle around an axis parallel to the direction of the magnetic field. If they have a velocity in the direction parallel to this axis as well, they will move in spirals around the same axis through the magnetic field. The trajectory of such an electron has the shape of a helix. The lower the energy of the electrons is, the smaller the radius of the helix will be. Since the energy of the secondary electrons is relatively low and because the direction of the magnetic field on and near the optical axis is almost parallel to the optical axis the secondary electrons are not able to escape the magnetic field in the gap sideways. The only possible way out of the magnetic field is upwards into the upper pole piece where the magnetic field gradually disappears. As the field strength lowers, the radius of the helix grows.

The common way to collect the secondary electrons is to deflect them, as they leave the magnetic field, with an attracting potential to a detector (Imeson, 1985). For this reason the upper pole piece contains an extra hole, which comes out near the optical axis, see figure 8.3. In this hole the secondary electron detector can be inserted.

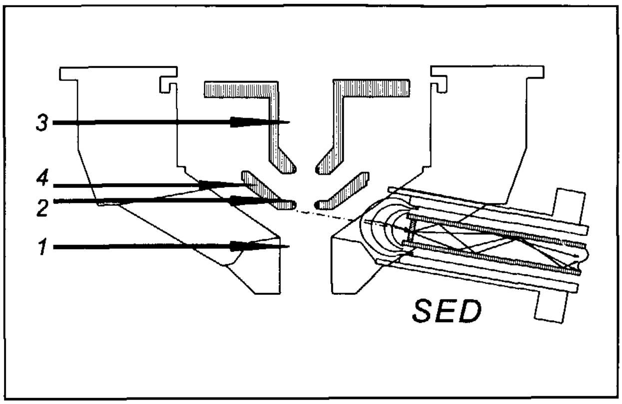

Fig. 8.3. *The standard SED and the positions for the SED in the dual beam instrument.*

Figure 8.3 shows schematically the longitudinal section of the upper pole piece, the electrodes and the top of the standard SED, an Everhart Thornley detector (see paragraph 8.1). The most important modification compared to the standard pole piece is the slanted side at the inner side of the pole piece. By the removal of material for this side the small hole near the axis has lost its shape. The small hole was used to reduce the field strength of the accelerating potential of the SED in order to form a deflecting and attracting potential of a few hundred Volts for the secondary electrons near the optical axis. Due to the adapted, more open configuration in the Fancier this potential could rise, which will have more influence on the primary beams. Another problem originates from the extra electrodes: they screen the detector. This might influence the shape of the accelerating field in a way that the secondary electrons are not deflected sufficiently to the detector. This becomes even a more important problem when the ion beam is the primary beam. The high voltage on the middle electrode will disturb the attracting field seriously and in this situation the question arises whether the secondary electrons will arrive at the detector at all.

Therefore it might be better to reposition the existing detector or even to develop a new collecting method. However, in both types of secondary electron detection, as described in the previous paragraph it is essential to attract the secondary electrons from the optical axis to the detector and to accelerate the secondary electrons to the tube or scintillator. Alternative attraction techniques for straight forward deflection have been described (Kruit, 1991) (Tsuno, 1996).

Figure 8.3 shows the positions of four fundamental alternatives. These four alternatives should be compared. As stated in chapter 7, next to the functioning of the SED itself, the nearby functions should be taken into account. These are of course the functions of the electrostatic objective lens for the ion beam and the magnetic objective lens for the electron beam. The expected difficulties in implementation have also been included in the weighing for the best alternative. The functions or aspects have been translated in the following criteria:

- expected collecting efficiency of the SED
- quality of the electrostatic objective lens
- quality of the ion beam
- quality of the magnetic objective lens
- quality of the electron beam
- practical implementation of the SED

For each alternative a short description will be given in which the criteria are evaluated. An overview is listed in table 8.1.

Alternative 1.

The detector deflects and attracts the secondary electrons as soon as they leave the magnetic field and before they are attracted by the electrostatic field of the ion objective lens. This alternative corresponds the most to the standard SED. Therefore it can be implemented easiest. However, in order to work properly the holes should be drilled lower in the pole piece, to keep the attracting potential low on the optical axis, or the electrostatic objective lens must be shifted upwards, to make use of the standard holes and detector. Anyhow the quality of one of the objective lenses will deteriorate. The other properties (collection efficiency, influence on both beams) will be about the same as the standard detector which are good but might have to be better for this high resolution instrument.

Alternative 2.

The secondary electrons are deflected to a detector at or near the middle electrode of the ion objective lens. It needs a very strong deflection field because the secondary electrons will be accelerated to approximately 20 kV in the hole of the middle electrode. This will deteriorate the ion beam strongly since the ions are exactly decelerated in the middle of the electrostatic objective lens. It will be clear that the focusing of ions and the electron will be affected negatively as well.

Alternative 3.

The secondary electrons are deflected and collected after they have gone through the electrostatic lens. This alternative is expected to have good secondary electron collection properties because the secondary electrons are "aligned" by the high voltage on the middle electrode. Every secondary electron will be pulled into the hole of the middle electrode. Finally when they are decelerated again, just above the upper electrode, the electrons can be attracted with a deflection grid, behind which an accelerating potential could be placed. A negative aspect is the inconvenient position of detection with respect the high voltage of both the middle electrode and the detector. Next to that this type of detector still needs a relatively large deflection field on the optical axis which is also present in the standard EM 420, but might has to be prevented in "the Fancier" because of the added ion beam.

Alternative 4.

The high voltage on the middle electrode of the ion objective lens is used for the collection of the secondary electrons. The electrode is put at a decelerating potential for ions of +19 kV (see figure 7.9). However the rotationally symmetric field cannot be used directly to attract the secondary electrons off-axis, because it is to be expected that the middle electrode functions as a lens for the secondary electrons.

This means that a secondary electron is accelerated towards the middle electrode, deflected to the optical axis and finally disappears through the hole in the middle electrode. To avoid losing these secondary electrons completely through the upper electrode, the latter can be put at a small negative potential. As the secondary electrons have an energy less than 50 eV the potential on the optical axis near the upper electrode will function as a mirror. The electrons might come off-axis, depending on the way they are reflected near the upper electrode and they can hit the middle electrode. But if they are still focused by the middle electrode, they will very likely be retarded by the magnetic field, so the secondary electrons will spiral between the upper electrode and the pole piece until they can come far enough off-axis to hit the middle electrode: an electron trap is created. A similar mechanism is used in a detector described by Kolarik and Mejzlik (Kolarik, 1990).

This alternative has negligible deteriorating effects on both the ion and the electron beam as well as on both objective lenses. This is because the potential for the detector is rotationally symmetric and therefore it only influences the primary beams in a rotationally symmetric way (additional lens effect). It can be corrected.

So at the same time the decelerating potential for the ions of about +19 kV (see figure 7.9) is used as an accelerating potential of the secondary electrons. Since the secondary electrons are accelerated to the part which actually holds the potential, the middle electrode can function as a scintillator as well. A consequence is that the scintillator must be able to conduct the light pulses to an optical guide. It is not straight forward how this can be realized. Also the detector efficiency is not known in advance. Some electrons can escape out of the electron trap, but it is unknown how many secondary electrons will return to the specimen. Therefore it will be discussed in paragraph 8.4. But if these aspects can be made satisfactory then this alternative of secondary electron detection appears to be the best as it is completely rotationally symmetric.

Table 8.1. *Evaluation of the criteria for the four fundamental alternatives. ++ means that considering a criterion a certain alternative is to be preferred. -- makes an alternative nearly to be excluded. + and - are values in between. +/- expresses that it is uncertain how the alternative will affect a function or criterion.*

possible place SED: Criteria:	(1)	(2)	(3)	(4)	(5)	(6)
between ion lens and magn. field + defl. field (Alt. 1)	+	-	+	-	+	++
at middle electrode of ion lens + defl. field (Alt. 2)	--	--	-	+	-	-
above ion lens + defl. field (Alt. 3)	+	+	+	++	+	-
middle electrode of ion lens (Alt. 4)	+/-	++	++	+	++	+

The outcome of the comparison between the alternatives is given in table 8.1. It is concluded that alternative four is the best. However, it is also the most complicated secondary electron detection strategy. A consequence of this detector strategy is that the electrons will land on the middle electrode. It is already mentioned in paragraph 8.1 that electronic amplification of this current has a non-sufficient signal-to-noise ratio. But also the channeltron cannot be used: electrons are not attracted to the opening of the tube but will end on the whole middle electrode. Therefore this electrode should be realized as scintillator. This converts the electrons into light which internally is reflected to the light guide.

8.3. Secondary Electron Detector collection efficiency

The detection efficiency is a combination of the light collection efficiency of the type of Secondary Electron Detector (see paragraph 8.1) and the electron collection efficiency. This collection efficiency reflects the amount of generated secondary electrons that is able to reach the detector. In order to estimate if, how many, and how the secondary electrons hit the middle electrode the computer program TRASYS (Wisselink, 1992) (Barth, 1990) has been used. TRASYS is able to calculate trajectories of charged particles which move through electrostatic or magnetic fields. In this case the fields of the electrostatic and magnetic objective lens have been put in the program. The forces of the magnetic field on the electron are derived by TRASYS by means of an MLD file (Lencová, 1992). The forces of the electrostatic field are calculated with the charge density method described by Harting and Read (Harting, 1976). The distribution of points on the electrodes is shown in figure 8.4. The middle electrode has been put at 19.06 kV (see figure 7.9).

Starting parameters of importance for the program are the initial position, the initial

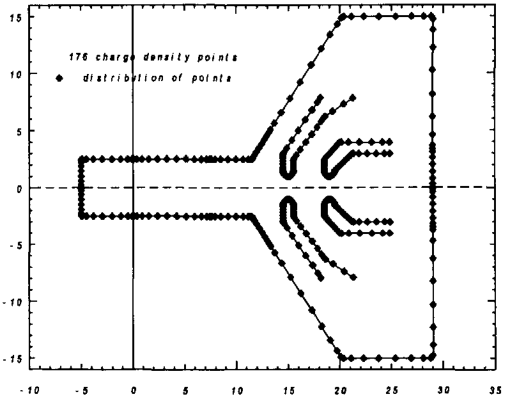

Fig. 8.4. *The distribution of points for the charge density method.*

angle in the RZ- and XY-plane and the initial energy of the secondary electron. The initial position is on the specimen (z=0) and on the optical axis (x =y= 0). For a number of opening angles in the RZ-plane, from 0 to 90 degrees, the trajectories have been calculated. The majority of secondary electrons has an energy between 0 and 12 eV, as shown in figure 8.1. Therefore the influence of different energies is examined by a series of calculations for energies below 12 eV. As stated in the previous section, the upper electrode has been put at a negative potential (-100V) to prevent secondary electrons from escaping through the hole in the upper electrode.

When examining the data of about 50 trajectories only three different types of trajectories are found. The first is shown in figure 8.5. In a close-up of the upper pole piece and the two electrodes, the RZ-plot of the trajectory of a secondary electron is given, which has left the specimen under an angle of 45 degrees with an energy of 3 eV.

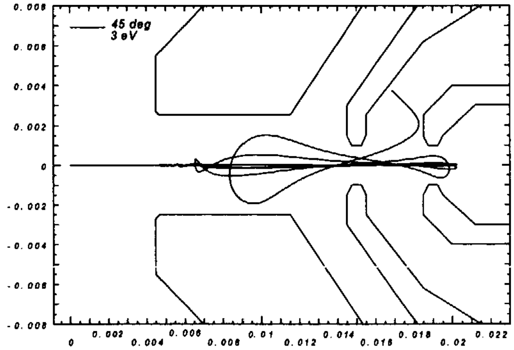

Fig. 8.5. *RZ trajectory of a 3eV secondary electron leaving the specimen with a 45° opening angle.*

When the secondary electron has been emitted from the specimen it starts to move in spirals. Each time the trajectory crosses the optical axis again the sign of R is reversed in the RZ-plot. The real trajectory in the XY-plane is shown in figure 8.6 for the same secondary electron. The smallest set of rings belongs to the helix at the beginning of the trajectory. The diameter of this helix is in the order of 5-10 μm and increases when the strength of the magnetic field decreases. As soon as the secondary electron leaves the magnetic field, its stops moving in spirals completely and is pulled into the hole of the middle electrode. From the middle electrode to the upper electrode the electron is decelerated until an equipotential of the electrostatic objective lens is reached at which the velocity in the Z-direction vanishes. Then the direction will be reversed into the electrostatic lens again. This does not mean that the velocity in the R-direction is zero at the turning point. Whether the velocity in the R-direction does or does not become zero depends on whether the incident trajectory does or does not come in perpendicular to the equipotential plane, at which v_z=0. If the velocity in the R-direction is not zero, at v_z= 0, the secondary electron might come off axis while decelerating. After the direction of the secondary electron has been reversed near the upper electrode, it will be accelerated again into the hole of the middle electrode.So, whenthe electron is out of the influence of the decelerating electrode it will move to the axis again. It will not reach the middle electrode.

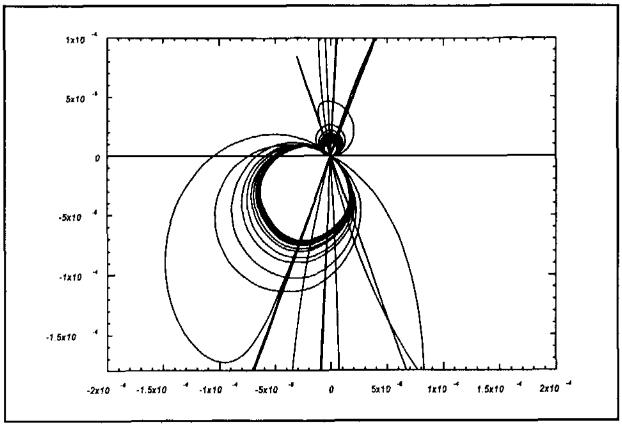

Fig. 8.6. *XY trajectory of a 3eV secondary electron leaving the specimen with a 45° opening angle.*

Since the upper pole piece (the lower electrode) is at earth potential, the secondary electron will be decelerated but cannot be mirrored in an electrostatic way. However, the magnetic field of the objective lens can act as a mirror for certain electrons (Landau, 1971). The electron moves in the direction of increasing axial component of the magnetic field, so that its tangential velocity increases. According to the energy conservation law, the axial velocity of the electron must decrease. At a certain point this velocity falls to zero and the entire kinetic energy of the electron is contained in the tangential velocity component. At this moment the electrostatic field of the middle electrode acts on the electron, so that its Z-velocity is reversed again into the electrostatic lens. By this reflection the electron can come even more off axis.

The whole process can repeat itself as the electron is pulled back into the hole of the middle electrode. In this way the electron can oscillate several times between the upper electrode and the upper pole piece, each time coming more off axis. Finally the electron slides between the upper and the middle electrode after which the electron will be attracted to the topside (shorted to TS) of the latter one, see figure 8.5, or it hits the edge of the hole at the center (shorted to C) of the middle electrode like in figure 8.7. This RZ-plot is of a secondary electron coming from the optical axis at the specimen, with an angle in the RZ-plane of 45 degrees and with an energy of 5 eV.

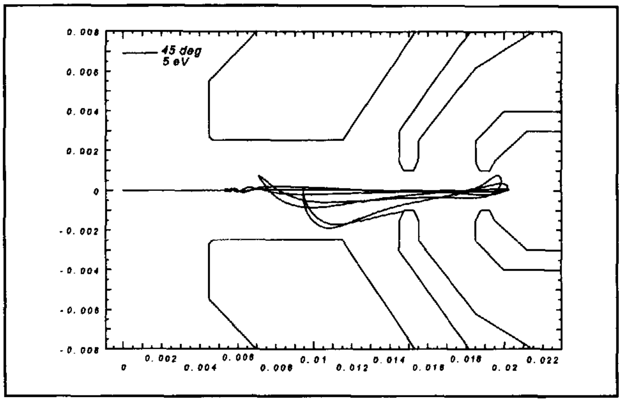

Fig. 8.7. *Trajectory of a 5eV secondary electron leaving the specimen with a 45° opening angle.*

However, if the trajectory of the electron, near the upper electrode, is perpendicular to the equipotential plane at which v_z becomes zero, then the secondary electron will come to a complete standstill in this equipotential plane. According to the energy conservation law, the potential of the equipotential plane at which it stops will be equal to the energy of the secondary electrons at the specimen. The result of this situation will be that the electron will follow its original path backwards.

The result is shown in figure 8.8 for the trajectory of a 10 eV secondary electron, which has been emitted with an opening angle of 45 degrees in the RZ-plane. The secondary electron is reflected near the upper electrode and penetrates the magnetic field again and falls back on the specimen. Whether the electron will penetrate the magnetic field, instead of being reflected by it, depends on its energy, the angle of incidence, and the distance to the optical axis, at the moment it enters the magnetic field. This is a part of the so called "magnetic bottle effect" (Landau, 1971).

In order to be able to estimate how many of the emitted secondary electrons will hit the middle electrode, the total number of secondary electrons emitted per primary electron and the information about the energy and the angular distribution of the secondary electrons must be known. Subsequently for every energy at different opening angles it must be determined whether the secondary electron hits the middle electrode or not. The result is listed in table 8.2

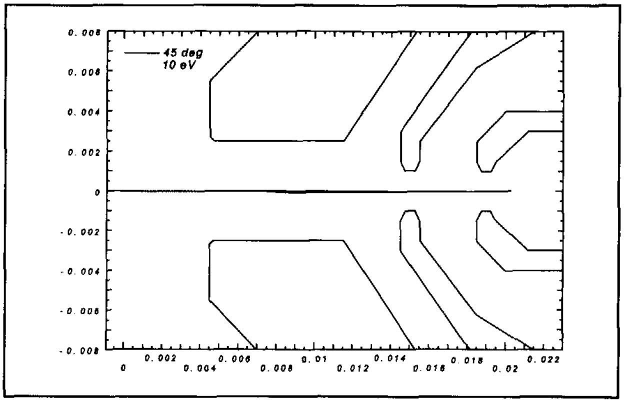

Fig. 8.8. *Trajectory of a 10eV secondary electron leaving the specimen with a 45° opening angle.*

Table 8.2. *The result of the trajectories of secondary electrons for different energies and opening angles with respect to the specimen normal. Electrons end up "back on the specimen", on the upper electrode ("electrode 1") or on the middle electrode ("electrode 2").*

	Energy of Secondary Electrons		
Angle (RZ)	3 eV	5eV	10eV
5 degrees	back on specimen	back on specimen	back on specimen
10 degrees	back on specimen	back on specimen	back on specimen
15 degrees	back on specimen	on electrode 2 (TS)	back on specimen
20 degrees	**on electrode 1**	**on electrode 1**	back on specimen
25 degrees	on electrode 2 (TS)	back on specimen	on electrode 2 (TS)
30 degrees	on electrode 2 (TS)	back on specimen	back on specimen
35 degrees	**on electrode 1**	**on electrode 2 C**	on electrode 2 (TS)
40 degrees	back on specimen	on electrode 2 (TS)	back on specimen
45 degrees	on electrode 2 (TS)	**on electrode 2 (C)**	back on specimen
50 degrees	on electrode 2 (TS)	**on electrode 2 (C)**	on electrode 2 (TS)

55 degrees	on electrode 2 (TS)	back on specimen	back on specimen
60 degrees	**on electrode 2 (C)**	back on specimen	back on specimen
65 degrees	**on electrode 2 (C)**	**on electrode 2 (C)**	**on electrode 2 (C)**
70 degrees	on electrode 2 (TS)	back on specimen	on electrode 2 (TS)
75 degrees	on electrode 2 (TS)	on electrode 2 (TS)	on electrode 2 (TS)
80 degrees	on electrode 2 (TS)	**on electrode 1**	on electrode 2 (TS)
85 degrees	on electrode 2 (TS)	**on electrode 2 (C)**	back on specimen

The trajectories with shaded boxes all end on the middle electrode or scintillator. TS means the secondary electron hit the topside (see figure 8.5) and C means that they hit the center or edge of the hole of the middle electrode (see figure 8.7). The emitted electrons with boxes that are not shaded are reflected to the specimen except for the ones that seem to hit the upper electrode (1). In practice they cannot hit the upper electrode because the negative voltage on it is higher than the energy of the secondary electrons. But the calculation was stopped by TRASYS as the trajectories came too close to this electrode. However, these electrons are expected to come on the middle electrode as well since the trajectories were already far off-axis.

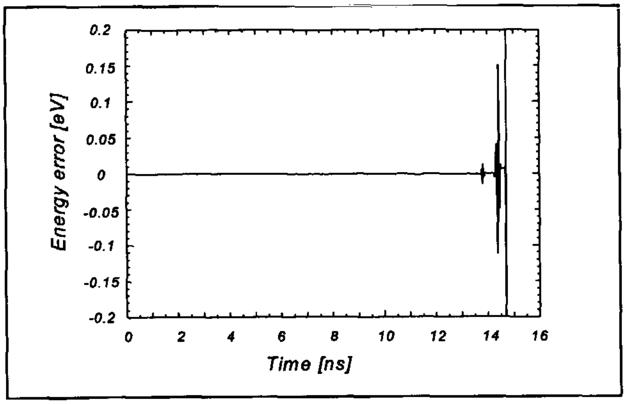

Fig. 8.9. *Energy error against the time of flight of 3eV secondary electrons at 45 degrees.*

The accuracy of a trajectory is reflected by the difference in the calculated total energy of a secondary electron at a certain position and its original starting energy. This error in the total energy is plotted in figure 8.9 as a function of the time, for the same electron as depicted in figure 8.5. Thanks to the accurate charge density method, the total error stays below a few tenths of an electronvolt, until the middle electrode has been reached. As the electron comes very close to the electrode surface the error increases rapidly and the program is halted. It takes 14.71 nanoseconds for this secondary electron to travel from emission on the specimen to the impact on the electrode. In general the calculations show that the time interval, between the emission of secondary electrons from the specimen and the hitting of the middle electrode, varies from 10 to 30 nanoseconds. The electrons with a higher energy appear to need less time than the lower energy electrons.

Although the final position of the trajectory looks random, the chances to arrive at the detector tend to be larger for the lower energy particles with higher opening angles. An explanation for this effect could be that these particular electrons have a lower velocity in the direction of the Z-axis, when entering the magnetic field again. This would allows the electrons to loose their energy in the Z-direction faster before they are at the specimen.

If the calculated trajectories represent the real detection distribution of secondary electrons, 30 out of 51 secondary electrons would come onto the detector. This is about 60 percent. However, the different contribution factors for different opening angles and energies, as depicted in figure 8.1, still have to be taken into account. This will cause the real percentage to deviate from the found 60%. Nevertheless the results from table 8.2 are useful for a rough evaluation of this detection method.

Still 21 electrons in table 8.2 do not come off axis, especially the ones with higher kinetic energy. The question arises whether the detection efficiency improves if the electrons start off axis. To examine this the emission point of the electrons has been shifted one micrometer off axis. The trajectories of 10 eV secondary electrons, with an opening angle of 0, 30 and 60 degrees in the RZ-plane, have been calculated, because these electrons do not arrive at the detector when starting on axis.

It shows that all secondary electrons are reflected back on the specimen. With this result it is to be supposed that the detection efficiency will not improve for a slightly off-axis spot on the specimen. However, an additional off-axis deflection mechanism will certainly improve the collection efficiency, but it should not be as strong as the standard secondary electron detector, otherwise the advantage of the "rotationally symmetric detector" will be lost.

In order to deflect the secondary electrons off axis, a magnetic or an electrostatic deflection field can be best. In case of a magnetic deflector the influence on the ion beam can be neglected. The optimum position to place such a small deflection field is where the secondary electrons have a low kinetic energy. Then the deflection will be relatively large which will result in a better detection efficiency. The place to position a small deflector is just above the upper electrode. At the other positions along the trajectories there simply is no room to implement a deflector or the electrons have too much energy in the Z-direction. The second type, an electrostatic deflector, pushes the electrons away from the axis when they go up and when they go down, back to the specimen. Therefore it is more effective in bringing the electrons off-axis.

Just above the upper electrode is the place where the secondary electrons are reflected by the equipotential plane. Figure 8.10 shows the 10 Volts equipotential which passes the hole of the upper electrode by more than a millimeter. This distance will increase when the potential on the upper electrode is lowered. When a small deflector is inserted at this point in the upper electrode, the electrons will be deflected the first time they are decelerated by the upper electrode.

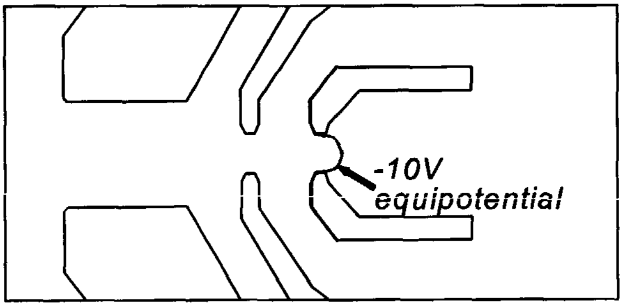

Fig. 8.10. *The equipotential line of -10 V near the upper electrode of the electrostatic objective lens.*

8.4. The design configuration

This paragraph will deal with the realization of the principle solution of the secondary electron detection method which has been derived in the previous paragraphs. The exploded view of the middle electrode is shown in figure 8.11. It consists of three parts. The largest part is a ring-shaped metal holder, which can be tightened to the Macor frame. It is supposed to hold the scintillator that fits exactly in the notch of the holder.

The third part is a ring to clamp the scintillator on the fixed position in the z-direction with respect to the holder. The assembly should function as middle electrode of the electrostatic objective lens and as scintillator in the secondary electron detector. This means that the middle electrode largely determines the electrostatic field in the electrostatic objective lens and therefore it needs to be positioned carefully with respect to the optical axis.

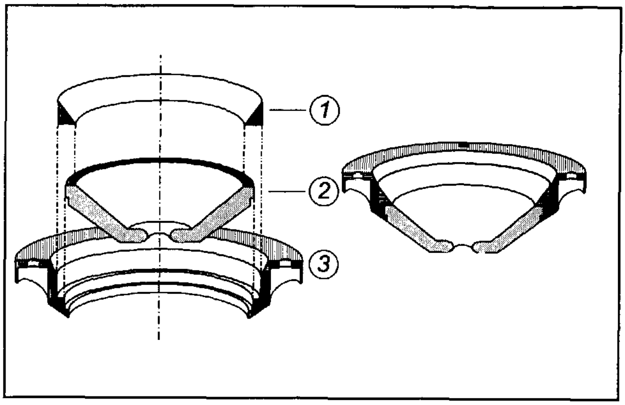

Fig. 8.11. *The middle electrode of the objective lens used as secondary electron detector. 1. clamp ring, 2. scintillator, 3. metal holder.*

A perfect scintillator converts the energy of an incoming secondary electron into a maximum number of photons in a minimum time interval, after which it conducts all photons directly and without losses into the optical guide. In practice the scintillator energy efficiency (Schauer, 1979) depends on:

1. *The conservation of the energy of the secondary electron until the scintillator has been reached.*

   The outside of the middle electrode is required to conduct electrical current in order to fix the shape of the electrostatic field by applying a high voltage to the outside of the electrode. Since a lot of scintillators are crystalline materials and do not conduct current, a metal layer is needed for this purpose.

   An aluminum layer of 50 nm thick, on the polished surface of the scintillator is recommended (Schauer, 1979). Firstly because aluminum has good light reflective properties and secondly because it is a light material, which limits the loss of energy of the secondary electrons. The loss of energy, ΔU_e, in this layer can be calculated with the Tompson-Whiddington law:

$$\Delta U_e = U_e - \sqrt{U_e^2 - b.\rho.x} \qquad (8.1)$$

U_e= energy of the secondary electron before it impacts on the middle electrode [eV]
x= thickness of the metal layer [cm]
ρ= density of the metal layer, aluminum 2.7 [g/cm^3]
b= constant, 4.10^{11} [eV^2.cm^2/g]

Accordingly at a thickness of 50 nm, the energy loss is 0.75 % of the original 19 keV that the electrons have before arriving at the middle electrode. This energy loss is negligible.

2. *The conversion of the kinetic energy of a secondary electron into the energy needed to generate a light pulse.*

The properties of scintillator materials have been compared (Autrata, 1983). Table 8.3 shows the comparison scheme.

The material of the scintillator can best be made of Yttrium Aluminum Garnet ($Y_3Al_5O_{12}$) doped by the activator Cerium (Ce^{3+}). This material is a single crystal scintillator. The choice for a single crystal instead of a scintillation powder on the surface of the middle electrode will be clear if one realizes that the bulk of the middle electrode must function as optical guide to the connection with the light guide. Since the shape of the scintillator gives rise to internal reflections, the surface of the scintillator needs to reflect the light pulses. The reflection coefficient will improve when a metal layer is coated on a polished middle electrode and not when the light pulse is diffused or absorbed by the powder on the surface.

It was found (Autrata, 1983) that the YAG:Ce3+-crystal has a very short decay time of the generated light pulse, which is necessary for a real time image of the specimen on a television. The measured decay time was 80 ns after a special heat treatment of the material. The YAG:Ce^{3+}-crystal appeared to be very resistant to radiation damage, which is required when the secondary electrons hit the scintillator with an energy of 19 keV. Moreover the YAG:Ce^{3+}-crystal has a very high Detection Quantum Efficiency (DQE) of 0.8 compared to the other scintillation materials. This DQE is the ratio of the squared signal to noise ratio that comes out of a scintillator of this material and the ratio of the ideal squared signal to noise ratio:

$$DQE = \frac{(SNR)^2_{out}}{(SNR)^2_{ideal}} \tag{8.2}$$

Table 8.3. *Comparison of various scintillation materials (Autrata, 1983).*

Decay time= time interval after stopping excitation during which the emission intensity decreases to 1/e value

lifetime= time to reach 50 % of the original efficiency at 5.10^{-9} A electron beam current

DQE= detective quantum efficiency of Everhart-Thornley detector

scintillator	structure	charact. emission [nm]	radiant efficiency [%]	decay time [ns]	lifetime [hr]	DQE coefficient
plastic NE 102 A	amorph. block	416		2.4	0.9	0.37
plastic film	amorph. film	416		2.4	10	0.45
glass (Li) Ne 901	amorph.	395		75	10 >230	0.10
anthracene	single crystal	447		30		
CaF_2 (Eu)	polycryst. powder	435		1000	5.10^3	0.22
CeP_5O_{14}	small crystals	335		12		
P 47	polycryst. powder	380-415	6-8	50	100	0.39 0.6-0.7 0.25-0.39
P 46	polycryst. powder	560	4	70 75	2.10^4	0.28
YAG: Ce^{3+}	single crystal	560		80	$>10^4$	0.8
YAP: Ce^{3+}	polycryst. powder	380	7	30		
YAP: Ce^{3+}	single crystal	380		40	$>10^4$	

3. *The transport of the photons in the scintillator to the connection with the light guide.*

To optimize the output the scintillator needs to be fully transparent and of a simple shape. The result will be a collection effciency that is lower than the above DQE, since the shape of a specific scintillator will stop some photons that would come out in the ideal situation. However the shape of the scintillator is largely determined by the demands on the shape of the middle electrode of the electrostatic objective lens.

If the original holes of the upper pole piece will be utilized, the light guide can be coupled to the scintillator as shows in figure 8.12. Only a small percentage of the photons can be led directly to the light guide, as can be seen in this figure. For the majority of the photons a number of reflections and a relatively long optical path are required to reach the connection to the light guide. It is to be expected that the self-adsorption is of importance as it is already 9 % for a flat YAG scintillator of diameter 9.6 mm and thickness of 0.5 mm (Autrata, 1983). Also the reflections at the 50 nm aluminum surface layer will adsorb photons. The reflection coefficient will be between 88 and 92.5 % in most practical situations.

If linear extrapolation is assumed, this means that only about half the amount of photons will reach the light guide after three reflections and an optical path of 30 mm which are not unrealistic parameters for the actual scintillator.

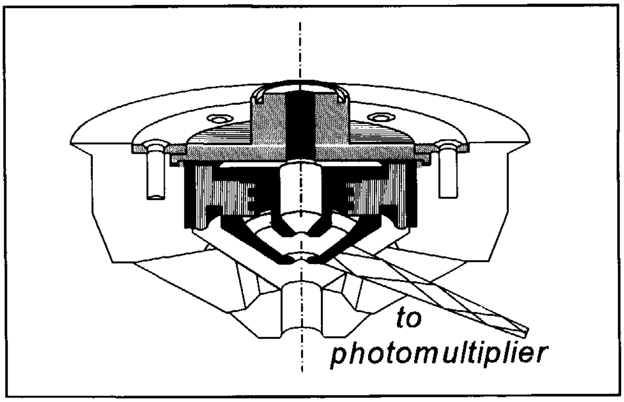

Fig. 8.12. *The configuration of the light output connection.*

4. *The output of photons into the light-guide.*

It is to be expected that the photons will arrive with different angles and different wave lengths at the transition between the scintillator and the light guide. For optimum transition the incident rays should come in close to the normal of the top of the light guide. This will make sure that the photons will enter the light guide and are reflected to its outside on their way to the photo multiplier.

Once the photons are led into the light guide, a low light adsorption coefficient of the bulk material of the light guide is required. Also a high reflection coefficient of the surface of the light guide will cause more photons to arrive at the photo multiplier. These factors depend on the kind of material, the index of refraction, the roughness of the surface and the light guide (Schauer, 1979).

Finally the photons end up at the photo multiplier. Here they are transferred back into electrons by a photo cathode. This current is amplified by scattering on the dynodes, see figure 8.2. In general the sensitivity of the photo multiplier is not equal for different wave lengths of the photons generated by the scintillator. The radiant sensitivity of the photo multiplier must be matched to the emission spectrum of the used scintillator material. The light pulses generated by the YAG:Ce^{3+}-crystal have a broad emission band of 175 nm (FWHM). The maximum of the emission band lies at λ=565 nm. A photo multiplier with an S20 photo cathode is recommended by Autrata. The radiant sensitivity of this photo cathode matches best with the emission spectrum of the YAG:Ce^{3+}-crystal.

8.5. Summary

A design has been presented of a rotationally symmetric secondary electron detector. The secondary electrons are pulled away from the specimen by the field of the magnetic objective lens. They are focused by a round electrode at high tension, the middle electrode of the electrostatic objective lens. This is followed by a round retarding electrode at -100 V, the upper electrode of the electrostatic objective lens. So they return in the direction of the specimen. However the magnetic field functions as a mirror too. Therefore the secondary electrons start spiraling between the retarding electrode and the upper pole piece until they have come far enough off-axis to land on the middle electrode instead of being focused by it.

In principle this detector has an important advantage over conventional detectors which deflect the secondary electrons off-axis: it does not deteriorate the primary ion and electron beam. The price that has to be paid is a lower collection efficiency. A conclusion that has also been drawn for other rotational symmetric secondary electron detectors (Autrata, 1993) (Koho, 1989). Especially high energy secondary electrons are not collected since they return back to the specimen. A collection efficiency of about 60 % of the total amount of secondary electrons is to be expected which is relatively high. It can be improved with a small deflection field near the upper electrode where the axial velocity of the secondary electrons is minimal.

Compared to the combined magnetic and electrostatic objective lens, as designed in chapter 7, only the middle electrode is adapted. In stead of a metal electrode a scintillator with a 50 nm aluminum layer is used. One of the unknown factors is the photon collection efficiency of this scintillator. It is realistic that only a part of the generated photons will reach the light guide to the photo multiplier because of the relatively complicated shape of the scintillator. A photo multiplier has been chosen as it allows a rotationally symmetric collection of the secondary electrons with the scintillator. Therefore it is in agreement with the basic idea behind this secondary electron detector: detection of the secondary electrons with a maximum detection efficiency but without disturbing the primary beam.

References

Autrata, R., P. Schauer and J. Kvapil, *Single-cristal-aluminates - A new generation of scintillators for scanning microscopes and transparent screens in electron optical devices*, Scanning Electron Microscopy 2, 1983, pp. 489-500

Autrata, R. and P. Schauer, *Collection of low energy signal electrons in the rotaionally symmetric electrostatic field of a detector*, Beitr. Elektronenmikroskop. Direktabb. Oberfl. 26, 1993, pp. 19-26

Barth, J.E., B. Lencová and G. Wisselink, *Field evaluation from potentials calculated by the finite element method for ray tracing: the slice method*, Nuclear Instruments and Methods A 298, 1990, pp. 263-268

Daberkow, I., K.H. Herrmann, L. Liu and W.D. Rau, *Performance of electron image converters with YAG single-crystal screen and Ccd sensor*, Untramicroscopy 38 , 1991, pp. 215-223

Harting, A. and F.H. Read, *Electrostatic lenses*, Elsevier Scientific Publishing Company, Amsterdam, 1976, pp. 32-40

Hughes, K.A., D.V. Sulway, R.C. Wayte and P.R. Thornton, *Application of Secondary-Electron Channel Multipliers to Scanning Electron Microscopy*, Journal of Applied Physics 38, 1967, pp. 4922-4923

Imeson, D., R.H. Milne, S.D. Berger and D. McMullan, *Secondary Electron Detection in the Scanning Transmission Electron Microscope*, Ultramicroscopy 17, 1985, pp. 243-250

Kelder, M.C.W., *Design and Fabrication of an Objective lens for ions, with an integrated Secondary Electron Detector, for a Scanning ion- and electron beam instrument*, Delft, 1994

Koho, J.S. and K.J.S. Koho, *Charged particle ray apparatus and method of observing samples*, patent application PCT/JP89/00810, 1989

Kolařik, V. and J. Mejzlík, *A design of a new axially symmetric secondary electron detector for the transmission electron microscope*, Measurements in Science and Technology 1, 1990, pp. 391-395

Kruit, P., *Magnetic Through-the-lens Detection in Electron Microscopy and Spectroscopy, Part 1*, Advances in Optical and Electron Microscopy 12, 1991, pp. 93-135

Landau, L.D. and E.M. Lifshitz, *The classical theory of fields*, Pergamon Press, Oxford, 1971, pp. 52-55

Lencová, B. and G. Wisselink, *Magnetic Lens Design program package*, licensed by Delft Particle Optics Foundation, 1992

Murata, M.F.G. Co., *Catalog of Ceratron-E Electron Multipliers*, by: Nijkerk Elektronika B.V., Amsterdam, 1996

Reimer, L., *Sacnning electron Microscopy, Physics of image formation and Microanalysis*, Springer-Verlag, Berlin, 1985

Schauer, P. and R. Autrata, *Electro-optical properties of a scintillation detector in SEM*, Journal of Microscopy, Spectroscopy and Electromicroscopy 4, 1979, pp. 633-650

Tsuno, K., N. Handa, S. Matsumoto and A. Mogami, *Optical properties of immersion objective lenses and collimation of secondary electrons in low voltage SEM*, SPIE 2858, pp. 46

Wisselink, G., *Trasys, computation of trajectories of charged particles through a system of electrostatic and magnetic fields*, licensed by Delft Particle Optics Foundation, 1992

9. Pattern generation facilities

Introduction

The place where the ion and electron beam meet the specimen is called the specimen area. It is the beating hart of "the Fancier", because here the nanostructures are written on the specimen. This means that here some facilities are needed for pattern generation. The objective lens to focus the ion and the electron beam on the specimen and the detector of secondary electrons have already been discussed in the former chapters.

In this chapter the development is described of the deflectors to direct the beams along a pattern and the gas introduction facility for beam induced etching and deposition. The deflectors have to function both for the ion beam and the electron beam. Once again, as with the objective lens, it will be a combination of electrostatic and magnetic fields.

For beam induced etching and deposition a gas introduction facility is needed. This will be discussed in the second part of this chapter. The developed facility can introduce both precursor materials for etching and deposition through one nozzle that is directed towards the specimen.

9.1. Positioning deflection systems.

The system for positioning the ion and the electron beam, also called positioning deflection system, is an important part in any pattern generation system. Pattern quality can only be guaranteed with a sufficiently accurate deflection system.

This accuracy has to be combined with velocity to get sufficiently throughput, especially in case of commercial available pattern generators. The strongest method optimizes the exposure scheme (Mulder, 1991). Traditionally a raster scan exposure scheme is used. The total specimen is scanned by the Gaussian beam (figure 9.1a), which yields a fixed throughput independent of the pattern density. The particle beam is switched off (blanked) when the beam is scanned over areas that should not be exposed. This scheme is similar to the exposure in a Scanning Electron Microscope (SEM). But the disadvantage for pattern generation is that it may spend quite some time scanning areas that should not be exposed. This can be very inefficient for sparse patterns.

In vector scan systems the time during which the beam is blanked is reduced. The exposure of the pattern is done by scanning the Gaussian beam over the appropriate areas (figure 9.1b). When the exposure of one area is finished, the beam is blanked and is deflected to the start point of the exposure of the next area, without fully scanning the unexposed area.

An even faster scheme uses variable beam sizes during the exposure of the pattern (figure 9.1c). This gives equal edge roughness as the other schemes but a larger probe size with more current is used where possible.

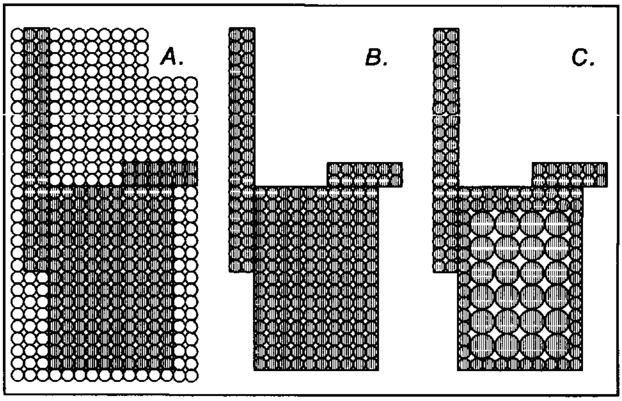

Fig. 9.1. *Exposure schemes of a pattern generator. A. raster scan, B. vector scan, C. variable beam size with vector scan.*

It is also possible to increase the throughput with other methods. Increase is possible by maximizing the field of view, the area over which the beam can be moved without specimen transport, as specimen transport is very time consuming. Very often the position deflection system is above the objective lens since the focal length of this lens is minimized. However, in this case a large field of view brings the beam further off-axis inside the objective lens or it gives the beam a large angle with respect to the axis of the lens. This causes larger aberration contributions. To guarantee the beam quality a variable axis immersion lens is often used (Léncova, 1989) (Pfeiffer, 1995). Here the beam central axis and the axis of the lens are brought together with deflectors.

Another method to increase throughput splits the pattern generation data in sub- and main field definitions. First the beam is positioned in a subfield. Then the patterns are written in this area but here only small deflection signals are necessary which can be transferred to the deflector at very high frequency (Slingerland, 1988).

In "the Fancier" the throughput is not the most important parameter, especially compared to accuracy. Therefore the throughput will only be optimized by using a vector scan system. A large field of view with fixed lens axis has a negative influence on the resolution mainly through the off-axis aberrations of the objective lens. However the maximum allowable value will be used. A variable axis combined ion and electron objective lens is decided to be too complicated. Also the price-to-performance-ratio of a sub- and main field scan system is too high to be realized in "the Fancier".

Therefore the design of the deflectors can focus on the accuracy of the patterns. Due to the small working distance of the objective lens it will be impossible to use a post-lens deflection system, in which the deflectors are placed between the lens and the target. The combined objective lens with secondary electron detector make in-lens deflection (Cleaver, 1987) very hard. Therefore the deflectors have to be placed above the lens circuit of the objective lens, a pre-lens deflection system.

The simplest pre-lens deflection system is a single deflector. This deflector has two disadvantageous. First, it causes the beam to enter the lens off-axis at an angle, as

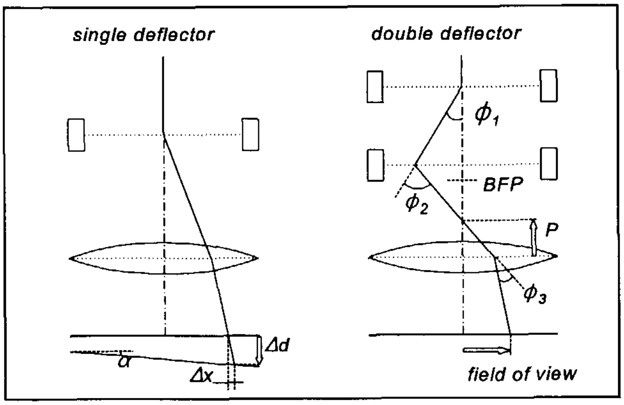

Fig. 9.2. *With a double deflector there is one extra degree of freedom: the position of the pivot point P.*

depicted in figure 9.2a. This increases the aberration contribution of this lens to the final probe size considerably. Second, the deflected beam will have an oblique angle at the specimen. Non-perpendicular landing will cause a position error due to specimen height variations and tilting as shown in figure 9.2a. In principle this can be corrected (Moore, 1983)

An extra degree of freedom is introduced by a double deflector as depicted in figure 9.2b. The position of the pivot, the point around which the beam is (virtually)deflected, can be moved along the optical axis of the instrument by variation of the ratio of excitations of the individual deflectors. This can be used to minimize the effect of the disadvantageous of a single deflector. In the specific case of center illumination, the pivot point of the deflection system is in the middle of the objective lens. Therefore the beam is on axis in the lens minimizing off-axis aberrations.

Another specific case has the pivot point in the back focal plane of the lens. The telecentric beam path based on the Köhler illumination (Hübner, 1996) provides normal beam incidence on the specimen over the whole scanning area. For a demagnifying objective lens this avoids position errors due to a slight variation in the working distance and minimizes additional aberration effects in case of a thick lens.

A calculation of the probe enlargement as a function of the position of the pivot point of the deflection system and the position on the specimen will give the optimum setting. The deflection angles of the central ray of the beam are given by

$$\phi_1 = \frac{-(l_2-P).x}{l_1.\left(\left(1-\frac{l_3}{f}\right).P+l_3\right)}$$

$$\phi_2 = \frac{(l_1+l_2-P).x}{l_1.\left(\left(1-\frac{l_3}{f}\right).P+l_3\right)} \qquad (9.1)$$

$$\phi_3 = \frac{-\frac{P}{f}.x}{\left(1-\frac{l_3}{f}\right).P+l_3}$$

ϕ_1= deflection angle by first deflector

ϕ_2= deflection angle by second deflector
ϕ_3= deflection angle by objective lens
P= distance between pivot point of the deflector and the center of the objective lens
x= distance from the optical axis of the system to the landing position of the beam
l_1= distance from center of first to second deflector
l_2= distance from center of second deflector to objective lens
l_3= distance from center of objective lens to specimen

A good approximation of the values of the off-axis aberrations can be found for thin lenses by assuming that the only deviation is that the strength of the lenses increases with a term that is proportional to the third power of the distance from the axis or the angle to the axis. It is reasonable to assume here that at least the electrostatic objective lens is thin as the focal length is considerably larger than the bore of the lens electrode.

$$\begin{aligned} x_c &= 0.34\ C_c.\frac{x_l}{b}.\frac{\Delta U}{U}, \quad y_c = 0.34\ C_c.\frac{y_l}{b}.\frac{\Delta U}{U} \\ x_s &= 0.18\ C_s.\frac{x_l.r_l^2}{b^3}, \quad y_s = 0.18\ C_s.\frac{y_l.r_l^2}{b^3} \end{aligned} \tag{9.2}$$

r_l= radius of a ray in the lens
x_l, y_l= position of the beam in the lens
x_c, y_c= chromatic aberration contribution to probe size
x_s, y_s= spherical aberration contribution to probe size

The parameters in the lens are given by

$$\begin{aligned} x_l &= r_0.\sin(\theta)+x_0, \quad y_l = r_o.\cos(\theta), \quad r_l = \sqrt{x_l^2+y_l^2} \\ r_0 &= b.\alpha_b, \quad x_0 = \frac{x-b.(\phi_1+\phi_2)}{1-\dfrac{b}{f}} \end{aligned} \tag{9.3}$$

α_b= opening angle of the beam

r_0= distance from the central axis of the lens to the center of the beam

Writing out the second part of equation (9.2) gives the five isotropic third order aberrations as listed in table 9.1.

Table 9.1. *Isotropic third order aberrations.*

origin	x-direction	y-direction
distortion	$0.18\ \frac{C_s}{b^3}.x_0^3$	0
field curvature	$2.\sin(\theta).\left(0.18\ \frac{C_s}{b^3}.x_0^2.\alpha_b\right)$	$2.\cos(\theta).\left(0.18\ \frac{C_s}{b^3}.x_0^2.\alpha_b\right)$
astigma-tism	$\sin(\theta).\left(0.18\ \frac{C_s}{b^3}.x_0^2.\alpha_b\right)$	$-\cos(\theta).\left(0.18\ \frac{C_s}{b^3}.x_0^2.\alpha_b\right)$
coma	$(2-2.\cos(\theta)).\left(0.18\ \frac{C_s}{b^3}.x_0.\alpha_b^2\right)$	$\sin(2\theta).\left(0.18\ \frac{C_s}{b^3}.x_0.\alpha_b^2\right)$
spherical aberration	$\sin(\theta).\left(0.18\ \frac{C_s}{b^3}.\alpha_b^3\right)$	$\cos(\theta).\left(0.18\ \frac{C_s}{b^3}.\alpha_b^3\right)$

It is possible to correct some of these contributions: distortion, astigmatism and field curvature. Astigmatism is corrected by dynamic excitation of a multi-pole lens, called stigmator. However this means dynamic stigmation with pattern generation. Compare this with a stigmator with static excitation that is required to correct for the inaccuracies introduced in the machining of the lens electrodes. A stigmator can be combined with the deflector. In a conventional lens field curvature is always positive, which means that the probe is focused before reaching the target. This can be corrected by dynamic focussing with the objective lens. Distortion is a non-linear effect of deflection and can be compensated by a change in the excitation of the deflectors.

Coma, spherical and chromatic aberration cannot be corrected in a simple system. Figure 9.3 and figure 9.4 show the effect of off-axis aberrations on respectively the ion and the electron probe size. It can be concluded from these figures that minimal effect occurs in case of center illumination with the pivot point in the center of the objective lens. This is explained by the fact that the beam is now on the axis of the lens.

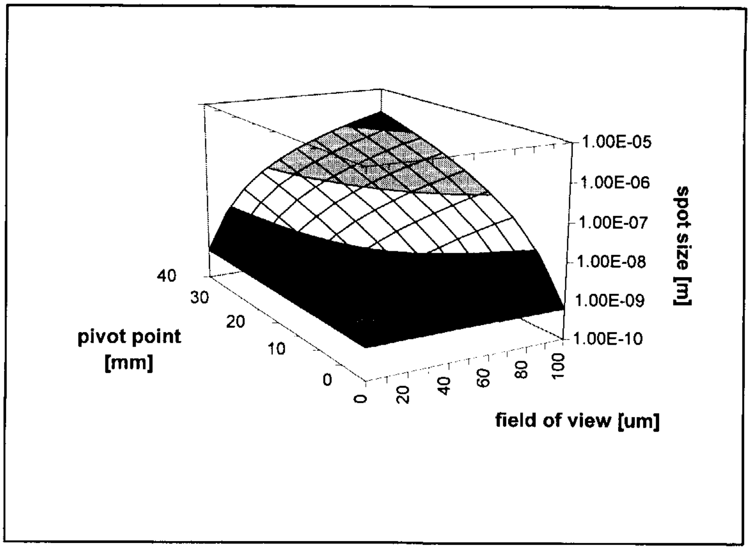

Fig. 9.3. *Effect of off-axis aberrations on the ion spot size.*
l_1= 28mm, l_2= 49mm, l_3= 15 mm, f= 14.6mm, C_s= 1247mm, C_c=49.mm

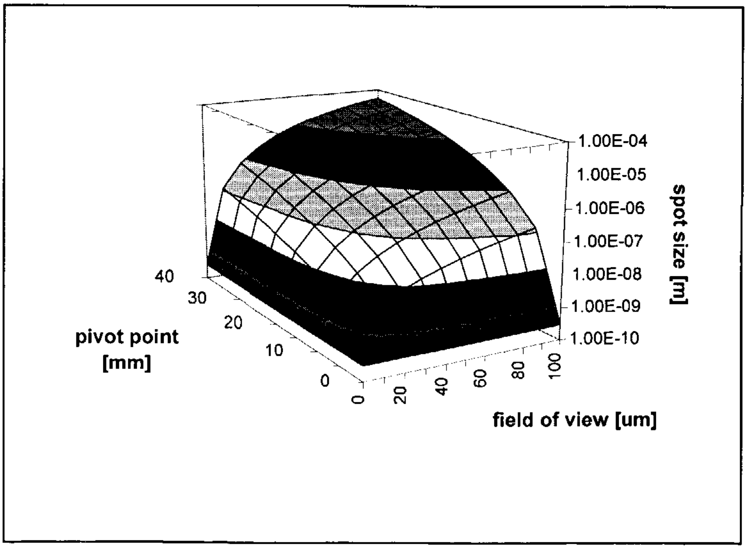

Fig. 9.4. *Effect of off-axis aberrations on the electron spot size.*
l_1= 26.75mm, l_2= 49.1mm, l_3= 2.9 mm, f= 2.9mm, C_s= 2.2mm, C_c=2.2.mm

If the beam stays on axis (x=0) the result is equal to the one described in chapter 4. If the distance from the axis of the system to the point of impact of the beam on the specimen increases the effects gets more important. But it is clear that center illumination gives minimal probe enlargement.

Now that the modes of operation of the pattern generation deflectors for ions and electrons are known (double deflector with pivot point in the center of the objective lens) the realization can be developed. The deflection angle of a magnetic deflector with infinitesimal broad pole pieces is given by

$$\phi_m = \frac{B.L_m}{2.\sqrt{2.\frac{M}{q}.U}}, \quad B = \frac{\mu_0.N.I}{d_m} \tag{9.4}$$

B= magnetic field strength
L_m= length of the magnetic pole piece
d_m= distance between the magnetic pole pieces
M/q= mass to charge ratio of the particles
U= energy of the particles
μ_0= magnetic permeability
N= number of turns of the magnetic coil
I= current through the magnetic coil

The deflection angle of an electrostatic deflector with infinitesimal broad electrodes is given by

$$\phi_e = \frac{E.L_e}{4.U}, \quad E = \frac{V_e}{d_e} \tag{9.5}$$

E= electrical field strength
L_e=length of the electrostatic electrodes
d_e= distance between the electrostatic electrodes
V_e=potential difference between the electrostatic electrodes

For the electrons there is already a double magnetic pre-lens deflector in the microscope which can give a field-of-view on the specimen ranging from 2x2.mm to 1x1µm for 120 keV electrons. If this deflector is also used for 30 keV Ar ions the field of view would be approximately 3.8 % of the electron field of view according to

$$fov_{ion} = \frac{b_{ion}}{b_{electron}} \cdot \sqrt{\frac{U_{electron} \cdot M_{electron}}{U_{ion} \cdot M_{ion}}} \cdot fov_{electron} \qquad (9.6)$$

fov_{ion}= field of view of the ions
$fov_{electron}$= field of view of the electrons
b_{ion}= image length of the objective lens for ions (15 mm)
$b_{electron}$= image length of the objective lens for electrons (2.9 mm)

However if both beams have to be on the specimen at the same time, each writing its own pattern, separate deflectors for both beams are required. So, for the ion beam a double electrostatic deflector has to be added to the microscope close to the objective lens. The maximum field of view of an electrostatic deflector is the product of the position addressability (1.0 nm) and the number of steps that can be made in the electrode excitation (2^{16}) and is equal to 66 μm. The actual field of view is chosen to be 50x50 μm to limit the effect of aberrations. In the assumption that for typical structure at the highest resolution 2 % of the field of view has to be exposed, the total exposure time is about 450 seconds for five times repeated illumination of the structure with an illumination dwell time of 1 μs (see paragraph 3.3.1).

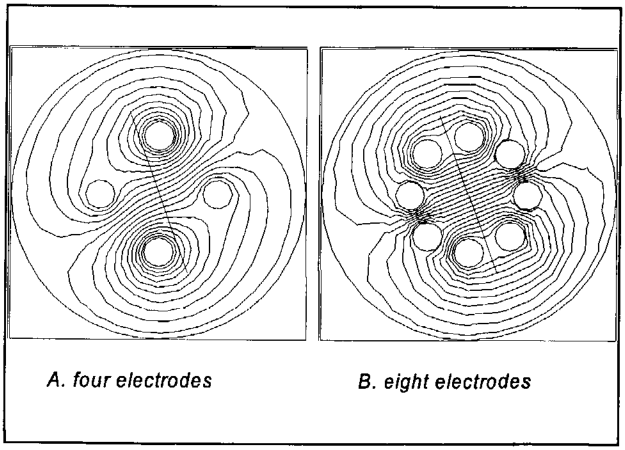
A. four electrodes
B. eight electrodes

Fig. 9.5. *The equipotential lines for deflection in the direction of the arrow.*

The simplest electrostatic deflector able to deflect in both x and y direction consists of four electrodes: two to deflect in each direction. Figure 9.5a shows the electric field that results from an excitation to deflect in the direction of the line. Especially between the electrodes the field deviates from the ideal parallel deflection field. This is much better achieved in case eight electrodes are used, see figure 9.5b. It also offers the possibility to use this element as stigmator.

The linertube of the condenser part of the objective lens can be used to position this deflector. Figure 9.6 depicts four alternatives for the electrode configuration. The section

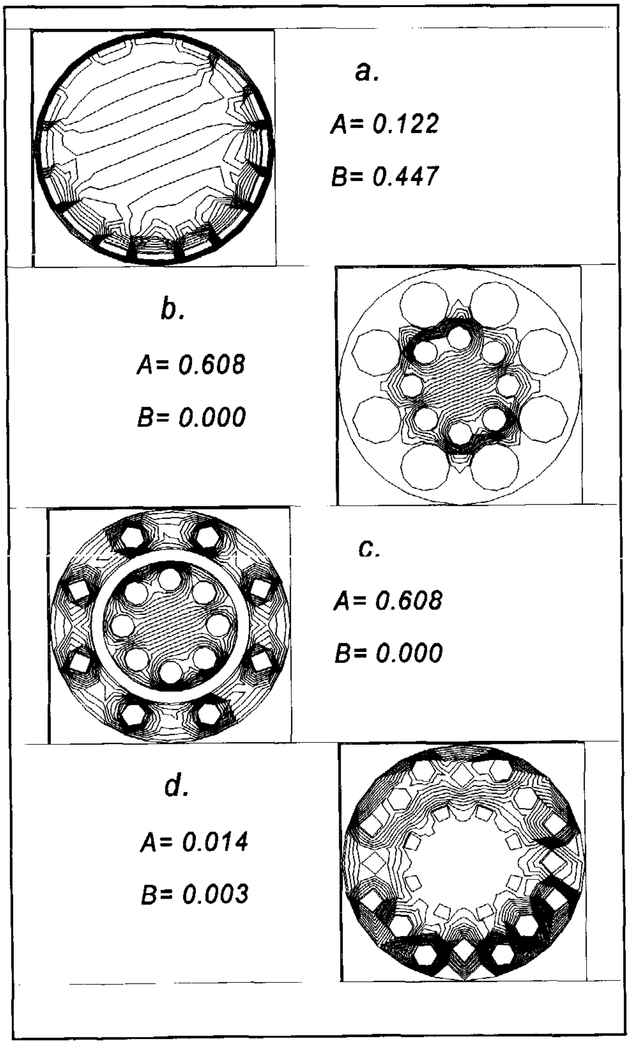

Fig. 9.6. *Cross-section of four alternatives for an electrostatic deflector, A and B indicate the transmission of the deflecting fields of the first and second deflector according to equation (9.7). The figures also show equipotential lines obtained with the program ELCUT (TOR, 1994).*

through the axis is made at the position of the first deflector. The electrodes can be on the linertube itself (figure 9.6a) as conductive strips separated by resistive material similar to the transport lens electrodes in the Delft Auger Microscope (van der Stam, 1993), or they can be inside the linertube (figure 9.6b-d).

The pictures show 16 electrodes. It is the result of the fact that the feedthroughs for the excitation of the upper and lower deflectors can best be above the deflectors near the C2 aperture as space is available here. Therefore at the position of the first deflector also the excitations of the second one are present. To prevent the beam from seeing this electrostatic field, the excitations of the second deflector have to be screened here. This is very hard in case the electrodes are on the linertubes. In case they are inside the linertube each electrode of the second deflector can be screened separately (figure 9.6b) or they can be screened collectively (figure 9.6c) It is also possible to have an innertube that transfers the field of the first deflector through holes in the tube (figure 9.6d).

To compare the alternatives two criteria can be developed: the measure in which the field of the first deflector is visible and the measure in which the second deflector is screened. To do this the potential on a circle of diameter 2 mm is calculated when the electrodes of the first deflector are put at a potential to deflect the beam and the electrodes of the second deflector are all on equal potential. Both potential distributions have an equal maximum. The potential at the circle is given by

$$\frac{V}{V_0} = A.\sin(\theta+\theta_0)+B \tag{9.7}$$

Here V_0 is the maximum potential that is applied to the electrodes. A is the amplitude of the deflection field, B is the transferred part of the second deflector at the specific radius from the center. Individual (figure 9.6b) and collective (figure 9.6c) give equal results: the second deflector is screened completely (B=0) while the deflection field is maximal (A=0.608). The results of the other two alternatives are worse. Less deflection field is transferred which means that higher potentials are required to give equal deflection while less screening is realized.

A field of view of 50 μm requires a maximum deflection angle of 4.5 mrad according to equation (9.1) and therefore a field in the deflector of 30 kV/m when the deflection length is 18 mm, according to equation (9.5). This is realized on the actual deflector with at maximum 225 V between the electrodes. Therefore a distance of only 0.25 mm between electrode and screen is enough.

Figure 9.8 shows the actual realization of the deflector. All feedthroughs are just below the Condenser-2 aperture. The deflector electrodes make contact with these feedthroughs since they are constructed as springs. The positioning of the electrodes is realized by elements made of Stycast 1266, a two-component epoxy with remarkably low outgassing (Faber, 1996). At the position of the upper deflector, the lower deflector is screened from the beam with a thin stainless steel screen. As all other materials in this deflector this is non-magnetic material to avoid interference with the magnetic deflector that is around this electrostatic deflector.

The outer electrodes are placed in the extension of the upper deflector in the middle Stycast 1266 element. The contact bridge here is made of Amicon CE3502, a one-component conductive epoxy (5.10^{-3} Ω.cm) (Grace, 1996). The lower deflector electrodes are round bars of 1 mm thickness. Also their position is defined by the position in the Stycast 1266 holders.

In principle contact between the ion or electron beam and the insulators has to be avoided. Since this can result in charging of the insulators which deflects or reshape the beams. Therefore the Stycast 1266 elements are covered with a metal, grounded shield. However at some places this is impossible from a construction point of view. The volume resistivity of Stycast 1266 is 10^{13} Ω.cm (Grace, 1996). With the dimensions of the insulator elements and a beam current of 10^{-14} A (see chapter 4) a maximum charging potential of 0.04 V results which can be neglected.

Finally the effect of aberrations of the deflector and the objective lens on the final probe size can be calculated. The aberrations of the deflector are of second order in position or angle because this is a non-rotational symmetric element. The position and the angle in the exit plane as a function of the position and angle in the entrance plane of the deflector for deflection in the x direction is given by (Slingerland, 1988)

$$x_o = x_i + L_e.\alpha_i + \frac{1}{2}.L_e.\phi + \left(-\phi.x_i.\alpha_i - \phi^2.x_i.\right) \tag{9.8}$$

$$\alpha_o = \alpha_i + \phi + \left(\frac{1}{8}.\phi^3 - \frac{1}{8}.\phi^2.\alpha_i - \frac{7}{4}.\phi^2.\frac{x_i}{L_e} - \frac{3}{4}.\phi.\alpha_i - \frac{1}{4}.\phi.\beta_i^2 + \phi.\frac{\Delta U}{U_0} \right) \tag{9.9}$$

$$y_o = y_i + L_e.\beta_i + \left(-\phi.x_i.\beta_i\right) \tag{9.10}$$

$$\beta_o = \beta_i + \left(-\frac{1}{2}.\phi.\alpha_i.\beta_i + \frac{3}{8}.\phi^2.\beta_i + \frac{1}{4}.\phi.\frac{y_i}{l_e} \right) \qquad (9.11)$$

Figure 9.7 shows the probe size of the ion beam at the boundary of the field-of-view both including and excluding the aberrations of the deflector.

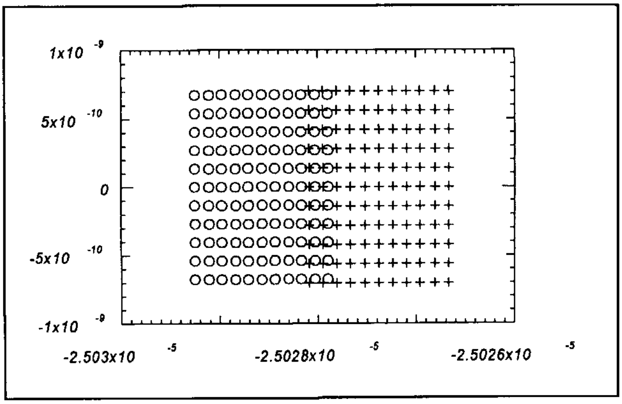

Fig. 9.7. *The influence of deflector aberrations on the probe size at the specimen.*

In can be concluded from this figure that the main effect of the deflector aberrations is a small shift of 2 nm, this can be corrected for. Furthermore the probe size increase by about 4.5 %.

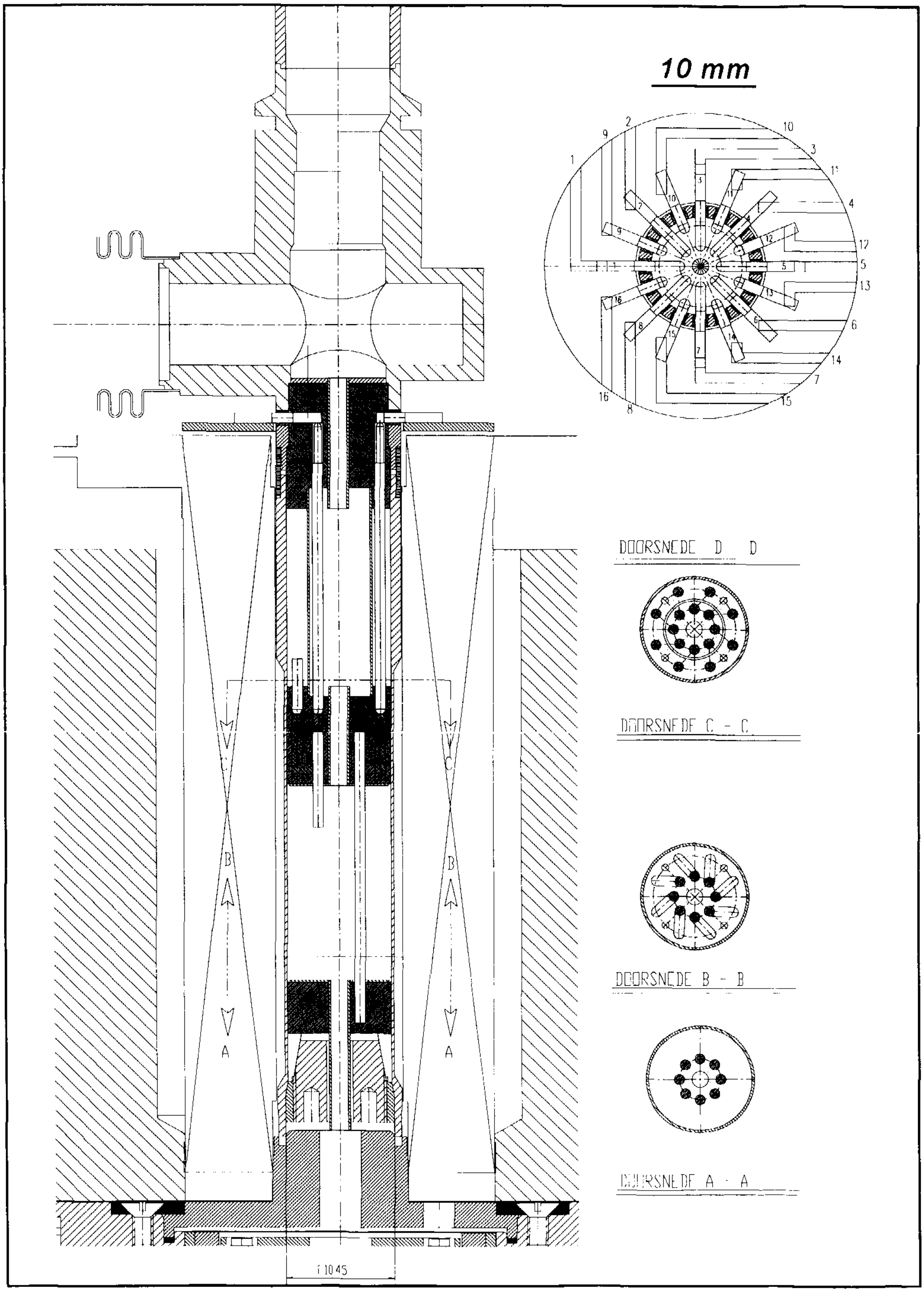

Fig. 9.8. *Technical drawing of the electrostatic deflector.*

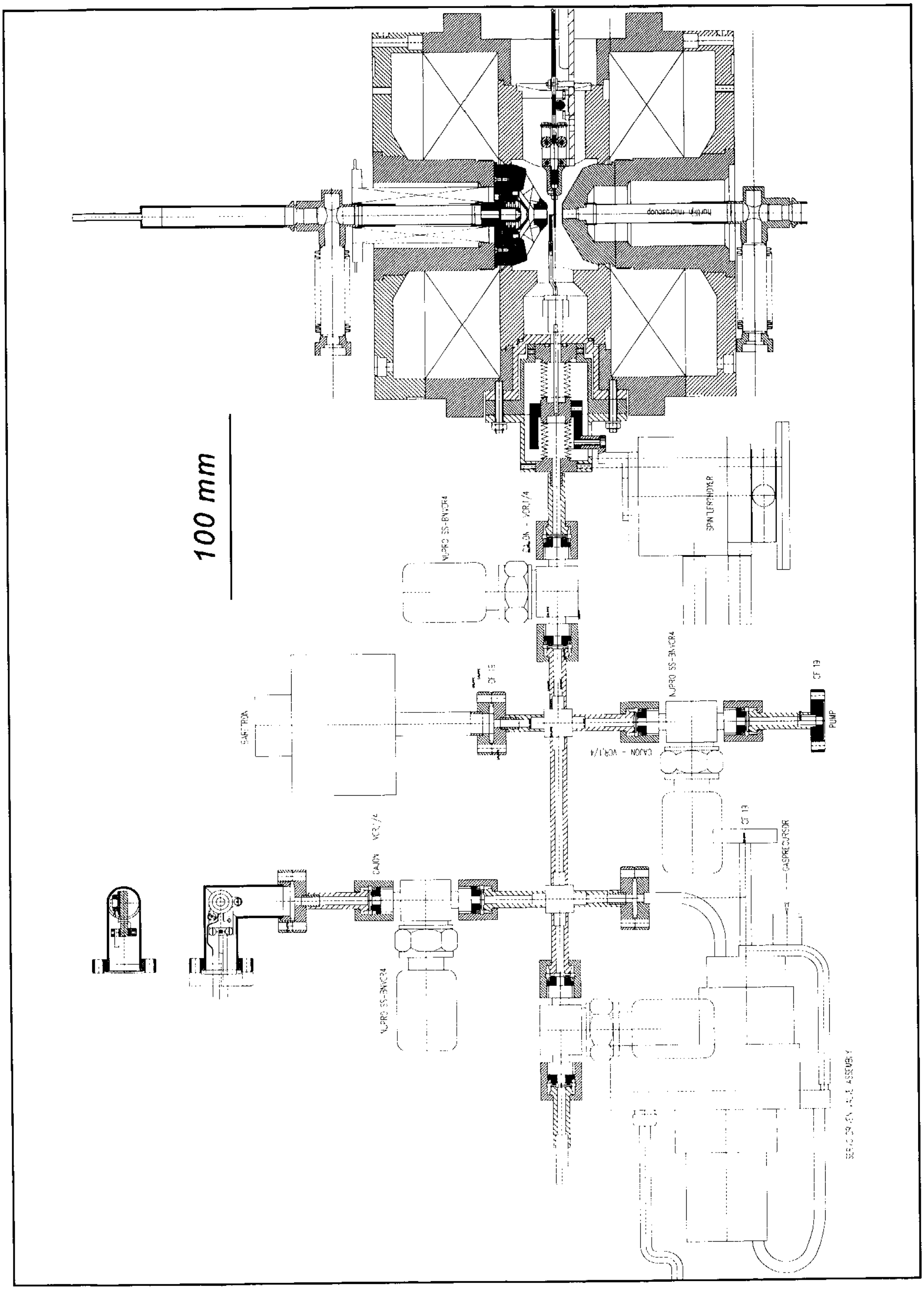

Fig. 9.9. *Precursor inlet system (a) gas precursor, (b) liquid or solid precursor.*

9.2. Precursor facilities

Some of the fabrication techniques require the use of gasses near the sample. Examples are beam induced etching and deposition where the beam transfers energy to an adsorbed precursor molecule. The result is a chemical reaction removing a specimen atom or leaving an atom from the precursor molecule. This technique is described in greater detail in paragraph 3.3. Here the facilities for monitoring, controlling and changing the amount of precursor and product gasses in the specimen environment is discussed.

In the first instance there is a contradiction: gas is introduced in a vacuum system. In order to maintain a gaseous environment in a TEM, the volume around the specimen must be isolated from the vacuum of the microscope column during the operation with the precursors. This means that the precursor gas has to be kept in a small area to keep the vacuum pressure in the system sufficiently low or it has to be introduced locally in an amount that is not limiting the production rate. So there are two basic designs which can be used to achieve this end:

1. An apertured cell close around the specimen, in which small apertures (10 μm typically) limit the gas flow from the cell environment into the vacuum system while still allowing the electron and ion beam to pass through unimpeded (Robards, 1996). A development of this design reduces the gas flow into the column by using differentially pumped pairs of apertures (Lee, 1991) instead of single apertures. This type of cell is easy to use, but some problems arise in "the Fancier". The secondary electrons for imaging have to leave this cell through the same aperture. As they start off-axis and are spiraling a relative large aperture should be used. These two functions of this single aperture cannot be combined.

   Only if the leak limiting aperture is positioned above the objective lens this problem of an environmental cell can be overcome. However the cell is now so large that it is not of practical use.

2. A more practical solution is a gas injector (Tuggle, 1996). The principle setup of the precursor facilities of this type is depicted in figure 3.14. The gas is introduced in a very small amount and directed to the place where it is actually needed: the field of view on the specimen. The precursor facilities are depicted in figure 9.9. A gas delivery system introduces precursor gas through a fine capillary in close proximity to the sample surface, a nozzle.

For such an arrangement, the gas flow Q, is determined as follows (Davies, 1996)

$$Q = \frac{\pi.v.d_i^3}{12.k.T.L.A}.\left(0.0368\ \frac{d_i.p^2}{(\lambda.p)} + 0.81\ p + 0.614\frac{(\lambda.p)}{p}.\ln\left[1 + 1.547\ \frac{d_i.p}{(\lambda.p)}\right]\right)$$
$$v = 4.\sqrt{\frac{k_B.T}{2.\pi.M}},\quad (\lambda.p) = \frac{k_B.T}{\sqrt{2.\pi}.D_{mol}^2} \qquad \textbf{(9.12)}$$

Q= gas flow [molecules/s]
p= reservoir gas pressure
L= length of the capillary tubing
d_i= inner diameter of the capillary nozzle
A= area where gas atoms strike the specimen
M= molecular mass of the precursor material
D_{mol}= molecular diameter of the precursor material
k_B= Boltzmann constant
T= gas temperature

At a certain length of the capillary and its internal diameter, different flow rates through the capillary onto the substrate can be obtained by varying the pressure, p, upstream within the gas reservoir. The flow of gas towards the specimen is the result of a pressure difference over the capillary. Therefore the pressure in the reservoir is kept constant. This pressure is sensed with a capacitance or absolute manometer, which is connected in closed loop via a controller to a fast acting servo control valve or a heater of the precursor material, see figure 9.9. Whether the valve or the heater is used depends on the type of precursor.

If the precursor is a gas at 300 K, like WF_6, a gas source is used. The transfer of gas to the reservoir is controlled with a valve. The gas source can be a lecture bottle, but for halogens, like F_2 and Cl_2, it is also possible to use a controllable gas source (Spencer, 1983). The basic of this halogen source is a solid state electrochemical cell $Ag/AgX/Pt\text{-}X_2$ in which silver halide is electrolyzed to silver and halogen.

However, if the precursor is a liquid or a solid at 300 K, like $Me_2Au(hfac)$, a heater is used to evaporate the material in the gas reservoir. The temperature strongly influences the evaporation rate according to

$$p = A.\exp\left(-\frac{U_e}{k_B.T_s}\right) \qquad \textbf{(9.13)}$$

p= vapor pressure
A= proportionality constant
U_e= energy of vaporization per molecule
T_s= temperature of the source material

The vapor pressure in equation (9.13) is equal to the pressure in the gas reservoir if the reservoir is evacuated with e.g. a turbo molecular pump before the precursor material is heated. Table 9.2 lists the vapor pressure of several precursor materials. A design parameter that can be drawn from this table is the maximum temperature of the reservoir. This will be 350 K allowing a vapor pressure of typically 100 Pa for most of the precursor materials.

The merit function is the concentration of adsorbed precursor molecules at the position of the specimen where the beam has to fabricate the structures. Therefore the gas density striking the surface is an important parameter. For molecular flow it is given by

Table 9.2. *The vapor pressure of several precursor materials as a function of the temperature.*

process	precursor	temperature [K]	pressure [Pa]	reference
Al deposition	$Al(CH_3)_2$	293	133	Gross, 1990
Al deposition	$Al(C_2H_5)_3$	293	67	Gross, 1990
Au deposition	$(Me)_2Au(hfac)$	293	93	Shedd, 1986
				Folch, 1995
		293	47	Blauner, 1989
Pt deposition	$MeCpPt(Me)_3$	299	15	Puretz, 1992
		328	67	
		273-303	$3471-1.1438.10^6/T$	Tao, 1990
		303-333	$2035-0.6969.10^6/T$	
W deposition	$W(CO)_6$	324	48	Takahashi, 1991
		330	79	
		328	53-67	Stewart, 1989
Si etching	XeF_2	293	599	Mitchell, 1987
		293	399	Harriott, 1994

$$F=\frac{Q}{A}=\frac{Q}{\left(0.5\,d_i+h.\frac{\tan(0.5\,\beta)}{\sin\alpha}\right)^2.\left[1+4.\left(\frac{1-\sin\alpha}{\sin\alpha}\right)+\frac{\pi}{2}.\left(\frac{1-\sin\alpha}{\sin\alpha}\right)^2\right]} \tag{9.14}$$

A= exposed area where the molecules strike the specimen
d_i= inner diameter of the nozzle
α= angle of the nozzle with horizontal
β= opening angle of the gas beam
h= height of the nozzle above the specimen

while the condition for molecular flow is given by

$$p<\frac{1}{137.d_i} \tag{9.15}$$

The inner diameter of the nozzle is chosen to be 200 μm. However this is not the internal diameter of the whole tubing. At the last 3 millimeter of the tube the diameter is decreased from 2 mm to the desired nozzle diameter. In this configuration it is possible to have a relatively high and molecular gas flow.

The exposed area has to be at least as large as the field of view (50x50 μm). The precursor gas is emitted from the nozzle with a divergence angle of at least 30 degrees (Kohlmann, 1991). The axis of the capillary makes an angle of 45 degrees with the horizontal to realize exposure of the right area on the specimen while the nozzle is not directly above it to let the ion and electron beams pass. With the above parameters it can be concluded from equation (9.14) that optimum exposure is realized if the nozzle is very close to the specimen. This is realized by equipping the nozzle tubing with an xyz-translator stage with 10 μm accuracy.

Equation (9.14) shows a quadratic relation between the gas density striking the specimen surface and the distance from the specimen to the nozzle. This is in agreement with experimental results (Winkler, 1996) (Blauner, 1989) as depicted in figure 9.12a. For a distance of 500 μm from the nozzle to the sample, the flow of precursor molecules arriving at the specimen can be calculated as a function of the gas pressure in the reservoir, see figure 9.12b. This parameter is chosen because it is the one that is used to control the gas flow during operation. The gas molecules arriving at the specimen have a certain probability to adsorb on it, see equation (3.11). The adsorption probability is often assumed to be one.

Once a molecule has been adsorbed on the specimen three processes can occur: there is a chance to desorb from the sample, there is a chance to diffuse out of the exposed area where the molecules strike the specimen and there is a chance to be used in a chemical reaction after an ion or electron has transferred enough energy.

The desoption process is described by equation (3.17). Desorption means the return of an adsorbed molecule into the vacuum. However if there is a concentration gradient of adsorbed molecules at the surface of the specimen, migration of precursor molecules will take place too. In the situation of precursor introduction through a nozzle, there is a gradient because only an area A of the surface is exposed.

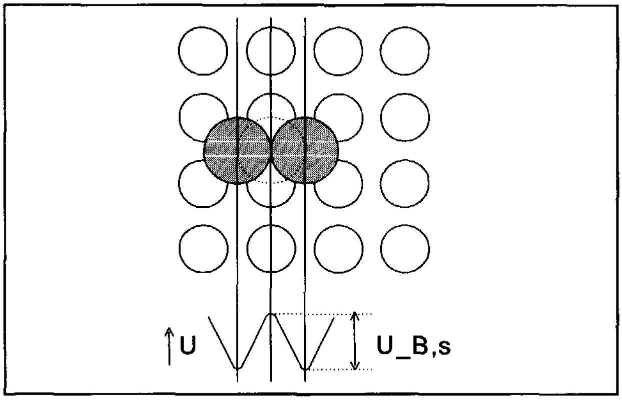

Fig. 9.10. Model of migration of adatoms over the specimen surface.

Consider the migration of an adatom on a BCC surface., as shown in figure 9.10. At equilibrium, this adatom has four nearest neighbors in the plane below it. In order to move from one equilibrium site to an adjacent equilibrium site, the adatom must pass through a configuration such as the one dotted in the figure. In this position, the adatom has only two nearest neighbors. The migration process will thus require an activation energy of roughly twice the nearest neighbor bond energy. The general conclusion would be that an activation energy is always required for an atom motion and that the energy required is a fraction of the heat of sublimation of the crystal. The intrinsic diffusivity is given by (Hudson, 1992)

$$D_a = \frac{l^2}{2.\tau_0}.\exp\left(-\frac{U_{B,s}}{k_B.T}\right) \tag{9.16}$$

l= adatom jump distance, on the order of interatomic spacing in the surface
τ_0= attempt meantime between surface diffusive jumps, 10^{-12} ... 10^{-14} s
$U_{B,s}$= activation energy for surface diffusion
k_B= Boltzmann constant
T= surface temperature

The migration or surface diffusion process can be described phenomenologically by

$$\frac{d^2C}{dx^2}+\frac{d^2C}{dy^2}=\frac{1}{D_a}.\frac{dC}{dt} \tag{9.17}$$

D_a= adatom diffusivity
C= concentration of adatoms

For the case of a circular exposed area of initially uniform concentration, the amount of material within the initially exposed area as a function of time is given by (Hudson, 1992)

$$\frac{dN_{ps}}{dt}=-N_{ps}.\int_{u=0}^{\infty}\left[\frac{J_1^2(a.u)}{r}\right].D_a.u^2.e^{-D_a.T.u^2}.du \tag{9.18}$$

N_{ps}= number of physisorbed adatoms
u= dummy variable
a= radius of the exposed area

The Bessel function is given by (Boyce, 1986)

$$J_1(a.u)=\frac{a.u}{2}\sum_{n=0}^{\infty}\frac{(-1)^n.(a.u)^{2n}}{(n+1)!.n!.2^{2n}} \tag{9.19}$$

The approximate short-time solution of equation (9.18) is (Hudson, 1992)

$$\frac{dN_{ps}}{dt}=-\frac{N_{ps}}{a}.\sqrt{\frac{D_a}{2.\pi.t}}=-N_{ps}.\frac{l}{a}\sqrt{\frac{1}{4.\pi.t.\tau_0}.e^{-\frac{U_{B,s}}{k_B.T}}} \tag{9.20}$$

In the assumption of no relaxation and no spontaneous reaction, the number of physisorbed precursor molecules within the exposed area can be calculated from

$$\frac{dN_{ps}}{dt}=g.F-N_{ps}.\left(\frac{g.F}{N_0}+\frac{1}{\tau_0}.e^{-\frac{U_B}{k_B.T}}+\frac{l}{a}\sqrt{\frac{1}{4.\pi.t.\tau_0}.e^{-\frac{U_{B,s}}{k_B.T}}}+\frac{m.s.J}{N_0}\right) \tag{9.21}$$

$$\begin{gathered}N_{ps}=\exp\left(-B.t-2.C.\sqrt{t}\right).\left[\int A.\exp\left(B.t+2.C.\sqrt{t}\right)\,dt+c_0\right]\\ A=g.F\ ,\quad B=\frac{g.F}{N_0}+\frac{1}{\tau_0}.e^{-\frac{U_B}{k_B.T}}+\frac{m.s.J}{N_0}\ ,\\ C=\frac{l}{a}\sqrt{\frac{1}{4.\pi.\tau_0}.e^{-\frac{U_{B,s}}{k_B.T}}}\end{gathered} \tag{9.22}$$

Compare this time dependent result with the static, no diffusion, solution given by equation (3.25). The percentage of surface sites that is occupied with a precursor molecule as a function of time is shown in figure 9.11 in case of no induction by the beam. Figure 9.12c gives the same value at t= 30s as a function of the reservoir pressure.

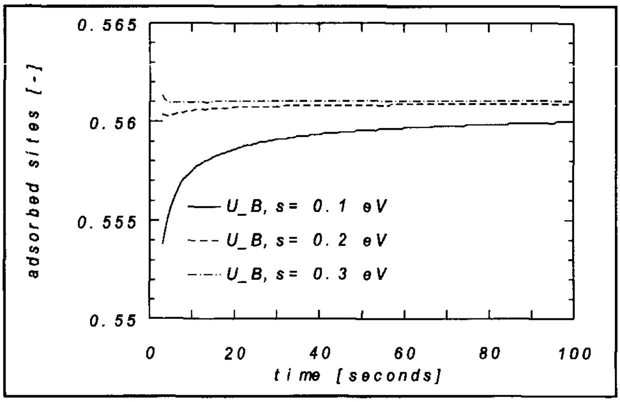

Fig. 9.11. *Adsorption concentration as a function of time including adsorption from the nozzle, desorption and surface migration, at t=0 the nozzle is opened, without energetic beam.*

Figure 9.12d gives the production yield as a function of the gas pressure. In these figures a current of 10^{-14} A in a probe of 2 nm is assumed, the number of reactions per ion is 30. It can be concluded that the production is limited by the available amount of precursor molecules. In practice the production yield can be larger, as an equilibrium situation is assumed in the above calculations. The actual situation has a scanning beam. In paragraph 3.3 it is demonstrated that the production yield in a precursor limited situation can be improved by a short dwell time, T_d, and a long refresh time, T_r. During this refresh time new gas molecules can adsorb.

The gas flow into the vacuum system comes to the expense of the vacuum pressure. The final pressure in the system is given by

$$p_{final} = \frac{Q.k_B.T_g}{S} \qquad (9.23)$$

S= pumping speed at the specimen

The result is shown in figure 9.12e for a pumping speed of 20 l/s. It is clear from the figures 9.12d and 9.12e that there is a trade-off between the production yield and the vacuum pressure.

Finally the amount of gas used is calculated. This consumption can be divided in two parts:

1. the gas that has left the reservoir through the nozzle to the specimen. This amount is actually used in the production of structures through beam induced etching and deposition. It is therefore called the nett consumption
2. The gas that has left the reservoir through the pumping line in figure 9.9. This is called the tare consumption.

Both fractions are given in figure 9.12f. The tare consumption is a result of the change in precursor material. Two precursor containers are connected to the inlet construction: one for etching and one for deposition. The reason is that it is very useful to have a fast switching facility from one precursor to the other. However every time a change is made the material that is in the central reservoir is pumped away and it is therefore consumed. By minimizing the reservoir volume and/or recycling the precursor this consumption is decreased. A typical switching strategy from precursor P1 to precursor P2 is as follows:

1. during operation with precursor P1 the valves V1 and V5 are open; V2, V3 and V4 are closed
2. close valve V5
3. switch off precursor P1 heater
4. put precursor container P1 in liquid nitrogen, the majority of the precursor will adsorb in the container

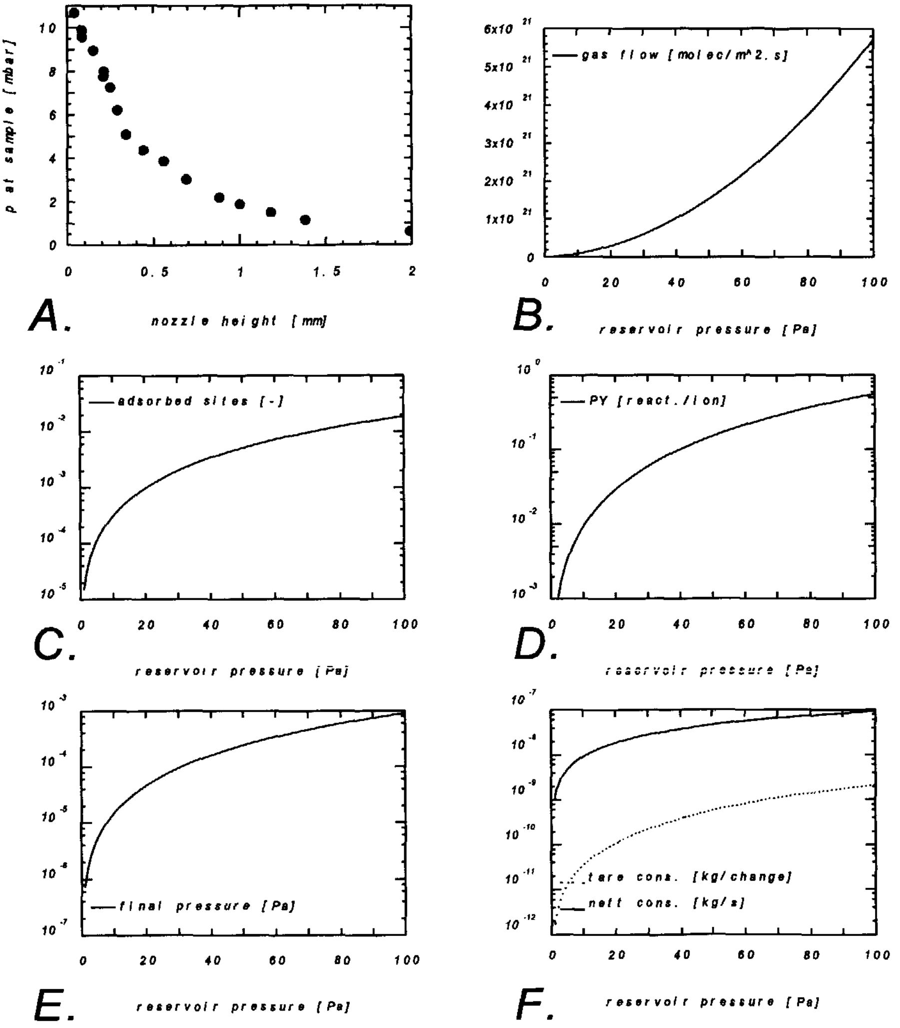

Fig. 9.12. *Precursor parameters (a) nozzle height influence, (b) gas flow through nozzle, (c) physisorption concentration 30 seconds after opening nozzle, (d) production yield, (e) final pressure and (f) precursor consumption as a function of the pressure in the reservoir(tare consumption is the loss of precursor material changing from precursor P1 to precursor P2, nett consumption is the consumption of precursor material during operation.*

5. close valve V1 after a few minutes
6. open valve V2, nitrogen is introduced which will mix with precursor P1
7. open valve V4 after a few minutes
8. the reservoir is evacuated while the concentration of precursor P1 in the pump output is below its critical level to avoid environmental or safety problems
9. close valve V2
10. close valve V4 if a low pressure is reached
11. open valve V3 to introduce precursor P2 to the desired pressure
12. open valve V5
13. during operation with precursor P2 the valves V2 and V5 are open; V1, V3 and V4 are closed

9.3. Summary

A double pre-lens deflector is used to combine the desired resolution of both the ion and the electron beam with a large field-of-view. It is possible to direct the beam through the center of the objective lens while still having a reasonable field-of-view of 50x50 μm for the ions and for the electrons ranging from 2x2 mm to 1x1 μm. This optical path minimizes the off-axis aberrations of the objective lens. The combination of these fields-of-view and the vector scan exposure scheme give reasonable production speed to avoid problems with stability. A typical structure can be written at the highest resolution within about 450 seconds. For the electron beam the magnetic double deflector of the electron beam can be used, but for the ion beam a new electrostatic deflector has been developed. It consists of two eight-poles that are positioned inside the linertube of the objective lens with inner diameter of 10 mm.

Now that the beams can be directed towards a specific position on the specimen pattern generation by means of direct implantation and sputtering is possible. However for beam induced etching and deposition a gas introduction system has been developed. The precursor gas is introduced through a nozzle. This minimizes the amount of precursor material in the vacuum system, by introducing the gas locally at the field-of- view on the specimen. This nozzle is connected to a reservoir with pumping and pressure measurement connection. Also the precursor containers for etching and deposition material are connected to this reservoir. By heating the container of a liquid or solid state precursor to a temperature of 350 K sufficient flow of gas through the nozzle can be realized for a wide range of precursors. If the precursor is in the gas state at room temperature a servo valve is used with feedback from the reservoir pressure.

All fabrication facilities as listed in chapter 3 can be realized in "the Fancier" with the above pattern generation facilities.

References

Blauner, P.G., J. Ro, Y. Butt and J. Melngailis, *Focused ion beam fabrication of submicron gold structures*, Journal of Vacuum Science and Technology B 7(4), 1989, pp. 609-617

Boyce, W.E. and R.C. DiPrima, *Elemetary Differential Equations and Boundary Value Problems*, John Wiley & Sons, Singapore, 1986, pp. 233

Cleaver, J.R.A., *In-lens deflection for scanning ion beam systems*, Optik 75(2), 1987, pp. 75-81

Davies, S.T. and B. Khamsehpour, *Focused ion beam machining and deposition for nanofabrication*, Vacuum 47(5), 1996, pp. 455-462

Faber, P., *Instrumentation for parallel-parallel coincidence electron microscopy*, thesis, Delft, 1996, pp. 77-85

Folch, A., J. Tejada, C.H. Peters and M.S. Wrighton, *Electron beam deposition of gold nanostructures in a reactive environment*, Applied Physics Letters 66(16), 1995, pp. 2080-2082

Grace Specialty Polymers, *Product description of Stycast 1266 and Amicon CE3502*, Westerlo, Belgium, 1996

Gross, M.E., L.R. Harriott and R.L. Opila, *Focused ion beam stimulated deposition of aluminium from trialkylamine planes*, Journal of Applied Physics 68(9), 1990, pp. 4820-4824

Harriott, L.R., *Focused-Ion-Beam-Induced Gas Etching*, Japanese Journal of Applied Physics 33, 1994, pp. 7094-7098

Hübner, B., R. Jede, I. Specht, R. Zengerle, *E-beam lithography by using a STEM with integrated laser interferometer stage*, Microelectronic Engineering 30, 1996, pp. 41-44

Hudson, J.B., *Surface Science*, Butterworth-Heinemann, Boston, 1992, pp. 107-118

Kohlmann, K.T., M. Thiemann and W.H. Brünger, *E-beam induced X-ray mask repair with optimized gas nozzle geometry*, Microelectronic Engineering 13, 1991, pp. 279-282

Lee, T.C., D.K. Dewald, J.A. Eades, I.M. Robertson and H.K. Birnbaum, *An environmental cell transmission electron microscope*, Review of Scientific Instruments 62(6), 1991, pp. 1438-1444

Léncova, B., *Design of a strong objective lens with large field of view of electron lithography*, Poster at Wetenschappelijke Vergadering IOP/FOM, Veldhoven, 1989

Mitchell, M.J., M. Suto, L.C. Lee and T.J. Chuang, *Chemiluminescence from F and* XeF_2 *etching reactions with silicon*, Journal of Vacuum Science and Technology B 5(5), 1987, pp. 1444-1449

Moore, R.D., *EL Systems: high throughput Electron Beam Lithography Tools*, Solid State Technology, 1983, pp. 127-132

Mulder, E.H., *On the throughput optimization of electron beam lithography system*, thesis, Delft, 1991

Pfeiffer, H.C.and W. Stickel, *PREVAIL - An E-Beam Stepper with Variable Axis Immersion Lenses*, Microelectronic Engineering 27, 1995, pp. 143-146

Purentz, J. and L.W. Swanson, *Focused ion beam deposition of Pt containing films*, Journal of Vacuum Science and Technology B 10(6), 1992, pp. 2695-2698

Robeards, A.W. and A.J. Wilson, *Procedures in Electron Microscopy*, Wiley, 1996, pp. 9.11.1-9.11.12

Shedd, G.M., H. Lezec, A.D. Dubner and J. Melngailis, *Focused ion beam induced deposition of gold*, Applied Physics Letters 49(23), 1986, pp. 1584-1586

Slingerland, H.N., *A fast ion beam pattern generator*, thesis, Wibro, Delft, 1988

Spencer, N.D., P.J. Goddard, P.W. Davies, M. Kitson and R.M. Lambert, *A simple, controllable source for dosing molecular halogens in UHV*, Journal of Vacuum Science and Technology 1(3), 1983, pp. 1554-1555

Stam, M.A.J. van der, J.E. Barth and P. Kruit, *Design of a multi mode transport lens with optimization program SOEM*, SPIE 2014, 1993, pp. 45-55

Stewart, D.K., L.A. Stern and J.C. Morgan, *Focused-ion-beam induced deposition of metal for microcircuit modification*, SPIE 1089, 1989, pp. 18-25

Tao, T., J. Ro and J. Melngailis, *Focused ion beam induced deposition of platinum*, Journal of Vacuum Science and Technology B 8(6), 1990, pp. 1826-1829

Takahashi, Y., Y. Madokoro and T. Ishitani, *Focused Ion Beam Induced Deposition in* *the High Current Density Regime*, Japanese Journal of Applied Physics 30(11b), 1991, pp. 3233-3237

TOR Cooperative Enterprise, St. Petersburg, Russia, 1994

Tuggle, D., *private communication*, FEI company, Beaverton, 1996

Winkler, D., H. Zimmermann, M. Mangerich and R. Trauner, *E-beam probe station with integrated tool for electron beam induced etching*, Microelectronic Engineering 31, 1996, pp. 141-147

10. Specimen stage

Introduction

The specimen is the place for fabrication of the structures and it is the subject for analysis. So it is the specimen where the resolution has to be realized. It is also the part of "the Fancier" that has to very flexible: it has to be brought in and out of the system and it has to be moved to the right position as the specimen is larger than the field of view of the beams. This makes the specimen very sensitive for vibrations.

Seismic floor inputs produce unacceptably high vibration levels for sensitive fabrication and analysis. Typically little can be done to reduce support motions. The presence of vehicle and foot traffic as well as manufacturing operations, necessitate reducing transmitted vibrations rather than source vibrations. Figure 10.1 shows the floor vibrations as a function of the frequency. The measurement has been performed at the position of "the Fancier".

Another source of undesired motion of a system is thermal expansion due to thermal instabilities and system vibrations due to direct payload by e.g. acoustic noise and pumps. Although the user may have control of these disturbances, both thermal effects, payload and base disturbances are usually significant.

In this chapter methods to minimize these effects on the specimen will be discussed. At the end the specimen facilities will be listed. These facilities result from demands in former chapters, like cooling and heating of the specimen and deceleration of the beam by the specimen.

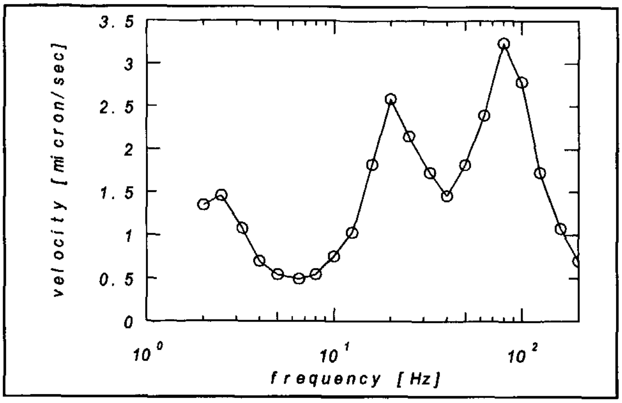

Fig. 10.1. *Floor vibrations at the position of "the Fancier" (Geerligs, 1996).*

10.1. Demands on stability

The motions will have influence on the system performance in two ways. First the optical axis of the system moves with respect to the ion and electron beam. This is because the beams themselves do not feel any influence of the floor vibrations since they are moving free in vacuum, except for the very short time that they are inside a lens. Suppose a straight line at the highest resolution has to be made. Vibration periods considerably longer than the time of flight of the particles from source to specimen (4 μs) do not have any influence. Considerably shorter periods result in larger aberration effects and dynamic misalignment, so the line gets broader and the fabrication resolution decreases. If the system is infinitely stiff this is the only effect that occurs.

The second effect is the result of moving parts of the system relative to each other. As the masses involved in this mode are smaller than of the whole system, the amplitudes are generally larger. For instance, external vibrations can lead to motions of the emitting needle with respect to the source optics. In time it seems as if the emitting area is larger resulting in a larger probe. Suppose a straight line at the highest resolution has to be made. Vibration periods considerably longer than the dwell time (the time to illuminate a pixel) result in wave effects in the line. Considerably shorter periods demonstrate a broader line.

This latter effect gets more severe if it occurs closer to the specimen. All lenses in the system are demagnifying. Therefore a motion of 10 nm of the image directly behind the source with respect to the condenser lenses will only result in a probe enlargement of 0.02 nm since it is demagnified 450 times. This can be neglected with respect to the probe size of 2 nm. However, a motion of 10 nm of the specimen with respect to the objective lens will increase the probe size 500%!

This is the reason why it is important to position the specimen extremely accurate with respect to the objective lens, especially the upper pole piece. On the other hand a certain flexibility is needed to transfer the specimen in and out of the system and to position an area of interest under the beam.

The overall demands on specimen stability is that a maximum size and position inaccuracy of 5 % of the probe size (2 nm) can be allowed during the time of operation. This is the time needed to fabricate or analyze a typical nanostructure. It is assumed to be 10 minutes. The 5 % error budget has to be divided over the five orthogonal degrees of freedom of the specimen, therefore only 2.3 % inaccuracy with respect to each individual degree of freedom can be allowed. Table 10.1 summarizes the demands, in this table also the dynamic range in each direction is given.

Table 10.1. *Demands on specimen stability, x, y and ϕ are the coordinates in the specimen plane, z is in the direction of the optical axis perpendicular to the specimen, θ is the tilting angle of the specimen with respect to the optical axis.*

	value	effect
x,y resolution		
vibration amplitude	0.046 nm	probe enlargement
drift	0.0046 nm/min	position error
x,y dynamic range	3 mm	
z resolution		
vibration amplitude	20 nm	defocus
drift	2 nm/min	defocus
z dynamic range	0 mm	
ϕ resolution	4.6 µrad	position error over field of view (50 µm)
ϕ dynamic range	0 rad	
θ resolution	400 µrad	defocus over field of view (50 µm)
θ dynamic range	0 rad	

The demands on stability and dynamic range seems to be opposite, as flexibility implies a certain instability. However elements only start to move with respect to each other if a force can act on one of them. Therefore it is possible to realize the demands by filtering these forces: the vibrations. This can be done passively or actively.

10.2. Passive stabilization

In the vast majority of cases, vibration control is achieved using passive elements such as springs, dampers and masses in the form of metallic, pneumatic, hydraulic or rubber devices. The elements are passive in the sense that no power source is required, i.e. the vibration control elements only store or dissipate the energy associated with the vibratory motion (Karnopp, 1974).

For simplicity "the Fancier" is considered as a rigid body with mass m. For purposes of illustration the effect of passive elements on motion in a single degree of freedom is modeled. Figure 10.2 schematically represents a passively mounted payload subjected to a base vibrating motion, y_b, and a payload force disturbance, $F_d = m.\ddot{y}_d$.

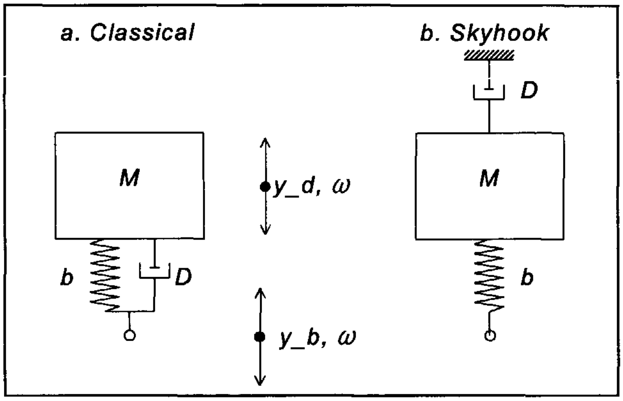

Fig. 10.2.*(a) Classical and (b) skyhook passive vibration isolators with base motion y_b and payload force $m.\ddot{y}_d$.*

Two different constructions of the damper are depicted: the damper in figure 10.2a generated forces proportional to the relative velocity over it, while the forces of the damper in figure 10.2b are proportional only to the relative motion of the payload. These constructions are called classical and skyhook (Beard, 1995) passive elements. The equation of motion of the mass M can be calculated for base motion or direct payload motion for the constructions of passive elements. They are given by

$$\begin{aligned} &\text{classical, base motion: } m.\ddot{y} + D.(\dot{y}-\dot{y}_b) + b.(y-y_b) = 0 \\ &\text{skyhook, base motion: } m.\ddot{y} + D.\dot{y} + b.(y-y_b) = 0 \\ &\text{payload motion: } m.(\ddot{y}-\ddot{y}_d) + D.\dot{y} + b.y = 0 \end{aligned} \tag{10.1}$$

D= damping coefficient
b= spring coefficient

The responses of these systems are given by the following equations and depicted in figure 10.3.

$$\begin{aligned} &\text{classical, base motion: } \frac{y}{y_b} = \frac{\sqrt{1+\left(\frac{D}{b}.\omega\right)^2}}{\sqrt{\left(1-\frac{m}{b}.\omega^2\right)^2+\left(\frac{D}{b}.\omega\right)^2}} \\ &\text{skyhook, base motion: } \frac{y}{y_b} = \frac{1}{\sqrt{\left(1-\frac{m}{b}.\omega^2\right)^2+\left(\frac{D}{b}.\omega\right)^2}} \\ &\text{payload motion: } \frac{y}{y_d} = \frac{\frac{m}{b}.\omega^2}{\sqrt{\left(1-\frac{m}{b}.\omega^2\right)^2+\left(\frac{D}{b}.\omega\right)^2}} \end{aligned} \tag{10.2}$$

ω= frequency

Figure 10.3 serves to illustrate some of the fundamental limitations of passive isolation methods. Practical passive damping elements result in a platform resonance of typically 3-5 Hz, as it is given by

$$\omega_{res} = \sqrt{\frac{b}{m}} = \sqrt{\frac{25}{h\ [cm]}}\ [Hz] \tag{10.3}$$

h= compression of a vertical (air) spring system under influence of the mass of the payload

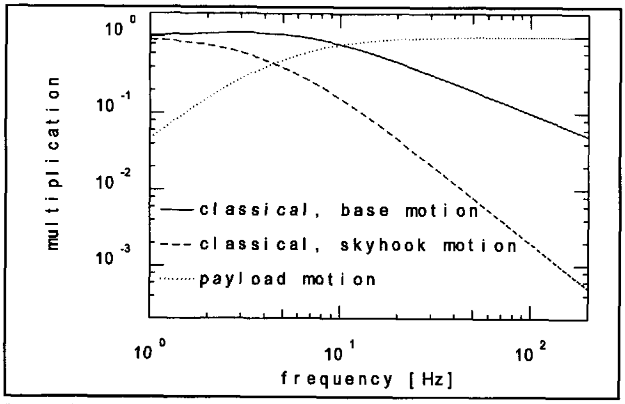

Fig. 10.3. *Responses of the passively isolated system to base motion and payload forces.*

When one combines now the base disturbance (figure 10.1) with its gain (figure 10.3) it can be seen that passive vibration damping is only effective for high frequency vibrations. For vibrations below about 100 Hz the isolation is insufficient to reach the demands as listed in table 10.1. This frequency is lower if a skyhook construction is used in stead of the classical construction. However it is very hard to realize this construction in a practical situation.

There seems to be another limitation as the result of the trade-off between base disturbance isolation and payload isolation. Improved rejection of base disturbances comes at the expense of the payload disturbance rejection and vice-versa. However these effects can be decoupled often. Acoustic noise is isolated from the payload by surrounding the system with a box with adsorbing material.

Two other vibration sources are the connection of "the Fancier" to the Next system and the turbo molecular pump. Figure 10.4 shows their position in "the Fancier". If they are connected stiff to the optical system they act as direct payload forces. However a bellow can be in between, allowing vacuum connection and vibration isolation by one element. The spring coefficient of such a bellow can be 3 N/mm. This means that the transfer of vibrations is equal to the base disturbances: vibrations at high frequencies are isolated while those at low frequencies are completely transmitted. The deviation between low and high frequencies is the resonance frequency as given in equation (10.3) which is for the spring coefficient of the bellow about 4.5 Hz.

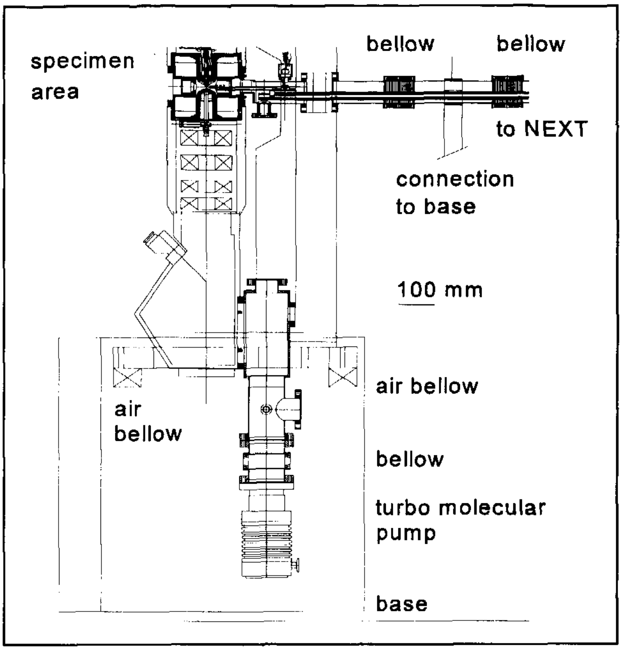

Fig. 10.4. *Isolation of vibrations from the Next system and the turbo molecular pump to the optical column of "the Fancier".*

The effect of vibrations of the turbo molecular pump is low below and above the resonance frequency, but it is significant around the resonance frequency. This is because the transfer function is effectively the product of the "base" transfer and the payload transfer as depicted in figure 10.3. Therefore it is essential that the vibration level of the turbo molecular pump itself is sufficiently low here.

In the connection between "the Fancier" and the Next system there are two bellows to limit the broad band of vibration amplitudes. The element between the bellows is stiffly connected to the base. Therefore this element has effectively a very high mass and low resonance frequency. So even for low frequency vibrations the Next system is decoupled from "the Fancier". However a second bellow is now needed to isolate the base disturbances, that are coupled by this middle element.

As an intermediate conclusion it is stressed that vibrations lower than some 100 Hz are not filtered enough by passive isolators due to physical and practical limitations of these isolators. This makes active damping necessary.

10.3. Active stabilization

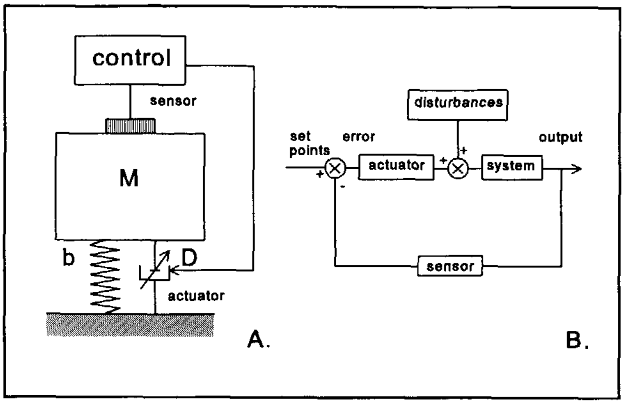

Fig. 10.5. *Principle of active stabilization.*

Figure 10.5 shows the principle of active positioning in one degree of freedom. It consists of a sensor to measure the displacement and a displacement actuator. Both are coupled in a negative feedback loop. The output is the actual vibration amplitude; this is measured by the sensor. It is compared with the set point, in this case zero as no vibrations are allowed to produce the error signal. The error is used by the actuator to generate a certain motion- this is making changes in the manipulated variables to return the output to the set point.

Very common active vibration dampers try to isolate the payload, in this case the microscope, from the vibration source, mostly the floor with its base disturbances (Beard, 1995). However this has a few disadvantages. Firstly, the mass that has to be positioned actively, is relatively high. This makes it hard to realize active damping at high frequencies. Secondly it damps the (low frequency) vibrations of the payload with respect to the base floor. Both can start vibrating by payload forces due to the turbo molecular pump and base disturbances respectively. This means that the system has come to a complete rest only if it can be assumed to be a rigid body. However in practice this is not the case, therefore payload vibrations still can have influence on the vibration performance of the individual elements of the system. The most critical element in that sense is the specimen with respect to the final lens, the objective lens. This is already argued before.

An alternative active vibration damper only positions this specimen with respect to the objective lens. The advantages are that an element with lower mass has to be positioned and that the unstiffness, as a result of the desired dynamic range, has no longer influence on the system performance. This comes at the expense of the low frequency isolation of the whole system. Therefore it is only a better solution if the system can be treated as a stiff body except for the element that is actively positioned. "The Fancier" is treated as a stiff body except for the specimen stage. This is a valid assumption: especially the source and the specimen are moving with respect to the system. But the source vibration amplitudes are demagnified 450 times as a result of the lenses between the source and the specimen. Therefore the active vibration damping will concentrate on positioning the specimen with respect to the objective lens.

10.3.1. Sensors

In order to obtain nanometer stage table repeatability, accurate position sensors are needed to determine the momentary stage position. Here, capacitive sensors (Heerens, 1986) are chosen because of their picometer resolution, vacuum compatibility, extremely low energy loss and relative small size compared to other sensors (van der Wulp, 1996). The basic principle is that one electrode is connected to a reference frame while the other one is connected to the floating object, i.e. the specimen. The capacitance of this set of electrodes is measured. The relation between the capacitance and the electrode geometry of an ideal (guarded) sensor is given by

$$C = \frac{\epsilon_0 . \epsilon_r . 4 . a . b}{d} \qquad \textbf{(10.4)}$$

C= capacitance
ϵ_0= electrical permeability
ϵ_r= relative permeability
2a.2b= the effective capacitive area of rectangular electrodes
d= distance between the electrodes

The performance of the capacitive sensor mainly depends on the measurement electronics. The most accurate measurement system is the alternating current bridge (ac-bridge) in combination with a phase sensitive method (Heerens, 1986). It suits best the dynamic range, the repeatability and the stability in the stage. A commercial ac-bridge can have a resolution (ΔC) of 10^{-6} pF. The maximum detectable capacitance difference is 200 pF and the bandwidth of the system is 20 kHz. The stability of the measurement electronics is better than 10^{-6} pF/hour (van der Wulp, 1996) (Heerens, 1995).

For practical reasons, four different setups of the capacitive sensors in "the Fancier" specimen area will be discussed and compared. A principle drawing is given in figure 10.6. The sensors in these pictures measure a specimen displacement along the x-axis, in the plane of the drawing. The two main differences between these pictures are the type of capacitive sensors (plate-distance geometry in figure a and b, in-plane geometry in figure c and d) and the position of the sensors.

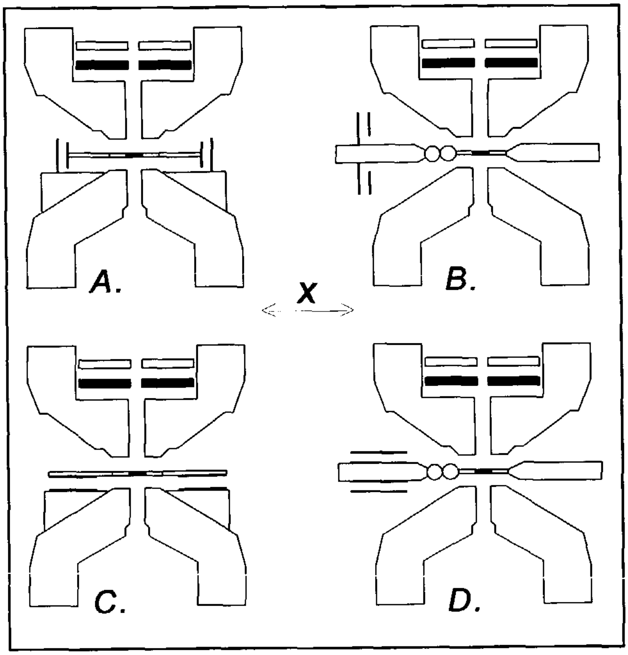

Fig. 10.6. *Capacitive sensor setups.(a.) plate-distance geometry on objective lens, (b.) plate-distance geometry on left ear, (c.) in-plane geometry on objective lens and (d.) in-plane geometry on left ear. All sensors in this figure measure the movements in the plane of the paper.*

In figure a and c the specimen displacement is measured with respect to the pole piece of the objective lens (van der Wulp, 1996). The specimen stage in the other pictures in figure 10.6 is based on the original specimen holder of the Philips EM420, the basic instrument of "the Fancier". This stage consists of two bars, often called the left and right ear of the goniometer. The left bar regulates specimen movements along the y-axis, while the right ear can generate specimen motion in the x, z and θ degree of freedom. These bars are connected by a sapphire ball at the end of each bar. The radius of curvature of these balls is equal to the distance to the center of rotation of the bars. Therefore the contact point of the balls is always at the connecting line between the two centers of rotation of the left and right ear. This is advantageous as specimen tilting is now possible while the same area of the specimen stays visible. The motion of the specimen is measured by detecting the position of the left ear (Heerens, 1996).

The differences will be discussed in greater detail.

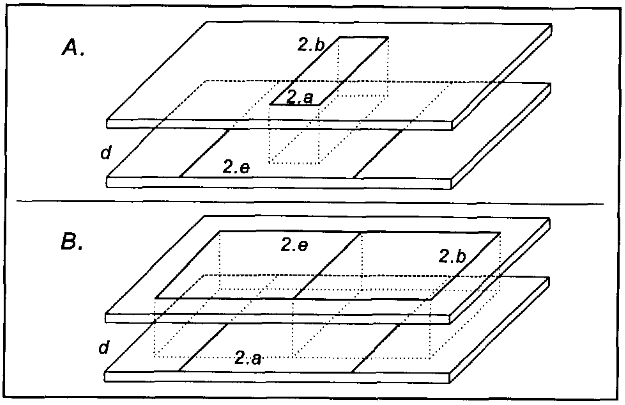

Fig. 10.7. *Capacitive sensor geometries.(a) plate-distance geometry and (b) in-plane geometry.*

The purpose of the plate-distance geometry is to measure displacements perpendicular to the electrode plates (see figure 10.7a). The capacitive variation as a result of a change in distance between the electrodes (Δd) is given by

$$\Delta C_{pd} = \frac{\epsilon_0.\epsilon_r.4.b}{\pi}.\ln\left[\frac{\cosh\left(\frac{\pi}{d}.(e+\frac{\Delta d.a}{2.d})\right)+\cosh\left(\frac{\pi}{d}.(a+\frac{\Delta d.e}{2.d})\right)}{\cosh\left(\frac{\pi}{d}.(e-\frac{\Delta d.a}{2.d})\right)+\cosh\left(\frac{\pi}{d}.(a-\frac{\Delta d.e}{2.d})\right)}\right] \tag{10.5}$$

In the assumption that e is infinitely large this equation simplifies to

$$\Delta C_{pd} = \frac{\epsilon_0.\epsilon_r.4.a.b}{d^2}.\Delta d \tag{10.6}$$

If there is a small tilting angle between the electrodes the capacitive change is given by

$$\Delta C_{pd} = \frac{\epsilon_0.\epsilon_r.4.a.b}{d^2}.\Delta d.\left[1 + \frac{-d^4+3.d^2.a^2+2.\Delta d^2.a^2}{3.d^4}.\theta^2 + O(\theta^4)\right] \tag{10.7}$$

The purpose of the in-plane geometry is to measure displacements parallel to the electrode plates (see figure 10.7b). The capacitive variation as a result of a change in the position of the electrodes relative to each other (Δx) is given by (Holman, 1996)

$$\Delta C_{ip} = \frac{\epsilon_0.\epsilon_r.2.b}{\pi}.\ln\left[\frac{\cosh^2\left(\frac{\pi}{2.d}.(\Delta x+a)\right).\left[\cosh\left(\frac{\pi}{d}.e\right)+\cosh\left(\frac{\pi}{d}.(\Delta x-a)\right)\right]}{\cosh^2\left(\frac{\pi}{2.d}.(\Delta x-a)\right).\left[\cosh\left(\frac{\pi}{d}.e\right)+\cosh\left(\frac{\pi}{d}.(\Delta x+a)\right)\right]}\right] \qquad \textbf{(10.8)}$$

In the assumption that e is infinitely large and that a/d>>1 this equation simplifies to

$$\Delta C_{ip} = \frac{\epsilon_0.\epsilon_r.4.b}{d}.\Delta x \qquad \textbf{(10.9)}$$

If there is a small tilting angle between the electrodes the capacitive change is given by (Holman, 1996)

$$\Delta C_{ip} = \frac{\epsilon_0.\epsilon_r.4.b}{d}.\Delta x.\left[1 + \frac{a^2-d^2-\Delta x}{2.\Delta x.d}.\theta + \frac{d^2+\Delta x^2}{3.d^2}.\theta^2 + O(\theta^3)\right] \qquad \textbf{(10.10)}$$

Figure 10.8 shows the sensitivity of both geometries for equal sizes of the sensors. It is clear that the plate-distance geometry is about 20 times more sensitive, this can be seen from the equations (10.5) and (10.8) since a/d>>1. Another important aspect are fringe effects due to a finite sensor size. However it shows that the relative error because of these effects is about 10^{-8} % for both geometries. So it can be neglected. This is in agreement with the "5d-rule". This rule states that the difference e-a must be larger than 5 times the plate-distance d for a predictability of one ppm (Holman, 1996).

A significant difference between the geometries is cross-talk. This is the effect that several degrees of freedom result in comparable capacitive changes. This makes it in principle impossible to measure the degrees of freedom independently. It shows (equation (10.10) that in the in-plane geometry the capacitive change depends linearly both on a distance disturbance and on a small tilting angle. This makes an extra sensor necessary to measure the tilting angle before the distance disturbance can be known. The plate-distance geometry depends quadratically on the tilting angle. As this angle is in general small (10^{-3} rad) this is a much weaker cross-talk.

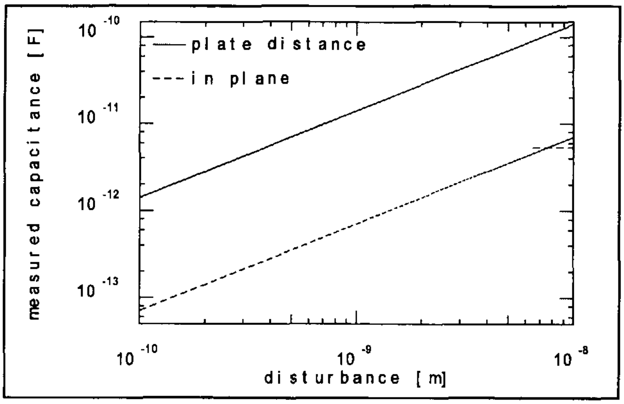

Fig. 10.8. *Sensitivity of the two capacitive sensor geometries. (a) plate-distance geometry and (b) in-plane geometry, a= 2 mm, b= 2 mm, e= 6 mm, d= 0.1 mm.*

The two concepts for the position of the sensors (see figure 10.6) also have a few differences.

1. space consumption

   In principle both concepts need the same space. But between the pole pieces the available space is much smaller. This is because the pole pieces, the objective aperture and the precursor inlet are positioned here too. On the other hand there are no other claims on the area near the left ear of the goniometer.

2. symmetry of the reference

   With a reference to the left ear of the goniometer there is per definition a dependency on environmental influences, especially temperature fluctuations are of importance. The distance between the point of reference and the specimen is about 30 mm and displacements because of thermal expansion over this distance are not detected. For a typical coefficient of thermal expansion of 10^{-6} K^{-1} and a maximum displacement due to temperature drift of 0.0046 nm/min (see table 10.1), a temperature stability better than 0.15 mK/min is required. This is very hard to achieve.

   When the reference is realized symmetrically around the specimen near the objective lens, the sensitivity is decreased. This is because the displacement of the specimen is here determined by the accuracy of the symmetry. If the inaccuracy of the symmetry is 0.05 mm, a temperature stability of 0.1 K can be allowed.

3. perfect rolling of the sapphire balls

   In between the left ear of the goniometer and the specimen there is a nod because of the sapphire balls. With a reference to the left ear of the goniometer it has to be assumed that there is a master-slave relation between the specimen and the left ear. This means that every movement of the specimen results in a movement of the left ear. It can be seen from the construction that this is not true for the tilt around the axis of the bars because the left ear is stiff in this degree of freedom. Another problem is the linearity in the cartesian coordinates. For a well functioning active positioning a linear relation between the specimen movement and the left ear movement has to be assumed. However the sapphire balls are not perfectly flat. The surface roughness will be 25 nm at minimum (Colijn, 1996). Therefore a movement of the specimen can mean a random movement of the left ear, because it can be energetically more advantageous not to follow the specimen. After this random step there is linearity between the two movements until it is again possible to pass a hill on the sapphire balls. This makes stabilization hard and mix and match impossible. These problems do not appear for the reference to the objective lens.

Besides the differences in relation to the capacitive sensors there are also some general differences between the original stage and a stage positioned on the objective lens

1. degrees of freedom

   With the original goniometer stage motion in all five degrees of freedom (x, y, z, ϕ and θ) can be realized. When the sample is positioned on the pole piece of the objective lens movements in the horizontal plane (x,y, and ϕ) are easily accessible. It is hard to change the height of the specimen with respect to the pole piece (z) and to tilt the specimen (θ). However these last two degrees of freedom have a dynamic range of zero (see table 10.1).

2. stiffness of the construction

   The original goniometer is a relatively soft construction, because of two reasons. Firstly the goniometer has mechanical hysteresis: if the specimen is moved in the x- or y-direction followed by the inverse motion it will not return at its original position. Secondly the specimen holder, the bar in the right ear, is pressed against a rubber ring. The force is a result of the pressure difference inside and outside the system. This means that there is a non-stiff connection between the system and the specimen. It is already argued before that this makes the performance sensitive to vibrations.

It is concluded from the above discussion that the best positioning of the sensors is symmetrically around the specimen, which means that a choice has to be made between the constructions depicted in figure 10.6a and 10.6c. A plate-distance sensor (figure 10.6a) gives the best performance since an in-plane geometry is less sensitive. It is also quadratically dependent on the tilting angle while an in-plane geometry is linear in the movement and the tilting angle.

The plate distance between the electrodes of the capacitive sensors is generally some tenths of micrometers. So it is impossible to realize the dynamic range of 3 mm in the horizontal plane while the electrodes of the sensor are at a fixed position. However this would mean that the electrodes that represent the reference to the objective lens cannot be connected stiffly to it.

Therefore it is advantageous to combine the best of both worlds: use the flexible in-plane geometry while its resolution is improved to the desired value by combining these sensors with plate-distance sensors. The latter are used to measure the distance between the two planes in which the in-plane sensors are positioned. By combining the information from two plate-distance sensors the tilting angle is known, independently. With this tilting angle the actual movement, measured by the in-plane sensors, is calculated. Figure 10.9 shows a realization of this combined in-plane/plate-distance sensor geometry. Measurements of the five degrees of freedom is possible according to:

$$\begin{aligned}
z:&\quad d_{sample} = \frac{d_{pd1}+d_{pd2}+d_{pd3}+d_{pd4}}{4}\\
\theta:&\quad \theta_{x,sample} = \frac{0.5(d_{pd1}+d_{pd2})-0.5(d_{pd3}+d_{pd4})}{h}, \quad \theta_{x,ip1} = \theta_{x,sample}\\
x,y:&\quad \Delta x_{sample} = \frac{\Delta x_{ip1,AB-CD}+\Delta x_{ip2,AD-BC}+\Delta x_{ip3,AB-CD}+\Delta x_{ip4,AD-BC}}{4}\\
\phi:&\quad \phi_{sample} = \frac{\Delta y_{ip1,AD-BC}-\Delta y_{ip3,AD-BC}}{2.h}+\frac{\Delta x_{ip2,AD-BC}-\Delta x_{ip4,AD-BC}}{2.h}
\end{aligned} \tag{10.11}$$

With the above equations and the equations 10.5 - 10.10 the sensor geometry can be dimensioned to fulfill the demands listed in table 10.1. The sensor sizes that result from this procedure are depicted in figure 10.9. Not only the demands on resolution but also on dynamic range are achieved while the reference plane stays connected to the objective lens.

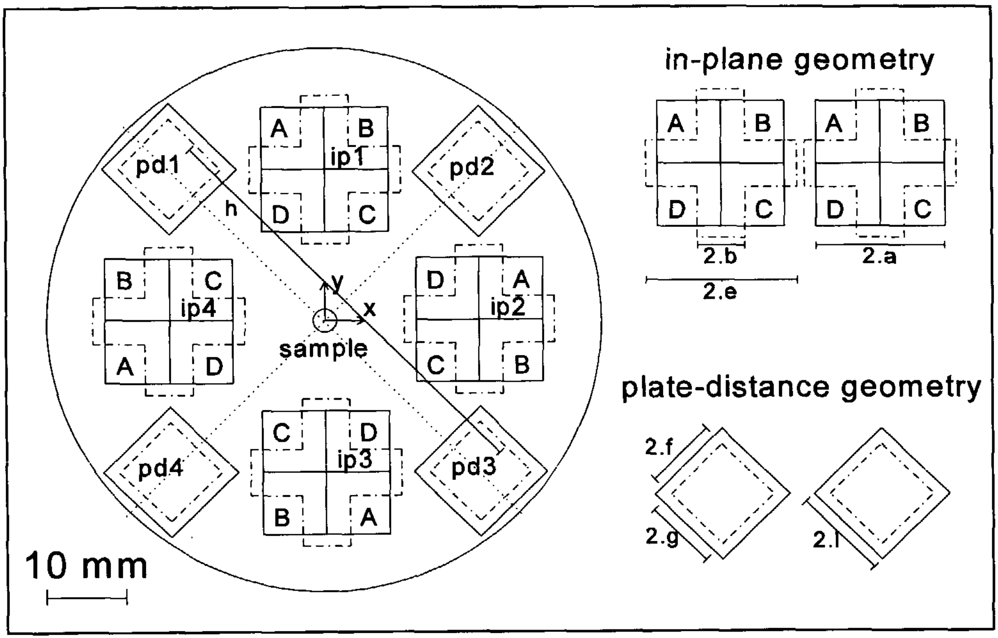

Fig. 10.9. *Sensor geometry with combined plate-distance and in-plane geometry. Continuous lines represent the electrode shapes connected to the sample, the dotted lines show the electrode shapes that form the reference electrode.*

10.3.2. Actuators

It is demonstrated in figure 10.5 that an active stabilization system also has an actuator to counter balance the disturbances that has been measured. The resolution of this actuator has to be better than the overall resolution as listed in table 10.1. Piezo electric transducers can fulfil this demand under vacuum conditions (Renner, 1990).

When certain solid materials are deformed, they generate within them an electric charge. This effect is reversible in that if a charge is applied the material will mechanically deform in response. This action is given the name piezo electric effect.

There are two types of piezo electric transducers: length deformation and scan deformation. In case of length deformation a voltage difference is applied to the top and bottom of a tube of piezo material. The length changes according to

$$\Delta l = d_{31}.\frac{l}{t}.\Delta V \qquad \textbf{(10.12)}$$

d_{31}= diectric property of the piezo material, 2.10^{-10} m/V (Staveley, 1994)
l= length of the tube
t= wall thickness of the tube
ΔV= applied voltage difference

In case of scan deformation a voltage difference is applied to two electrodes that are tangentially positioned on a tube of piezo material. With four electrodes at 90 degrees with respect to each other the top of the tube can scan. The motion of this top with respect to the bottom can be calculated

$$\Delta x = 0.9\ d_{31}.\frac{l^2}{\frac{OD+ID}{2}.t}.\Delta V \tag{10.13}$$

OD= outer diameter of the tube
ID= inner diameter of the tube

The position of these actuators can be designed taking into account the need for active stabilization to frequencies of vibration of several hundreds Hz. Therefore it is impossible to position the actuators far away from the specimen. This does not only make the connection weak but also slow. Besides it is preferable to load the actuators only in the axial direction. Since the piezo material is ceramic, this is the direction in which they are strongest.

The piezo electric actuators can be positioned between the reference plane, the objective lens, and the specimen. Each piezo has one inner and four outer electrodes resulting in three degrees of freedom. To obtain millimeter translations in x- and y-direction, the table is actuated by the inertial sliding mechanism. A sawtooth voltage is applied over the piezos which results in small translation steps of the table (van der Wulp, 1995). If there is not enough space for large enough piezos, one large tube can be positioned in the bar that holds the specimen. For instance this bar can be in the right hand ear of the standard goniometer also allowing relatively easy specimen motion. However this has a large disadvantage : the bar in the right hand ear is pressed against a rubber ring. Therefore the position of the backside of the piezo tube is not fixed and will also change under the influence of the piezo tube lengthening. This means that there is not a complete known relation between the piezo tube length and the specimen position in this setup.

However it can be concluded that piezo actuators are suitable: they are small enough to be positioned near the specimen and they are accurate enough.

10.4. Specimen facilities

The specimen is the place where resolution, production yield and production quality has to be realized. To improve these parameters the specimen can actively influence them by some specimen facilities. Active positioning with sensors and actuators is an example that was already described in the former paragraph. In this paragraph two other specimen facilities will be given: a decelerating specimen and a temperature controlled specimen.

10.4.1. Decelerating specimen

The resolution of the structures is mainly defined by a combination of Coulomb interactions between the beam particles and specimen interactions between the beam particles and the sample. With respect to the beam energy these interactions behave opposite. Higher beam energy gives lower Coulomb interactions but also higher specimen interactions. A way to decouple these effects is the use of a decelerating specimen. Figure 4.16 showed the improvement in resolution.

The technical solution of a decelerating specimen puts the specimen at a high positive potential: ions with 30 keV transport energy will land on the specimen with only 790 eV if the specimen is at 29.210 eV. Figure 4.16 showed that this energy gives optimum structure resolution. In the design of such a decelerating specimen two effects should be considered. Firstly the insulator length to avoid flash-over and secondly a uniform deceleration. This means that the equipotential planes between the objective lens and the specimen have to be flat to avoid aberrations. A technical solution for a stand-alone focused ion beam can be found in literature (Aihara, 1989).

10.4.2. Temperature controlled specimen

It was demonstrated in chapter 3 and 9 that the production yield of beam induced pattern generation is mainly limited by the adsorption density of precursor molecules on the specimen. The mean time of physisorption can be improved significantly by lowering the specimen temperature as has been described in equation (3.15)

$$\tau_{des} = 10^{-13}.\exp\left(\frac{U_B}{k_B.T}\right) \qquad \textbf{(10.14)}$$

τ_{des}= mean time before desorption
U_B= surface binding energy
T= temperature of specimen

So specimen cooling will increase the production yield exponentially, but this is not the only effect of cooling. It also influences the quality of deposited and etched structures, firstly by the contamination. It seems to be reasonable to assume that also the mean time of physisorption of contaminating molecules is enlarged. Contamination is caused by a cross-linking of adsorbed organic molecules under energetic beam irradiation. However contamination films can also be reduced in thickness by etching effects as an energetic beam induced chemical reaction with adsorbed residual gas molecules (H_2O, H_2, N_2, O_2 and CO). It has even been reported (Hirsch, 1993) that with specimen cooling in combination with a cryoshield at the same low temperature, the contamination has decreased to low values at about -30 °C. A further decrease of temperature results in an increasing etching rate. Etching will surely depend on the composition of the rest gas in the system.

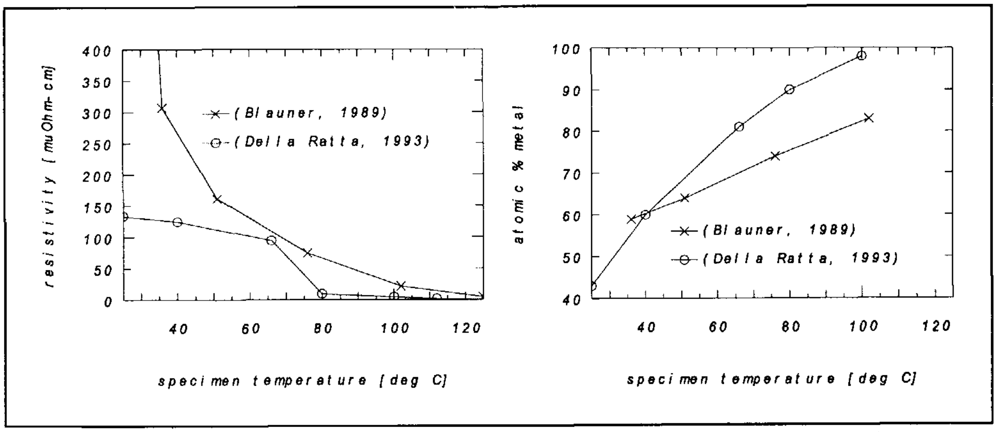

Fig. 10.10. *Fabrication quality of beam induced deposited structures as a function of the specimen temperature. (Blauner, 1989): $Me_2Au(hfac)$, 40 keV Ga, (Della Ratta, 1993): Cu(hfac)TMVS, 35 keV Ga.*

A more important effect of the specimen temperature on structure quality is depicted in figure 10.10. The composition of the deposited structure and the resistivity are depicted here as a function of the specimen temperature. It can be concluded from this figure that there is a correlation between the resistivity and the metal content of the deposited structure. The metal content decreases with lower specimen temperatures. The high resistivity of room-temperature beam induced metal deposits results from incomplete desorption of by-products (Blauner, 1989). A possible explanation for this is that the film is growing too rapidly for the by-product molecules to escape readily, but it is most likely that a microstructural effect is responsible for this trend. Transmission electron microscopy of Cu deposition shows (Della Ratta, 1993) that the low temperature films apparently consist of small, 20 nm islands of copper surrounded by a low Z-matrix, presumably mostly carbon. This is in agreement with another explanation for this effect (Schößler, 1996). For platinum containing deposits the conductivity is very probably due to the hopping of electrons from crystallite to crystallite due to the nanocrystallinity of the deposited film, ohmic behavior can be excluded as a consequence of the temperature characteristics. At higher temperatures, the islands grow and contact each other. At 100 °C the film appears to be polycrystalline metal film.

Therefore the specimen need to be at about 100 °C to deposit structures with sufficiently low resistivity especially if carbon containing precursor molecules are used. However this also has a negative effect on the production yield since the mean time of physisorption is lowered.

10.5. Summary

The specimen for all systems is a piece of 1 cm^2 Si, the structures are written in a central area of 3 mm. This specimen has to be transported in and out of "the Fancier". Also during fabrication the specimen has to be moved since the structure can be larger than the field of view. This flexible positioning of the specimen has to be realized in combination with a stiff positioning with respect to the objective lens (motions smaller than 0.046 nm) during fabrication to avoid structure enlargement because of vibrations from the base and pumps connected to "the Fancier". Especially low frequency vibrations (<100 Hz) are a problem since they are not filtered enough by passive dampers.

Therefore the position of the specimen with respect to the objective lens is controlled actively. In a feedback loop the specimen position can be measured by capacitive sensors and moved with piezo electric tubes. Both sensors and actuators can best be positioned symmetrically around the specimen to avoid as much as possible the problems of the standard goniometer of the EM 420. These are for instance the strong influence of temperature fluctuations on the specimen position and the weakness of the construction.

For the capacitive sensors an idea has been described to combine in-plane and plate-distance sensors. This makes it possible to combine the best of both worlds: flexibility of the in-plane sensor and accuracy or sensitivity of the plate-distance sensor. In this combination the cross-talk between the movement and tilting in an in-plane sensor is minimized by measuring the plate distance of the in-plane sensor with a plate-distance sensor.

Finally two specimen facilities are discussed. It turns out that for a decelerating specimen it has to be at a potential of about 30 kV. In case of beam induced pattern generation the temperature not only influences the production yield but also the product quality. At room temperature films consists of small metal islands surrounded mostly by carbon since the reaction by-products are incorporated in the film. At higher temperatures, about 100 °C, the film appears to be polycrystalline. Therefore specimen heating to 100 °C is also a required facility for the specimen stage.

The mechanical realization of these specimen facilities has not been developed completely.

References

Aihara, R., H. Kasahar, H. Sawaragi, M.H. Shearer and W.B. Thompson, *Optical system for a low-energy focused ion beam*, Journal of Vacuum Science and Technology B7(1), 1989, pp. 79-82

Beard, A.M., A.H. von Flotow, D.H. Schubert, *A practical product implementation of an Active/Passive vibration Isolation system*, 1995

Blauner, P.G., Y. Butt, J. Sang Ro, C.V. Thompson and J. Melngailis, *Focused ion beam induced deposition of low-resistivity gold films*, Journal of Vacuum Science and Technology B7(6), 1989, pp. 1816-1818

Colijn, P.F., *private communication*, TU Delft, 1996

Della Ratta, A.D., J. Melngailis and C.V. Thompson, *Focused-ion beam induced deposition of copper*, Journal of Vacuum Science and Technology B11(6), 1993, pp. 2195-2199

Geerligs, B., *private communication*, TU Delft, 1996

Heerens, W. Chr., *Applications of capacitance techniques in sensor design -Review Article*, Journal of Physics E: Scientific Instruments 19, 1986, pp. 897-906

Heerens, W. Chr., *Multi-terminal capacitor geometries: Concepts for designing sensors* *in a smart way*, Journal A 32(3), 1991, pp. 52-59

Heerens, W. Chr., *Ideas about an absolute specimen replacement strategy*, Proceedings of the International Seminar on Quantitative Microscopy, Braunschweig, 1995

Heerens, W. Chr., *Concept voor positie- en stabiliteitsmeting voor standing wave illumimation probehouder en voor ionen bundel patroongenerator voor het Next project*, Delft, 1996, unpublished

Hirsch, P., M. Kässens, M, Püttmann and L. Reimer, *Contamination in a Scanning Electron Microscope and the Influence of Specimen Cooling*, Scanning 16, 1994, pp. 101-110

Holman, A.E., *A novel scanning tunneling microscope with inherent scan linearization*, thesis, Delft, 1996

Karnopp, D., M.J. Crosby and R.A. Harwood, *Vibration control using Semi-Active Force Generators*, Journal of Engineering for Industry, 1974, pp. 619-626

Renner, Ch., Ph. Niedermann, A.D. Kent and Q. Fisher, *A vertical piezoelectric inertial slider*, Review of Scientific Instruments 61(3), 1990, pp. 965-967

Schößler, A., A. Kaya, J. Kretz, M. Weber and H.W.P. Koops, *Electrical and field emission properties of nanocrystalline materials fabricated by electron-beam induced deposition*, Microelectronic Engineering 30, 1996, pp. 471-474

Staveley Sensors, *Product description of EBL Piezoceramic Tubes*, East Hartford, 1994

Wulp, H. van der and R. van Dalen, *Nanometer positioning device with 1 millimeter range for use in a TEM*, IPES, 1995

Wulp, H. van der, H.F. van Beek, B.M. Mertens, *A pieze-driven TEM stage with nanometer position stability*, ASPE conference 1996

Wulp, H. van der, M. Hoogteijling, P.V. Pistecky, *Piezoelectric nano-actuator with large dynamic range and extreme position stability*, Aktuator conference, 1996

11. Mechanical and electronic design of the FANCIER

Introduction

"The Fancier" is one of the instruments for nanofabrication that are brought together in the NEXT project. All instruments in the NEXT project are linked by an Ultra High Vacuum transport system. The first paragraph of this chapter will describe how a specimen can be transferred from the transport system into "the Fancier".

Also "the Fancier" can only work properly when the pressure is sufficiently low. There are several reasons for good vacuum. Firstly the ions and electrons need to travel through the system without collisions with the residual gas atoms. Secondly, residual gas atoms can adsorb on the sample. This can change the properties of the fabricated structures considerably. The second paragraph of this chapter will describe how good vacuum can be achieved in "the Fancier".

In all previous chapters it is assumed that the particles move exactly on the optical axis of the system formed by the line that connects the centers of the optical elements. Only the pattern generation deflector will bring the ions and the electrons off-axis in this assumption. However in general this is not the case, for example the lenses are not all exactly on the same straight line and the emitting tip is not perfectly in the center of the extractor electrode. The third paragraph of this chapter will describe how the ion beam can be directed through the centers of all optical elements. This is realized by several deflectors.

These deflectors, but also the lenses and the 90°-deflectors of the energy filter, need a *power supply that can be controlled. The electronic design of "the Fancier" is described in the fourth paragraph.*

11.1. Connection of the FANCIER to the NEXT system

The NEXT system contains chambers for specimen preparation, deposition and etching by a Scanning Tunneling Microscope (STM), atom and polymer manipulation by an STM, Electron Spectroscopy for Chemical Analysis (ESCA), cryostat analysis and "the Fancier". A specimen should be brought from one of these instruments to another. Imagine: a specimen is brought in the NEXT system through the loadlock. First it is cleaned in the preparation chamber, then it is moved into "the Fancier". Here metal contacts are written with a distance of 20 nm. This is followed by the fabrication of an atomic groove in the silicon with the etch STM. In the manipulation chamber metal atoms are positioned in the groove between the contacts. Finally the conductivity of this atomic wire can be measured in the cryostat.

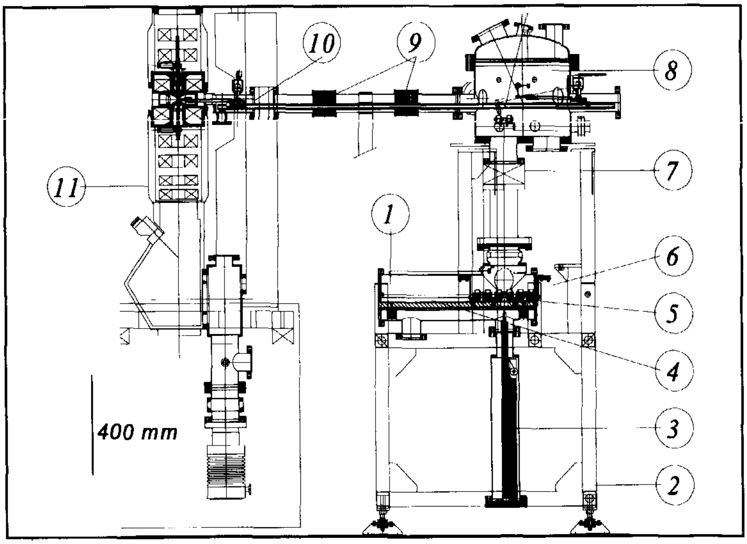

Fig. 11.1. *The transport system from the NEXT transport tube to "the Fancier".*

It is not allowed to bring the sample at atmospheric pressure during these fabrication steps; the structures would be destroyed. Therefore all chambers of the NEXT system are connected to a transport tube (figure 1.5 and pos. 1 in figure 11.1) of 19 meters long that is at a pressure of 10^{-10} mbar. This pressure is low enough to avoid serious deposition on the specimens during the time of transport. Though this tube the specimens can be moved on the train (pos. 5 in figure 11.1). This train rolls on a rail (pos. 4 in figure 11.1) inside the vacuum, while the train can be displaced by moving a magnet outside the vacuum. Therefore the train is equipped with two NiFe plates (pos. 6. in figure 11.1) that are attracted to the magnets. On the train there are three containers (pos. 5 in figure 11.1) with the specimens. The specimens have been placed in these containers like plates in a plate-rack. However, in "the Fancier" the specimens will be used with their side of interest at the top.

If the train is parked at one of the specific positions where a fabrication or analysis chamber is positioned above it, a vertical bar (pos. 3 in figure 11.1) can be pushed through the train. This vertical bar takes with it a specimen container upwards into one of these chambers since there is a hole in each container in which a pin of the vertical push bar fits.

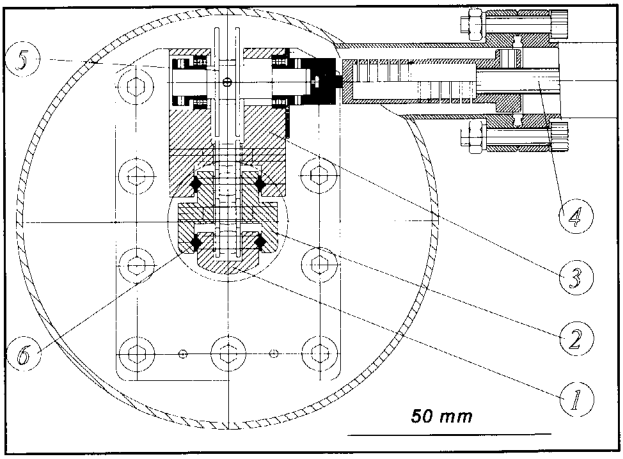

Fig. 11.2. *The vertical transport, pos.3 in figure 11.1.*

A special, telescopic, Ultra High Vacuum compatible transport system has been developed for "the Fancier", see figure 11.2 for a horizontal cross-section. A telescopic system is necessary since the distance between the floor of the room and the train is shorter than the distance from the train to the chamber (pos. 8 in figure 11.1). The principle of the transport system is similar to the staircase on the roof of a fire service car. The three elements (pos. 1, 2 and 3 in figure 11.2) can slide with respect to each other. The largest one (pos. 3 in figure 11.2) has been connected to the base flange, so the other two will move up to the manipulation chamber. As bearing Al_2O_3 balls (pos. 6 in figure 11.2) are used on the TiC coated aluminum elements. The actual movement of the elements is realized by a stainless steel "plate" of 0.02 mm that meanders between the top and the bottom of each element. It is connected to the lowest side of the first element (pos.1 in figure 11.2). It is guided by a bearing on the bottom of this element to the top of the second element (pos. 2 in figure 11.2). Here it is bended again over a bearing to the bottom of it. Finally the plate is guided over the top of the third element (pos. 3 in figure 11.2) and it is connected to a rod (pos. 5 in figure 11.2). The plate can now be winded around the rod that is connected to a rotation feedthrough (pos. 4 in figure 11.2). Therefore the elements are forced upwards during winding of the stainless steel plate, taking with it a specimen container. During unwinding of the metal plate, the elements come downwards under the influence of gravity.

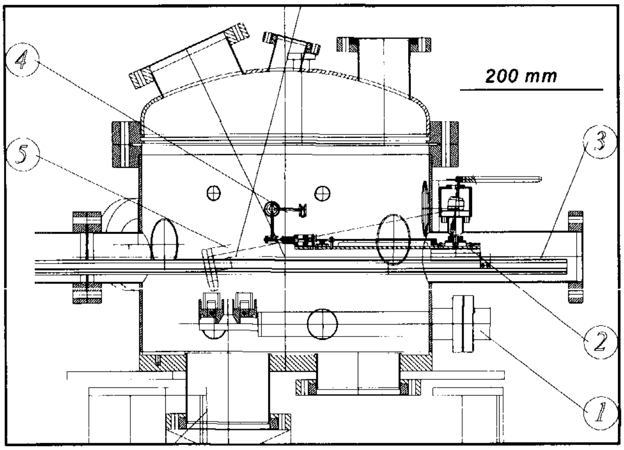

Fig. 11.3. *The manipulation chamber, pos. 8 in figure 11.1.*

Now the container is in the manipulation chamber, see figure 11.3. First it can be parked here on a linear motion feedthrough (pos. 1 in figure 11.3) allowing the vertical transport system to be pull backwards. This makes it possible to close the valve (pos. 7 in figure 11.1) and to move the train to another chamber in the NEXT system.

In the manipulation chamber of "the Fancier" an individual specimen can be picked up with a wobbler-stick (pos. 5 in figure 11.3) and positioned on a rotation feedthrough (pos. 4 in figure 11.3). It was mentioned before that the specimens have to be rotated to bring their side of interest to the top. The rotation feedthrough performs this function and brings the specimen in the right position for transport to "the Fancier". Figure 11.4 shows a picture of the manipulation chamber.

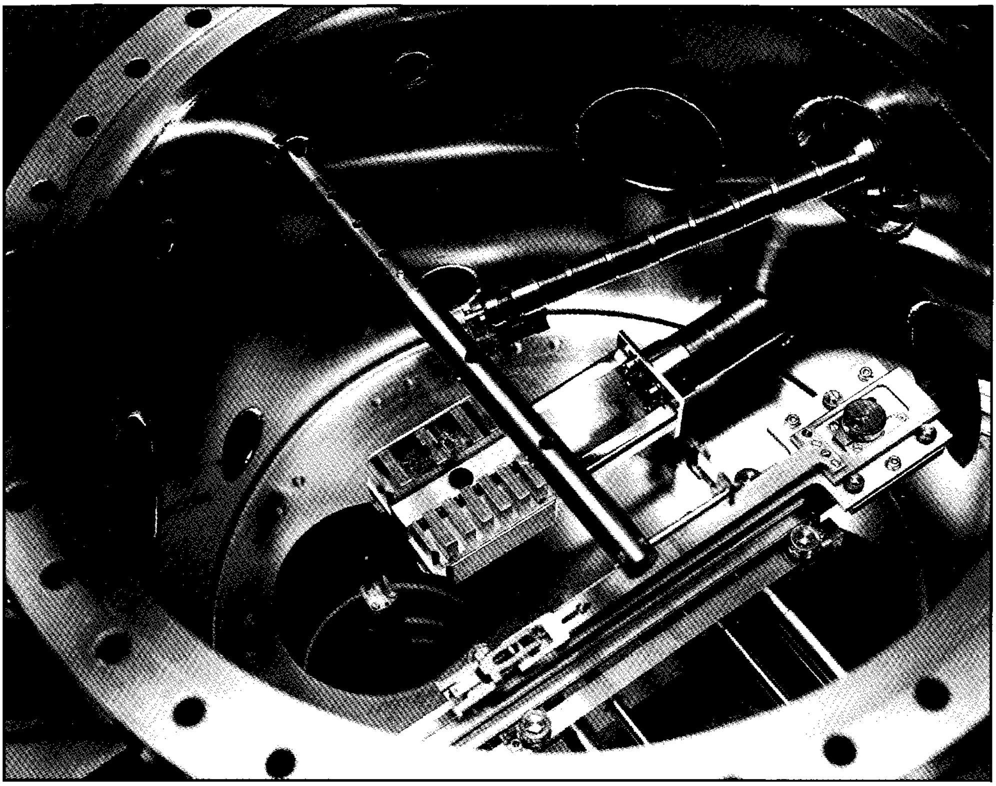

Fig. 11.4. *The manipulation chamber.*

The final step in transport is horizontally from the manipulation chamber (pos. 8 in figure 11.1) to the specimen area of "the Fancier" (pos. 11 in figure 11.1). This manipulation is realized by a bi-directional transporter (pos. 3 in figure 11.3, pos. 2 in figure 11.5) It is a rail that can be moved by a rack-and-pinion connected to a rotation feedthrough on the manipulation chamber. A second rotation feedthrough moves a train (pos. 2 in figure 11.3, pos. 3 in figure 11.5) on that rail by pulling a metal wire. This metal wire goes over the ends of the bi-directional rail allowing the train to be positioned anywhere on the rail.

On the rail there is a specimen holder (pos. 7 in figure 11.5) that can pick up a specimen in the manipulation chamber and deliver it in the specimen area and vice versa. Figure 11.5 shows the pick-up station at the side of "the Fancier", an identical one is at the manipulation chamber. The bi-directional transporter is parked (pos. 1 in figure 11.5) to minimize its motion during specimen loading and unloading by the specimen holder. This specimen holder keeps the specimen between "thumb and finger". Wether this set is open or closed depends on the position of the push-pull bar (pos. 5 in figure 11.5) that is operated by a wobbler-stick (pos. 4 in figure 11.4). Since this wobbler stick is connected to a rack- and-pinion on the train. Therefore its rotational motion is translated into a push-pull motion of the bar and therefore into a pick-up or deliver action of the specimen holder.

When the specimen is delivered inside "the Fancier" the rail of the bi-directional transporter is pulled back till it is completely at the right side of the valve (pos. 10 in figure 11.1) between the specimen area and the manipulation chamber. This has two functions. Firstly the precursor gas cannot come into the manipulation chamber. Secondly the rail is hanging freely in the system so the only connection between the NEXT system and "the Fancier" is by means of the bellows in the horizontal tube. However these bellows (pos. 9 in figure 11.1) have been designed to prevent the transfer of vibrations to "the Fancier" (see chapter 10).

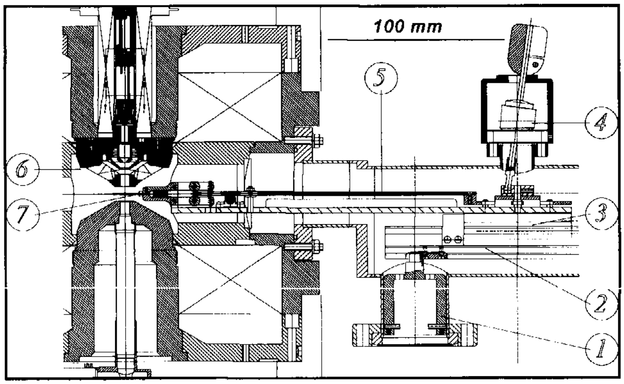

Fig. 11.5. *The horizontal transport.*

11.2. Vacuum system

In the standard vacuum of most Scanning Transmission Electron Microscopes (STEM) the sample is subjected to a pressure in which most samples are covered with one or more monolayers of contamination within a few seconds. This is also the case in the EM 420, the basic instrument of "the Fancier". The use of a STEM as an instrument for pattern fabrication on the surface makes it necessary to improve the, relatively, poor vacuum of the standard microscope.

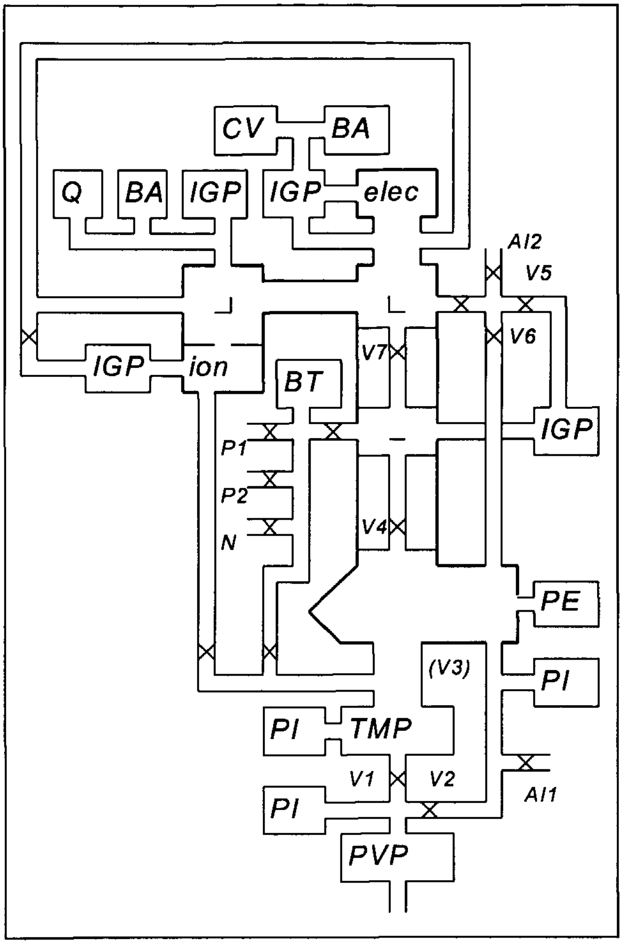

Fig. 11.6. *The vacuum system. PVP= pre-vacuum pump, TMP= turbo molecular pump, IGP= ion getter pump, PI= Pirani gauge, PE= Penning gauge, CV= convectron gauge, BT= Baretron gauge, Q= quadrupole mass spectrometer, P= precursor, N= nitrogen gas, AI= air inlet.*

The standard vacuum in most commercially available microscopes is in the 10^{-7} mbar range with water vapor and hydro-carbons as the main contaminating gases. The hydro-carbons originate from the use of an oil diffusion pump, rotational pre-vacuum pump and O-rings. The hydro-carbons can be connected with each other as the result of energetic particles like electrons forming plastic like materials. However it is possible to limit the amount of hydro-carbons from being in the system drastically. In "the Fancier" the oil diffusion pump is replaced by a turbo molecular pump and the rotational pre-vacuum pump by a membrane pump, both are oil free. These pumps are used to evacuate the whole instrument making use of the vacuum by-pass. The by-pass is a tube to enable a large pumping speed at every part of the instrument, see figure 11.6.

An overall improvement of the pressure is possible by adding larger pumps, but this gives only the desired result if the construction and design of the system is adapted. Rubber rings should be replaced by metal ones, gliding rings by bellows. To obtain Ultra High Vacuum conditions in the specimen area this area has to be redesigned completely as was done before (Bleeker, 1991). The decision has been made to keep this area in its original construction. However the vacuum can be improved by adding a cold finger around the specimen. The contaminations will preferably adsorb on this cold ring reducing the amount of contaminations on the specimen.

The design considerations for Ultra High Vacuum have been implemented in the newly designed parts of "the Fancier". This means the ion optical system towards valve V7 in figure 11.6 and the electron source chamber. Near valve V7 there is a small aperture that enables differential pumping. Therefore in both source regions the pressure can be below 10^{-8} mbar since individual ion getter pumps are connected to the source regions.

The precursor inlet is also incorporated in the vacuum system. It has been described in chapter 9 that the inlet reservoir has to be evacuated before the second precursor material can be used. This is realized by introducing nitrogen gas in the reservoir to reduce the precursor concentration and pumping with the turbo molecular pump.

11.3. Optical alignment

The best performance is achieved if the ion and the electron beam pass through the center of all optical elements. Otherwise off-axis aberrations get important in defining the probe size. In general these aberrations are larger than the chromatic and spherical aberrations discussed in the chapters 4 till 7.

To realize perfect alignment of the beams and the center of the optical elements, mechanical pre-alignment is performed in all elements. For example by using the Al_2O_3 balls in the electrostatic condenser lens, see chapter 5. However, the alignment of the optical elements with respect to each other is achieved optically with correction deflectors. Three methods to check wether the beam is in the center of an optical element are the following:

1. center of hole

   Every condenser lens and objective lens of the ion optical system operates with an insulated middle electrode. Also at the entrance and exit plane of the 90°-deflectors there are (fringing) electrodes with circular holes. If the beam is scanned over these elements and the current that falls on the electrode is used for the image, a ring will be visible. The mechanical middle of the bore can be found as the center of this ring. The bore size of one to six millimeters makes that the accuracy of this method is about 10-60 μm.

2. reduction of the shift by Δf

   The next method makes use of the lens effect itself. In case of misalignment the probe moves on the image plane if the focal length is changed. With shorter focal length the accuracy increases, so when the misalignment is further minimized the focal length can be made shorter step-by-step.

3. circle of inversion

   The spherical aberration of a lens can also be used in an alignment procedure. A known target like a square grid must be used and the beam must be focused at a plane below this target. If a pencil beam enters the lens further away from the optical axis the beam is bent more towards it. If the beam is scanned above the lens, there is a radial distance from the center of the lens where the deflection of the scan is compensated by the spherical aberration. This is illustrated in figure 11.7a. This circle is imaged with infinite magnification. The middle of the lens can be found by the middle of the ring circle of inversion as shown in figure 11.7b. With shorter focal length this can be made more accurate.

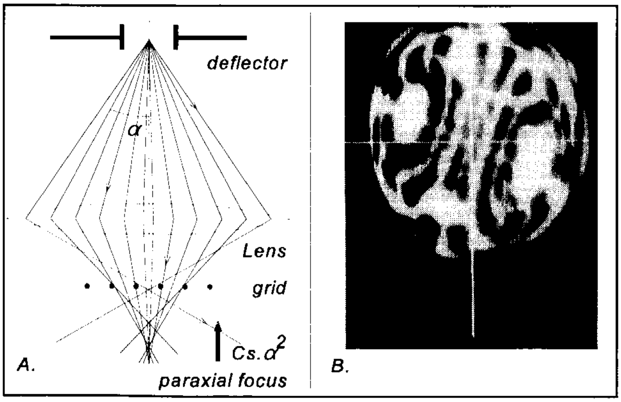

Fig. 11.7. *Circle of inversion originating from spherical aberration, (a.) principle, (b.) result of 127 μm grid.*

A practical alignment procedure can be as described below.

1. start ion emission
2. move mass filter aperture out of beam line
3. connect defl.-1 to ground
4. scan with defl.-2
5. focus beam with source lens on E-cond.-1 lens
6. find setting of defl.-2 so that beam goes through center of E-cond.-1 lens
7. fix setting of defl.-2 on this value
8. scan with defl.-1.
9. focus beam with the source lens on defl.-2
10. connect defl-1 to ground
11. scan with defl.-3
12. focus beam with E-cond.-1 lens on E-cond.-2 lens
13. find setting of defl.-3 so that beam goes through center of E-cond.-2 lens
14. fix setting defl.-3 on this value
15. make focal length of E-cond.-1 lens shorter
16. scan with defl.-1, defl.-2 and defl.-3 follow so that beam goes through center of E-cond.-1 and E-cond.-2 lens
17. focus beam with E-cond.-2 lens on sens-1
18. find setting of defl.-1 so that beam goes through center of sens-1
19. fix setting of defl.-1, defl.-2 and defl.-3 on this value
20. move mechanically mass filter aperture symmetrically around beam
21. scan with defl.-3
22. change setting E-cond.-1 lens
23. adapt setting of defl.-2 so that beam stays in position during change
24. scan with defl.-4
25. apply potentials to first 90°-deflector
26. find setting of defl.-4 so that beam goes through center of sens-2
27. fix setting of defl.-4
28. connect defl.-6 to ground
29. open the energy selecting slit
30. scan with defl.-5
31. focus with E-cond.-2 lens on sens-3
32. find setting of defl.-5 so that beam goes through center of sens-3

33. fix setting of defl.-5
34. move mechanically energy selecting slit around beam
35. focus with E-cond.-2 lens on energy selecting slit
36. scan with defl.-6
37. apply potentials to second 90°-deflector equal to first 90°-deflector

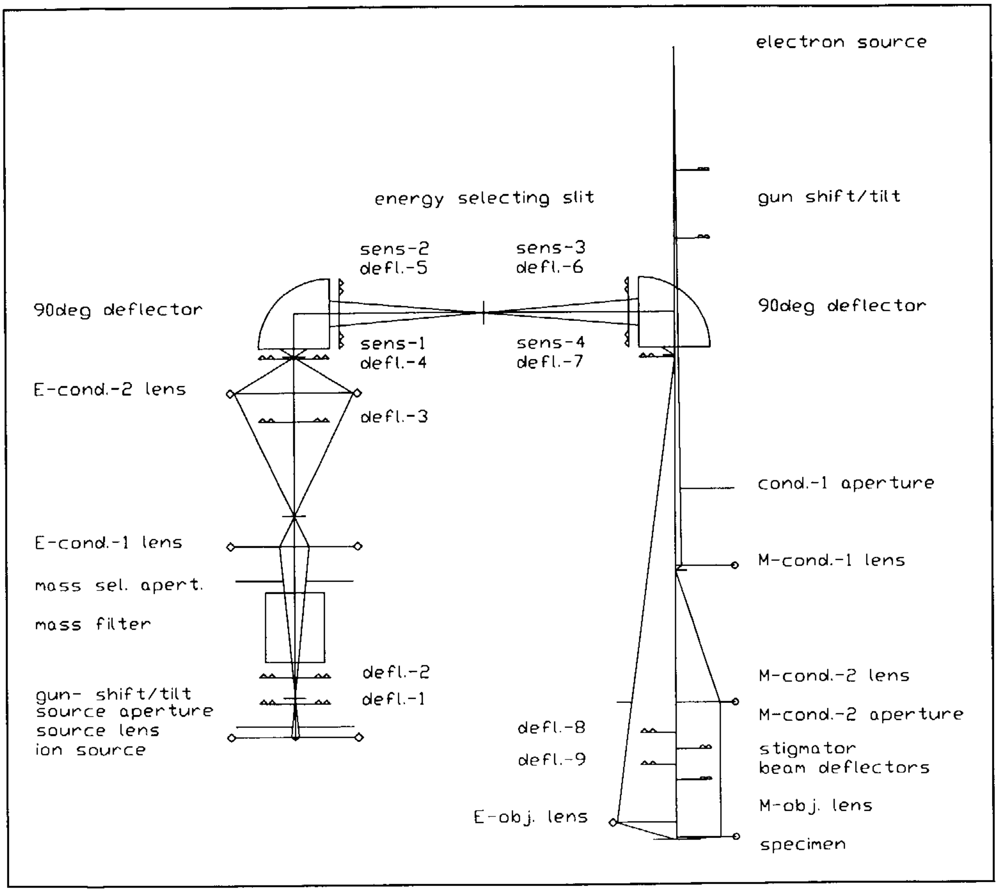

Fig. 11.8. *The optical system for the ion beam with alignment facilities.*

38. adapt length of horizontal column so that system is symmetric by changing the distance between the cubes in figure 6.1
39. find setting of defl.-6 so that beam goes through center of sens-4
40. fix setting of defl.-6
41. scan with defl.-7
42. find setting of defl.-7 so that beam goes through center of M-cond.-2 aperture, this

aperture has been positioned in the electron beam alignment procedure

43. fix setting of defl.-7
44. scan with defl.-8
45. find setting of defl.-8 so that beam goes through center of objective lens
46. fix setting of defl.-8
47. scan with combined defl.-8 and defl.-9 so that beam goes through center of objective lens

11.4. Electronic control and supplies

In the ion optical part of "the Fancier" there are 8 optical elements to be controlled for lenses and 90°-deflectors, while there are 9 octupoles for alignment, stigmation and pattern generation. In the illumination system of the electron optical part there are 3 lenses and 4 deflectors/stigmators. Between all of these elements there are optical relations. These relations for the lenses of the individual optical parts have already been discussed in chapter 4. However there are also relations between the ion and the electron optical part when both beams have to be manipulated at the same time for-in-situ observation with the electron beam during fabrication with the ion beam.

The best method to combine all those relations in a flexible way is computer control. Figure 11.9 shows the basic setup of the electronic system of "the Fancier".

Most of the relations between the optical elements are described in software. The output

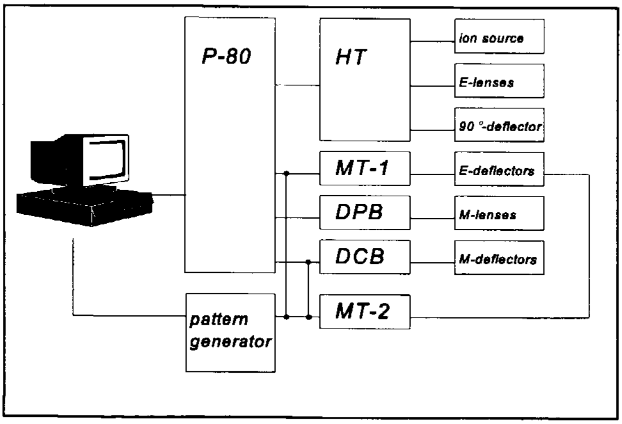

Fig. 11.9. *The electronic system of "the Fancier".*

of the computer is transferred to the P80 system. This is a data acquisition system specially designed by Philips to control particle optical columns like electron microscopes. It has data converters with 20 bits stability for the lenses and multiple DACS that can be used to control deflectors and stigmators. With P80 it is possible to supply the magnetic lenses and deflectors directly by DPB and DCB units.

However for electrostatic systems P80 cannot be used directly. A special High Tension supply (HT) for the lenses of the ion optical system. Since stability is the most important parameter, one power supply of 30 keV is used for all lenses. This means that variations in the voltage with periods longer than the time of flight of the ions do not have influence on the performance of the ion beam. But not all lenses are at the same potential. Therefore a small power supply is added to the basic one for every individual lens. This HT unit also supplies the heater for the Liquid Metal Ion Source (LMIS).

For the deflectors of the ion optical system of "the Fancier" slow supplies (MT-1) of -300...+300 V have been developed. They are too slow for pattern generation, here another medium tension supply is used (MT-2).

References

Bleeker, A.J., *Optical and mechanical design for 1 nm resolution Auger spectroscopy in an Electron Microscope*, thesis, Delft, 1991

12. Summary & Samenvatting

12.1. Summary and Conclusion

Focused ion and electron beams are widespread tools in microfabrication, but their applicability for nanofabrication is not straightforward. In this thesis the design of an instrument for nanofabrication using a focused ion and electron beam is discussed. This instrument is called "the Fancier", Fabrication and Analysis of Nanostructures Combining Ion and Electron Regulation. It is one of the instruments that is developed in the NEXT project to study mesoscopic structures.

At the Delft University of Technology, significant contributions have been made to the field of mesoscopic physics, the study of effects connected with reduced dimensionality in the solid state. These effects are not only a scaling of the effects of conventional macroscopic structures, it is to be expected that new quantum mechanical physical properties will be observed. To fabricate devices on a molecular level, to investigate quantum transport and interactions in systems with very few electrons, and to extend mesoscopic phenomena to room temperature, completely new techniques are necessary in the longer run.

The NEXT project, Nanoscale Experiments and Technology, aims to observe the new quantum mechanical phenomena, but first to develop several of the new structure fabrication techniques. Most of the instruments in the NEXT project are based on Scanning Tunneling Microscopes (STM). If the needle of such a microscope is brought to within a nanometer from the specimen an electrical current will start with a quantum mechanical origin: tunneling. With the energy, transferred to the specimen by this tunneling current, a chemical reaction on the specimen surface can be induced. This reaction can result in a nanometer sized metal structure or etched groove. Also manipulation of polymers and atoms is possible using the STM as a hoisting crane. Besides the Scanning Tunneling Microscopes also an instrument with a focused ion and electron beam on the same optical axis, is part of the NEXT system: "the Fancier".

A beam of ions offers several unique fabrication techniques like direct deposition of ions on the specimen surface, direct implantation of ions in the specimen and sputtering of atoms from the specimen. With a particle beam a chemical reaction can be induced resulting in etching or deposition, like with an STM. The production rate and flexibility with a particle beam are much better than with an STM. However it is very hard to obtain fabriction with nanometer resolution with a particle beam. Therefore the main point of research in the Fancier project is to obtain this high resolution.

The resolution of a structure fabricated by a particle beam is influenced by two process steps. The first process step is focusing of the particles in a small probe, while in the second process step the energy of the ions or electrons is transferred into the specimen: the specimen interaction. This takes into account the lateral spread of the effect of a single impacting particle. Specimen interactions are often disregarded in case of ions since they are only visible when the ions are focused to within a nanoscale probe.

The properties of the specimen interaction have been simulated for energetic particles as a function of their mass and energy by a Monte-Carlo program. The trajectory of individual particles is simulated by repeatedly calculating the nuclear and electronic interaction with the specimen atoms during the scattering of the particle in the specimen. Although Monte-Carlo simulations are very time consuming, they are used since no analytical description of the resolution of specimen interactions is known. However, the implantation profile of several ion species on a Si sample has been calculated and compared to simulated results. The simulated Monte-Carlo results have also been compared to analytical models for the production yield, energy and angular distribution of sputtered atoms and secondary electrons. It can be concluded that the results of the Monte-Carlo model are in sufficiently good agreement with these experimental and analytical results to assume that the results of the Monte-Carlo model for the resolution of the specimen interaction are useful too.

In general it can be concluded that the best resolution is obtained for high mass, low energy particles. The explanation is that these particles are stopped very effectively in a specimen keeping the interaction between the ions and the sample very localized. Figure 12.1 summarizes the resolution of an Ar ion beam with infinitesimal small lateral probe size for structure fabrication by implantation, sputtering and beam induced etching and deposition. It can be concluded that the highest resolution is achieved for pattern generation by sputtering.

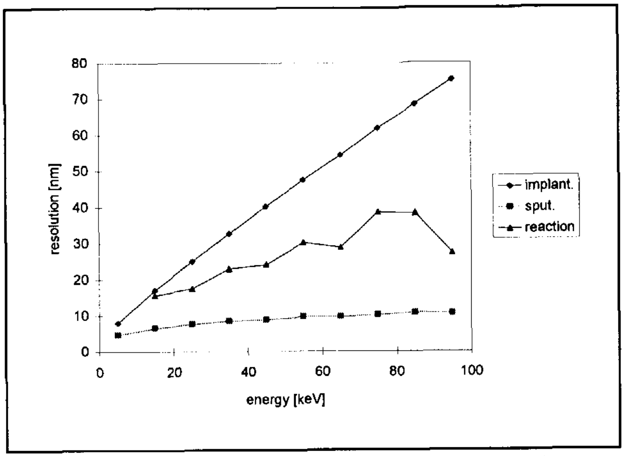

Fig. 12.1. *Resolution of fabrication with Ar ions (a.) direct implantation, (b.) sputtering, (c.) beam induced pattern generation.*

Once the nanostructures have been created, they need to be observed. The most convenient method is measuring the secondary electron yield coming from the specimen after bombarding with a primary beam in scanning mode. For one pixel of an image 10^4 secondary electrons are needed for a reasonable signal-to-noise ratio. Unfortunately, it is not only secondary electrons that are emitted after bombarding with ions, also emission of sputtered atoms will occur. This will erode the specimen. If it is required that at most one monolayer may be removed, only electrons can be used to observe the structures with a resolution better than 20 nm.

Until here only the specimen interactions have been discussed. Structure fabrication with ions should be possible with nanometer resolution especially for heavy ions at low energy. Nanoobservation is only possible with electrons if energetic particles would be used. Therefore it is advantageous to design the optics of "the Fancier" not only to focus the beams in a nanoscale probe but also to combine both the ion and the electron beam.

The basic instrument of "the Fancier" is a Transmission Electron Microscope with a resolution of 0.65 nm after slightly modifying it. These modifications are necessary to add the ion beam system. The optical systems for both beams are designed partially around the same optical axis. One of the modifications to the electron beam system is the secondary electron detector, since the ion beam would be deflected by the attracting field of the standard secondary electron detector.

A rotationally symmetric secondary electron detector has been developed. The secondary electrons are pulled away from the specimen by the field of the magnetic objective lens. They are focused by a round electrode at high tension, followed by a round retarding electrode at -100 V. So they return in the direction of the specimen. However the magnetic field functions as a mirror too. Therefore the secondary electrons start spiraling between the retarding electrode and the upper pole piece until they have come far enough off-axis to land on the middle electrode instead of being focused by it.

In principle this detector has an important advantage over conventional detectors which deflect the secondary electrons off-axis: it does not deteriorate the primary ion and electron beam. The price that has to be paid is a lower collection efficiency. Especially high energy secondary electrons are not collected since they return to the specimen. A collection efficiency of about 60 % of the total amount of secondary electrons is to be expected. It can be improved with a small deflector near the retarding electrode where the axial velocity of the secondary electrons is minimal.

The middle electrode is made of YAG material, which is scintillating. A scintillator is able to transfer an electron current into a photon current. It is covered with a 50 nm thick aluminum layer at high tension to attract the secondary electrons. One of the unknown factors is the photon collection efficiency of this scintillator. It is realistic that only a part of the generated photons will reach the light guide to the photo multiplier because of the relatively complicated shape of the scintillator. A photo multiplier has been chosen as it allows a rotationally symmetric collection of the secondary electrons with the scintillator. Therefore it is in agreement with the basic idea behind this secondary electron detector: detection of the secondary electrons with a maximum detection efficiency but without disturbing the primary beam.

The main part of research in the Fancier project directed at obtaining a nanometer ion probe with an optical system that is added to the Transmission Electron Microscope. The first element is the ion source, specially developed for the different fabrication techniques. For sputtering and beam induced pattern generation an Ar Gas Field Ion Source is chosen. These fabrication techniques make use of the energy of the ions but the ion species is not of direct importance. Inert gas ions are used to prevent deterioration of the electrical properties of the specimen by the implanted ions. In a Gas Field Ion Source the gas is introduced locally near the sharp tip of a needle that is at a high electric field. The inert gas atom is ionized when an electron tunnels from the atom to the tip. This is only possible if the gas atom is only a few nanometers away from the tip. The emission current can be improved by cooling the tip to a desired temperature. At this temperature the adsorbed gas atoms start hopping on the needle because of thermal accommodation. During every hop there is a chance for ionization because the atoms come into the ionization zone. Above this temperature the thermal accommodation is too weak to start hopping, while at a lower temperature the height of the hops decreases until the atoms only migrate over the surface without being ionized.

First experiments in a test setup show that the brightness of a Gas Field Ion Source is high enough for "the Fancier". Sources with comparable brightness but a wider energy distribution are Liquid Metal Ion Sources. In this source the material to be ionized in is the liquid phase on the needle. This makes emission possible of a wide range of ion species, like Au for direct deposition of metal lines and B and As for implantation of dopant material in Si. These elements are part of an alloy (AuSi, PdBAs) to prevent operating the ion source at a very high temperature. This would induce unwanted chemical reactions with the tip. An important parameter for stable emission from a Liquid Metal Ion Source is good wetting of the needle with the overlayer, the material to be ionized. It is realized in a separate Ultra High Vacuum system where the needle and the overlayer material are cleaned before they are brought in contact with each other.

Both source types need source extraction optics. This can be a tetrode system where the emission current and focal length can be set independently. In the design an optimum has to be found between lens aberrations (they can be of importance as the source lens is magnifying), alignment of the electrodes (the particles are emitted with a large opening angle and therefore they are far off-axis), Coulomb interactions (the current density is very high in the source region) and aperture erosion (the current is large in the source region).

Behind the source optics, the condenser optics are positioned to demagnify the beam. Two types of lenses have been considered: rotationally symmetric and quadrupole lenses. The advantage of a quadrupole lens is its lower excitation potential. But for a lens which gives a stigmatic image with arbitrary focal length and magnification four quadrupoles have to be combined. The conclusion is drawn that a rotationally symmetric lens is preferable if there is enough space available. The designed condenser lens has a minimal focal length of 6 mm. Its aberration coefficients are small enough to make the assumption valid that the aberration contribution of the condenser lenses to the final probe size can be disregarded compared to the aberration contribution of the objective lens.

The ions emitted from a Liquid Metal Ion Source have an energy spread of about 5 eV (Full Width at Half Maximum of the distribution). This wide energy distribution does not allow focusing of the ions in a nanometer probe because of the influence of chromatic aberrations. However there are four techniques to decrease the influence of the chromatic aberration on the final probe size: increasing the beam energy (but this increases the contribution of the second process step of structure fabrication, the specimen interaction), decreasing the opening angle (but the probe current is decreased by a factor four when the opening angle is halved), an optical element with negative chromatic aberration coefficient like an electrostatic mirror (but the ions are stopped by this mirror which gives large beam interaction effects) and an energy filter.

Although this filter decreases the probe current by a factor two when the energy spread is halved, it seems to be the optimum solution to achieve a nanometer probe. The main parts of the horizontal column are two 90°-deflectors and a slit, together this is the energy filter. The first 90°-deflector separates the ions with different energies. They end up at different positions at the energy selecting slit. The width of the slit defines the energy spread of the ion beam that is transferred to the specimen. The second 90°-deflector brings all ions, that have passed the energy selecting slit, together at the same point near the exit plane of this deflector. This makes the horizontal column achromatic, which means that the images near the entrance plane of the first 90°-deflector and near the exit plane of the second 90°-deflector are equal except for the energy spread of the ions in these images that has been limited. The 90°-deflectors have spherical electrostatic electrodes with a mean radius of curvature of 30 mm. This is decided mainly to make it easy to tune the system as a spherical deflector is double focusing. So a real image is formed at the slit position. At the slit ions with an energy that differs too much from the central energy of the beam, are stopped because they end up at a larger distance from the central axis than the slit width. However other effects than energy spread can bring the ions off-axis too, like vibrations of the system. As a result of the optimization between length of the horizontal column and the slit size the system behavior is not dominated by vibrations. The slit has to be adjusted with micrometer accuracy; for the calculated optimum energy spread the slit size is 4.8 μm.

For the alignment of the system multipoles are positioned at the entrance and exit slit of the 90°-deflectors, while the position of the slit can be adjusted. Also the part of the knife edges in front of the beam can be adjusted to refresh them as they are eroded by the ion beam.

A high resolution particle beam instrument that combines an ion and an electron beam on the same optical axis, needs at least one combined lens: the objective lens. To obtain the smallest aberration contribution to the probe the final lens has to be close to the specimen. Only in case of a combined lens this can be achieved for both beams. For the electron beam the standard magnetic lens can be used. An electrostatic Einzel lens has been integrated with the magnetic lens, because the magnetic lens is too weak to focus the ion beam properly. The upper pole piece functions as part of the magnetic lens and as third electrode of this electrostatic Einzel lens.

The quality of the magnetic lens has not been deteriorated. It still has a spherical and chromatic aberration coefficient of 2.2 mm. The spherical and chromatic aberration coefficient of the new electrostatic lens are 1247 mm and 49.5 mm respectively. The construction is made such that the integrated lens can be mounted in the instrument in the same way as a standard upper pole piece. The electrodes of this lens are also the electrodes in the secondary electron detector as discussed above.

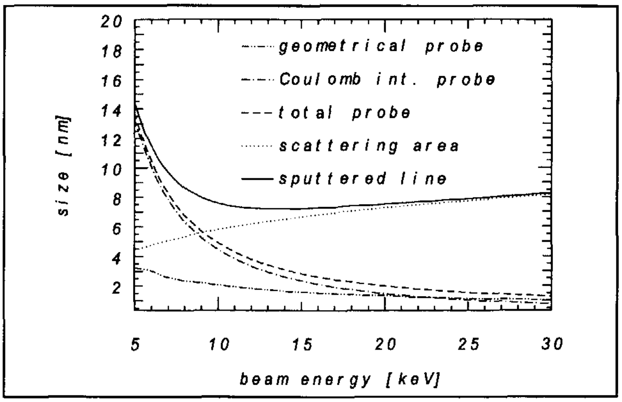

Fig. 12.2. *Size of structure in Si sputtered with Ar ions (10^{-14} A probe current) as a function of the energy of the ions. The probe size, a combination of the geometrical probe contribution (demagnified source size, chromatic and spherical aberration) and the probe contribution from Coulomb interactions, is depicted as well as the scattering area of the ions in the specimen.*

Figure 12.2 shows the resolution of the ion optical system of "the Fancier" as a function of the energy of the ions. The probe size is restricted to 2 nm by reducing the chromatic aberration contribution with an energy filter based on two position dispersive 90°-deflectors. It is assumed that the beam goes through the center of all lenses and is free of second order aberrations. However the lenses are not perfectly positioned on the same optical axis and the holes of the lenses are not perfectly circular. Therefore alignment deflectors are necessary since misalignment can enlarge the probe size considerably. With nine octupoles in the ion optical system the beam is directed through the center of all lenses enabling to reach the desired properties.

The effect of Coulomb interactions on the beam is decreased by a small aperture near the source. This aperture limits the beam current such that the system can be described by equations of the Pencil beam regime. It only stops those ions that would be stopped anyway later in the system because of their large angle to the optical axis. So they would have effect on the probe only through interactions with ions that should be focused in the probe to the specimen. This effect is decreased by stopping them.

The size of fabricated structures results from a convolution of the place distributions of the two process steps of structure fabrication: the distribution of the ions in the probe at the specimen and the distribution of the specimen interaction of an individual ion. The minimal structure size in case of sputtering in Si with Ar ions is 7 nm. Compared to commercially available combined ion and electron beam instruments with non-coincident beams, this means a significant smaller probe size equal current density. With a decelerating specimen the resolution of the sputtered line can even be improved to 3 nm. This gives also the possibility for structure fabrication by direct deposition where the landing energy of the ions has to be less than 1 keV.

Focusing of the beams in a nanoscale probe is necessary but not sufficient for the fabrication of mesoscopic structures. For all fabrication techniques the beams have to be directed along the desired pattern by deflectors. A double pre-lens deflector is used to combine the desired resolution of both the ion and the electron beam with a large field-of-view. It is possible to direct the beam through the center of the objective lens while still having a reasonable field-of-view of 50x50 μm for the ion at the highest resolution and for the electrons ranging from 2x2 mm to 1x1 μm. This optical path minimizes the effect of off-axis aberrations of the objective lens. The combination of these fields-of-view and the vector scan exposure scheme gives reasonable production speed to avoid problems with stability. A typical structure can be written with the ion beam at the highest resolution within about 450 seconds. For the electron beam the magnetic double deflector of the electron microscope can be used, but for the ion beam a new electrostatic deflector has been developed. It consists of two eight-poles that are positioned inside the linertube of the objective lens with inner diameter of 10 mm.

Now that the beams can be directed towards a specific position on the specimen pattern generation by means of direct implantation and sputtering is possible. However for beam induced etching and deposition a gas introduction system has been developed. The precursor gas is introduced through a nozzle. This minimizes the amount of precursor material in the vacuum system, by introducing the gas locally at the field-of-view on the specimen. This nozzle is connected to a reservoir with pumping and pressure measurement connection. Also the precursor containers for etching and deposition material are connected to this reservoir. By heating the container of a liquid or solid state precursor to a temperature of 350 K a sufficient flow of gas through the nozzle can be realized for a wide range of precursors. If the precursor is in the gas state at room temperature a servo valve is used with feedback from the reservoir pressure. In case of beam induced pattern generation not only the reservoir temperature is of importance but also the specimen temperature. It influences the production yield and the product quality. At room temperature films consists of small metal islands surrounded mostly by carbon since the reaction by-products are incorporated in the film. At higher temperatures, about 370 K, the film appears to be polycrystalline. Therefore specimen heating to 370 K is a required facility for the specimen stage. All fabrication techniques as listed above can be realized in "the Fancier" with the above pattern generation facilities on the NEXT samples.

The specimen for all systems in NEXT is a piece of 1 cm^2 Si, the structures are written in a central area of 3 mm. This specimen has to be transported in and out of "the Fancier". Since "the Fancier" is part of the NEXT system an Ultra High Vacuum compatible connection has been developed with vertical motion of the specimen containers by a telescopic transporter, rotation of an individual specimen and horizontal transport into the specimen area by a bi-directional transporter. Not only during transport but also during fabrication the specimen has to be moved since the structure can be larger than the field of view or more structures should be written on a single specimen. This flexible positioning of the specimen has to be realized in combination with a stiff positioning with respect to the objective lens (relative motions smaller than 0.046 nm) during fabrication. Especially low frequency vibrations (<100 Hz) are a problem since they are not filtered enough by passive dampers.

Therefore the position of the specimen with respect to the objective lens will be controlled actively. In a feedback loop the specimen position can be measured by capacitive sensors and moved with piezo electric tubes. Both sensors and actuators can best be positioned symmetrically around the specimen to avoid as much as possible the problems of the standard goniometer of the EM 420. These are the results of for instance the strong influence of temperature fluctuations on the specimen position and the weakness of the construction. For the capacitive sensors an idea has been described to combine in-plane and plate-distance sensors. This makes it possible to combine the best of both worlds: flexibility of the in-plane sensor and accuracy or sensitivity of the plate-distance sensor. In this combination the cross-talk between the movement and tilting in an in-plane sensor is minimized by measuring the plate distance of the in-plane sensor with a plate-distance sensor.

At the first page of the *introduction to nanotechnology* it was written that "we may now look forward to significant advances in molecular engineering technologies that will enable us to construct our devices atom by atom, much as a builder constructs a house brick by brick or as nature evolves living cells." More than 300 pages later it can be concluded that this is not yet realized. However a design has been presented for a combined ion and electron beam system that should be able to fabricate and analyze structures with typical sizes of nanometers. These structures can be metal lines, grooves in Si or doped islands in Si. The system is under construction as this moment. The author hopes that "the Fancier" will be a useful instrument in nanofabrication for the near future.

12.2. Samenvatting en Conclusies

Gefocusseerde bundels van elektronen en ionen zijn veel gebruikte hulpmiddelen voor het vervaardigen van structuren met afmetingen van micrometers, maar nu toepasbaarheid voor het vervaardigen van structuren met afmetingen van nanometers is niet eenvoudig. Dit proefschrift behandelt het ontwerp van een instrument voor nanofabrikage op basis van een gefocusseerde bundel elektronen en ionen. Dit instrument wordt "the Fancier" genoemd, "Fabrication and Analysis of Nanostructures Combining Ion and Electron Regulation". Het is één van de instrumenten die ontwikkeld wordt in het NEXT project om mesoscopische structuren te bestuderen.

Aan de Technische Universiteit Delft is veel onderzoek gedaan aan mesoscopische fysica, de studie van effecten die optreden bij miniaturisering van structuren in de vaste stof. Deze effecten zijn niet alleen een schaling van effecten die ook bij grotere structuren optreden, maar het is de verwachting dat ook nieuwe quantummechanische effecten zullen worden waargenomen. Op de lange termijn zijn compleet nieuwe technieken nodig om structuren te vervaardigen op moleculaire schaal, om transportverschijnselen op quantumniveau en interacties in systemen met slechts enkele elektronen te onderzoeken en om bekende mesoscopische effecten bij kamertemperatuur waar te kunnen nemen.

Het NEXT project, "Nanoscale Experiments and Technology", heeft als doel het observeren van de nieuwe quantummechanische fenomenen, maar vooruit lopend daarop zullen verschillende nieuwe technieken voor fabricage van structuren worden ontwikkeld. Het grootste deel van de instrumenten in het NEXT project maakt gebruik van Scanning Tunneling Microscopen (STM). Indien de naald van deze microscoop binnen een nanometer van het preparaat gebracht wordt zal er een elektrische stroom ontstaan die als oorzaak een quantummechanisch effect heeft: tunnelen. Met de energie, die naar het preparaat wordt overgedragen door deze tunnel stroom, kan een chemische reactie in gang worden gezet aan het oppervlak van het preparaat. Deze chemische reactie kan het ontstaan van een metalen structuur of een geëtste groef met een afmeting van een nanometer tot gevolg hebben. Ook is het mogelijk om polymeren en atomen te manipuleren met de STM alsof het een hijskraan is. Naast de Scanning Tunneling Microscopen maakt ook een instrument met een gefocusseerde bundel ionen en elektronen, die over dezelfde optische as bewegen, deel uit van het NEXT systeem: "the Fancier".

Een bundel ionen biedt verschillende unieke fabricage technieken zoals direct neerleggen van ionen op het oppervlak van het preparaat, direct inschieten van ionen in het preparaat en sputteren van atomen uit het preparaat. Met een bundel deeltjes kan ook een chemische reactie tot stand worden gebracht die etsen of deponeren tot gevolg heeft. De produktiesnelheid en flexibiliteit met een bundel deeltjes is veel groter dan met een STM. Maar het is erg moeilijk om de resolutie van fabricage met een bundel deeltjes op een nanometer te krijgen. Daarom zal het belangrijkste onderwerp van onderzoek in het Fancier project zich richten op het verkrijgen van deze hoge resolutie.

De resolutie van een structuur die gefabriceerd wordt met een bundel deeltjes, wordt beïnvloedt door de twee proces stappen. In de eerste proces stap worden de deeltjes gefocusseerd in een kleine probe, terwijl in de tweede proces stap de energie van de inslaande ionen of elektronen wordt overgedragen aan het preparaat: de preparaat interactie. Dit houdt onder andere rekening met de laterale spreiding van het effect van één enkel inslaand deeltje. Preparaat interacties worden vaak buiten beschouwing gelaten in het geval van ionen omdat ze alleen zichtbaar zijn wanneer de ionen gefocusseerd worden tot een probe op nanometer schaal.

De preparaat interacties van de energetische deeltjes zijn gesimuleerd als functie van hun massa ene energie door een Monte-Carlo programma. Het traject van een individueel deeltje wordt gesimuleerd door het berekenen van de nucleaire en elektronische interactie met de atomen van het preparaat tijdens het botsingsproces van het deeltje in het preparaat. Ondanks dat Monte-Carlo simulaties erg tijdrovend zijn, worden ze toch gebruikt omdat geen analytische beschrijving van de resolutie van de preparaat interactie bekend is. Het implantatieprofiel van verschillende ionen soorten in een Si preparaat zijn vergeleken met gesimuleerde resultaten. De gesimuleerde Monte-Carlo resultaten zijn ook vergeleken met analytische modellen voor de produktiesnelheid, energie en hoek verdeling van de gesputterde atomen en secundaire elektronen. Op grond hiervan can worden geconcludeerd dat de resultaten van het Monte-Carlo model in voldoende mate overeenstemmen met deze experimentele en analytische resultaten om te veronderstellen dat de resultaten van het Monte-Carlo model voor de resolutie van de preparaat interactie ook bruikbaar zijn.

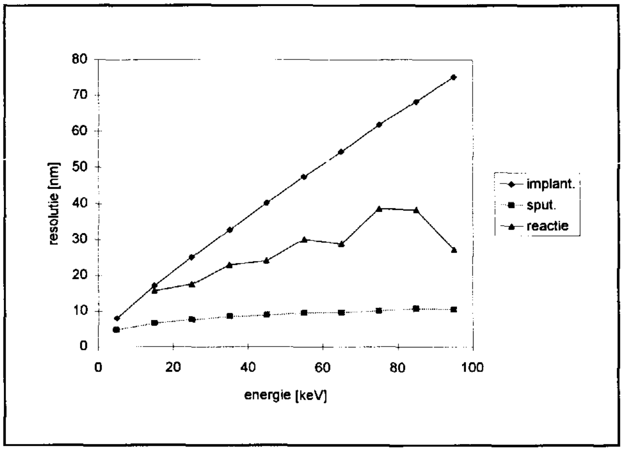

Fig. 12.3. *Resolutie van structuurfabrikage met Ar ionen (a.) direct implanteren, (b.) sputteren, (c.) bundel gestimuleeld patroon genereren.*

In het algemeen kan worden geconcludeerd dat de beste resolutie wordt verkregen bij gebruik van deeltjes met een hoge massa en weinig energie. De verklaring is dat deze deeltjes zeer effectief worden gestopt waardoor de interactie tussen de ionen en het preparaat zeer lokaal plaats vindt. Figuur 12.3 vat de resolutie samen van een bundel met Ar ionen met oneindig kleine afmeting van de probe voor fabricage van de structuren door middel van inplanteren, sputteren en bundel gestimuleerd etsen en deponeren. Het kan worden geconcludeerd dat de beste resolutie wordt verkregen wanneer de structuren worden vervaardigd door sputteren.

Wanneer de structuren eenmaal gemaakt zijn, is het noodzakelijk om ze te bekijken. De meest voor de hand liggende methode is het meten van de secundaire elektronen stroom die van het preparaat afkomt na beschieting met een primaire bundel in scannende toestand. Voor één beeldpunt van een plaatje zijn 10^4 secundaire elektronen noodzakelijk om een redelijke signaal-ruis-verhouding te krijgen. Helaas komen er niet alleen secundaire elektronen vrij na beschieting met ionen, ook emissie van gesputterde atomen zal optreden. Dit zal het preparaat beschadigen. Indien het noodzakelijk is dat maximaal één laag atomen mag worden verwijderd, dan kunnen slechts elektronen worden gebruikt om structuren te bekijken met een resolutie beter dan 20 nm.

In het bovenstaande zijn alleen de preparaat interacties besproken. Fabricage van structuren met nanometer resolutie zou op grond daarvan mogelijk zijn in het bijzonder met zware ionen met weinig energie. Nano-observatie is alleen mogelijk met elektronen indien energetische deeltjes worden gebruikt. Daarom is het voordelig om het lenzenstelsel van "the Fancier" zodanig te ontwerpen dat niet alleen de bundels in een probe op nanoschaal worden gefocusseerd maar ook zodanig dat de ionen en de elektronen bundel worden gecombineerd.

Het basisinstrument van "the Fancier" is een Transmissie Elektronen Microscoop met een resolutie van 0.65 nm na het uitvoeren van enige aanpassingen. Deze aanpassingen zijn noodzakelijk om het systeem van de ionen bundel toe te voegen. De optische stelsels van beide bundels worden zo ontworpen dat ze deels rond dezelfde optische as liggen. Eén van de aanpassingen aan hete systeem van de elektronenbundel betreft de secundaire elektronen detector, omdat de ionen bundel afgebogen zou worden door het aantrekkende veld van de standaard secundaire elektronen detector.

Een rotatiesymmetrische secundaire elektronen detector is ontwikkeld. De secundaire elektronen worden bij het preparaat vandaan getrokken door het veld van de magnetische objectieflens. Ze worden gefocusseerd door een ronde elektrode op hoogspanning, gevolgd door een ronde afstotende elektrode op -100 V. Daardoor keren ze weer terug in de richting van het preparaat. Echter het magnetische veld fungeert ook als een spiegel. Daarom beginnen de secundaire elektronen te spiraliseren tussen de afstotende elektrode en de bovenste poolschoen totdat ze voldoende ver van de as zijn afgekomen dat ze landen op de middelste elektrode in plaats van erdoor gefocusseerd te worden.

In principe heeft de detector een belangrijk voordeel boven conventionele detectoren die de secundaire elektronen afbuigen ten opzichte van de as: de primaire ionen en elektronen bundel worden niet beïnvloedt. De prijs die daarvoor betaald moet worden is een lagere detectie efficiëntie. In het bijzonder secundaire elektronen met veel energie worden niet gedetecteerd omdat ze terugkeren naar het preparaat. Een detectie efficiëntie van ongeveer 60% van de totale hoeveelheid secundaire elektronen kan worden verwacht. Dit kan worden verbeterd door het opstellen van een kleine afbuiger nabij de afstotende elektrode waar de axiale snelheid van de secundaire elektronen minimaal is.

De middelste elektrode wordt gemaakt van YAG materiaal, dat scintillerend is. Een scintillator is in staat om een stroom van elektronen in een stroom van fotonen om te zetten. Deze wordt bedekt met een laagje aluminium van 50 nm dikte dat op hoogspanning staat om de secundaire elektronen aan te trekken. Een van de onzekere factoren is de foton detectie efficiëntie. Het is realistisch dat slechts een deel van de ontstane fotonen de lichtgeleider zullen bereiken die naar de photo muliplier leidt. Dit is het gevolg van de relatief gecompliceerde vorm van de scintillator. Een photo multiplier is gekozen omdat deze, in combinatie met een scintillator, de rotatiesymmetrische detectie van secundaire elektronen mogelijk maakt. Daarom is het in overeen stemming met de basis gedachte achter deze secundaire elektronen detector: detectie van secundaire elektronen met een zo groot mogelijke detectie efficiëntie maar zonder de primaire bundel te beïnvloeden.

Het grootste deel van het onderzoek in het Fancier project is erop gericht om een nanometer probe van ionen te verkrijgen met een optisch systeem dat toegevoegd wordt aan de Transmissie Elektronen Microscoop. Het eerste element is de ionenbron, speciaal ontwikkeld voor de verschillende fabricage technieken. Voor sputteren en bundel geïnduceerde schrijven van patronen wordt een Ar Gas Veldemissie Ionenbron gekozen. Deze fabricage techniek maakt gebruik van de energie van de ionen maar het soort ionen is niet van direct belang. Edelgas ionen worden gebruikt om te voorkomen dat de elektronische structuur van het preparaat wordt beïnvloedt door de geïnplanteerde ionen. Bij een Gas Veldemissie Ionenbron wordt het gas ingespoten in de buurt van de scherpe top van een naald die op hoogspanning staat. Het edelgas atoom wordt geïoniseerd wanneer een elektron van het atoom naar de naald tunnelt. Dit is alleen mogelijk als het gasatoom slechts enkele nanometers van de top van de naald is verwijderd. De emissiestroom kan nu worden verbeterd door de naald te koelen tot een bepaalde temperatuur. Bij deze temperatuur beginnen de geadsorbeerde gasatomen te hoppen over de naald ten gevolge van thermische accommodatie. Tijdens elke hop is er een kans op ionisatie omdat het atoom telkens in de ionisatiezone komt. Boven deze temperatuur is de thermische accommodatie te zwak om hoppen te laten beginnen, terwijl bij lagere temperaturen de hoogte van de hops afneemt totdat de atomen slechts nog bewegen over het oppervlak zonder te worden geïoniseerd.

De eerste experimenten in een testopstelling hebben laten zien dat de helderheid van een Gas Veldemissie Ionen bron voldoende hoog is voor "the Fancier". Bronnen met een vergelijkbare helderheid maar een bredere energieverdeling zijn Vloeibaar Metaal Ionenbronnen. Bij deze bron bevindt het materiaal dat geïoniseerd moet worden zich in vloeibare toestand op de naald. Dit maakt emissie mogelijk van vele soorten ionen, zoals Au voor directe depositie van metaal lijnen en B en As voor implantatie van materiaal voor dotering van Si. Deze elementen maken deel uit van een mengsel (AuSi, PdBAs) om te voorkomen dat de bron bij te hoge temperaturen gebruikt moet worden. Dit zou ongewenste chemische reacties met de naald kunnen induceren. Een belangrijke parameter voor stabiele emissie van een Vloeibaar Metaal Ionenbron is goede bevochtiging van de naald met de bedekkingslaag die bestaat uit het materiaal dat geïoniseerd moet worden. Dit wordt gerealiseerd in een apart Ultra Hoog Vacuüm systeem waarin the naald en het materiaal van de bedekkingslaag schoon worden gemaakt alvorens ze in contact met elkaar worden gebracht.

Beide brontypes behoeven bron extractie optiek. Dit kan een tetrode systeem zijn wat het mogelijk maakt om de emissiestroom en de brandpuntsafstand onafhankelijk in te stellen. In het ontwerp moet een optimum worden gevonden tussen de lensaberraties (zij kunnen van belang zijn als de bronlens vergrotend is), uitlijning van de elektrodes (de deeltjes wordt geëmitteerd met een grote openingshoek en daarom zijn ze ver van de as verwijderd), Coulomb interacties (de stroomdichtheid is erg hoog in het gebied van de bron) en diafragma erosie (de stroom is erg hoog in het gebied van de bron).

Na de bronoptiek worden condensor lenzen geplaatst om de bundel te verkleinen. Twee lenstypes zijn beschouwd: rotatiesymmetrische en quadrupool lenzen. Het voordeel van een quadrupool lens is de lagere voedingsspanning. Echter voor een stigmatisch beeld met variabele brandpuntsafstand en vergroting moeten vier quadrupolen worden gecombineerd. De conclusie is getrokken dat een rotatiesymmetrische lens de voorkeur geniet als er voldoende ruimte beschikbaar is. De ontworpen condensor lens heeft een minimale brandpuntsafstand van 6 mm. Zijn aberratie coëfficiënten zijn voldoende klein om de veronderstelling geldig te maken dat de bijdragen van de aberraties van de condensor lenzen aan de uiteindelijke probegrootte verwaarloosd kunnen worden vergeleken met de aberraties van de objectief lens.

De ionen die geëmitteerd worden uit een Vloeibaar Metaal Ionen Bron, hebben een energiespreiding van ongeveer 5 eV (Volle Breedte op Halve Hoogte van de verdeling). Deze brede energiedistributie staat niet toe dat de ionen gefocusseerd worden in een probe met nanometer afmeting vanwege de invloed van chromatische aberraties. Echter er zijn vier technieken om de invloed van chromatische aberraties op de uiteindelijk probegrootte te verkleinen: verhogen van de bundelenergie (maar dit versterkt de bijdrage van de tweede proces stap van structuur fabricage, de preparaat interacties), afname van de openingshoek (maar de stroom neemt af met een factor 4 als de openingshoek wordt gehalveerd), een optisch element met een negatieve chromatische aberratie coëfficiënt zoals een elektrostatische spiegel (maar de ionen worden gestopt door deze spiegel hetgeen tot grote effecten van bundel interacties leidt) en een energiefilter.

Ondanks dat dit filter de stroom met een factor twee laat afnemen als de energiespreiding wordt gehalveerd, lijkt het de beste oplossing te zijn om een nanometer grote probe te verkrijgen. De belangrijkste onderdelen van de horizontale kolom zijn twee 90°-afbuigers en een spleet, samen vormen zij het energiefilter. De eerste 90°-afbuiger scheidt de ionen op basis van hun energie. Zij eindigen op verschillende posities bij de energie scheidende spleet. De breedte van de spleet bepaalt de energiespreiding van de ionen die doorgelaten worden op weg naar het preparaat. De tweede 90°-afbuiger de ionen, die door de spleet zijn heen gekomen, samen op hetzelfde punt nabij het uitgangsvlak van deze afbuiger. Dit maakt de horizontale kolom achromatisch, wat betekent dat de afbeeldingen nabij het intree valk van de eerste 90°-afbuiger en nabij het uittreevlak van de tweede 90°-afbuiger gelijk zijn met uitzondering van de energiespreiding van de ionen in de twee afbeeldingen, die is beperkt. De 90°-afbuigers hebben bolvormige elektrostatische elektrodes met een gemiddelde kromtestraal van 30 mm. Dit is besloten voornamelijk om het inregelen van het systeem eenvoudig te maken omdat een bolvormige afbuiger dubbel focusserend is. Aldus wordt een reële afbeelding gemaakt bij de spleet.

Bij de spleet worden ionen tegen gehouden met een energie die te sterk afwijkt van de centrale energie van de bundel omdat ze eindigen op een afstand vanaf de centrale as die groter is dan de spleetbreedte. Echter ook door andere effecten dan energiespreiding kunnen de ionen van de as afkomen, zoals door trillingen van het systeem. Als gevolg van het optimaliseren tussen de lengte van de horizontale kolom en de spleetbreedte wordt de gedrag van het systeem niet gedomineerd door trillingen. De spleet moet worden ingesteld met micrometer nauwkeurigheid; voor de berekende optimaal energiespreiding bedraagt de spleetbreedte 4.8 μm.

Voor het uitlijnen van het systeem worden multipolen geplaatst bij het intree en het uittreevlak van de 90°-afbuigers, terwijl ook de spleet positie kan worden ingesteld. Ook het gedeelte van de meskanten waarop de bundel terecht komt kan worden ververst omdat zij beschadigd worden door de ionenbundel.

Een deeltjes optisch instrument voor hoge resolutie dat een ionen en een elektronen bundel samenbrengt op dezelfde optische as, behoeft minimaal een gezamenlijke lens: de objectieflens. Om de kleinste bijdragen van aberraties aan de probe te krijgen moet de laatste lens dicht bij het preparaat wordt opgesteld. Slechts in het geval van een gezamenlijke lens kan dit voor beide bundels worden bereikt. Voor de elektronen bundel kan de standaard magnetische lens worden gebruikt. Een elektrostatische lens is geïntegreerd met de magnetische lens, omdat de magnetische lens te zwak is om ook de ionenbundel voldoende te kunnen focusseren. De bovenste poolschoen fungeert als deel van de magnetische lens en als derde elektrode van deze elektrostatische Einzel lens.

De kwaliteit van de magnetische lens is er niet door verslechterd. De sferische en chromatische aberratie coëfficiënten bedragen nog steeds 2.2. mm. De sferische en chromatische aberratie coëfficiënten van de nieuwe elektrostatische lens zijn 1247 mm en 49.5 mm respectievelijk. De constructie is zodanig gemaakt dat de gezamenlijke lens bevestigd kan worden in het instrument op dezelfde wijze als een standaard bovenste poolschoen. De elektrodes van deze lens zijn tevens de elektrodes in de secundaire elektronen detector zoals hierboven beschreven.

Figuur 12.4. toont de resolutie van het ionen optische systeem van "the Fancier" als functie van de energie van de ionen. De afmeting van de probe is beperkt tot 2 nm door de chromatische aberratie bijdrage te beperken met een energiefilter gebaseerd op twee plaats scheidende 90°-afbuigers. Het wordt verondersteld dat de bundel door het hart van alle lenzen gaat en tweede orde aberraties geen invloed van betekenis spelen.. Echter in het algemeen zijn de lenzen niet perfect op dezelfde optische as geplaatst en zijn de gaten in de lenzen niet perfect rond. Vandaar dat afbuigers voor uitlijning nodig zijn omdat foute uitlijning kan leiden tot een aanzienlijk grote afmeting van de probe. Met negen octupolen in het ionen optische systeem wordt de bundel door het hart van alle lenzen

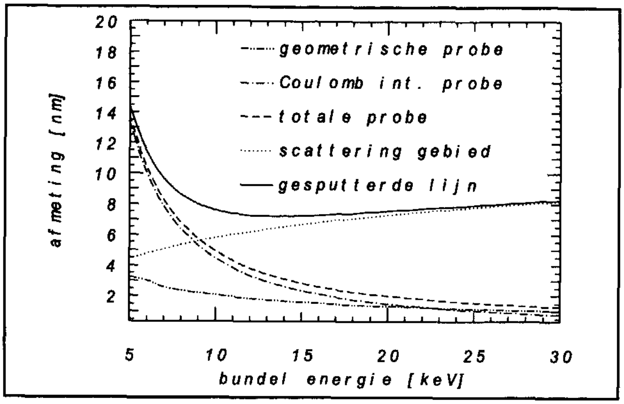

Fig. 12.4. *Afmeting van een structuur in Si gesputtered met Ar ionen (10^{-14} A probe stroom) als functie van de energie van de ionen. De probe afmeting, een combinatie van the geometrische probe bijdrage (verkleinde bron, chromatische en spherische aberraties) en de probe bijdrage van Coulomb intercaties, is afgebeeld samen met het scatter gebied van de ionen in het preparaat.*

geleid teneinde de verlangde resolutie te behalen.

De invloed van Coulomb interacties op de bundel wordt beperkt door een klein diafragma nabij de bron. Dit diafragma beperkt de bundelstroom zodanig dat het systeem kan worden beschreven door de vergelijkingen van een "Pencil beam". Slechts die ionen worden gestopt die toch al zouden worden tegen gehouden verder in het systeem vanwege hun grote hoek ten opzichte van de optische as. Daarom zouden ze alleen effect hebben op de probe door hun interacties met de ionen die in de probe op het preparaat worden gefocusseerd. Dit effect wordt beperkt door ze tegen te houden.

De afmeting van de gefabriceerd structuren volgt uit een convolutie van de plaats distributie van de twee proces stappen van fabricage van structuren: de distributie van de ionen in de probe op het preparaat en de distributie van de preparaat interacties van een individueel ion. De kleinste afmeting van een structuur bedraagt 7 nm bij vervaardiging door middel van sputteren. Vergeleken met commercieel verkrijgbare gecombineerde ionen- en elektronenbundel systemen met niet samenvallende bundels, betekent dit een significant kleinere probeafmeting bij gelijke stroomdichtheid. Met een vertragend preparaat kan de resolutie van de gesputterde lijn zelfs worden verbeterd tot 3 nm. Dit biedt ook de mogelijkheid voor fabricage van structuren door middel van directe depositie waarvoor de landingsenergie van de ionen kleiner moet zijn dan 1 keV.

Focusseren van de bundel in een probe op nanometer schaal is noodzakelijk maar niet voldoende voor de fabricage van mesoscopische structuren. Voor alle fabricage technieken moet de bundel gericht worden langs het gewenste patroon met afbuigers. Een dubbele afbuiger vóór de objectieflens wordt gebruikt om de verlangde resolutie van zowel de ionen- als de elektronenbundel te combineren met een groot gezichtsveld. Hiermee is het mogelijk om de bundel door het centrum van de objectieflens te sturen terwijl het gezichtsveld nog 50x50 μm kan zijn voor de ionen bij de hoogste resolutie en voor de elektronen varieert van 2x2 mm tot 1x1 μm. Dit optische schema minimaliseert de invloed van niet rotatiesymmetrische aberraties van de objectieflens. De combinatie van deze gezichtsvelden met het vector scan protocol van belichting geeft voldoende produktiesnelheid om problemen met stabiliteit te voorkomen. Een typische structuur kan geschreven worden met de ionen bundel op de beste resolutie binnen ongeveer 450 seconden. Voor de elektronenbundel kan de dubbele magnetische afbuiger van de elektronen microscoop worden gebruikt, maar voor de ionenbundel is een nieuwe elektrostatische afbuiger ontwikkeld. Hij bestaat uit acht-polen die geplaatst zijn binnen de uitlijningsbuis van de objectieflens met een binnendiameter van 10 mm.

Nu de bundels gericht kunnen worden op een specifieke positie op het preparaat kunnen structuren worden vervaardigd door middel van directe implantatie en sputteren. Echter voor bundel geïnduceerd etsen en deponeren moet een systeem voor gastoevoer worden ontwikkeld. Het precursor materiaal wordt toegevoerd door een dunne buis. Dit verkleind de hoeveelheid precursor materiaal in het vacuüm systeem doordat het gas lokaal in het gezichtsveld op het preparaat wordt binnen gelaten. Deze dunne buis is verbonden aan een reservoir met aansluitingen voor pompen en druk meten. Ook de precursorcontainers met het materiaal dat nodig is voor etsen en deponeren zijn verbonden aan dit reservoir. Door de container met vloeibare of vaste precursor te verhitten tot een temperatuur van 350 K ontstaat een voldoende grote stroom van damp door de dunne pijp voor een grote verscheidenheid van precursoren. Als de precursor in de gasfase is bij kamertemperatuur wordt een servoklep gebruikt met terugkoppeling van de reservoirdruk. In het geval van bundel geïnduceerd vervaardigen van patronen is niet alleen de reservoir temperatuur van belang maar de temperatuur van het preparaat. Het beïnvloedt de snelheid van produktie en de kwaliteit van het produkt. Bij kamertemperatuur bestaan de films uit kleine metalen eilanden vooral omgeven door koolstof omdat de bijprodukten van de reactie opgenomen zijn in de structuren. Bij hogere temperaturen, ongeveer 370 K, worden de films polykristallijn. Vandaar dat verwarming van het preparaat tot 370 K een vereiste faciliteit is voor de preparaathouder. Alle fabricage technieken zoals die hierboven zijn opgesomd, kunnen worden uitgevoerd in "the Fancier" met de beschreven faciliteiten voor patroon vervaardiging op NEXT preparaten.

Het preparaat voor alle systemen in NEXT is een stukje Si van 1 cm^2, de structuren worden geschreven in een centraal gebied van 3 mm. Dit preparaat moet in en uit "the Fancier" worden gesluisd. Omdat "the Fancier" del uit maakt van het NEXT systeem is een Ultra Hoog Vacuüm verbinding ontwikkeld met verticale beweging van de containers met preparaten door een telescopische manipulator, rotatie van een individuele preparaat en horizontaal transport naar de preparaatruimte door een bi-directionele manipulator. Niet alleen tijdens transport maar ook tijdens fabricage is het noodzakelijk om het preparaat te verplaatsen omdat de structuur groter kan zijn dan het gezichtsveld of omdat verschillende structuren op één preparaat moeten worden geschreven. Deze flexibele positionering van het preparaat moet gerealiseerd worden in combinatie met een stijve plaatsen ten opzichte van de objectieflens (relatieve verplaatsingen kleiner dan 0.046 nm) tijdens fabricage. In het bijzonder laag frequente trillingen (100 Hz) vormen een probleem omdat ze onvoldoende gefilterd worden passieve dempers.

Daarom wordt de positie van het preparaat ten opzichte van de objectieflens actief gecontroleerd. In een terugkoppellus kan de positie van het preparaat worden gemeten door middel van capacitieve sensoren en verplaatst met piëzo elektrische actuatoren. Zowel de sensoren als de actuatoren kunnen het beste symmetrisch worden opgesteld rond het preparaat om zoveel mogelijk de problemen van de standaard goniometer van de EM 420 te voorkomen. Deze zijn bijvoorbeeld het gevolg van de sterke invloed van temperatuurschommelingen op de positie van het preparaat en het gebrek aan stijfheid van de constructie. Voor de capacitieve sensoren is een idee beschreven om in-het-vak en vlak-afstand sensoren te combineren. Dit maakt het mogelijk het beste van beide te combineren: flexibiliteit van de in-het-vlak sensoren en nauwkeurigheid of gevoeligheid van de valk-afstand sensor. Bij deze combinatie wordt de overspraak tussen de verplaatsing en kanteling bij een in-het-vlak sensor geminimaliseerd door het meten van de afstanden tussen de elektrodes van de in-het-vlak sensor met een plaat-afstand sensor.

Op de eerste pagina van de *introduction to nanotechnology* staat geschreven dat "we belangrijke vooruitgang in de techniek van het fabriceren op moleculaire schaal mogen verwachten die ons in staat stellen om onze structuren atoom voor atoom te construeren, op vergelijkbare wijze als een bouwvakker een huis steen voor steen bouwt of zoals de natuur levende cellen ontwikkeld. Meer dan 300 pagina's verder kan worden geconcludeerd dat dit nog niet gerealiseerd is. Echter een ontwerp is gepresenteerd voor een gecombineerd ionen- en elektronenbundel systeem dat in staat moet worden geacht om structuren te fabriceren en te analyseren met typische afmetingen van nanometers. Deze structuren kunnen metalen lijnen, groeven in Si of gedoteerde eilanden in Si zijn. Het systeem is in opbouw op dit moment. De auteur spreekt de hoop uit dat "the Fancier" in de nabije toekomst een nuttig instrument zal zijn voor nanofabrikage.

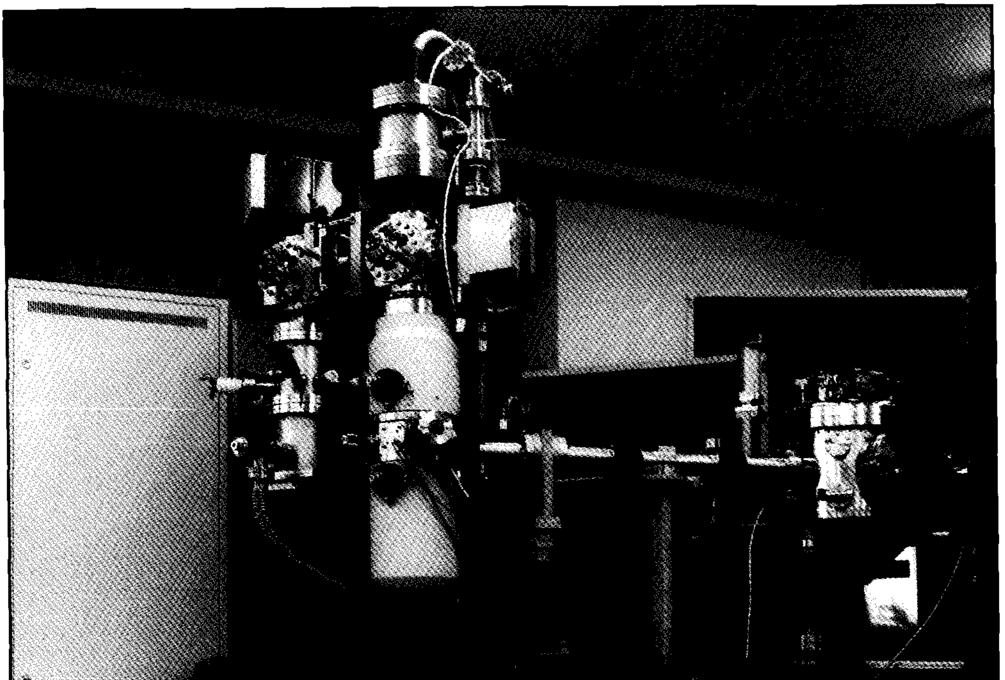

Fig. 12.5. *The Fancier.*

List of publications

P.W.H. de Jager and L.J. Vijgen
Beam interactions in a Focused Ion Beam system with a Liquid Metal Ion Source
Published in: Microelectronic Engineering 23, 1994, pp107-110

P.W.H. de Jager and P.Kruit
Applicability of focused ion beams for nanotechnology
Published in: Microelectronic Engineering 27, 1995, pp. 327-330

ir. P.W.H. de Jager
A method to fabicate nanostructures with a focused ion beam
Published in: Surface and Interface Research and Engineering Delft University of Technology, 1995, pp. 31

P.W.H. de Jager, C.W. Hagen and P.Kruit
The influence of ion beam parameters on pattern resolution
Published in: Microelectronic Engineering 30, 1996, pp. 353-356

P.W.H. de Jager, M.C.W. Kelder and P.Kruit
A combined objective lens for electrons and ions
Published in: Microelectronic Engineering 30, 1996, pp. 427-430

P.W.H. de Jager and P. Kruit
A micro ion probe for in-situ sputtering in the TEM
Published in: Surface and Interface Research and Engineering Delft University of Technology, 1996, pp. 51

P.W.H. de Jager and P. Kruit

Optical design of a combined ion and electron beam system for nanotechnology

Published in: Journal of Vacuum Science and Technology B14(6), 1996, pp. 3753-3758

Dankwoord

Op de voorpagina van dit proefschrift staat één naam en dat is eigenlijk onterecht. Het ontwerpen en bouwen van "the Fancier" (Engels voor iemand die iets bijzonders kweekt) was alleen maar mogelijk omdat een groot aantal mensen hun steentje hebben bijgedragen. In de eerste plaats mijn begeleiders die me de vrijheid hebben gegeven om mijn eigen ideeën te verwezenlijken en zelfs de vrijheid hebben gegeven om op allerlei gebieden binnen de faculteit actief te zijn. *Bedankt daarvoor Pieter Kruit en Bart Geerligs.*

Daarnaast was er een vakgroep waar gemotiveerde AIO's/OIO's, studenten en technici hard werken combineren met gezelligheid. Dan wordt een werkkamer een beetje je thuis. *Bedankt daarvoor (ex-)collega's van de vakgroep Deeltjes Optica.* Speciaal wil ik de studenten noemen die tot "het team" hebben behoord: Maik Bauer, Martijn Fransen, Mark Kelder, Odette Lemmens, Arjen Leine en Lex Molenaar. *Bedankt voor jullie inzet en samenwerking.*

Technische natuurkundig onderzoek zoals het bouwen van "the Fancier", vraagt om meer dan denkers alleen. Dankzij de prettige samenwerking met Otto Wolfs is de hele constructie tot stand gekomen. Vele van zijn tekeningen zijn in dit proefschrift terug te vinden. Dankzij de niet aflatende inzet van alle medewerkers van de afdeling Mechanische Ontwikkeling ontstonden de mooiste onderdelen. Maar zeker dankzij de samenwerking met de technici van de vakgroep Deeltjes Optica ontstond een geheel: "the Fancier". Met name Jan de Looff wil ik bedanken: vele uren hebben we samen gepraat en gesleuteld. *Bedankt voor het vertrouwen dat jullie in mij hadden.*

Mijn aanwezigheid op de faculteit Technische Natuurkunde van de TU Delft heeft mij vele vrienden opgeleverd en heb ik ervaren als een fijne tijd. Daarom wil ik tenslotte iedereen bedanken die mij heeft gesteund in de afgelopen jaren, in het bijzonder mijn twee grootste fans: mijn vader en mijn moeder.

Laat samen werken ook samenwerken zijn.

Curriculum Vitae

Pieter Willem Herman (Patrick) de Jager
geboren 15 juni 1969 te Rotterdam

1981-1987	Voorbereidend Wetenschappelijk Onderwijs aan het Gymnasium Erasmianum te Rotterdam
1987-1992	Technische Natuurkunde aan de Technische Universiteit Delft
1992-1996	Assistent In Opleiding aan de Technische Universiteit Delft, vakgroep Deeltjes Optica
1996-1997	Toegevoegd Onderzoeker aan de Technische Universiteit Delft, vakgroep Vaste Stof - Nano Fysica